A thesis submitted in fulfilment of the requirements for the degree of
Doctor of Philosophy and the Diploma of Imperial College London

---

Computational Analysis of the Haemodynamic Performance of Novel Endovascular and Surgical Procedures for Complex Aortic Diseases

---

Author:
Yu Zhu

Supervisor:
Prof. Xiao Yun Xu

Department of Chemical Engineering
Imperial College London
February 2020

Copyright

Declaration of Originality

I hereby declare that this thesis and the work presented in it are my own as the result of my own investigation expect where otherwise stated. This thesis has not been submitted in whole or in part to another university for the award of any other degree or professional qualifications.

February 29, 2020

Yu Zhu

Acknowledgements

First and foremost, I would like to express my sincerest and deepest gratitude to my supervisor, Prof. Xiao Yun Xu, for the continuous support of my Ph.D. study and related research, for her patience, motivation, and immense knowledge. Her guidance helped me in all the time of research and writing of this thesis. I could not have imagined having a better supervisor for my Ph.D. study. Besides my supervisor, I would like to thank my clinical collaborators, Prof. Mohamad Hamady and Dr. Mirsadraee Saeed, who always made themselves available when I needed advice on clinical data. Thank you very much for reviewing articles, proving insightful comments and valuable advice, and explaining patiently the clinical aspects of this project.

My unconditioned love and gratitude to my parents, not only for funding this research project, but also for your endless support and love. Thank you so much for everything, nothing would have been possible without your sacrifices, encouragement and selfless love. A huge thanks also goes to my other family members, especially my grandparents for their encouragements and supports.

Thank you to all the members from the *Xu Group:* Cindy, Wenbo, Rocky, Andris, Claudia, Shelly, Boram, Toyin, Nasrul, Selene, Moath, Howard, Xiaoxin, Chloe, Emily, Sam, George, Nigel, Baolei, MeiYan, and Simone, for making the office such a warm and happy place and for all the fun we had in the last four years. I will never forget the time that I spent in the office and I will keep those cherished memories forever. In particular, a word of sincere gratitude to Dr. Zhuo Cheng and Dr. Kandail Harkamaljot for their unreservedly technical help and assistance from day one, and for patiently answering my endless stream of questions, even after they have moved on from our group. Thank you also to Prof. Nigel Wood for the weekly inspiring conversations.

Last but certainly not least, I would like to thank my girlfriend, Xinyue, for her encouragements and supports. Though we could only meet once or twice a year, I could still feel her supporting throughout the last four years. Thanks her for understanding that I could not accompany with her: waiting is the company of the longest love.

Abstract

Novel branched stent-grafts (BSG) have been developed for endovascular repair of complex thoracic aortic aneurysms (TAA) involving the aortic arch or thoracoabdominal aorta, but their haemodynamic performance has not been adequately studied. In addition, surgical replacement of the ascending aorta with a Dacron graft remains the gold standard for type A aortic dissection (TAAD), although 12% of patients are at risk of aortic rupture due to further dilatation of the residual dissected aorta. The underlying mechanisms for progressive aortic dilatation following TAAD repair are poorly understood, but haemodynamic and biomechanical factors are believed to play an important role. Therefore, the present study aims to provide more insights into the haemodynamics in novel BSGs developed for treating complex aortic diseases, and a comprehensive evaluation of flow and biomechanical conditions in post-surgery TAADs by means of state-of-the-art computational methods.

The first part of this thesis focuses on evaluating the haemodynamic performance of novel BSG designs, including thoracoabdominal branch endoprosthesis (TAMBE) and dual-branched thoracic endograft. Haemodynamics in idealised and patient-specific BSG models has been analysed by examining side branch outflow waveforms, wall shear stress related indices, and displacement forces, in order to assess their long-term durability. The numerical results show that all the stent-graft models examined in this study are capable of providing normal blood perfusion to side vessels, and are at low risk of in-stent thrombosis and device migration. Furthermore, it has been shown that geometric variations in TAMBE do not affect the key haemodynamic results, indicating its potential suitability for a variety of visceral artery anatomies. Comparisons of dual-branched thoracic endograft models with different inner tunnel diameters suggest that BSGs with larger inner tunnel diameters than the respective vessels would be preferred. Comparisons between the pre- and post-intervention models show that insertion of a dual-branched stent-graft significantly alters the flow pattern in the aortic arch, some of which may have a detrimental effect in the long term, thus requiring follow-up studies.

The second part of the thesis provides a comprehensive analysis of the haemodynamic and biomechanical conditions in surgically repaired TAAD. Geometric and haemodynamic parameters have been analyzed and compared between the group of patients with stable aortic diameter and another group with progressive aortic dilatation. The number of re-entry tears $(6 \pm 5 \text{ vs } 2 \pm 1; \mathrm{P} = 0.02)$ and luminal pressure difference $(1.3 \pm 1 \text{ vs } 11.7 \pm 14.6 \text{ mmHg}; \mathrm{P} = 0.001)$ have been identified as potential predictors of progressive aortic dilatation in TAAD patients following surgical repair. This is an important finding and can potentially assist clinicians to make the most appropriate choice or surgical plan for individual patients. Based on the finite element analysis of four patient-specific cases, there are no clear differences in biomechanical parameters between the stable and unstable groups. Furthermore, a preliminary fluid-solid interaction (FSI) simulation performed on a single TAAD model has demonstrated the important influence of wall compliance on pressures in the true and false lumen. Compared to a rigid wall model, the FSI simulation results show a reduction in systolic pressure by up to 10 mmHg and a slight increase in diastolic pressure. However, pressures in the true and false lumen are affected in the same way, so that the luminal pressure difference remains the same between the rigid and FSI models.

Contents

Abstract iv

List of Figures x

List of Tables xv

Nomenclature xvi

Chapter 1. Introduction 1

1.1 Motivation for Research and Research Strategy 4

1.2 Research Objectives and Thesis Outline 6

Chapter 2. Literature Review 7

2.1 Cardiovascular System and the Aorta 7

2.2 Thoracic Aortic Aneurysm 9

2.2.1 Pathophysiology of Thoracic Aortic Aneurysms 9

2.2.2 Clinical Manifestations 12

2.2.3 Management 12

2.2.4 Post-Operative Complications with TEVAR 21

2.3 Aortic Dissection 22

2.3.1 Risk Factors Associated with Aortic Dissection 24

2.3.2 Diagnosis and Imaging Techniques 24

2.3.3 Open Surgical Repair of Type A Dissections 26

2.4 Numerical Studies of TAA and AD 26

2.4.1 Numerical Studies of Thoracic Aortic Aneurysm 27

2.4.2 Computational Studies of Aortic Dissection 28

2.5 Summary 30

Chapter 3. Mathematical Models and Boundary Conditions 31

3.1 Governing Equations 31

3.1.1 Finite Volume Method (FVM) 32

3.1.2 Finite Element Method (FEM) 33

3.1.3 Fluid-Solid Interaction (FSI) Theory 35

3.2 Geometry Reconstruction and Mesh Generation 36

3.2.1 Idealised Models of Stent-Graft 36

3.2.2 CT Images and Patient-Specific Models 37

3.2.3 Mesh Generation 39

3.2.3.1 Mesh Independence Tests 40

3.3 Numerical Modelling 42

3.3.1 Blood Properties 42

3.3.2 Flow Models 42

3.4 Physiologically Realistic Boundary Conditions 45

3.4.1 Inflow and Wall Boundary Conditions 45

3.4.2 Outflow Boundary Conditions 46

3.5 Comparisons of Two Most Commonly Used Outlet Boundary Conditions 49

3.5.1 Model Geometry and Boundary Conditions 49

3.5.2 CFD Model Details 51

3.5.3 Comparison of Numerical Results against Known Values 51

3.5.4 Comparison of Two Outlet Boundary Conditions 52

3.6 Summary 57

Chapter 4. Application 1: Evaluating the Haemodynamic Performance of Thoracoabdominal Branch Endoprosthesis (TAMBE) 58

4.1 Introduction 58

4.2 Methodology 59

4.2.1 Model Geometry 59

4.2.2 Computational Details 61

4.2.3 Evaluation of Key Haemodynamic Parameters 62

4.3 Results 63

4.3.1 Flow in Branch Vessels 63

4.4.2 Near Wall Haemodynamic Parameters 64

4.4.3 Displacement Force 65

4.4 Discussion 67

4.5 Summary 71

Chapter 5. Application 2: Evaluating the Haemodynamic Performance of a Novel Branched Stent-Graft for Thoracic Endovascular Aortic Repair (TEVAR) 73

5.1 Analysis of Blood Flow in an Idealised Model of Dual-Branched Stent-Graft for Endovascular Repair of the Aortic Arch 73

5.1.1 Introduction 73

5.1.2 Methodology 74

5.1.2.1 Model Geometries and Mesh Generation 74

5.1.2.2 Boundary Conditions and Numerical Procedures 76

5.1.3 Results 77

5.1.3.1 Flow in the Supra-Aortic Vessels 77

5.1.3.2 Wall Shear Stress 79

5.1.3.3 Displacement Forces Acting on the Branched Stent-Grafts 79

5.1.4 Discussion 80

5.1.5 Summary 85

5.2 Patient-Specific Analysis of Aortic Flow before and after Thoracic Endovascular Repair with a Dual-Branched Stent-Graft[1] 85

5.2.1 Introduction 85

5.2.2 Methodology 86

5.2.2.1 Model Geometries and Mesh Generation 86

5.2.2.2 Boundary Conditions and Numerical Approaches 87

5.2.2.3 Haemodynamic Indices 89

5.2.3 Results 90

5.2.3.1 Anatomical Features 90

5.2.3.2 Flow Patterns 91

5.2.3.3 Wall Shear Stress 96

5.2.3.4 Endothelial Cell Activation Potential (ECAP) 103

5.2.3.5 Displacement Forces 104

5.2.4 Discussion 104

5.2.5 Comparisons between the Idealised Models and the Patient-Specific Models 106

5.2.6 Summary 107

Chapter 6. Application 3: Computational Analysis of Haemodynamic Conditions of the Aorta after Surgical Repair of Type A Aortic Dissections 108

6.1 Introduction 108

6.2 Methodology 109

6.2.1 Data Acquisition and Geometry Reconstruction 109

6.2.2 Boundary Conditions 113

6.2.3 Computational Details 115

6.3 Results 115

6.3.1 Anatomical Features 115

6.3.2 Flow Patterns 118

6.3.3 Wall Shear Stress 124

6.3.4 Pressure Difference between True and False Lumen 126

6.3.5 Statistical Analysis 130

6.3.6 Turbulence Intensity 130

6.4 Discussion 132

6.5 Summary 135

Chapter 7. Biomechanical Analysis of Type A Aortic Dissection after Surgical Repair and Fluid-Solid Interaction Simulation 136

7.1 Introduction 136

7.2 Methodology 137

7.2.1 Geometry Reconstruction and Mesh Generation 137

7.2.2 Finite Element Modelling 138

7.2.3 Fluid-Solid Interaction 140

7.3 Results 142

7.3.1 Comparison of Biomechanical Properties of Different Wall Models 142

7.3.2 Comparison between FSI model and Rigid Wall Model 143

7.4 Discussion 146

7.5 Summary 151

Chapter 8. Conclusions and Recommendations 152

8.1 Summary of Main Conclusions 152

8.1.1 Haemodynamic Assessment of TAMBE 152

8.1.2 Haemodynamic Evaluation of a Novel Double-Branched Stent-Graft 154

8.1.3 Evaluation of Haemodynamic Conditions in Surgical Repaired TAADs 155

8.1.4 FE and FSI Analysis of Post-Surgical TAAD 156

8.2 Limitations 157

8.2.1 Blood as a Newtonian Fluid 157

8.2.2 Rigid Wall Assumption 157

8.2.3 Lack of Complete Patient-Specific Pressure and Flow Data 158

8.2.4 Smooth Stent-Graft Walls 158

8.2.5 Cohort Size and *in vivo* Validation 159

8.3 Recommendations for Future Work 160

8.3.1 Virtual Stent-Graft Deployment 160

8.3.2 Incorporation of Thrombus Formation Model 160

8.3.3 Effect of Aortic Root Motion 160

References 162

Appendix A: Presentations and Publications 186

Appendix B: Copyright Permissions 188

List of Figures

1.1 Bifurcated stent-graft for treatment of infrarenal AAA. A healthy aortic neck is necessary or it would not be possible to use the stent-grafts. **A** The main stent-graft endoprosthesis is advanced to the aneurysm site under fluoroscopic conditions. **B** The contralateral iliac limb is positioned in the main stent-graft endoprosthesis and deployed stent-graft forms an artificial conduit for blood flow. Reproduced with permission from Blum et al. (1997), Copyright Massachusetts Medical Society. 2

1.2 **A** Aortic dissection involving the ascending aorta (Type A). A tear in the ascending aorta produces a new channel for blood flow, known as false lumen (FL). Figure reproduced from https://thoracickey.com/10-systemic-vascular-disease/. **B** Surgical repair of type A aortic dissection with ascending aortic replacement results in incomplete resection of re-entry tears in the descending aorta, which may lead to late progressive aortic dilatation. Figure reproduced from Kuratani, (2014) 4

2.1 (a) The schematic of the aorta including the main branches and sections. Figure available at: https://my.clevelandclinic.org/health/treatments/17527-thoracic-aortic-aneurysm-surgery and (b) constitutive layers of a healthy arterial wall (Peate and Nair 2016). 9

2.2 Anatomic classification of thoracic aortic aneurysms (TAAs). Aortic root (a) or ascending aortic aneurysms (b) are accounting for 60% of TAAs, followed by (d) descending thoracic aortic aneurysm (40%), (c) aortic arch aneurysm (10%), and (e) thoracoabdominal aortic aneurysm (10%). Figure adapted from https://weillcornell.org/aortic-aneurysm-and-dissection-repair. .. 10

2.3 Classified zones for the management of thoracic aortic aneurysms. 13

2.4 Two major approaches for aortic valve-sparing operation. (A) Re-implantation of the aortic valve and (B) remodelling of the aortic root (David et al. 2015). 14

2.5 The most common aortic arch surgical repair can be performed through either (a) traditional hemi-arch repair or total arch repair including (b) the island approach, (c) the branched graft approach, (d) the two-stage elephant trunk approach, and (e) the frozen elephant trunk approach. Figure (a) – (c) were reproduced from Lemaire et al. (2011), while (d) and (e) were extracted from Kourliouros et al. (2011). 15

2.6 Four of the commercially available thoracic branched endografts. (A) Valiant Mona LSA (Medtronic) and (B) Gore TAG/TBE (Gore & Associates) are single-branched endografts while (C) dual-branched stent-graft (Bolton Medical) and (D) Zenith arch branched graft (Cook Medical) have two inner tunnels. Figure reproduced from van Bakel et al. (2018). 17

2.7 Respective components of the chimney stent-grafts. A: transverse view of the chimneys grafts, CG represents the renal stent-graft and arrows highlight the potential ''gutters'' between the two stent-grafts. B: configurations of snorkel and periscope chimney stent-graft (Patel et al. 2013). 19

2.8 The latest multi-branched stent-grafts were developed for endovascular repair of complex thoracoabdominal aortic aneurysms. (A) Zenith t-branch stent-graft (Cook Medical), (B) the GORE® EXCLUDER® Thoracoabdominal Branch Endoprosthesis (TAMBE, Gore & Associates) with four antegrade portals, and two retrograde renal portals (C). Figure reproduced from Mendes et al. (2016). 20

2.9 Aortic dissection involves bleeding within the medial layer, forcing the layers to separate and form an intimal flap. (a) In most cases, aortic dissection is caused by an intimal tear, whereas in

some patients, aortic dissection may also result from rupture of vasa vasorum (b). Figure adapted from Nienaber et al. (2016). 23
2.10 The most common classification systems of aortic dissection: Stanford and DeBakey (Nienaber and Eagle 2003). 25

3.1 Discretisation of a domain into control volumes. Adopted from Versteeg and Malalasekera (2007). 32
3.2 Workflow of patient-specific geometry reconstruction from CT scans to mesh generation. (A) CT angiogram of type A dissection with the target lumen areas identified; (B) Multi 2-D cross-sectional slices are manually segmented to separate the true and false lumen; (C) A patient's dissection geometry is defined as the fluid domain of interest. (D) Meshing, where the fluid domain is discretised into a large number of computational cells with local mesh refinement performed; (E) Hybrid unstructured mesh comprising of a tetrahedral core and prismatic wall layers for inlet. 39
3.3 Plots of maximum WSS versus different mesh sizes for two post-surgical TAAD models. 41
3.4 Windkessel effect of vessel wall where elastic energy is stored and released by the aorta during systole and diastole, respectively. Figure adopted from Roy et al. (2012). 47
3.5 Electrical analogues of Windkessel models. (a) 2-EWM; (b) 3-EWM; (c) 4-EWM. Figure modified from Rachid (2017). 48
3.6 Schematic of the computational model employed in this study. Volumetric flow rate waveform was prescribed at the inlet with the assumption of Womersley velocity profile, while two different outlet boundary conditions: 3-EWM and flow split were applied at all outlets in order to directly compare the results. 50
3.7 Predicted pressure waveforms for every outlet with two outlet boundary conditions. Top: flow split BC; bottom: 3-EWM BC. 55
3.8 Predicted flow rate waveforms for each outlet with two different boundary conditions. Retrograde iliac flow during part of diastole was only predicted by the 3-EWM BC. 55
3.9 Comparison of time-averaged wall shear stress (TAWSS) distributions between two boundary conditions: left for 3-EWM and right for flow split. 56
3.10 Comparison of oscillating shear index (OSI) distributions between two boundary conditions: left for 3-EWM and right for flow split. 56
3.11 Comparison of relative residence time (RRT) distributions between two boundary conditions: left for 3-EWM and right for flow split. 57

4.1 (A) Original TAMBE geometry with key dimensions labelled. (B) The modified TAMBE geometry adopted in this study. 60
4.2 Schematic of all the analysed TAMBE geometries: (A) TAMBE model 1, (B) non-planar TAMBE model, (C) TAMBE model 2, (D) TAMBE model 3, (E) TAMBE model 4, and (F) TAMBE model 5. All the planar models are shown in the coronal plane, while the non-planar model is shown in the sagittal plane. The renal take-off angle (TOA) is defined as the angle between main stent-graft endoprosthesis and the renal stent-graft centreline axis. APA refers to anterior/posterior neck angle that is defined as the angle between the y-axis and a line that is perpendicular to the inlet surface in the sagittal plane. 61
4.3 Schematic of the computational model employed in this study. Volumetric flow rate waveform extracted from Taylor et al. (2002) was prescribed at the inlet along with Womersley velocity profiles, while a 3-EWM model was applied at all outlets. 63

4.4 Predicted flow rate waveforms in different branches for all the TAMBE models: (A) renal, (B) iliac, (C) coeliac and (D) SMA. It shows that geometric variations hardly altered flow waveforms in the main branches. 64
4.5 Instantaneously velocity streamlines near the inner portals and inside the branch stent-grafts at maximum flow deceleration. (A) TAMBE model 1, (B) non-planar TAMBE model, (C) TAMBE model 2, (D) TAMBE model 3, (E) TAMBE model 4, and (F) TAMBE model 5. All the models are displayed in the coronal plane. Two large and symmetric flow recirculation zones (FRZs) around the entrance to the renal branches are marked by yellow stars. Red and blue arrows indicate the primary and secondary FRZs inside the renal branches, respectively. The secondary FRZ is absent for TAMBE model 2. 66
4.6 Comparison of TAWSS between all the simulated models, with particular attention to the renal stent-grafts. TAWSS values higher than 10 Pa are shown in red and highlighted, together with the maximum TAWSS values. (A) TAMBE model 1, (B) non-planar TAMBE model, (C) TAMBE model 2, (D) TAMBE model 3, (E) TAMBE model 4, and (F) TAMBE model 5. All the models are displayed in the coronal plane. 68
4.7 ECAP contours for all the simulated TAMBE models in the coronal plane. (A) TAMBE model 1, (B) non-planar TAMBE model, (C) TAMBE model 2, (D) TAMBE model 3, (E) TAMBE model 4, and (F) TAMBE model 5. ECAP is defined as the ratio of OSI to TAWSS, so it can be used to identify regions that simultaneously exposed to high OSI and low TAWSS. Regions where ECAP values higher than 5 (shown in red) were associated with thrombus formation. Similar ECAP distributions were found for all models, with a region of high ECAP (> 5) near the intersection between the bridging stent-grafts and the main stent-graft. 69
4.8 (A) Time variation of the magnitude of displacement forces acting on all the TAMBE stent-grafts. (B) Direction of the displacement force for all the planar TAMBE models as indicated by a red arrow in the coronal plane. (C) Direction of the displacement force for the nonplanar TAMBE model as indicated by a red arrow in the sagittal plane. 70

5.1 The aortic arch model (left) and the three stent-graft models with an inner tunnel diameter of 8 mm, 10 mm, and 12 mm, for stent-graft 1, stent-graft 2, and stent-graft 3, respectively. The LCCA-LSCA bypass procedure was included in all three stent-graft models as highlighted by a red square in stent-graft 1. The LCCA and LSCA were artificially extended by 20 mm so that the resolved flow field was not influenced by the location of outlet boundaries. 75
5.2 Pulsatile velocity waveform adopted from the literature (Tan et al. 2009) was prescribed at the inlet with the assumption of a flat velocity profile. 77
5.3 Predicted flow rate waveforms over one cardiac cycle for all the simulated models at different outlets. 78
5.4 Comparison of instantaneous velocity streamlines between the non-stented (A), stent-graft 1 (B), stent-graft 2 (C), and stent-graft 3 (D) models at two characteristic time points: peak systole (top), and mid-systolic deceleration (bottom). 80
5.5 Comparison of velocity contours in the sagittal plane along with in-plane velocity vectors between the three BSG models: (A) Stent-graft 1, (B) Stent-graft 2, and (C) Stent-graft 3, at mid-systolic deceleration (0.29 s). Detailed flow patterns are shown by local enlargement of the LCCA-LSCA bypass (right column). FRZs in the bypass graft are indicated by red arrows. 82
5.6 Comparison of TAWSS in the four models: (A) non-stented aortic arch (reference case), (B) stent-graft 1, (C) stent-graft 2, and (D) stent-graft 3. TAWSS distributions are displayed in different views to identify areas with (a) very high (>10 Pa) and (b) very low (< 0.4Pa) values. The maximum TAWSS on the walls of all stented geometries are highlighted by the black arrows. 83

5.7 Comparison of resultant displacement forces acting on the stent-graft models. Time dependence of displacement forces follows the pressure waveform very closely. 83
5.8 Two patient-specific models reconstructed from pre- and post-intervention CT images. 87
5.9 Schematic of the computational model employed in this study. Velocity waveform was prescribed at the inlet along with the assumption of a flat velocity profile, while a 3-element Windkessel model was applied at all outlets. 88
5.10 Schematic diagram showing resistance at LCCA and LSCA in the pre- and post- intervention models. 89
5.11 Comparisons of instantaneous velocity streamline in pre- and post- intervention models of (A) patient 1 and (B) patient 2, at three characteristic time points of a cardiac cycle, namely, peak systole (0.15 s), mid-systolic deceleration (0.29 s), and diastole (0.74 s). Blood flow was found to be more organised after intervention as a result of repaired aneurysm. 92
5.12 A,B,C: Comparison of axial velocity contours along with in-plane velocity vectors before and after intervention in the main aortas, IA and LCCA of patient 1(left) and patient 2 (right) at peak systole (0.15s) and mid-systolic deceleration (0.29s).. 94
5.13 Comparison of TAWSS before (left) and after (right) intervention for patient 1 (top) and patient 2 (bottom). Regions with TAWSS values higher than 2.5 Pa are shown in red. Higher TAWSS values were observed in the post-intervention models of both patients. 96
5.14 Comparison of circumferential-averaged wall shear stress (CWSS) at different planes before and after intervention for patient 1 (left) and patient 2 (right) over a cardiac cycle. The CWSS was evaluated as the spatial-averaged WSS along the intersection lines between the cross-sectional planes and the aortic walls (P1-P4) and the arch vessel walls (P5-P8). 98
5.15 Comparison of CWSS range in a cardiac cycle before and after intervention for patient 1 (left) and patient 2 (right). CWSS range at each time-step was calculated as a difference between the maximum and minimum CWSS along the intersection lines between the cross-sectional planes and the aorta (P1-P4), the IA (P5 & P6), and the LCCA (P7 & P8). The maximum ranges of CWSS over a cardice cycle were then identified and highlighted in red. 102
5.16 Comparisons of ECAP distributions between the post-intervention aortas of patient 1(left) and patient 2 (right). Regions highlighted by the red circles had higher ECAP values. 103
5.17 The magnitude of displacement forces experienced by the double-branched stent-grafts of both patients. The displacement force is exerted by blood flow as it passes through the endograft and time dependence of displacement forces follows the pressure waveform very closely. 104

6.1 Geometries of the 17 aortic dissection models. Patients with stable aortic diameters (Group 1) are shown in blue while those with unstable aortic diameters (Group 2) are displayed in red. A transparent view is given in the right for each model where the primary entry tears are indicated by red cycles. 113
6.2 (A) Velocity measurements acquired by Doppler ultrasound; (B) Flow waveform at the inlet of the ascending aorta of a type B dissection taken from the literature (Pirola et al. 2019); (C) Scaled flow waveform based on patient-specific heart rate and maximum inlet velocity; (D) Schematic of the computational model employed in this study. 114
6.3 Instantaneous velocity streamlines for all the 17 models at two characteristic time points: peak systole (left) and mid-systolic deceleration (right). 124
6.4 TAWSS contours in the aortic dissection models of the 17 subjects. Regions with TAWSS higher than 2.5 Pa are shown in red. 125
6.5 Comparison of the maximum TAWSS on the aortic wall between two groups. 126

6.6 Pressure variations in the TL and FL along the dissected aorta for two selected cases: patient G1#9 from group 1 (a) and patient G2#4 from group 2 (b). P1-P8 refer to eight cross-sectional planes along the centrelines of the dissected aorta. P1 is 2 cm distal from the origin of LSCA and P2-P8 are evenly spaced below P1 with an interval of 3 cm. ……128
6.7 Pressure difference between the true and false lumen (PTL - PFL) at the selected cross-sectional planes along the aorta. 129
6.8 The maximum pressure difference between the true and false lumens (absolute values) for all the patients. Group 1 (blue), group 2 (red). 130
6.9 Turbulence intensity (Tu) iso-surfaces in patient G2#6 at peak systole (left) and mid-systolic deceleration phase (right). Tu levels of approximately 8% are shown in blue while much higher Tu levels of approximately 50% are displayed in red. 132

7.1 Reconstructed patient-specific models for the four cases selected for FEA. Graft (light grey) and the aorta (dark grey) are indicated by arrows. 137
7.2 Tetrahedral mesh elements for the dissected wall model (solid domain) are shown for (A) 3D geometry, (B) inlet, and (C) Outlet. 138
7.3 Detailed mesh elements are shown for (A) the FSI model, (B) outlet cross-sectional plane, and (C) cut plane. It can be seen clearly from (B) and (C) that the solid domain (light blue) was discretised into tetrahedral elements, while the fluid domain (red) was meshed with a tetrahedral core and prismatic layers at the wall. 139
7.4 Schematic of the computational model employed for FSI simulation. For flow analysis, patient-specific flow waveform was prescribed at the inlet, while a 3-EWM was applied at all outlets. For structural analysis, zero-displacement constraints were set at inlet and at all outlets. In addition, an external pressure corresponding to the diastolic pressure was applied on the outer walls to recoil the geometry from its diastolic configuration. 141
7.5 Spatial distribution of total displacement in the 4 selected models for FEA. Top: two patients from Group 1; bottom: two patients from Group 2. 142
7.6 Spatial distributions of von Mises stress distributions in all four models. (A) Two patients from Group 1; (B) two patients from Group 2. 145
7.7 Comparison of instantaneous velocity streamlines obtained from the rigid wall model (top) and FSI model (bottom) at peak systole (left) and mid-systolic deceleration (right). 146
7.8 Comparison of volumetric flow rate over a cardiac cycle at the four tears. Locations of the entry-tear and three re-entry tears are highlighted by the red cycles. 147
7.9 Comparison of TAWSS distributions between the rigid wall (left) and FSI (right) models. 147
7.10 Comparison of pressure variations between the rigid wall and FSI models at three selected cross-sections (P1-P3). 148

8.1 Example of incorporating the complete patient-specific pressure and velocity data on type B dissection. (a) *In vivo* pressure measurements. (b) Pre- and (d) post-TEVAR geometric models with flow distributions among all the outlets. (c) Inlet and outlet boundary conditions. Inlet velocity profiles were obtained from the 4D MRI data. Figure adopted from Pirola et al.(2019). 159

List of Tables

3.1 CT scanners and the relative scan parameters used in this study. 38
3.2 Summary of mesh independence tests results showing maximum WSS and maximum velocity and pressure in a region near the proximal tear for different meshes, together with the corresponding percentage difference between two consecutive meshes. 41
3.3 Estimated values of central resistance (R1), peripheral resistance (R2) and compliance (C) for all the outlets. 51
3.4 Comparison of mean flow rates in each artery obtained with two different outlet boundary conditions, together with the corresponding percentage difference from the target values. 52
3.5 Minimum, maximum and mean pressures in each branch artery with 3-EWM outlet BC. 52
3.6 Reported ranges of NWH parameters that are atherogenic. 54

4.1 TOAs and lengths of the renal branches for all the simulated geometries. 60
4.2 Endothelial Cell Activation Potential (ECAP) 99th percentile values for all the simulated TAMBE models. 69

5.1 Essential geometric dimensions used to construct the computational model. 76
5.2 Comparison of mean flow at each outlet in the non-stented aortic arch and 3 stented models, along with the respective percentages of flow split. 79
5.3 Cycle-averaged and maximum displacement forces acting on all the stent-graft models. 84
5.4 Windkessel parameters for all model outlets, include the idealised models simulated in Section 5.1. 90
5.5 Comparison of lumen diameters (mm) between the pre- and post-intervention models. 91
5.6 Comparison of SRI at different locations before and after intervention for both patients. 103
5.7 Cycle-averaged and maximum displacement forces acting on all the stent-graft models. 104

6.1 A summary of key geometric parameters. 117
6.2 Summary of geometric and haemodynamic parameters for the two groups with stable aortic diameters (Group 1) and progressive aortic dilatation (Group 2). 131

7.1 Calculated constants of the Mooney-Rivlin material model. 140

B.1 Figure Copyright permissions. 189

Nomenclature

Abbreviations

EVAR	Endovascular Aneurysm Repair
AAA	Abdominal Aortic Aneurysm
FSG	Fenestrated Stent-Graft
BSG	Branched Stent-Graft
TAA	Thoracic Aortic Aneurysm
TEVAR	Thoracic Endovascular Aortic Repair
LSCA	Left Subclavian Artery
TAAA	Thoracoabdominal Aortic Aneurysm
TAMBE	Thoracoabdominal Branch Endoprosthesis
AD	Aortic Dissection
TL	True Lumen
FL	False Lumen
TAAD	Type A Aortic Dissection
TBAD	Type B Aortic Dissection
CFD	Computational Fluid Dynamic
WSS	Wall Shear Stress
CT	Computed Tomography
CTA	Computed Tomography Angiography
FSI	Fluid-Solid Interaction
DTAA	Descending Thoracic Aortic Aneurysm
TGF-beta	Transforming Growth Factor-beta
BAV	Bicuspid Aortic Valve
TAV	Tricuspid Aortic Valve
ATAA	Ascending Thoracic Aortic Aneurysm
LCCA	Left Common Carotid Artery
IA	Innominate Artery
SMA	Superficial Mesenteric Artery
ET	Elephant Trunk

FDA	Food and Drug Administration
CG	Chimney Graft
MRI	Magnetic Resonance Imaging
TEE	Transoesophageal Echocardiography
IRAD	International Registry of Acute Aortic Dissection
TAWSS	Time-Averaged Wall Shear Stress
OSI	Oscillating Shear Index
RRT	Relative Residence Time
PDE	Partial Differential Equation
FDM	Finite Difference Method
FVM	Finite Volume Method
FEM	Finite Element Method
CV	Control Volume
SST-Tran	Shear Stress Transport Transitional
3-EWM	3-Element Windkessel Model
ODE	Ordinary Differential Equation
BC	Boundary Condition
NWH	Near Wall Haemodynamic
ECAP	Endothelial Cell Activation Potential
TOA	Take-Off Angle
APA	Anterior/Posterior neck Angle
FRZ	Flow Recirculation Zone
DA	Descending Aorta
CWSS	Circumferential Wall Shear Stress
SRI	Shear Range Index
DF	Displacement Force
ATAAD	Acute Type A Aortic Dissection
LVOT	Left Ventricular Outflow Tract
FEA	Finite Element Analysis
PET	Polyethylene terephthalate

Symbols

ρ	Blood density
∇	Vector operator
μ	Blood viscosity
$\emptyset$	General variables for transport equation
Γ	Diffusion coefficient
Re	Reynolds number
$R_e^{\wedge}$	Peak Reynolds number
α	Womersley number
ω_f	Fundamental frequency of pulsatile flow
k	Turbulence kinetic energy
Tu	Turbulence intensity
ϵ	Specific turbulence dissipation rate
ω	Eddy dissipation rate
μ_t	Turbulence viscosity
v_t	Eddy viscosity
γ	Intermittency factor
$\overline{Re_{\theta t}}$	Momentum thickness Reynolds number
μ_P	Blood plasma viscosity
$\boldsymbol{\tau}$	Stress tensor
τ_t	Time-constant of exponential diastolic pressure drop
τ_ω	Wall shear stress
δ	Cartesian distance
λ	Stretch
ε	Strain
ν	Poisson’ ratio
θ	Angle
i	$\sqrt{-1}$
π	3.14
A	Inlet area
a_n, b_n	Fourier coefficients

C	Compliance
c	Pulse wave velocity
D	Aortic diameter
E	Young’s modulus
$\mathbf{f}$	Body force per unit volume
F_d	Displacement force
F_1	Blending function
Δf	Doppler shift
f_0	Ultrasound transmission frequency
I_1, I_2	First and second invariants of the strain tensor
J_0, J_1	Bessel functions of the first kind of order zero and one
$\boldsymbol{n}$	Normal unit vector
p, P	Blood pressure
P_{out}	Distal vasculature pressure
Q	Volumetric flow rate
r, R	Aortic radius
R_1	Proximal resistance
R_2	Distal resistance
R_t	Total resistance
T	Period of the cardiac cycle
t_r	Residence time
T	Cauchy stress
$\mathbf{u}, \mathrm{U}$	Blood velocity
u'	Turbulent velocity fluctuations
W	Strain energy
y^+	Viscous wall unit

Chapter 1

Introduction

Background I: Endovascular Repair of Aortic Aneurysms

Aortic aneurysm refers to abnormal dilatation of the aortic segment and if left untreated, it can have dire consequences. Aortic aneurysms accounted for approximately 152,000 deaths worldwide in 2013, rising from 100,000 in 1990 (GBD 2013 Mortality and Causes of Death Collaborators. 2015). The most common site for aortic aneurysms is the infrarenal abdominal aorta, followed by thoracic aneurysms in the ascending aorta. The traditional method for treating aortic aneurysms is open surgical repair, which is not only a very traumatic experience for the patient, but is also related to high mortality and morbidity rates. As an alternative, endovascular aneurysm repair (EVAR) is a minimally invasive method in which a stent-graft is deployed in the aneurysm sac through a small puncture made in the groin. After deployment, stent-graft works as an artificial conduit for blood flow, excluding the aneurysm sac from high-pressure blood flow and thus preventing wall rupture (Figure 1.1).

The term ''stent-graft'' was initially proposed by Dotter et al. (1983), referring to an expandable coil or spiral spring used to improve blood flow by maintaining the luminal diameter. However, this stent-graft differed from current endografts in terms of application and function. The concept of modern endograft was originated from Cragg et al. (1983), who developed a stent-graft for EVAR using a nitinol coil covered with synthetic woven fabric. In 1991, Parodi et al. reported the world's first successful endovascular repair of abdominal aortic aneurysm (AAA) in human, after which more and more physicians around the world started practising this procedure and within two decades, endovascular treatment replaced open surgery as first line choice for AAA patients (Giles et al. 2009).

In fact, most of the stent-grafts available in the early years could only be used for treating infrarenal AAAs, and only if there was a healthy proximal aortic neck, as shown in Figure 1.1. A healthy proximal aortic neck is crucial because it serves as a landing zone for the proximal part of stent-grafts, thereby providing a haemostatic sealing to ensure exclusion of the aneurysm from any blood perfusion. However, this is not possible in cases that involve an angulated aortic neck, altered neck wall composition (such as the presence of thrombus or calcification), short neck length and complex aneurysmal involvement of the juxtarenal, paravisceral and the thoracoabdominal aorta. Deploying a stent-graft above the renal arteries can extend the proximal landing zone but would block blood flow to the kidneys, which can be fatal. It was not until 1999 that Brown and Powell firstly proposed the concept of fenestrated stent-graft (FSG) to overcome this issue. FSG is a customized device with each fenestration on the main endograft corresponding to an ostium of the renal artery and once aligned, a separate stent-graft can be introduced into each renal artery to maintain blood perfusion. Despite their promising results (Bungay et al. 2011; Halak et al. 2006; Shahverdyan et al. 2015), FSGs require weeks to be manufactured and as a result, these devices are not only expensive but also unsuitable for emergency cases. Off-the-shelf branched stent-graft (BSG) can be seen as a successor to FSG, providing a more secure seal with at least 2 cm of overlapping zone between the main stent-graft endoprosthesis and visceral vessel branches. BSG is the latest endograft design that can accommodate large variations in aneurysm morphology and reduce the need for customization.

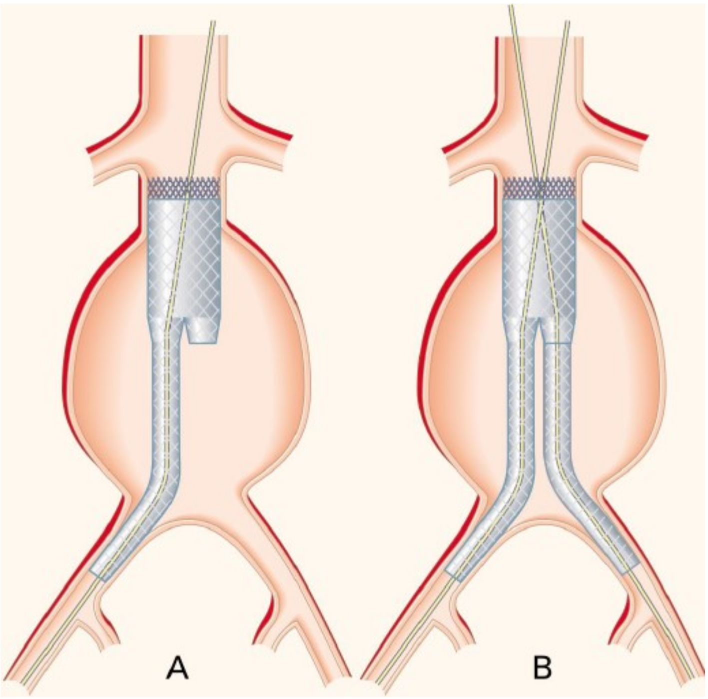

Figure 1.1. Bifurcated stent-graft for treatment of infrarenal AAA. A healthy aortic neck is necessary or it would not be possible to use the stent-grafts. **A** The main stent-graft endoprosthesis is advanced to the aneurysm site under fluoroscopic conditions. **B** The contralateral iliac limb is positioned in the main stent-graft endoprosthesis and deployed stent-graft forms an artificial conduit for blood flow. Reproduced with permission from Blum et al. (1997), Copyright Massachusetts Medical Society.

Although EVAR was originally proposed and adopted for treating diseases of the abdominal aorta, efforts to adapt this technology for the thoracic aorta have been made. Thoracic aortic aneurysm (TAA) patients will benefit greatly from continued development of endovascular techniques because surgical treatment of TAA is more challenging and carries a high operative risk (Katzen et al. 2005). The first successful deployment of stent-graft for TAA exclusion was reported by Dake et al. in 1994, after which thoracic endovascular aortic repair (TEVAR) has been continuously evolving, though the major focus was on the descending segment that is distal to the left subclavian artery (LSCA).

Only recently, attention has been paid to developing endografts that can be used more proximally in the aorta, to treat aneurysms in the aortic arch. Devices for arch repair need to be flexible enough to conform to the inner curvature of the aortic arch, and meanwhile maintain sufficient blood perfusion to the arch vessels. With these challenges in mind, several manufacturers have developed branched endografts that can incorporate the flexibility and compliance of the arterial wall, including Gore, Medtronic, Zenith and Bolton, to name only a few. Around the same period, novel designs have also been developed for treating complex thoracoabdominal aortic aneurysms (TAAAs), i.e. Cook Medical released the first commercially available multi-branched stent-graft, known as Zenith t-Branch stent-graft, followed by GORE® EXCLUDER® thoracoabdominal branch endoprosthesis (TAMBE). Although limited clinical experience worldwide has demonstrated their promising short- to mid-term results (van Bakel et al. 2018; Greenberg et al. 2008; Oderich et al. 2017, 2019; Oderich and Silveira 2016; Sweet et al. 2015), the long-term durability of branched endografts remains unanswered.

Background II: Surgical Repair of Type A Aortic Dissection

As shown in Figure 1.2A, aortic dissection (AD) occurs when the inner layer of the aortic wall tears and blood flows in between the inner and outer layers of the wall, developing a false lumen (FL) in the aorta alongside the original true lumen (TL). Although AD is relatively rare, occurring in 3-5 people per 100,000 per year (Thrumurthy et al. 2012), it is generally considered as one of the most catastrophic diseases that can affect the aorta. The weakening of the aortic wall that occurs in this pathology can lead to aortic rupture within minutes or hours of the acute event, after which the patient's risk of death increases 1 % per hour (Trimarchi et al. 2010). Aortic dissection can be classified into two categories based on the location of primary entry tear: Type A if the entry tear is located in the ascending aorta whilst Type B when the entry tear is situated in the descending aorta.

Medical treatment or endovascular repair is typically adopted for type B aortic dissection (TBAD), while type A aortic dissection (TAAD) represents a more lethal condition that requires urgent surgical intervention to reduce its life-threatening complications. The main aim of surgical repair is to identify and resect the primary entry tear, which is typically located at 2 to 5 cm above the valvular commissure at the outer curvature of the ascending aorta (Kallenbach et al. 2002). Figure 1.2B shows supra-commissural replacement of the ascending aorta, which is an established surgical technique for the treatment of TAAD. Clearly, operative survival does not guarantee freedom from subsequent aortic events, as 64% to 90% operative survivors have a patent FL (Fattouch et al. 2009; Halstead et al. 2007; Kimura et al. 2008; Tan et al. 2005; Zierer et al. 2007). FL patency has been identified as a strong risk factor associated with late adverse outcomes, such as progressive aortic dilatation (Halstead et al. 2007; Marui et al. 1999; Masuda et al. 1991; Onitsuka et al. 2004; Sueyoshi et al. 2004). In fact, following surgical repair, almost 50% of patients with a patent FL have been reported to develop aneurysmal dilatation (Zierer et al. 2007), which may lead to sudden aortic rupture and even death. However, the underlying mechanisms leading to progressive aortic dilatation are still unclear, and there is currently no reliable indicator that can predict the long-term outcome of these patients.

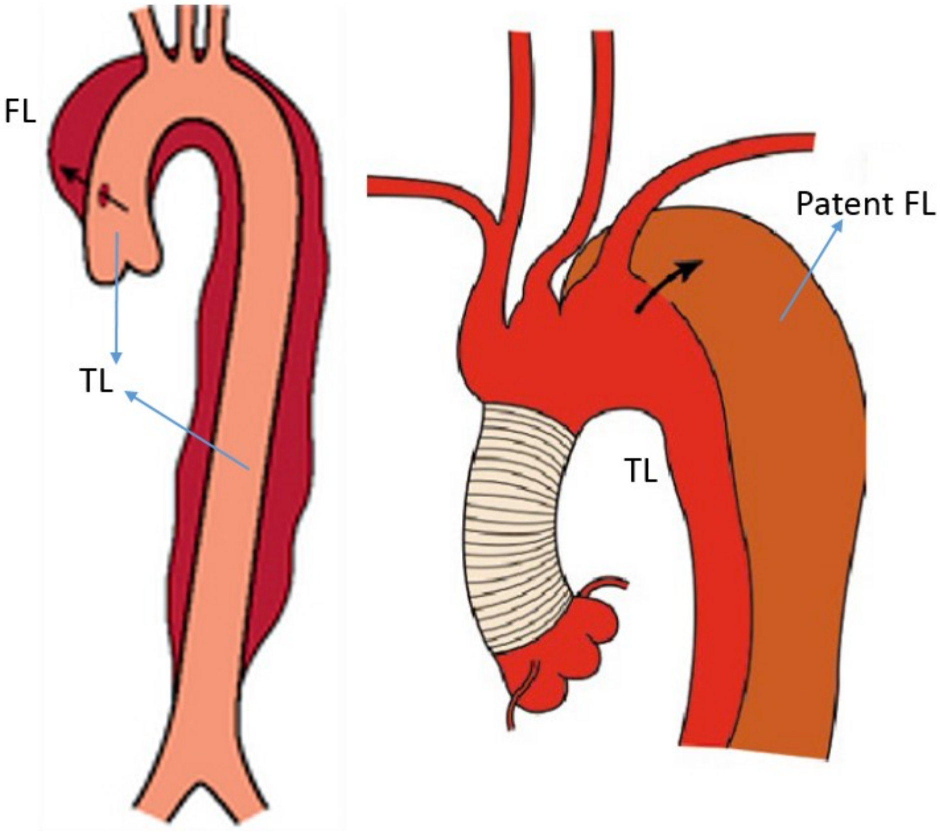

Figure 1.2. A Aortic dissection involving the ascending aorta (Type A). A tear in the ascending aorta produces a new channel for blood flow, known as false lumen (FL). Figure reproduced from https://thoracickey.com/10-systemic-vascular-disease/. **B** Surgical repair of type A aortic dissection with ascending aortic replacement results in incomplete resection of re-entry tears in the descending aorta, which may lead to late progressive aortic dilatation. Figure reproduced from Kuratani, (2014) .

1.1 Motivation for Research and Research Strategy

Compared to endografts used in the treatment of abdominal aneurysms, thoracic endografts are subjected to more aggressive haemodynamic forces, increasing the likelihood of future complications, such as device migration, kinking, and subsequent structural failure. Stent-graft migration can also cause the seal between the aortic wall and the stent-graft to break, thus allowing blood to leak into the aneurysm sac which may require repeat intervention. Additionally, paraplegia remains a potential complication (Buth et al. 2007) resulted from occlusion of blood flow to vital side vessels, due to either stent-graft migration or thrombosis within the stent-graft. Previous computational fluid dynamics (CFD) studies of endovascular AAA repair have shown the advantage of CFD in providing detailed flow phenomenon and haemodynamic conditions in a variety of clinically relevant scenarios (Avrahami et al. 2012; Georgakarakos et al. 2014; Kandail et al. 2014, 2015, 2016; Kleinstreuer et al. 2008; Sun and Chaichana 2010; Šutalo et al. 2008). However, little is known about the haemodynamic performance of novel stent-grafts developed for treating complex aortic diseases including aortic arch aneurysms and TAAAs. Work presented in this thesis addresses this gap in the knowledge by detailed analysis of blood flow in newly designed thoracic stent-grafts, in an attempt to assess their long-term durability.

With regards to progressive aortic dilatation in patients with a patent FL after repair of TAAD, previous studies have identified certain anatomical features as potential risk indicators, including FL patency, maximum diameter, FL area, and the size and location of entry tears (Chang et al. 2008; Evangelista et al. 2012; Kunishige et al. 2006; Marui et al. 1999; Onitsuka et al. 2004; Sueyoshi et al. 2004), but these cannot explain why aortic dilatation occurs. On the other hand, haemodynamic parameters, such as total intraluminal pressure and wall shear stress (WSS) have been reported to directly affect the function of aortic wall (Malek et al. 1999; Rinaudo et al. 2014; Sakamoto et al. 2010), which may play a role in the progression of aneurysmal dilatation. However, knowledge of haemodynamic conditions in repaired TAAD is lacking, and their role in subsequent progressive aortic dilatation has not been investigated. Hence, one chapter in the thesis is devoted to elucidating the role of haemodynamics in the development of aneurysmal dilatation, which may help identify new risk factors for more reliable prediction of late complications for individual patients, thus improving their long-term survival rate.

Complex geometrical features of the aortic aneurysm and dissection often result in abnormal flow patterns and stress distributions. Although some flow parameters can be measured *in vivo* by using ultrasound or magnetic resonance imaging, it is still difficult to acquire information on the entire flow field at sufficiently high accuracy for the calculation of near-wall haemodynamic parameters such as WSS. Furthermore, local pressure cannot be measured non-invasively. For these reasons, CFD has become an indispensable tool for studies of blood flow in the cardiovascular system. This thesis is concerned with the evaluation of endovascular and surgical procedures for the treatment of complex aortic diseases by means of CFD. Computational models for newly designed endografts have been created based on idealised geometries with representative dimensions and patient-specific geometries extracted from medical images. Using idealised stent-graft models is important when assessing new designs when relevant patient-specific data is lacking. The obtained CFD results can be used to assess the long-term durability of novel endovascular devices, and to elucidate the role of haemodynamic factors in late progressive aortic dilatation for surgically repaired type A aortic dissection patients.

1.2 Research Objectives and Thesis Outline

This thesis aims to provide the first comprehensive analysis of blood flow in novel EVAR and TEVAR endografts for the treatment of complex aortic diseases, and in surgically repaired type A aortic dissections. The specific objectives of the research include:

a. To develop a CFD model for the latest multi-branched stent-graft (TAMBE) designed for treating TAAAs, and to evaluate the effects of key geometric parameters on the haemodynamic performance of TAMBE.
b. To develop a CFD model for a novel dual-branched thoracic endograft for the treatment of TAAs involving the aortic arch, and to investigate the effects of inner tunnel diameters on the overall haemodynamic performance of the device based on idealised geometry.
c. To build patient-specific models of the aforementioned dual-branched thoracic endograft based on computed tomography angiography (CTA) images and to analyse the haemodynamic performance of the device in these patients.
d. To build patient-specific models of post-surgical type A aortic dissections based on CTA images, and to determine anatomical features, flow patterns, and distributions of haemodynamic stresses in these models.
e. To identify anatomical and haemodynamic factors that are correlated with the development of aneurysmal dilatation in these patients.

The thesis consists of eight chapters. In Chapter 2, a comprehensive literature review is given of research covering the medical background on both TAA and TAAD, including pathology of the diseases and the currently available treatment options. Chapter 2 also includes a review of CFD studies of flow in models of TAA and aortic dissection. In Chapter 3, the governing equations for blood flow, together with the relevant numerical methods are described, after which the detailed methodology utilized in this thesis is provided, including geometry reconstruction, numerical methods and boundary conditions. Finally, the implementation and validation of the developed methodology are presented. Chapter 4 presents a detailed analysis of blood flow patterns in hypothetical models of a novel device TAMBE for abdominal aortic aneurysms, while Chapter 5 focuses on a dual-branched stent-graft for TEVAR of thoracic aortic aneurysms using both hypothetical and patient-specific geometries. In Chapter 6, anatomical and haemodynamic data on surgically repaired type A aortic dissection patients are analysed to identify the main factors associated with progressive aortic dilatation. Chapter 7 presents a fluid-solid interaction (FSI) simulation of one of the dissected patients, and the results from the FSI simulation are compared with the corresponding CFD results to evaluate the assumption of rigid aortic wall. Finally, conclusions and future works are summarised in Chapter 8.

Chapter 2

Literature Review

2.1 Cardiovascular System and the Aorta

The essential components of the human cardiovascular system include the heart, blood vessels and blood. Through the pulmonary artery, oxygen-depleted blood is pumped into the lungs where gas exchange takes place, and oxygen-rich blood is then returned to the left atrium via pulmonary veins. This newly oxygenated blood enters the left ventricle from where it is pumped through the aorta to different organs of the body. In this system, blood is pumped periodically to provide the entire body with oxygen and nutrients and to remove metabolic wastes (Hall 2010).

The aorta is the largest artery, mainly consisting of the ascending aorta, aortic arch and descending aorta (Figure 2.1 (a)). The ascending aorta originates from the left ventricle, extends obliquely upward and then to the right, forming the aortic arch with a total length of around 5 cm. Three arteries, namely, the innominate artery (IA), left common carotid artery (LCCA), and left subclavian artery (LSCA), arise from the upper part of the arch and are responsible for providing oxygenated blood to the upper part of the body. The descending aorta follows continuously from the aortic arch, and is usually subdivided into the thoracic and abdominal segment. Several arteries derive from the descending aorta supplying blood to the organs in the chest and abdomen, such as the liver, kidneys, to name only a few. The aortic bifurcation is located at the distal end of the abdominal aorta, where it bifurcates into the common iliac arteries to supply blood to the pelvis and lower limbs.

The presence of heart valves ensures that blood flows in the correct direction through the heart. As the aortic valve opens periodically, blood is ejected into the aorta and corresponding to each ejection, a pressure pulse is generated, which drives a pulsatile flow with a mean forward motion. For a healthy adult, this process is repeated around 70 times per minute, amounting to approximately 3 billion times per expected life (Nichols et al. 2011). This means that arterial walls are subject to repetitive tensile stresses. To withstand pressure fluctuations and the resulting wall tension, arterial walls are quite elastic and must regenerate and remodel themselves continuously. A normal aortic wall is composed of three layers (Figure 2.1 (b)), namely intima, media and adventitia, details of which are described below.

Intima

It is the innermost layer that provides a smooth surface for blood to flow through. This is a very thin layer made up of endothelial cells, a basal membrane and supporting connective tissue (Holzapfel et al. 2000). The intima layer is shear-sensitivity since it is in direct contact with blood and the action of blood flow on the intima layer will induce shear stress, which is critical in endothelial cell activation (Raghavan et al. 2005).

Media

This is the middle layer of the artery which is separated from the inner and outer layers by the internal elastic lamina and external elastic lamina, respectively. The tunica media is composed of smooth muscle cells, elastic lamina, elastin fibrils and collagen fibrils. The elastin and collagen fibrils orient regularly and interconnect closely with smooth muscle cells forming a complex three-dimensional network in a helical structure, which affords the media with high strength and resilience in both the longitudinal and circumferential directions. In fact, elastin can bear very light loads but provide elastic recoil for the artery while collagen is much stiffer and can undertake much higher loads and thus preventing over-dilation and rupture of the vessel (Kleinstreuer et al. 2007). Integrity of and cooperation between these compositions make the media the most important layer in response to mechanical actions (Raghavan et al. 1996).

The composition of aortic wall changes with pathologies, such as abdominal aortic aneurysms (AAA). For a healthy adult, collagen accounts for around 54.8% of the aorta, while elastin and smooth muscle cells occupy 22.7% and 22.6%, respectively, but in AAA walls, collagen can reach up to 95.5%, almost double the amount in normal aortic walls (He and Roach 1994). Nichols et al. (2011) also confirmed that the normal collagen-to-elastin ratio was 1.58 and the ratio increased sharply in AAA. Moreover, as described by Kleinstreuer et al. (2007), an aneurysm usually forms after elastin degradation and it grows slowly in the early stages since collagen also degrades although offset by collagen production. In the late stage, the rate of collagen degradation exceeds the rate of AAA wall remodelling, leading to possible aneurysm rupture.

Adventitia

This is the outermost layer which provides additional support and structure to the aorta and consists mainly of connective tissues including collagen fibrils, fibroblast and fibrocytes. The tunica adventitia becomes much stiffer as the level of pressure increases, which helps the artery resist overstretching and rupture.

2.2 Thoracic Aortic Aneurysm

Aneurysm derives from the Greek word, *aneurusma*, meaning widening, and therefore aortic aneurysm (AA) can be defined as a portion of the aortic wall weaken and distend permanently. As the aneurysm expands, it may rupture which can be fatal. Although thoracic aortic aneurysm (TAA) is less common than abdominal aortic aneurysm (AAA) (Assar and Zarins 2009), with an estimated incidence of 5 – 10 cases per 100,000 patients per annum (Kuzmik et al. 2012), it represents a life-threatening cardiovascular disease. One study reported that 59% of patients with ruptured TAA died before they reached a hospital (Johansson et al. 1995). For those patients who could survive to operation, the mortality rate is still higher than 20% during the procedure, whether they were treated by surgical repair or endovascular repair (Gopaldas et al. 2011). As shown in Figure 2.2, TAAs can be classified based on their location. Aortic root or ascending aortic aneurysms are most common (60%), followed by aneurysms of the descending aorta (40%), arch aneurysms (10%), and thoracoabdominal aortic aneurysms (10%) (Isselbacher 2005).

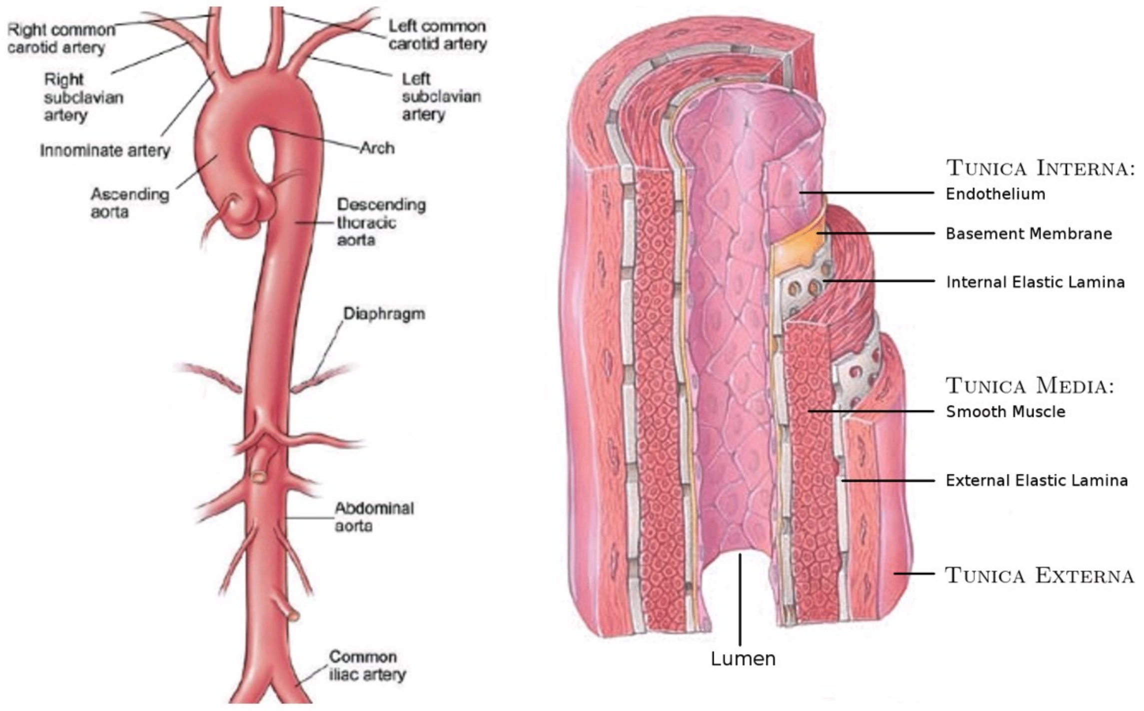

(a) (b)

Figure 2.1. (a) The schematic of the aorta including the main branches and sections. Figure available at: https://my.clevelandclinic.org/health/treatments/17527-thoracic-aortic-aneurysm-surgery and (b) constitutive layers of a healthy arterial wall (Peate and Nair 2016).

2.2.1 Pathophysiology of Thoracic Aortic Aneurysms

The exact reason for TAA formation is still unknown, but it is believed to be multifactorial and primarily cystic medial degeneration, resulting in gradual wall weakening. Cystic medial degeneration is characterized by destruction of the smooth muscle, collagen and elastin of the blood vessels, which can be triggered by both genetic and non-genetic aetiologies (Clare et al. 2016).

Non-genetic aetiologies include atherosclerosis and traumatic injury mainly causing the descending thoracic aortic aneurysms (DTAAs) (Guo et al. 2001, 2006; Isselbacher 2005). Atherosclerosis causes medial degeneration as a result of inflammatory response (Guo et al. 2006). Traumatic injury to the aorta can lead to a partial or complete transection of the descending aorta distal to the left subclavian artery. Most of the patients with such horizontal tears die within an hour. However, 1% to 2% of these patients develop a chronic pseudoaneurysm at the site of initial tear, which is not identified initially (Isselbacher 2005). Syphilis, on the other hand, mainly affects the ascending thoracic aorta through direct spirochetal infection of the aortic media. This process leads to an obliterative endarteritis of the vasa vasorum and therefore resulting in destruction of the collagen and elastic tissue, fibrosis, calcification, and aortic dilation (Isselbacher 2005).

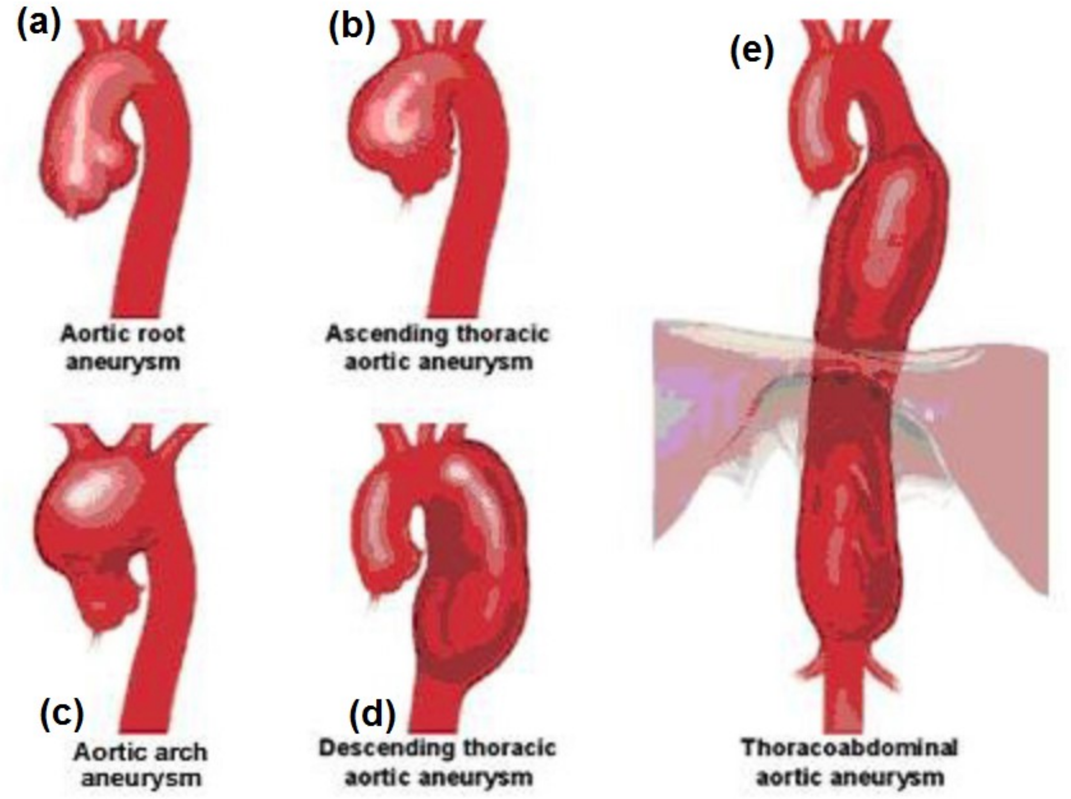

Figure 2.2. Anatomic classification of thoracic aortic aneurysms (TAAs). Aortic root (a) or ascending aortic aneurysms (b) are accounting for 60% of TAAs, followed by (d) descending thoracic aortic aneurysm (40%), (c) aortic arch aneurysm (10%), and (e) thoracoabdominal aortic aneurysm (10%). Figure adapted from https://weillcornell.org/aortic-aneurysm-and-dissection-repair.

Ascending thoracic aortic aneurysms frequently result from genetic aetiologies, such as Marfan syndrome and bicuspid aortic valves. These diseases are caused by genetic disorders of the connective tissue. For example, Marfan syndrome is a result of mutations in FBN1 gene for fibrillin-1, which is an essential component of microfibrils of elastin that are mainly located in the medial aortic wall (Pyeritz 2016; Robinson et al. 2006). These mutations lead to an abnormal microfibril structure, which further contributes to dysregulated transforming growth factor beta (TGF-beta) signalling and altered cell matrix interaction (Dietz et al. 2006). These abnormalities result in Marfan syndrome causing a predisposition to develop predominately aortic aneurysms and dissections (Pyeritz 2016). Similar to Marfan syndrome, Loeys-Dietz syndrome can also affect TFG-beta signalling but through a mutation in transforming growth factor beta receptor type 1 or 2 genes (TGFBR 1 and TGFBR 2) (Loeys et al. 2005). Ehlers-Danlos syndrome is a less common connect tissue disorder attributed to a mutation in the COL3A1 gene encoding type III collagen (Germain 2002). Ehlers-Danlos patients can be associated with various cardiovascular complications and 28 % of them have aortic root dilations (Wenstrup et al. 2002). All these syndromes increase the risk of developing a TAA in young patients (Isselbacher 2005; Loeys et al. 2005).

Bicuspid aortic valve (BAV) has been reported to relate to ascending aortic dilation, regardless of the valve is normally functioning or dysfunctional (Cecconi et al. 2005; Nistri et al. 1999; Nkomo et al. 2003; Siu and Silversides 2010). BAV causes a TAA as a result of cystic medial degeneration. Based on recent studies, abnormal behaviour of smooth muscle cells within the aortic media can cause abnormal functions of the extracellular matrix protein fibrillin 1, which triggers detachment of smooth muscle cells from the extracellular matrix. These abnormalities result in the release of matrix metalloproteinases (MMPs) and their tissue inhibitors, further leading to increased apoptosis of smooth muscle cells and degeneration of the medial layer. As a result, the structural integrity and flexibility of the aorta are destructed, increasing the potential risk of aortic dilatation (Fedak et al. 2003; Siu and Silversides 2010; Tadros et al. 2009; Verma and Siu 2014). Patients with Turner syndrome are associated with a high incidence of ascending TAA (ATAA), up to 42% (Elsheikh et al. 2001), and this value would be much higher in those patients also present with BAV.

Familial thoracic aortic aneurysm syndrome was observed when 19% of patients had a family history of a TAA (Coady et al. 1999). The most common inheritance pattern was autosomal-dominant mode, where a gene affecting the vascular wall integrity is transmitted. However, there is large variability in the expression and penetrance, such as autosomal-dominant with reduced penetrance or versus X-linked dominant. When compared with a sporadic group, familial TAA group exhibited a younger age (58.2 vs. 65.7 years) but greater growth rate (0.21 vs. 0.16 cm) (Albornoz et al. 2006).

2.2.2 Clinical Manifestations

TAAs are silent but lethal since they are seldomly detected before an acute event, such as a dissected or even a ruptured aneurysm. In most cases, they are discovered coincidently during physical examination for an unrelated problem or until symptoms appear (Hall 2010). Clinical symptoms include chest pain, back pain, flank pain, hoarseness, dysphagia, and dyspnoea (Svensson et al. 2008), and once present, aneurysms must be resected regardless of their size (Isselbacher 2005).

Once a TAA is confirmed, clinicians currently reply on the maximum diameter to estimate its risk of rupture, due to the lack of other reliable methods to accurately predict how an aneurysm may progress and at what point it may rupture. As reported by Coady et al. (1997), the median rupture size for ATAAs is approximately 6 cm, which is significantly lower than 7.2 cm for DTAAs. Therefore, all patients with ascending aortic aneurysms larger than 6 cm should be considered for either open or endovascular repair unless there are excessive perioperative risks or unfavourable anatomical features. In fact, based on the 2014 European Society of Cardiology (ESC) guidelines on the diagnosis and treatment of aortic diseases, surgical repair of asymptomatic aneurysms of the ascending aorta and aortic arch is usually recommended when the maximum diameter is $\geq$ 5.5 cm, or if the maximum descending thoracic aortic diameter is $\geq$ 6 cm (Erbel et al. 2014). For ascending aortic aneurysms, a lower threshold of 5 cm can be considered in patients with Marfan syndrome (Erbel et al. 2014). Nevertheless, a less invasive endovascular repair of DTAAs can be performed at a threshold value of 5.5 cm (Hiratzka et al. 2010). Other indications for TAA repair include patients with saccular aneurysm sacs, thoracic aortic pseudoaneurysms, and symptomatic aneurysms.

Aneurysm repair is also recommended for patients with a growth rate of larger than 3 mm per year (Erbel et al. 2014; Katzen et al. 2005). TAA is an indolent process with a growth rate of 0.1 cm annually in the ascending aorta, compared with 0.29 cm per year in the descending aorta (Coady et al. 1997). TAA growth rate also depends on its initial size, for example, a small TAA (4 cm) usually expands 0.1 cm per year while a large TAA (8 cm) grows almost twice as fast (Coady et al. 1997). As mentioned previously, the underlying pathophysiologic mechanism can affect TAA growth rate as well. For example, growth rate of a familial TAA group is 0.21 cm per year, which is much higher than 0.16 cm and 0.1 cm per year, for sporadic TAA and Marfan patients, respectively (Albornoz et al. 2006).

2.2.3 Management

There are two broad methods for treating TAAs and the traditional method is open surgery, which involves surgical replacement of part of the aorta. During the surgical procedure, the chest is cut open to expose the aneurysm, which is followed by clamping the proximal and distal parts of the diseased aorta to temporarily impede blood flow to the aneurysm sac. The diseased aorta segment is then removed and replaced by a synthetic prosthetic-graft. Since the procedure is quite complex, involving a large incision and a long period of ischaemia, the mortality rate is high. Thoracic endovascular aortic repair (TEVAR) has been developed over 2 decades and is less invasive when compared with open surgical repair. It uses a stent-graft which consists of a metal meshwork tube (stent) formed by stainless steel or nitinol wires and a polymer-based graft mounted on the tube. The stent-graft is usually delivered to the aneurysm site through a femoral artery without the need for thoracotomy or aortic clamping, thus eliminating major bleeding complications that may occur during open surgical repair. After deployment, stent-graft serves as an artificial conduit for normal blood flow while preventing any blood flow from entering the aneurysm sac.

The management of TAA can be complicated and varies according to the affected location of the aneurysm. As shown in Figure 2.3, aneurysms can be categorized by zones, as described by Clare et al. (2016): Z0 is located in the ascending aorta, including the takeoff of IA, Z1 and Z2 are located immediately distal to the IA and the LCCA, respectively, and Z3 and Z4 are located distal to the LSCA, representing the descending thoracic aorta. Additionally, Z3 refers to an aneurysm locating closely to the origin of the LSCA (within 2 cm). Treatment methods are summarised below based on these classified zones.

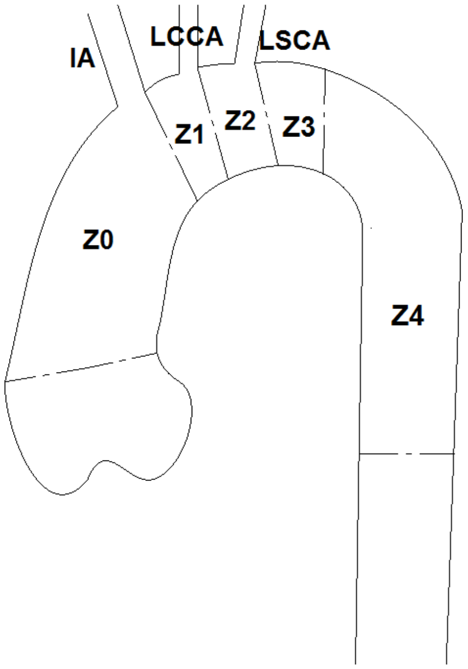

Figure 2.3. Classified zones for the management of thoracic aortic aneurysms.

Z0: Aortic Root and Ascending Aorta

Although endovascular repair is conceptually more appealing than open surgery, its application in this region is still limited due to unfavourable anatomical features. For example, stent-graft must be short in this region to avoid impeding blood perfusion to the branch vessels. A short graft may be less stable and cause migration needing secondary interventions. Moreover, a stiff endograft system must be placed in the left ventricle through the aortic valve, which increases the risk for ventricular perforation (Clare et al. 2016). Therefore, stent-grafting of the ascending aorta should only be reserved for high-risk patients (Kolvenbach et al. 2011).

Surgery for ATAA or aortic root aneurysm involves replacing the ascending aorta with or without preservation of the aortic valve. In fact, the more-recent aortic valve-sparing techniques are much preferable, as they avoid the requirement of lifelong anticoagulation medication (Nienaber et al. 2016). As shown in Figure 2.4, valve-sparing approaches include re-implantation of the aortic valve or remodelling of the aortic root. A main difference between these two approaches is whether the original annulus is resected or not. In cases of severe aortic valve diseases, the aortic valve has to be replaced through either a composite valve graft, or a separate valve that is assembled into a Dacron graft during the procedure (Clare et al. 2016). Valve replacement approach has been reported to cause a much higher mortality rate than valve-spring techniques (De Oliveira et al. 2003).

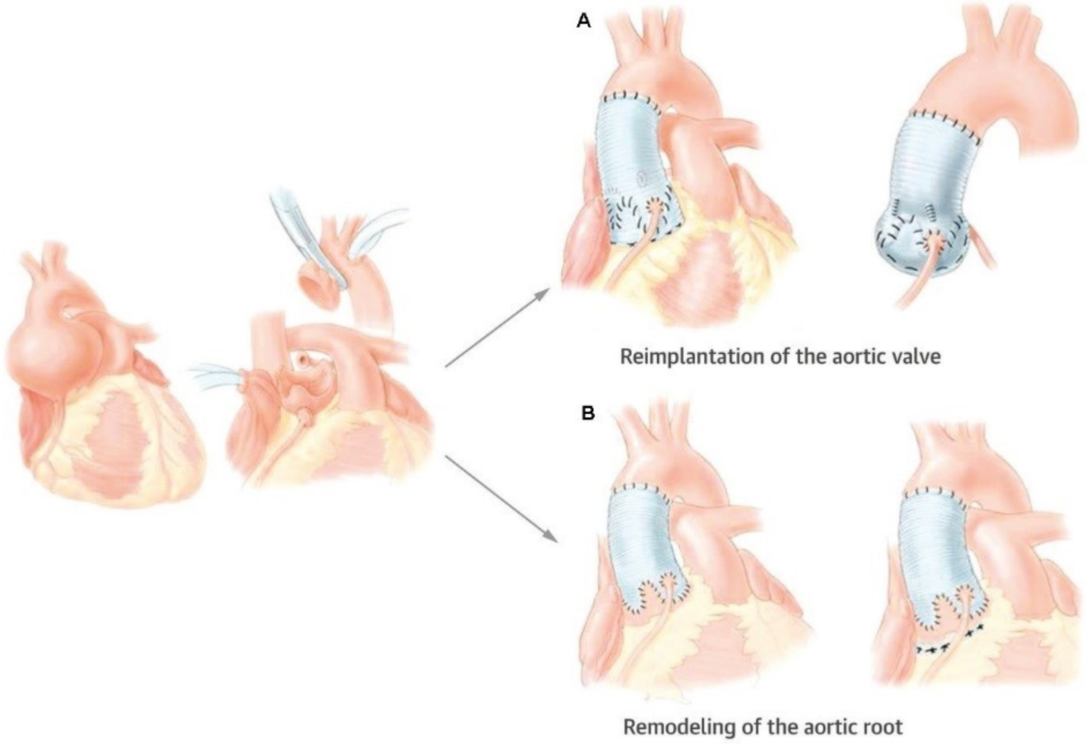

Figure 2.4. Two major approaches for aortic valve-sparing operation. (A) Re-implantation of the aortic valve and (B) remodelling of the aortic root (David et al. 2015).

Z1-Z2: Aortic Arch

Open Surgical Repair*:* the conventional procedure for treatment of aortic arch pathologies is open surgery, which has been developed over several decades since the first reported case in 1964 (Borst et al. 1964). As shown in Figure 2.5, aortic arch surgical repair can be performed through: (a) a hemi-arch technique, (b) an arch island technique (en bloc), (c) a branched graft technique, (d) a conventional two-stage elephant trunk (ET) procedure, or (e) a frozen ET procedure. A hemi-arch technique is applied for patients with aneurysmal involvement limited to the proximal aortic arch. This is the simplest arch repair approach with favourable outcomes. Both the arch island technique and branched graft technique were developed for a more complex total arch replacement. Although there was no statistically significant difference in post-operative mortality rates between these two methods (Shrestha et al. 2014), branched graft technique may reduce not only cardiopulmonary bypass time but also risks of future embolic events (Clare et al. 2016). The most complicated ET technique was developed for treatment of extensive aneurysms involving the aortic arch and descending aorta (Borst et al. 1983; Karck et al. 2003; Miyamoto 2014). Stage one of the conventional ET procedure involves a midline sternotomy to replace the diseased arch with a synthetic graft, with the distal end of the ET graft being freely suspended within the descending aorta, as shown in Figure 2.5 (d). The second stage can then be completed by either suturing a thoracic aortic graft to the ET graft via left thoracotomy, or by placing a stent-graft. Since the original two-stage ET approach has been reported to relate to high mortality rates, single stage approaches have been adopted, such as the frozen ET technique (Figure 2.5 e), which was first proposed by Karck et al. (2003). This is a hybrid approach that combines the conventional arch replacement with downstream deployment of a stent-graft through an open arch. When compared with the conventional two-stage ET technique, the frozen ET may potentially reduce the risk of thrombus formation (Kourliouros et al. 2011).

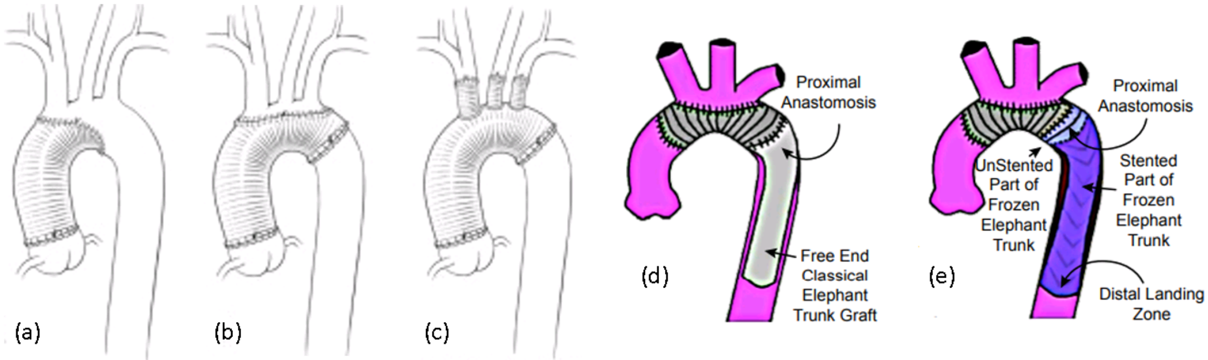

Figure 2.5. The most common aortic arch surgical repair can be performed through either (a) traditional hemi-arch repair or total arch repair including (b) the island approach, (c) the branched graft approach, (d) the two-stage elephant trunk approach, and (e) the frozen elephant trunk approach. Figure (a) – (c) were reproduced from Lemaire et al. (2011), while (d) and (e) were extracted from Kourliouros et al. (2011).

Surgery for aortic arch is associated with significant early morbidity and mortality. Despite the technique has been developed over several decades and modern surgery is always accompanied with the introduction of extracorporeal circulation to decrease the risk of cerebral ischaemia, a significant mortality rate of 7% - 17% is reported (Shirakawa et al. 2014).

Hybrid: according to Bavaria et al. (2013), hybrid arch repair can be classified into three types, where type 3 is the frozen ET procedure as mentioned above. Types 1 and 2 both include debranching of the supra-aortic vessels followed by TEVAR of the arch. However, type 2 involves an additional procedure of ascending aorta or hemi-arch replacement. Although hybrid approach is considered less invasive than open surgery as there is no need for aortic cross-clamping and hypothermic circulatory arrest, the mortality rate remains high (Benedetto et al. 2013; Iba et al. 2014; Tokuda et al. 2016).

Endovascular Repair: Endografting of the aortic arch can be classified based on the location of the proximal landing site, using the same anatomical map shown in Figure 2.3. For example, Z3 means that stent-graft is deployed in the distal arch, Z2 if stent-graft is placed distal to the LCCA region with the LSCA being occluded, Z1 is located immediately distal to the IA which means that both the LCCA and LSCA are occluded and Z0 is located in the ascending aorta, thus blocking all three supra-aortic vessels (Balm et al. 2000).

In order to maintain the long-term durability of TEVAR, a healthy proximal aortic neck is crucial because it can provide a haemostatic sealing to ensure exclusion of the aneurysm without developing type I endoleaks, while achieving adequate fixation of the device to prevent migration. However, this is difficult for arch repair as a result of its angulated nature, together with the presence of three supra-aortic vessels with their roots being close to each other. Although intentionally covering some of the upper vessels can extend the proximal landing zone, this may result in other adverse consequences, such as stroke, upper extremity and cerebral ischaemia (Waterford et al. 2016; Zamor et al. 2015). Therefore, a major challenge is to maintain blood perfusion to the upper vessels while ensure a sealing zone for stent-graft. To overcome this challenge, branched and fenestrated stent-grafts (FSGs) have been developed. FSGs are customized devices with each fenestration on the main endograft corresponding to an ostium of the supra-aortic artery, thereby ensuring blood perfusion into the brain. FSGs have shown high technical success (Bungay et al. 2011; Halak et al. 2006; Shahverdyan et al. 2015), but these highly customized devices usually require weeks to be made, hence not suitable for urgent cases . Off-the-shelf branched stent-grafts (BSGs) have recently been developed to replace FSG. Novel BSG devices are designed to be adaptable to a wide range of anatomical features and therefore conceptually more appealing.

Figure 2.6 shows several commercially available BSG devices, including the *Valiant Mona LSA (Medtronic)*, *Gore TAG/TBE (WL Gore & Associates)*, *Relay thoracic stent-graft system (Bolton Medical)*, and *Zenith arch branched graft (Cook Medical)*. Gore TAG, among the others, was the first Food and

Drug Administration (FDA) approved thoracic endo-device in 2005, while Boston Relay Prosthesis was a more recent FDA approved endo-device in 2012. The Valiant Mona LSA and Gore TAG are single-branched endografts primarily for Z2 deployment. Both devices use a bridging stent to connect to the LSCA; however, the Gore device has a retrograde oriented inner branch, which is absent in the Medtronic device. This orientation appears to cause no adverse clinical consequences (Patel et al. 2016). The other two devices were developed mainly for Z0 aortic treatment with two side branches extending into the IA and LCCA, separately. An additional procedure of LSCA revascularization is required and usually performed through a LCCA-LSCA bypass, which may increase the risk of neurologic complications (Ferrer and Cao 2018). When comparing the Boston device with the Cook device, the main differences are location and size of the two internal branches. In the Boston design, two inner tunnels have the same size and are positioned equidistant from the proximal edge of the main stent-graft, while in the Cook design, the inner tunnel connecting to the LCCA is often smaller and placed diagonally behind the IA inner branch (van Bakel et al. 2018). Moreover, in the Bolton design, both tunnels are fixed by inner dull barbs to prevent potential dislocation of the branches.

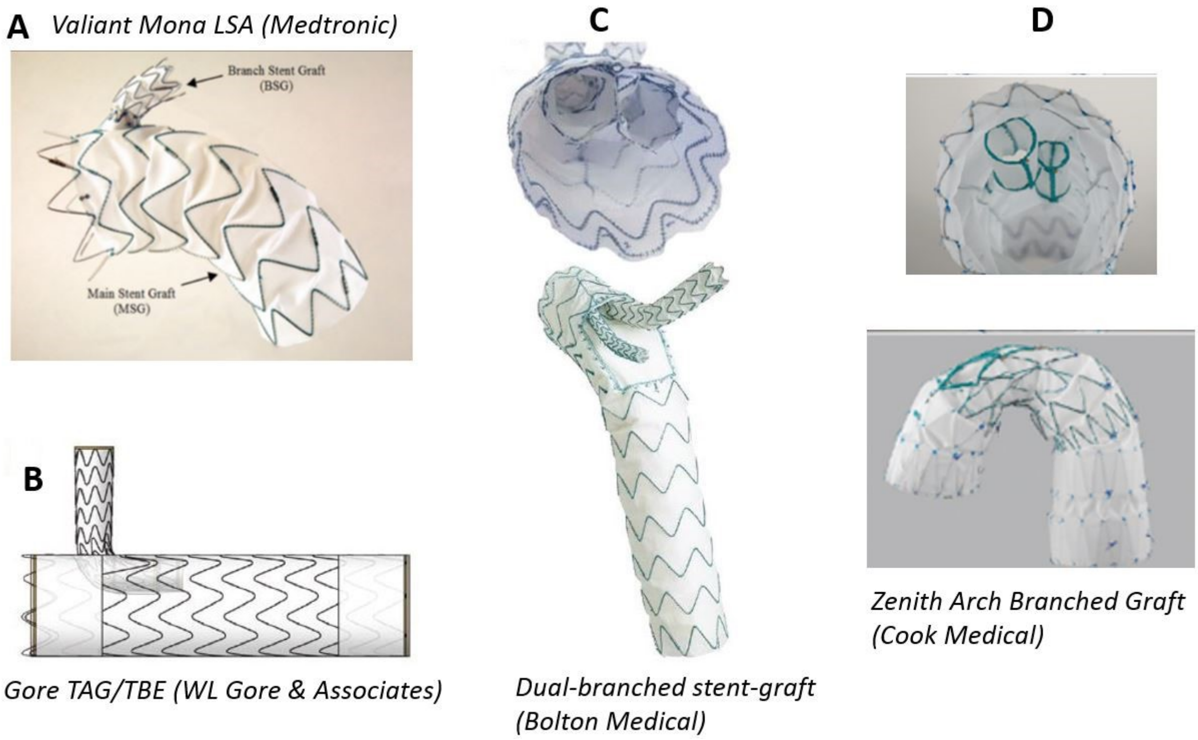

Valiant Mona LSA (Medtronic)

Gore TAG/TBE (WL Gore & Associates)

Dual-branched stent-graft (Bolton Medical)

Zenith Arch Branched Graft (Cook Medical)

Figure 2.6. Four of the commercially available thoracic branched endografts. (A) Valiant Mona LSA (Medtronic) and (B) Gore TAG/TBE (Gore & Associates) are single-branched endografts while (C) dual-branched stent-graft (Bolton Medical) and (D) Zenith arch branched graft (Cook Medical) have two inner tunnels. Figure reproduced from van Bakel et al. (2018).

A complete review of the currently available BSG devices for the treatment of arch pathologies (zone 0-2) can be found in van Bakel et al. (2018). A total of 302 patients were included in their studies based on the PubMed database, with an overall technical success rate of 94%. Although the short- and mid-term patency remained high, their long-term performances have not been evaluated. Moreover, both the stroke and re-intervention rates were high at 14% and 10%, respectively.

Z3-Z4: Descending Thoracic Aortic Aneurysms

TEVAR has become the preferred option for DTAA treatment. Successful repair depends on proximal and distal seal, which usually requires at least 20 mm of the healthy aorta serving as a landing zone. However, up to 40% of patients cannot meet this criterion as they have a complex aneurysmal location near the LSCA (Matsumura et al. 2009). In these cases, a single-branched stent-graft can be used for Z2 deployment, providing adequate proximal fixation while maintaining blood perfusion to the LSCA. A more complex situation is when aneurysms extend from the thoracic aorta to the abdominal aorta, known as thoracoabdominal aortic aneurysm (TAAA). Endovascular repair of TAAA is complicated as several or all of the vital visceral arteries, including the coeliac trunk, superficial mesenteric artery (SMA), and renal arteries are involved. Although open surgery remains the gold standard approach for treatment of TAAA, rapid development of endo-device in recent years enables the possibility of total endovascular therapy for TAAA. Based on single-centre clinical trials, endovascular repairs of TAAAs have shown promising early results with lower perioperative morbidity and mortality rates when compared with open surgical repair, though assessment of their long-term durability is still required (Oderich et al. 2017; Sweet et al. 2015).

Some novel techniques developed for endovascular repair of complex TAAA are summarised below.

Chimney Stent-Graft

As shown in Figure 2.7, chimney grafts (CG) are partially inserted into the side branches while the remaining parts are extended either above the proximal edge (snorkel) or below the distal edge (periscope) of the main stent-graft endoprosthesis. In all cases, CG inside the aortic lumen should always be in parallel with the main stent-graft and with a high degree of oversizing to avoid ‘’gutters’’, which is defined as the gap between the main stent-grafts and the visceral stent-grafts. The presence of gutters could result in type I Endoleaks (Patel et al. 2013). Moreover, for the snorkel case, CG should be deployed via brachial or axillary access, which involves a long distance between the target visceral and the brachial puncture site to delivery guide-wires through the wide, curved aortic arch (Šutalo et al. 2008) and thus increasing the possibility of further complications, such as thrombo-embolic events. The chimney technique is mostly used for a short TAAA that involves the distal descending aorta extending to the upper abdominal aorta. This technique is not suitable for a more extensive TAAA because the visceral CG have to be long enough to reach the proximal or distal neck (Kolvenbach et al. 2011).

Multi-Branched Stent-Graft

The biggest challenge in endovascular repair of TAAA is the limited physician access to the variable visceral branch anatomies. Although FSGs with customized designs show promising results with excellent visceral branch patency (Bungay et al. 2011; Halak et al. 2006; Shahverdyan et al. 2015), making these devices can take a long time and technical difficulties such as specially designed bridging stent-grafts to access the visceral arteries also need to be considered.

The latest technique developed for TAAA exclusion is the multi-branched stent-grafts, which are off-the-shelf devices and could be used for emergent cases. Cook Medical released the first commercialized off-the-shelf multi-branched endograft, known as Zenith t-branch stent-graft (Figure 2.8A). Zenith t-branch stent-graft has 'cuffs' that are physically sewn to the walls of the main stent-graft endoprosthesis in order to acquire a more secure seal. These cuffs can be protruded into renal and other visceral arteries, providing at least 2 cm of overlapping zone between the branch stents and the main stent-graft and therefore are more robust. However, one major limitation of this device is that it requires both femoral and branchial access due to the alignment of the external cuffs.

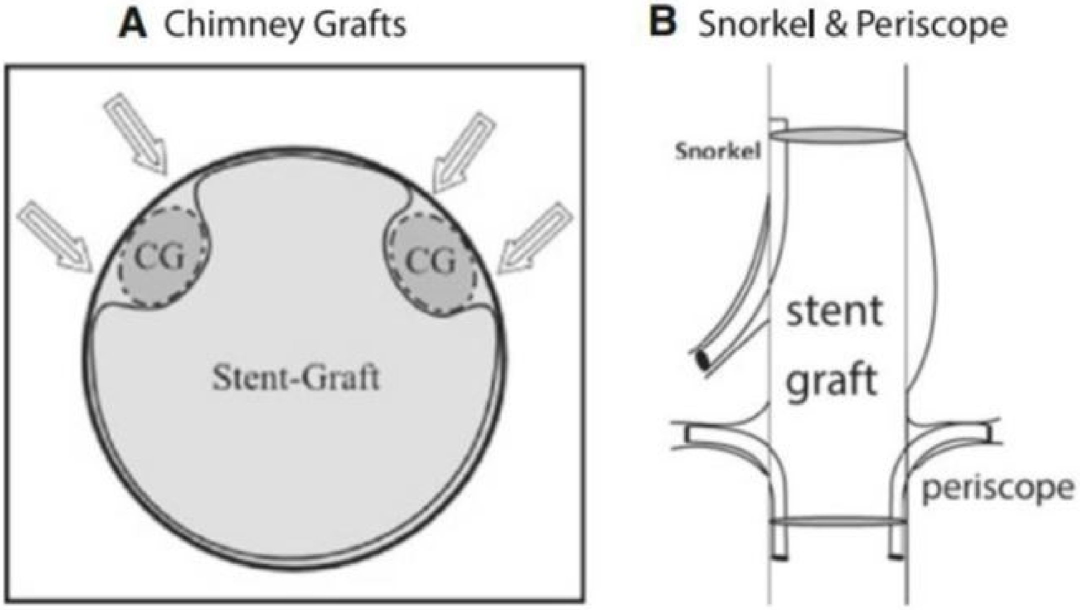

Figure 2.7. Respective components of the chimney stent-grafts. A: transverse view of the chimneys grafts, CG represents the renal stent-graft and arrows highlight the potential ''gutters'' between the two stent-grafts. B: configurations of snorkel and periscope chimney stent-graft (Patel et al. 2013).

The GORE® EXCLUDER® Thoracoabdominal Branch Endoprosthesis (TAMBE) is also an off-the-shelf, four-branched modular stent-graft integrated with a distal bifurcated component and iliac limb extensions. For the side branch component, GORE® EXCLUDER® introduced a new concept comprising of a nitinol stent frame and conformable ePTFE, which is then used with the balloon-expandable covered stent-graft, the GORE® EXCLUDER® BX Endoprosthesis. It has two downward branches for the mesenteric and coeliac vessels and branches can be either antegrade (Figure 2.8B) or retrograde (Figure 2.8C) for renal arteries. TAMBE can be applied to extensive anatomies where more than 80% of patients with complex thoracoabdominal aortic aneurysms (TAAAs) are expected to meet the requirement of vessel incorporation based on a previous study of the anatomy of the visceral arterials (Mendes et al. 2014). The retrograde renal configuration is required for patients with an up-going renal artery or with a narrow aortic segment and limited space between the SMA and renal ostia. Currently used patient-specific devices generally need a minimum of 8 weeks for planning and designing, which can be reduced or even eliminated with this off-the-shelf device. Moreover, TAMBE requires less degree of precision during device deployment when compared with fenestrated stent-grafts due to the characteristics of specially designed multiple bridging branches, preloaded guidewires, constrained mid-segment and step-by-step implantation approach.

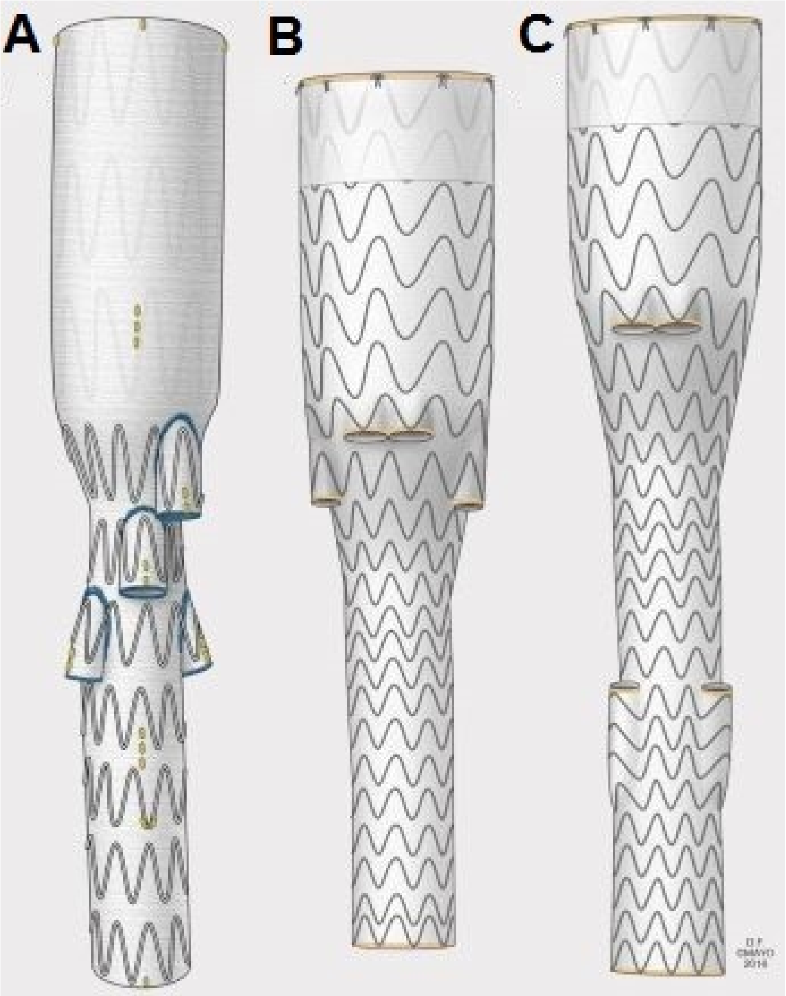

Figure 2.8. The latest multi-branched stent-grafts were developed for endovascular repair of complex thoracoabdominal aortic aneurysms. (A) Zenith t-branch stent-graft (Cook Medical), (B) the GORE® EXCLUDER® Thoracoabdominal Branch Endoprosthesis (TAMBE, Gore & Associates) with four antegrade portals, and two retrograde renal portals (C). Figure reproduced from Mendes et al. (2016).

2.2.4 Post-Operative Complications with TEVAR

Although endovascular artic repair offers many advantages over open surgery, including less peri-operative and 30-day mortality, less time in intensive care and hospital, some patients may require secondary interventions due to postoperative complications, such as endoleaks and endograft migration.

Endoleaks

The terminology ‘’endoleak’’ was first proposed by White et al. (1996) and is defined as persistence seepage of blood into an excluded aneurysm sac after stent-graft placement. As one of the most common complications of TEVAR, it may eventually lead to aneurysm rupture. Endoleaks can be classified into four different types as described below:

Type I endoleaks

Leakage of blood occurs at one of the stent-graft attachment sites: either the proximal end (Type IA) or distal end of endograft (Type IB).

Type II endoleaks

This type of endoleak occurs when there is reverse blood flow from the lumbar artery to the aneurysm sac.

Type III endoleaks

Blood infiltrates into the aneurysm sac through the stent-graft body due to rupture of the graft material.

Type IV endoleaks

Fabric porosity of the graft wall accounts for this type of endoleaks.

Endoleaks are the most common post-operative complications associated with TEVAR, although their occurrence is significantly less frequent than that reported for AAA endograft treatment (Thurnher and Grabenwöger 2002). The most common endoleaks for EVAR of AAA are type II (40% of all), whereas TAA endoleaks occur mainly due to poor sealing between the device and the aortic wall, namely, type I endoleaks (Resch et al. 2001). This is rational since endografts deployed in a tightly curved aorta may result in a wedge-shaped gap between the aortic wall and the under surface of the graft, known as bird-beak configuration and thus increasing the incidence of type IA endoleaks (Ueda et al. 2010). In fact, type I endoleak represents a more serious clinical situation since it allows direct communications between the aneurysm sac and blood flow. This may increase the intra-sac pressure significantly which can lead to measurable growth in aneurysm sac size and high risk of rupture and therefore requiring immediate intervention (Buth et al. 2003). Endotension is referred to as type V endoleak by some physicians, which is defined as continuous expansion of an excluded aneurysm sac without clear evidence of leakage. The pathology of type V endoleaks is still unclear (Bashir et al. 2009).

Endograft Migration

Displacement forces are exerted relentlessly on all endovascular devices due to the pulsatile nature of blood flow and with their cumulative impact over time, the long-term durability of the device is challenged. Once the fixation fails, migration or disconnection occurs which can lead to type I endoleak and increased risk of aneurysm rupture. In some cases, component fractures may lead to reduction in stent strength and loss of radial force and thus resulting in migration as well (England and McWilliams 2013). Moreover, clinical success following EVAR is partially defined by thrombosis, shrinkage or stabilization of the aneurysm (Zhang et al. 2014), implying that the morphology of the original diseased aortic wall changes, which can also result in graft migration (Harris et al. 1999).

2.3 Aortic Dissection

As shown in Figure 2.9, a tear may occur in the intima of a weakened wall under the persistent impact of pulsatile blood flow. This may initiate aortic dissection (AD) by allowing blood to enter the medial layer, which could split the wall layers apart. Bleeding into the medial layer creates a new channel of blood flow, known as false lumen (FL), which is separated by an intimal flap from the original pathway of blood flow that is called true lumen (TL). AD results from an intimal tear in most cases, while intramural haematoma as a result of ruptured vasa vasorum can be another cause of dissection in some patients (Nienaber et al. 2016). AD is one of the most catastrophic aortic diseases relating to severe complications such as malperfusion, aneurysmal dilatation, aortic valve insufficiency and tamponade. These complications may result in sudden aortic rupture, circulatory failure, and death in patients without timely treatment (Nienaber et al. 2016). Reported annual incidence of acute AD ranges between 3-5 cases per 100,000 people, but this value might be underestimated as the disease is often detected only at necropsy (Mehta et al. 2002; Thrumurthy et al. 2012). Mortality rate associated with AD is significant, and patient’s risk of death increases 1% - 2% hourly after the onset of symptoms (Trimarchi et al. 2010). The five-year and ten-year survival rates for patients with successful initial treatment of acute AD and persistent FL in the descending aorta range between 50% - 80% and 30% - 60%, respectively (Bernard et al. 2001; Yu et al. 2004).

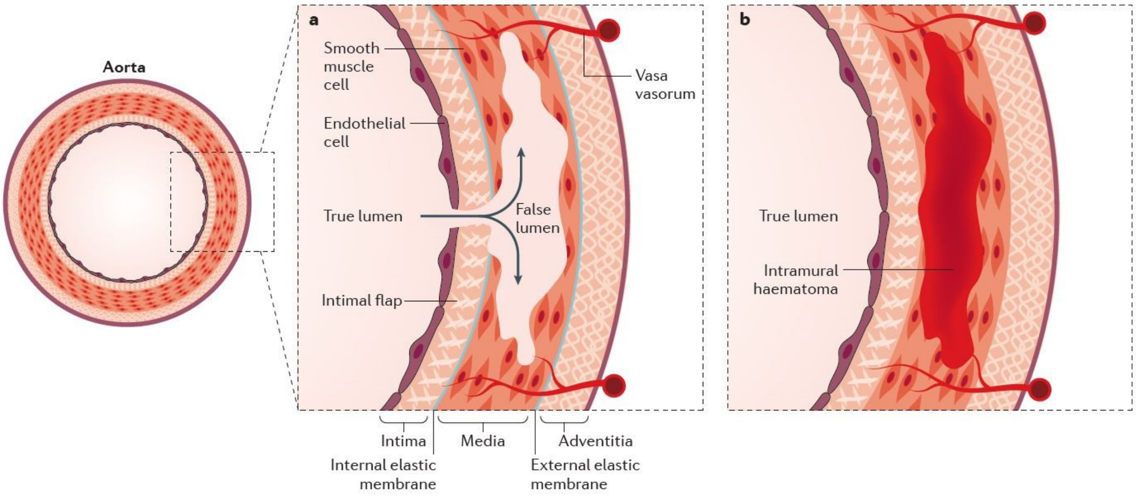

Figure 2.9. Aortic dissection involves bleeding within the medial layer, forcing the layers to separate and form an intimal flap. (a) In most cases, aortic dissection is caused by an intimal tear, whereas in some patients, aortic dissection may also result from rupture of vasa vasorum (b). Figure adapted from Nienaber et al. (2016).

In the first two weeks from the onset of an AD, patients are generally considered as in the acute stage, which is associated with a very high risk of death, especially when the ascending aorta is involved. After the initial acute period, the conditions are classified as subacute (3 months after onset) and chronic stages (after 3 months) (Nienaber et al. 2016). This classification once played an important role in treatment decision making, but has now been replaced by classification systems based on anatomical features, such as extent of the dissection and location of the intimal tear.

As shown in Figure 2.10, the most commonly used systems include the DeBakey system and the Stanford system. DeBakey system involves three main groups: Type I where dissection originates in the ascending aorta and extends distally to involve at least the aortic arch and frequently the descending aorta; Type II where dissection is confined to the ascending aorta; and Type III where the intimal tear is in the descending aorta usually just distal to the origin of the LSCA. The Stanford classification system divides dissections into two groups, Type A and Type B, depending on location of the false lumen. Type A dissection involves the ascending aorta while Type B dissection involves the descending but not the ascending aorta. Type A dissection is more common than type B as approximately two-thirds of intimal tears occur in the ascending aorta (Crawford 1990). The Stanford classification has become the most widely used system among surgeons and physicians: Type A dissection usually requires an emergent open surgery whereas the preferred treatment options for Type B dissection include endovascular repair or medical therapy (Nienaber et al. 2016).

2.3.1 Risk Factors Associated with Aortic Dissection

Similar to TAA, the exact cause of AD is unknown but is related to destruction of the aortic integrity such that the structural or functional properties of the aorta are compromised. Hypertension is generally considered as the most common risk factor of AD. The aortic wall is subject to increased load in hypertension, thus increasing the risk of development of an intimal tear. Hypertension is also associated with increased local production of pro-inflammatory cytokines and matrix metalloproteinases (MMPs), which are capable of degrading extracellular matrix (Yin and Pickering 2016). Based on statistical analyses of 4428 dissection patients, 77% of them had hypertension, followed by 27% of patients with atherosclerosis and 16% with prior cardiac surgery (15%) (Pape et al. 2015). However, younger AD patients (< 40 years of age) are more likely to be associated with a monogenic syndrome or BAV (59% of these patients) than hypertension (34%) or a history of atherosclerosis (1%) (Januzzi et al. 2004). Dilatation of the aortic root can also predispose the aorta to dissect if the patients present with Marfan syndrome or BAV (Nienaber et al. 2016). Other possible risk factors reported by the International Registry of Acute Aortic Dissection (IRAD) include pre-existing cardiovascular diseases, such as aneurysms, and genetic disorders such as Marfan's, Ehlers-Danlos, Loeys-Dietz and Turner's syndromes (Hagan et al. 2000). Men aged between 65-75 are more prone to AD (Hagan et al. 2000). In addition, elimination of dyslipidaemia and cessation of smoking are probably equally important in prevention of AD (Nienaber et al. 2016).

2.3.2 Diagnosis and Imaging Techniques

Early detection of AD is challenging because it has a variety of clinical presentations. The most common sign of the onset of AD is a sudden severe chest pain, described as stabbing, tearing or ripping in nature. The pain may shift in different regions including the back and the abdomen, as a result of propagation of the dissection (Hagan et al. 2000). Given that late diagnosis and treatment of AD is related to increased morbidity and mortality rate, imaging is necessary for timely diagnosis. The most commonly used non-invasive imaging techniques include echocardiogram, computed tomography (CT), and magnetic resonance imaging (MRI).

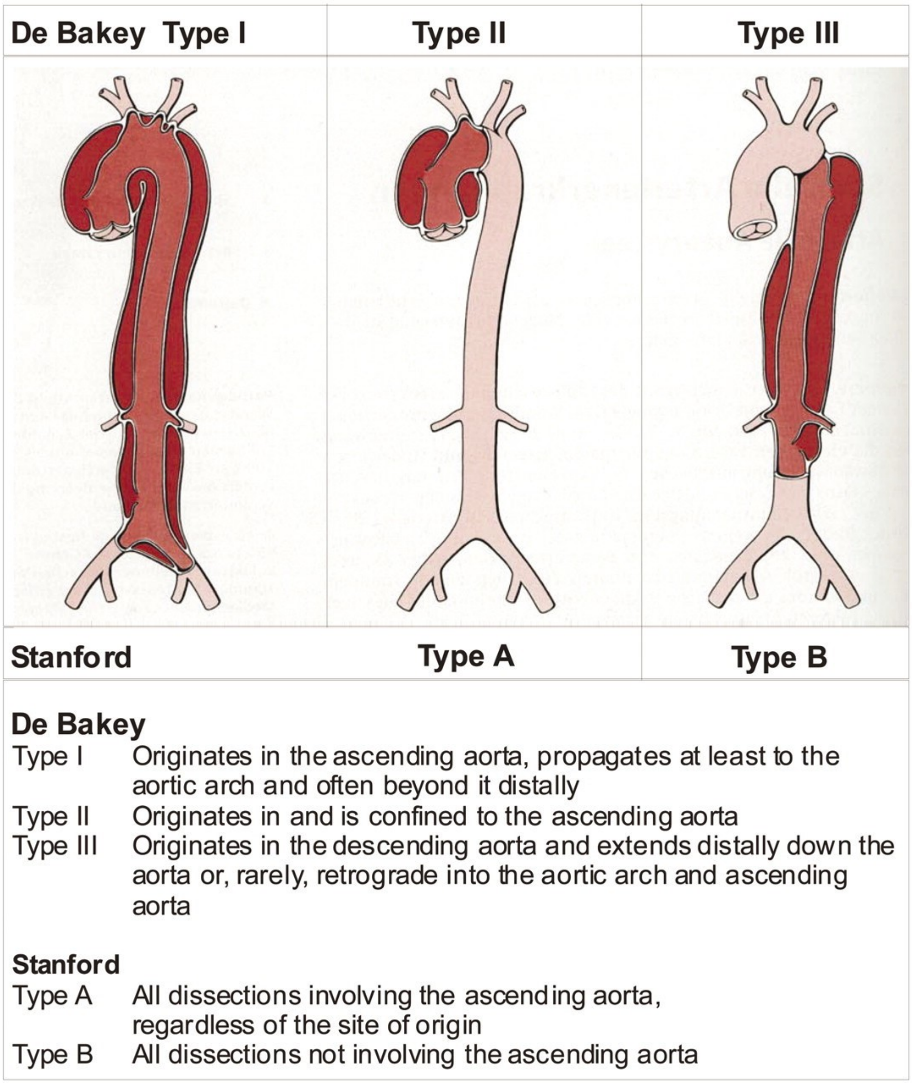

De Bakey

Type I	Originates in the ascending aorta, propagates at least to the aortic arch and often beyond it distally
Type II	Originates in and is confined to the ascending aorta
Type III	Originates in the descending aorta and extends distally down the aorta or, rarely, retrograde into the aortic arch and ascending aorta

Stanford

Type A	All dissections involving the ascending aorta, regardless of the site of origin
Type B	All dissections not involving the ascending aorta

Figure 2.10. The most common classification systems of aortic dissection: Stanford and DeBakey (Nienaber and Eagle 2003).

CT imaging is recommended in current guidelines (Erbel et al. 2014) but a major concern is the ionizing irradiation generated during the procedure, which has great impact on young patients. MRI is advised for dissection patients who are in subacute and chronic stages (Nienaber et al. 2016). MRI can provide accurate anatomical information including the extent of dissection and the location of tears. 4-D flow MRI also allows direct measurements of velocities and wall motion, which can be applied as realistic boundary conditions for patient-specific computational modelling. However, MRI usually takes longer time and is sensitive to metal objects and thus its wider applicability is limited (Nienaber et al. 2016). Transoesophageal echocardiography (TEE) is applied in emergent conditions, such that acute aortic syndromes can be diagnosed at the bedside. Although TEE has shown high sensitivity and specificity for diagnosing dissection in the ascending aorta (Shiga et al. 2006), its applicability is limited by poor capability to visualize the descending aortic pathologies, requiring further investigation to confirm the diagnosis. According to the statistical analysis from IRAD, the most popular diagnostic choice for identifying dissections is CT in 63%, followed by TEE and MRI, in 32% and 1%, respectively (Moore et al. 2002). Invasive angiography technique accounts for the rest 4% of use and it has been largely replaced by these non-invasive imaging techniques.

2.3.3 Open Surgical Repair of Type A Dissections

Aortic dissection can be managed by surgical or endovascular intervention, or medically. Stanford Type A dissection usually requires immediate open surgery as delayed diagnosis and treatment increase mortality rate (Pacini et al. 2013). The purpose of surgery is to replace the diseased segment of the aorta that involves the intimal tear with a synthetic graft (Nienaber et al. 2016). Surgical repair of AD can necessitate a variety of operations, from simple replacement of the ascending aorta to a more complex total arch replacement. However, there is still a debate among surgeons about whether to choose a more conservative surgical approach or a more aggressive approach. Although the most conservative approach of treating the ascending aorta alone has the lowest reported perioperative risk and overall mortality (Westaby et al. 2002), it increases the risk of later complications such as aneurysmal dilatation of the remaining dissected aorta (Halstead et al. 2007). Dissection aneurysm is one of the most common complications in AD, with a reported occurrence of 20% to 40 % within 1 to 5 years (Masuda et al. 1991). Anatomical features, such as FL patency, maximum aortic diameter, FL area, and entry tear size and location were all reported to possibly relate to rapid aneurismal growth and death (Chang et al. 2008; Evangelista et al. 2012; Kunishige et al. 2006; Marui et al. 1999; Onitsuka et al. 2004; Sueyoshi et al. 2004).

After surgery, complete thrombosis of the false lumen is one the most desirable clinical outcomes. On the contrary, partial thrombosis of the distal aorta can result in adverse consequences since it may occlude the distal tear, impede outflow and therefore elevate false lumen pressure. High pressure leads to increased circumferential tension, which may cause aortic wall expansion and even rupture (Song et al. 2010). Tsai et al. (2008) carried out experiments in different dissection models to assess pressure changes within the FL. Their results also demonstrated that impaired outflow from the FL could result in increased false lumen diastolic pressure. Moreover, partial thrombosis was observed more frequently in patients with ascending or hemiarch replacement than those who were treated by a total arch replacement (Song et al. 2010).

2.4 Numerical Studies of TAA and AD

Aortic aneurysms and dissections have complex 3D geometries which lead to unusual flow patterns and stress distributions. To capture a wide array of flow patterns and flow characteristics, such as velocity, pressure and stress fields within an aneurysm or a dissection, numerical simulations are required as they can provide information that is difficult to measure *in vivo*. The most commonly used numerical method is computational fluid dynamic (CFD) which is based on geometrical and mathematical discretisation and thus complex geometries are segmented into small and simple-shaped elements. By solving the discretised equations governing the fluid flow, approximated solutions can be obtained. Numerical simulations are not only cheaper, faster and more flexible than *in vitro* experiment, they are also non-invasive and can be combined with medical images to simulate *in vivo* conditions. For this reason, there has been an increasing interest in using CFD to gain deeper insights into the haemodynamics within the human body and its relation to certain cardiovascular diseases.

2.4.1 Numerical Studies of Thoracic Aortic Aneurysm

The number of computational studies on TAAs is far less compared to AAAs, possibly due to the relatively rarity of this pathology and the difficulties in simulating the dynamics of the aortic arch. Early studies focused on DTAAs. Borghi et al. (2008) carried out fluid-structure interaction (FSI) simulations of patient-specific TAAs reconstructed from MR images and found that slow and recirculating blood flow dominated in the aneurysm sac. In addition, the peak wall stresses were much higher in TAAs when compared to a normal aorta, and the value of peak wall stress was not related to the maximum aneurysm diameter (Borghi et al. 2008). A similar computational study reported that aneurysms undergoing surgical interventions had significant higher peak wall stresses than aneurysms undergoing continued surveillance, suggesting that peak wall stress had a strong correlation with aneurysm expansion rate (Shang et al. 2013). Tan et al. (2009) performed a numerical study on patient-specific TAA adopting the Shear Stress Transport Transitional (SST Tran) model, which was found to produce more accurate results than laminar flow simulation when compared with *in vivo* MR velocity measurements. To study the influence of uncovered bare-metal stents on flow in TAA, Zhang et al. (2015) compared haemodynamics in three cases of simplified TAA models (without stent, a single stent and two overlapping stents). They found that overlapping stents significantly reduced blood velocity within the aneurysm, especially in the aneurysm sac. Moreover, reduced time–averaged wall shear stress (TAWSS) and oscillating shear index (OSI), as well as elevated relative residence time (RRT) were also observed on the aneurysm walls. These findings indicated that overlapping stents might create a favourable haemodynamic environment for thrombus formation within the aneurysm, thereby helping to stabilise the aneurysm.

Several numerical studies have been conducted on blood flow in the human aortic arch, where geometrical complexities such as tortuosity, non-planarity and the presence of supra-aortic branches are included to understand their effects on blood flow (Mori and Yamaguchi 2002; Tse et al. 2013). Due to the curved nature of aortic arch, flow was largely skewed towards the inner curvature, giving rise to complex flow patterns with strong secondary flow in the distal arch. Moreover, blood flow presented with strong helical nature during systole, rotating clockwise in the ascending aorta and anti-clockwise in the distal arch (Tse et al. 2013). CFD simulations have also been performed to investigate the role of blood flow patterns and haemodynamic parameters in pathological changes of the aorta (Numata et al. 2016; Pirola et al. 2018; Tokuda et al. 2008). In addition, FSI simulations have been performed on the aortic arch with and without an aneurysm (Gao et al. 2006, 2008; Tan et al. 2009). Most recently, Miyazaki et al. (2017) applied different turbulence models to evaluate the effect of turbulence on blood flow in the aortic arch by comparing 4D MRI measurements with CFD simulation results. While most of previous computational studies focused on flow in normal and diseased aortic arch, only a few considered the influence of stent-grafts (Van Bakel et al. 2018; Van Bogerijen et al. 2014; Konoura et al. 2013; Midulla et al. 2012; Nardi and Avrahami 2017). Nardi and Avrahami (2017), among others, compared the haemodynamic performance of different endovascular procedures for the treatment of aortic arch aneurysm, including surgical repair, hybrid approach and chimney technique. Their study showed that surgical repair exhibited the best haemodynamic performance, while the chimney procedure produced the maximum WSS and pressure drop, together with highly disturbed and vertical flow. Van Bogerijen et al. (2014) employed patient-specific models to examine flow conditions after TEVAR with a focus on the bird-beak configuration.

2.4.2 Computational Studies of Aortic Dissection

Almost all CFD studies on AD found in the literature focused on Stanford type B dissection. Patient-specific geometries reconstructed from CT scans were employed in several studies to examine the detailed flow phenomenon and haemodynamic conditions (Chen et al. 2013; Cheng et al. 2010, 2014; Ko et al. 2017). Their key findings were quite similar such that flow patterns were extremely complex especially in the false lumen which is characterised by flow separation and recirculation. In addition, the helical nature of blood flow might have an effect on the wrapping of the FL around the TL (Tse et al. 2011). Blood flow was accelerated when it entered the FL through the intimal tear, forming a high-velocity jet that directly impinged on the opposing aortic wall. This jet caused high values of wall shear stress (WSS) near the intimal tear, which could increase the risk for further tear dilatation. Cheng et al. (2014), among others, also compared their computational results with phase-contrast MRI velocity data and confirmed the capability of CFD for qualitative prediction of the complex flow features, although quantitative differences exist as a result of model assumptions (Cheng et al. 2014).

Several authors analysed the influence of morphological variations on haemodynamic changes (Cheng et al. 2013; Karmonik et al. 2011; Simon et al. 2016; Tang et al. 2012; Wan Ab Naim et al. 2014). Tang et al. (2012) proposed an idealised dissected model to assess the effects of different biomechanical factors on the normal forces acting on the FL walls, including blood pressure, size of the dissected aneurysm, as well as tear numbers and distance. Large aneurysm sac and high blood pressure were found to lead to a rise in the load on FL wall while the influence of other parameters were negligible (Tang et al. 2012). FL flow was found to positively correlate with the size of primary entry tear (Cheng et al. 2013), while the number of re-entry tears had a great impact on luminal pressure (Karmonik et al. 2011; Wan Ab Naim et al. 2014) and flow direction (Simon et al. 2016). An *in silico* experiment showed that covering the sole exit tear resulted in increased pressure and intra-luminal pressure difference (Wan Ab Naim et al. 2014). Moreover, endovascular repair of Stanford type B dissection can result in stent-graft remodelling because of continuing expansion of the TL. In addition, increasing stent-graft diameter was found to be associated with a rise in haemodynamic displacement force, which would increase the risk of distal migration (Cheng et al. 2008). Karmonik et al. (2011) conducted another computational study on quantifying haemodynamic forces by comparing the results between pre- and post- stent graft deployment in type B aortic dissection. Their results demonstrated that WSS and dynamic pressure reduced after endovascular repair. Dynamic pressure is defined as the force that blood flow exerts on the aortic wall in a perpendicular direction, and high dynamic pressure has been related to adverse clinical consequences (Karmonik et al. 2011). Since a fully thrombosed FL after treatment has been reported to have an improved outcome (Tsai et al. 2007), Menichini et al. (2018) developed a computational model for predicting FL thrombosis in TBAD following TEVAR and their results showed an overall good agreement with *in vivo* data.

Several studies also reported that CFD may assist in predicting progressive aneurysmal dilatation in TBAD (Cheng et al. 2015; Shang et al. 2015; Xu et al. 2017). Shang et al. (2015) found that patients with rapidly expanding aneurysms were accompanied by larger entry tears, which allowed higher percentage of blood flow into the FL. In addition, TAWSS on the aortic wall might also be associated with rapid expansion of the aorta. On the other hand, Cheng et al. (2015) reported that pressure difference between the true and false lumen might be related to subsequent aortic expansion, and it has been found to be dependent on the number and size of tears (Dillon-Murphy et al. 2016; Tsai et al. 2008). However, the rigid wall assumption is likely to affect the predicted pressure and shear stress values, as accounting for arterial wall compliance could reduce the obtained peak values. This has been reported by Soudah et al. (2015), who observed significant differences in pressure obtained with a rigid wall computational model and the *in vitro* experiment on an elastic model. Coupling the flow model with a compliant wall model of AD is very challenging since the wall thickness and material properties vary in different components of the vessel wall and are impossible to measure in vivo. Alimohammadi et al. (2015) carried out FSI simulations on a patient-specific dissection with the assumption of hyperelastic wall behaviour and uniform wall thickness. By comparing with the results of rigid wall models, their study indicated that although high WSS was not significantly altered by the wall motion, FSI simulations should be performed to accurately evaluate other parameters such as OSI.

2.5 Summary

In this chapter, an overview of the human circulatory system, as well as the pathology, diagnosis and treatment options of TAA and AD has been presented, with a particular focus on endovascular repair of TAA and surgical repair of TAAD. Blood flow analysis is an essential component when addressing vascular pathologies, and the technology of CFD has been widely adopted in studying blood flow and haemodynamic conditions in normal and diseased aorta. Considerable amounts of computational studies have been carried out to investigate the correlation between haemodynamic factors, such as flow patterns and WSS, and the initiation and propagation of TAA and AD. However, only a limited number of numerical studies have been reported on (branched) stent-grafts for aortic arch aneurysms (Van Bakel et al. 2018; Van Bogerijen et al. 2014; Konoura et al. 2013; Midulla et al. 2012; Nardi and Avrahami 2017), and there is no such study on stent-grafts for complex TAAAs. In addition, no systematic analysis of the effect of haemodynamic factors on subsequent progressive aortic dilatation in surgically repaired TAAD has been found so far. Therefore, the rationale behind this research was to fill these gaps in the literature by adopting an advanced CFD approach to: a) simulate blood flow in novel BSGs developed for treating complex aortic diseases including aortic arch aneurysms and TAAAs, and assess their long-term durability, b) study haemodynamic conditions in repaired TAAD, and investigate their role in progressive aorta dilatation.

Chapter 3

Mathematical Models and Boundary Conditions

In this chapter, the fundamental equations that govern blood flow in large arteries are described, together with a summary of the numerical methods employed to discretise the governing equations into a set of algebraic equations so that they can be solved numerically. This is followed by a detailed description of geometry reconstruction, including idealised and patient-specific models, together with mesh generation. Further details about the numerical model, including models for transitional flow are given in the third section. Finally, the physiologically realistic boundary conditions used in this thesis are described in detail.

3.1 Governing Equations

The motion of a fluid is governed by a system of equations which can be derived from the conservation principles of mass, momentum and energy. Considering blood flow in the cardiovascular system, the fluid (i.e. blood) can be considered as incompressible with a constant density at normal physiological temperature, and the system is assumed to be isothermal. Therefore, the flow can be fully described by the equations of mass and momentum conservation, which are written as follows:

The mass equation is:

$$\nabla \cdot \mathbf{u} = 0 \tag{3.1}$$

where ρ is the flow density, ∇ is the divergence operator and $\mathbf{u}$ is the velocity vector which can be expressed as:

$$\nabla = \mathbf{i}\frac{\partial}{\partial \mathrm{x}} + \mathbf{j}\frac{\partial}{\partial \mathrm{y}} + \mathbf{k}\frac{\partial}{\partial \mathrm{z}} \tag{3.2}$$

$$\mathbf{u} = \mathrm{u}\mathbf{i} + \mathrm{v}\mathbf{j} + \mathrm{w}\mathbf{k} \tag{3.3}$$

The momentum equation can be derived from Newton's second law and expressed as:

$$\frac{\partial(\rho\mathbf{u})}{\partial t} + \nabla \cdot (\rho\mathbf{uu}) = -\nabla \mathrm{p} + \nabla \cdot \boldsymbol{\tau} + \rho\mathbf{f} \tag{3.4}$$

where p is the pressure, $\boldsymbol{\tau}$ represents the stress tensor, and $\mathbf{f}$ indicates the body force acting on the fluid per unit volume. As blood can be assumed as a Newtonian fluid in large vessels where shear rate is usually greater than 100 s^{-1}, equation (3.4) can be simplified as:

$$\frac{\partial(\rho\mathbf{u})}{\partial t} + \nabla \cdot (\rho\mathbf{uu}) = -\nabla \mathrm{p} + \mu\nabla^2\mathbf{u} + \rho\mathbf{f} \tag{3.5}$$

where μ is the viscosity of the fluid. So equations (3.1) and (3.5) are the governing equations for incompressible, isothermal and Newtonian fluid flow, also known as the Navier-Stokes equations. These partial differential equations (PDEs) are usually solved by means of numerical methods, including finite difference, finite volume, and finite element methods. These involve replacing the partial differential equations with a set of algebraic equations and discretising the spatial and time domains into small volumes and time units, where approximate solutions are obtained computationally. Therefore, the accuracy of numerical solutions is highly depended on the accuracy of the spatial and temporal discretisation schemes used, as well as the quality and size of the mesh and time-step. Finite difference method (FDM) is the oldest for numerical solution of PDEs, operating directly on the governing differential equations based on Taylor series expansion to generate a system of algebraic equations. This method is mostly used for simple geometries, which are generally discretised into structural meshes (see Section 3.2.3).

3.1.1 Finite Volume Method (FVM)

Finite volume method is the most commonly used method in CFD solvers. It is operated on equivalent integral equations over each cell or control volume (CV). Figure 3.1 shows the discretisation of a domain into CVs. The first step is to interpolate a number of nodal points in the space between A and B. The control volume boundaries are then placed mid-way between adjacent nodes so that each node is surrounded by a CV.

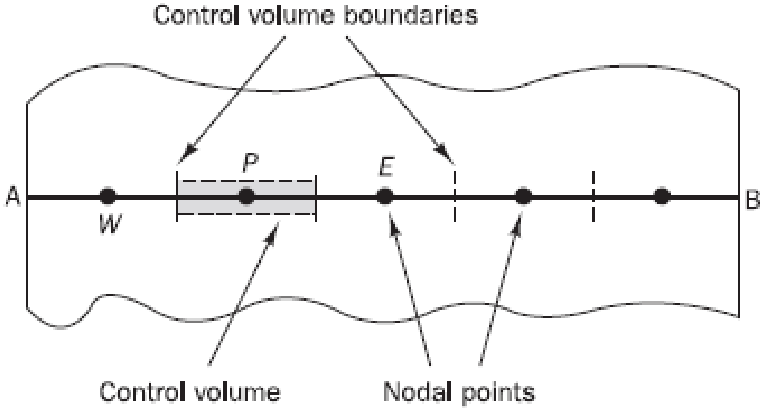

Figure 3.1. Discretisation of a domain into control volumes. Adopted from Versteeg and Malalasekera (2007).

For simplicity, the conservation equations for a Newtonian fluid flow can be expressed in a general form as:

$$\frac{\partial(\rho\emptyset)}{\partial t} + div(\rho\emptyset\mathbf{u}) = div(\Gamma\mathrm{grad}\emptyset) + S_{\emptyset} \quad (3.6)$$

Equation (3.6) is the so-called transport equation for a general variable $\emptyset$. It represents the equality of various transport processes, including the rate of change term and the convective term on the left hand side and the diffusive term and the source term, respectively, on the right hand side, where Γ is the diffusion coefficient. By setting $\emptyset$ equals to 1, u, v, w and choosing appropriate values for diffusion coefficient Γ and source terms, it becomes special forms of the PDEs for mass and momentum conservation. Equation (3.6) is used as the starting point for computational procedures in the FVM, and the key step of FVM is the integration of equation (3.6) over a 3-D CV. Meanwhile, the volume integrals of the convective and diffusive terms are converted to surface integrals based on Gauss's divergence theorem, as shown below:

$$\frac{\partial}{\partial t}\left(\int_{CV} \rho\emptyset dV\right) + \int_A \boldsymbol{n} \cdot (\rho\emptyset\mathbf{u}) dA = \int_A \boldsymbol{n} \cdot (\Gamma \mathrm{grad}\emptyset)\, dA + \int_{CV} S_{\emptyset} dV \tag{3.7}$$

Where the vector $\boldsymbol{n}$ is the direction normal to surface element dA, and equation (3.7) is a statement of the conservation of a fluid property for a finite size CV. As shown in detail by Versteeg and Malalasekera (2007), the discretised equation for interior nodes can be expressed as the following general form:

$$a_P\emptyset_P = \sum a_{nb}\emptyset_{nb} + S \tag{3.8}$$

Where subscript '*P*' refers to the interior node that is surrounded by a CV and Σ indicates summation over all neighbouring nodes (*nb*). In addition, a_P and a_{nb} are the linearized coefficients for $\emptyset_P$ and $\emptyset_{nb}$, respectively. FVM is the most popular approach employed in current commercial CFD software, such as ANSYS CFX (ANSYS Inc, Canonsburg, PA, USA), which has been used for the work presented in this thesis.

3.1.2 Finite Element Method (FEM)

FEM is also operated on the integral forms of the governing equations and the solution domain is discretised into finite elements that are generally unstructured. In the basic steps of FEM, the solution of an element is approximated by a shape function at the surrounding nodal points and equations are developed for the element. FEM is more popular in structural analysis of solids. One of the most common methods used for structure analysis is based on the principle of virtual displacements, which states that the strain energy of an elastic body is equal to the work done by the forces applied, i.e. the total internal virtual work is equal to the total external virtual work:

$$\int_V \bar{\varepsilon}^T \tau dV = \int_V \overline{\mathbf{U}}^T \mathbf{f}^B dV + \int_V \overline{\mathbf{U}}^{S^T} \mathbf{f}^S dS \tag{3.9}$$

where $\overline{\mathbf{U}}$ is the virtual displacement vector, $\bar{\varepsilon}$ is the corresponding virtual strain, and superscript *T* indicates the transpose matrix. τ represents the stresses in equilibrium with the applied loads, $\mathbf{f}^B$and

$\mathbf{f}^S$, which are the externally applied body loads (forces per unit volume) and the surface traction (forces per unit surface area) on surface *S*, respectively.

In FEM, a body is discretised into finite elements which are interconnected at nodal points on the element boundaries. Based on interpolation functions, the continuous displacement $\bar{\mathbf{u}}$ of element m is approximated by the displacement at the N finite element nodal points,

$$\bar{\mathbf{u}}^{(m)}(x,y,z) = \mathbf{H}^{(m)}(x,y,z)\bar{\hat{\mathbf{U}}} \tag{3.10}$$

where **H** is the displacement interpolation matrix and $\bar{\hat{\mathbf{U}}}$ is a vector of the three global displacement components, U_i, V_i and W_i at all nodal points. The corresponding elements strain is based on the strain-displacement relationship:

$$\bar{\varepsilon}^{(m)}(x,y,z) = \mathbf{B}^{(m)}(x,y,z)\bar{\hat{\mathbf{U}}} \tag{3.11}$$

B is the strain-displacement matrix. The element stress can then be calculated based on the specified stress-strain relations:

$$\tau^{(m)} = \mathbf{D}^{(m)}\varepsilon^{(m)} \tag{3.12}$$

where **D** is the elasticity matrix of element m.

Equation (3.9) is now rewritten as a sum of integrations over the volume and areas of all finite element:

$$\sum_m \int_{V^{(m)}} \bar{\varepsilon}^{(m)T}\,\tau^{(m)}dV^{(m)} = \sum_m \int_{V^{(m)}} \bar{\mathbf{u}}^{(m)T}\mathbf{f}^{B(m)}dV^{(m)} + \sum_m \int_{S_1^{(m)},\ldots,S_q^{(m)}} \bar{\mathbf{u}}^{S(m)^T}\mathbf{f}^{S(m)}dS^{(m)} \tag{3.13}$$

where *q* is the number of faces for element m. Substituting the expressions for displacement, strain, and stress would result in:

$$\bar{\hat{\mathbf{U}}}^T\left[\sum_m \int_{V^{(m)}} \mathbf{B}^{(m)T}\,\mathbf{D}^{(m)}\mathbf{B}^{(m)}dV^{(m)}\right]\bar{\hat{\mathbf{U}}} = \bar{\hat{\mathbf{U}}}^T\left[\begin{array}{c}\left\{\sum_m \int_{V^{(m)}} \mathbf{H}^{(m)T}\mathbf{f}^{B(m)}dV^{(m)}\right\} \\ +\left\{\sum_m \int_{S_1^{(m)},\ldots,S_q^{(m)}} \mathbf{H}^{S(m)^T}\mathbf{f}^{S(m)}dS^{(m)}\right\}\end{array}\right] \tag{3.14}$$

Equation (3.14) can then be expressed in a general form by relating the nodal displacements to the nodal forces:

$$\mathbf{KU} = \mathbf{R} \tag{3.15}$$

where the global stiffness matrix **K** is given by the summation of all the element stiffness matrix $\mathbf{K}^{(m)}$:

$$\mathbf{K} = \sum \mathbf{K}^{(\boldsymbol{m})} = \sum_m \int_{V^{(m)}} \mathbf{B}^{(m)T}\,\mathbf{D}^{(m)}\mathbf{B}^{(m)}dV^{(m)} \tag{3.16}$$

and the nodal load vector **R** is a sum of element body forces, $\mathbf{R}_{B,}$ and surface forces, $\mathbf{R}_S$, where

$$\mathbf{R}_B = \sum_m \mathbf{R}_B^{(m)} = \sum_m \int_{V^{(m)}} \mathbf{H}^{(m)T} \mathbf{f}^{B(m)} dV^{(m)} \tag{3.17}$$

$$\mathbf{R}_S = \sum_m \mathbf{R}_S^{(m)} = \int_{S_1^{(m)},\dots,S_q^{(m)}} \mathbf{H}^{S(m)^T} \mathbf{f}^{S(m)} dS^{(m)} \tag{3.18}$$

FEM has been widely adopted in computational structural mechanics (CSM) software, such as ANSYS Structure (ANSYS Inc, Canonsburg, PA, USA), which has been employed for work presented in Chapter 7 to study wall mechanics in aortic dissections.

3.1.3 Fluid-Solid Interaction (FSI) Theory

A FSI model allows flow-induced deformation of a structure to be determine, which is then used to move the boundary of the fluid flow. One of the most commonly applied methods for FSI is the arbitrary Lagrangian-Eulerian (ALE) approach, which utilises the best features of both, Lagrangian and Eulerian approaches, and combines them into one. The Lagrangian approach is typically adopted in solid mechanics to define the structural domain as each node of the computational element follows the associated material particle during motion. The Eulerian method is widely used in fluid dynamics as the computational element in the fluid domain is fixed in space and the continuum moves with respect to the grid. A FSI model can be considered as a combination of three coupled sub-problems: a geometry problem that defines a new reference configuration, namely, the ALE map; and fluid and solid problems which comprise the conservation equations for the fluid and solid, respectively (Crosetto et al. 2011).

In the ALE configuration, the continuity and momentum equations governing the flow are given as:

$$\frac{\partial \rho_f}{\partial t} + \nabla \cdot (\rho_f \mathbf{v}) = 0 \tag{3.19}$$

$$\rho_f \frac{\partial \mathbf{v}}{\partial t} + \rho_f \left[(\mathbf{v} - \mathbf{d}_f) \cdot \nabla \mathbf{v} \right] = -\nabla p + \nabla \cdot \boldsymbol{\tau}_f + \mathbf{F}_f \tag{3.20}$$

where $\mathbf{v}$ is the fluid velocity vector, ρ_f is the fluid density, $\boldsymbol{\tau}_f$ is the fluid stress tensor, $\mathbf{F}_f$ is the body force (per unit volume) acting on the fluid, p is the pressure and $\mathbf{d}_f$ is the moving boundary velocity vector. The term $(\mathbf{v} - \mathbf{d}_f)$ refers to the relative velocity of the fluid with respect to the moving coordinate velocity.

The governing equation for the solid domain is given by the following momentum conservation equation:

$$\nabla \cdot \boldsymbol{\tau}_s + \mathbf{F}_s = \rho_s \ddot{\mathbf{d}}_s \tag{3.21}$$

where $\boldsymbol{\tau}_s$ is the solid stress tensor, $\mathbf{F}_s$ is the force (per unit volume) acting on the solid, ρ_s is the solid density, and $\ddot{\mathbf{d}}_s$ is the local acceleration of the solid. The fluid and solid domains are then coupled at the FSI interfaces, where the following conditions are applied: (a) displacements of the fluid and solid domain must be compatible, (b) tractions at these boundaries must be at equilibrium, and (c) the no-slip condition is still valid.

$$\begin{gathered} \mathbf{u}_s = \mathbf{u}_f \\ \boldsymbol{\tau}_s \hat{\mathbf{n}}_s = \boldsymbol{\tau}_f \hat{\mathbf{n}}_f \\ \frac{\partial \mathbf{u}_f}{\partial t} = \mathbf{v} \end{gathered} \tag{3.22}$$

where **u** and $\boldsymbol{\tau}$ are displacement vectors and stress tensors, respectively, with the subscript *s* indicating a property of solid and *f* of fluid. Vector $\hat{\mathbf{n}}$ is the boundary normal direction. A preliminary FSI analysis of a surgically repaired TAAD has been performed (Chapter 7) in order to investigate the effects of wall compliance on haemodynamic parameters.

3.2 Geometry Reconstruction and Mesh Generation

A detailed CFD analysis of haemodynamics includes applying the fundamental mass and momentum conservation equations to realistic 3-D geometries, and solving the equations on a highly resolved mesh together with physiologically realistic boundary conditions. CFD simulation of blood flow is a multi-step process which can be summarised as follows:

1. Build 3-dimensional (3-D) geometry that contains the fluid domain of interest;
2. Fluid domain is discretised into a large number of small computational cells, known as numerical grid (meshing). Variables are discretised and stored in these cells;
3. The governing equations are solved numerically (e.g. by using a FVM-based solver) to obtain values of variables of interest in every cell.

This section will focus on the first two processes. Idealised geometric models can be created by means of design software such as SolidWorks (Dassault Systems, Velizy, France), while patient-specific models are usually reconstructed from medical images, such as contrast-enhanced CT scans which were used in this study.

3.2.1 Idealised Models of Stent-Graft

Hypothetical models mimicking the TAMBE device and a double-branched stent-graft were constructed using SolidWorks (Dassault Systems, Velizy, France) with standard device dimensions. For the branched stent-graft model, an idealised model of the aortic arch was developed first, based on physiologically representative dimensions and positions of supra-aortic vessels obtained from the literature. This was then modified to incorporate two inner tunnels, representing a dual-branched stent-graft for Z0 deployment. Although not patient-specific, these hypothetical models allow a systematic study on the effects of variations in critical geometric dimensions, such as renal branch take-off angle and diameters of the inner tunnels, on predicted flow patterns. Details of the geometric models can be found in the relevant chapters.

3.2.2 CT Images and Patient-Specific Models

As described in the previous chapter, contrast-enhanced CT scan is the most commonly used diagnostic technique for aortic aneurysms and dissection, owing to its high sensitivity and rapid scan process. CT scan has also been applied extensively for detecting tumours, internal injuries, heart diseases, and other cardiovascular diseases. Since high resolution CT images contain detailed morphological information, they were used to reconstruct the patient-specific geometries in this study, including pre- and post- TEVAR models of TAAs and type A aortic dissections.

Some important scan parameters for CT images include slice thickness, slice increment, pixel size, and resolution matrix, all of which can affect the accuracy of geometry reconstruction. Slice thickness refers to the axial resolution of a scan, and slice increment is the distance between two continuous cross-sectional images (Chadwick and Lam 2010). In addition, the resolution matrix is described by an array of rows and columns of pixels in the cross-sectional images. Thinner slice thickness and smaller slice increment would be preferred for high spatial resolution, while a smaller pixel size is desirable for better in-plane resolution. Table 3.1 summarises the scan parameters of CT images used in this study. It can be noted that CT images acquired for the study of type A dissections offered higher in-plane and axial resolutions, which allowed the complex geometry and small tears to be reconstructed. Although the low-resolution CT images were used to reconstruct the pre- and post- operative TAAs, they were sufficient to include all the important geometric features. However, lower spatial resolution might introduce more uncertainty in the measurement of aortic diameter, which would further result in larger uncertainty in the predicted wall shear stress values. Therefore, high-quality CT images are desired when possible.

In this study, multislice transverse images were processed using an image analysis software Mimics 20.0 (Materialise HQ, Leuven, Belgium), which provides a set of powerful functions for image segmentation, smoothing and measurement of geometric dimensions. Figure 3.2 shows the workflow from CT image segmentation to 3-D geometry reconstruction and mesh generation.

Table 3.1. CT scanners and the relative scan parameters used in this study.

	Study of pre- and post- TEVAR	Study of type A dissection
Slice thickness (mm)	1-2	0.63 – 1
Slice increment (mm)	1	0.5 – 0.8
Pixel size (mm)	0.63 – 0.98	0.4 – 0.7
Resolution matrix (pixels)	512 × 512	512 × 512
CT scanner	Philips Ingenuity 128	Siemens Somatom 128

For patient-specific geometry reconstruction, the first step was to identify the regions of interest. As shown in Figure 3.2 (A), several essential anatomical features can be recognised clearly from the CT images for aortic dissection, including the entry and re-entry tears, the intimal flap, and the true and false lumen. Once the regions of interest were identified, thresholding was carried out in Mimics by specifying the maximum and minimum pixel intensity values. This process allowed the pixels with grayscales within the specified range to be highlighted in a uniform colour. When a certain grayscale range is chosen to cover the target lumen areas, it is inevitable that other unintended regions are included which need to be separated from the regions of interest by using a split mask tool in Mimics. This involved splitting of a single mask into two separate masks, and the separated mask that contains only the aorta was then manually segmented slice by slice to distinguish the TL from FL. The final masks were smoothed by the Discrete Gaussian filter based on a linear smoothing enhancement algorithm. 3-D geometry reconstruction was then performed through surface rendering, which involved delineating lumen contours of the anatomical structures from each slice in the transverse plane and generating a 3-D surface by superimposing and lofting these contours in the coronal plane. Although the lumen contours have been smoothed by Gaussian filter, it is often necessary to smooth the 3-D surface in order to eliminate any reconstruction errors. 3-D surface smoothing was performed by using a cubic spline algorithm. The efficiency of smoothing is highly dependent upon the number of iterations since the geometry surface could be much smoother if the smoothing procedure is repeated for more iteration times. However, if too much smoothing is performed, it could result in loss of some important physiological features, therefore a balance must be achieved between the smoothing factor and geometric fidelity. In this study, cross-sectional contours were extracted from the reconstructed 3D surface, which were then mapped back to the raw CT images to check if the contours well presented the edges of the aortic lumen.

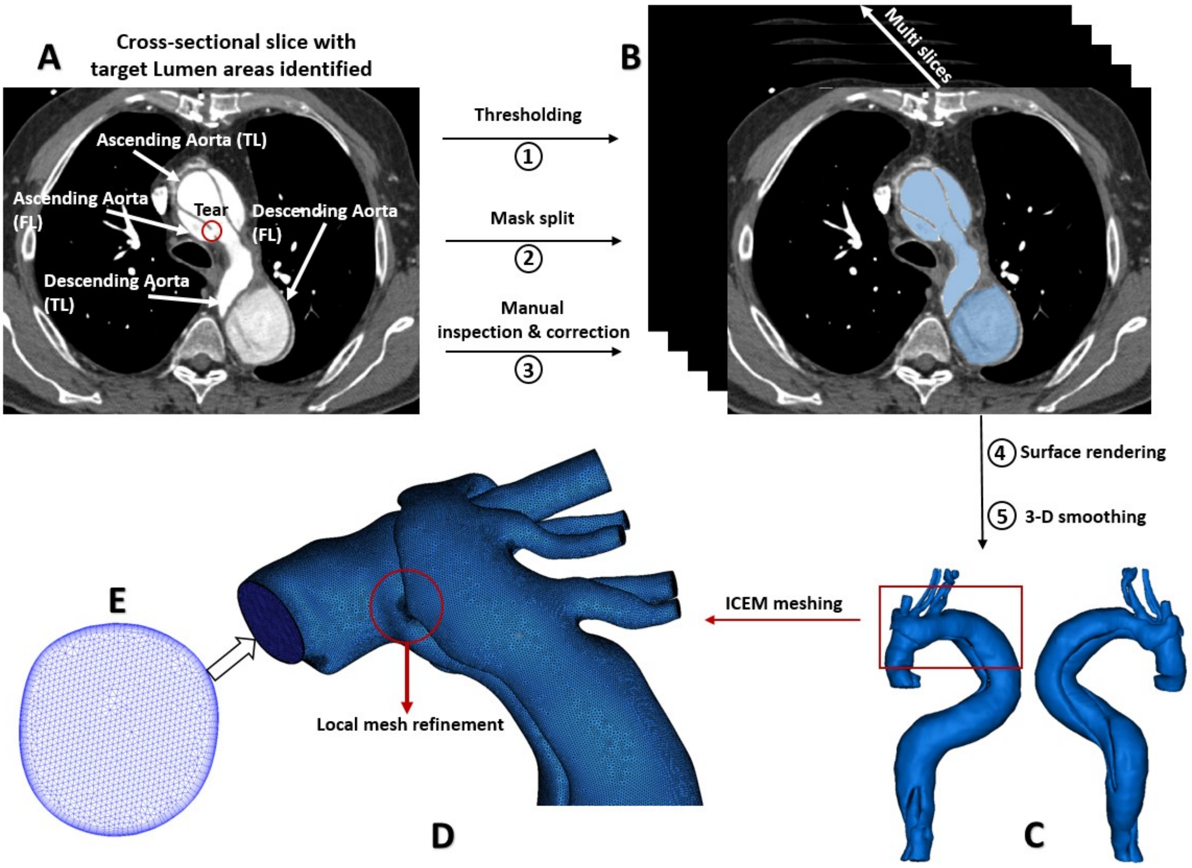

Figure 3.2. Workflow of patient-specific geometry reconstruction from CT scans to mesh generation. (A) CT angiogram of type A dissection with the target lumen areas identified; (B) Multi 2-D cross-sectional slices are manually segmented to separate the true and false lumen; (C) A patient's dissection geometry is defined as the fluid domain of interest. (D) Meshing, where the fluid domain is discretised into a large number of computational cells with local mesh refinement performed; (E) Hybrid unstructured mesh comprising of a tetrahedral core and prismatic wall layers for inlet.

3.2.3 Mesh Generation

After the 3-D geometry has been created or reconstructed, it needs to be discretised into a large number of small computational cells in a process known as mesh generation. Computational mesh was generated by using ANSYS ICEM CFD (v15.0, ANSYS Inc., Canonsburg, PA). Meshing is one of the most important steps in CFD simulations since the quality and density of a computational mesh have an important influence on the convergence and accuracy of the numerical solution. There are basically two types of meshes: structured and unstructured. A structured mesh typically consists of quadrilateral (2D) or hexahedral (3D) elements with each interior nodal point being surrounded by an exactly equal number of adjacent elements. Structured mesh is appropriate and efficient for use with a large number of solution algorithms. However, it is difficult to generate for complex geometries, in which case an unstructured mesh can be created more easily since it allows any number of elements to meet at a single node.

Since the stent-graft and aortic dissection models included in this study have complex geometric features, unstructured mesh is considered more appropriate and has been adopted. The mesh contains tetrahedral elements in the core and prism elements in the near wall region (Figure 3.2 (E)), the latter are necessary for adequately resolving blood velocities in the boundary layer and accurately predicting haemodynamic wall parameters such as wall shear stress (WSS). In addition, local mesh refinement was performed in areas with sharp corners or high curvatures, such that for aortic dissection, the mesh density is usually increased in the region around the tear (Figure 3.2 (D)), to ensure adequate mesh resolution in this region, and thus capturing any complex flow patterns induced by the tear. Further details about mesh quality and grid independent test are provided in the following section.

3.2.3.1 Mesh Independence Tests

Mesh sensitivity tests were performed for each model geometry included in this thesis to ensure that a mesh independent solution has been achieved. Two post-surgical TAAD models (Chapter 6) are shown here to illustrate the detailed procedure adopted. The initial mesh had a maximum global element size of 2 mm and local refinement with a maximum element size of 1 mm in areas of sharp corners and around the tears. Finer mesh was generated by reducing both the global and local element sizes. Additionally, for the transitional flow simulations presented in Chapter 5 and Chapter 6, a very fine near wall resolution of y^+ (a dimensionless distance from the wall to the first node from the wall) less than 2 was ensured by dividing the boundary layers into 10 prism layers.

Mesh independence tests were carried out based on steady flow simulations at conditions corresponding to peak systole. This was because it would not be practical to run pulsatile flow simulations for multiple meshes created for each geometry owing to the long computational time. According to previous studies of aortic aneurysms and dissections, essential flow features can be captured by steady flow simulations under representative flow conditions. Performing steady flow simulations at peak systolic flow (maximum velocity during a cardiac cycle) also represent the most challenging condition for a given geometry. The same boundary conditions and flow simulation settings were adopted for different meshes in order to facilitate direct comparison of results. Convergence of the numerical simulation was ensured by the meeting the following three conditions: (a) the residual RMS error values must be less than 10^{-4}, (b) parameters of interest at the monitor points, such as the outlet flow rate and pressure, must reach a steady solution, and (c) the overall imbalance in the domain must be lower than 1%.

The simulation results were compared between different meshes in terms of maximum WSS in the entire model, as well as maximum velocity and pressure at a transverse plane through the proximal tear (a region of physiological interest and high numerical sensitivity). For dissection models, a mesh was considered sufficient when differences in maximum WSS and velocity between the adopted mesh and a finer mesh were less than 5% and 3%, respectively. The results of mesh sensitivity tests for the two selected post-surgical TAAD models are summarised in Table 3.2 and Figure 3.3. It is clear that after an initial steep increase in the maximum WSS value between two consecutive meshes, it started to plateau as the mesh became much finer. Therefore, M3 containing approximately 3.5 and 7.4 million elements for post-surgical TAAD model 1 and model 2, respectively, should be adopted for final simulations.

Table 3.2. Summary of mesh independence tests results showing maximum WSS and maximum velocity and pressure in a region near the proximal tear for different meshes, together with the corresponding percentage difference between two consecutive meshes.

		Post-surgical TAAD model 1				Post-surgical TAAD model 2		
	Elements number	Max. WSS (Pa)	Max. V (m/s)	Max. P (Pa)	Elements number	Max. WSS (Pa)	Max. V (m/s)	Max. P (Pa)
M1	916153	18.49	0.51	13685.4	1921605	42.68	0.53	13832.8
M2	2088914	21.20	0.53	13685.9	4473877	41.17	0.58	13834.9
M3	3525088	25.83	0.56	13686.2	7365583	53.44	0.58	13839.2
M4	6216778	26.35	0.57	13687.7	10114460	55.48	0.59	13832.6
Difference (%)	M1-M2	14.7	3.9	0.004	M1-M2	3.5	9.4	0.02
	M2-M3	21.8	5.7	0.002	M2-M3	29.8	-	0.03
	M3-M4	2.0	1.8	0.01	M3-M4	3.8	1.7	0.05

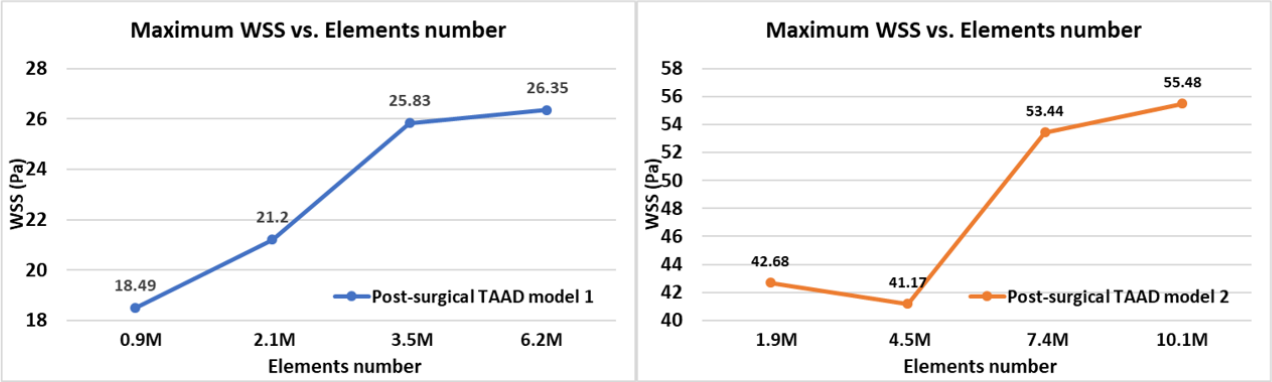

Figure 3.3. Plots of maximum WSS versus different mesh sizes for two post-surgical TAAD models.

3.3 Numerical Modelling

3.3.1 Blood Properties

In this study, blood was treated as an incompressible and Newtonian fluid with a density of 1060 kg/m^3 and a dynamic viscosity of 0.004 Pa.s. Although blood is not a Newtonian fluid, it is widely accepted that the non-Newtonian behaviour of blood can be neglected in large arteries, where shear rates are high and the influence of blood cells is negligible. The Newtonian blood assumption has been extensively used in previous numerical studies, including the flow simulations of a TAA (Tan et al. 2009) and in TBAD (Cheng et al. 2010, 2014; Pirola et al. 2019). To examine the effect of non-Newtonian viscosity of blood on flow in TBAD, Cheng et al. (2010) employed the Quemada model to describe the non-Newtonian behaviour of blood (Quemada 1978) and they showed similar results in terms of wall shear stress and pressure distributions obtained with the Quemada model and the Newtonian assumption.

3.3.2 Flow Models

First, it is necessary to determine the flow regime under each model conditions, i.e. whether the flow is laminar, transition or turbulent. This was done by evaluating the Reynolds number (Re), which is defined as the ratio of inertial force to viscous force and expressed as $Re = \frac{\rho U D}{\mu}$, where ρ is the flow density (1060 kg/m^3 for blood), U is the mean velocity, μ is the dynamic viscosity (0.004 Pa.s for blood) and D is the vessel diameter (Holmlund 2013). For steady flow in a straight, circular pipe, the critical Re for transition to occur was found to be 2000, below which the flow could be considered laminar (Wood 1999). Once Re exceeds 2000, the inertial forces in the flow become sufficiently large compared to the viscous forces, breaking down laminar flow first to a transitional state and then turbulent. In real arteries, however, the critical Re for blood flow to transition can also be influenced by other factors, such as arterial wall roughness, upstream disturbances, and spatial and temporal retardation.

Previous *in vivo* studies have reported that blood flow in the human aorta may become transitional: a transition from laminar to turbulent was observed in the ascending aorta of healthy individuals, and consistently turbulent flow was recorded in patients with heart valve pathologies (Stein and Sabbah 1976). Based on an experimental study of velocity distribution in canine aortas, Nerem et al. (1972) found the onset of turbulence was always associated with the deceleration phase of the flow at the end of systole, when the adverse pressure gradient caused the unstable velocity profiles. Nerem et al. (1972) also showed that the threshold for flow to transition from laminar to turbulent can be estimated using an empirical correlation:

$$R_e^{\wedge} = K\alpha \tag{3.23}$$

$$\alpha = \frac{D}{2}\sqrt{\frac{\omega_f \cdot \rho}{\mu}} \tag{3.24}$$

where ω_f is the fundamental frequency of the pulsatile flow, and K is 150 for the ascending aorta and 250 for the descending aorta. $R_e^{\wedge}$ is the critical Re and α is the Womersley number, which are functions of peak flow and heart rate, respectively. Equation (3.23) suggests that for unsteady flow in the aorta, the unsteadiness mediates the influence of Re on transition as the higher the value of α, the higher the critical Re. For the TAMBE models presented in Chapter 4 (See section 3.5 and Chapter 4 for more detail), the peak Re was found to be 1754 and the corresponding α was 26.7. Based on this α, the critical Re (250α) will be 6675, which is significantly higher than the peak Re. Therefore, blood flow was assumed to be laminar in the TAMBE models.

In Chapters 5 and 6, the dual-branched stent-graft models and the post-surgical TAAD models involve the ascending aorta so the flow conditions are different. In Chapter 5, the peak Re was 3530 at the inlet of all the idealised aortic arch models (Section 5.1), and it was between 3148 and 3731 at the inlet of the patient-specific pre- and post- operative TAAs (Section 5.2). The corresponding Womersley numbers were 23.2 for the idealised models and varied between 17.4 and 20.6 for the patients-specific models. Based on these parameters, the critical Re (150α) were lower than the peak Re, indicating possible presence of disturbed flows. For the dissection models presented in Chapter 6, the peak Re varied from 1620 to 4035 at the inlet and Womersley numbers from 16.5 to 31.2. Although not all these cases met the condition for transition to occur in the ascending aorta, the extremely complex geometric structure of the aortic dissection including narrowing, expansion, bending and especially the presence of tears between two lumens increased the likelihood of transition to turbulent flow. The Re were reported to exceed 8200 at peak systole in the flow jet passing through a tear (Cheng et al. 2010). These Reynolds numbers were sufficiently high to warrant consideration for possible presence of transitional or even turbulent flow.

To account for possible turbulence behaviour, the hybrid $k-\epsilon$ / $k-\omega$ shear stress transport transitional (SST-Tran) model, as proposed by Menter et al. (2006), was adopted for the simulations presented in Chapters 5 and 6. The initial SST model combines the best behaviour of the $k-\epsilon$ and $k-\omega$ (Wilcox 1998) models to achieve better accuracy and wider applicability. The $k-\epsilon$ and $k-\omega$ models are the most commonly used two-equation Reynolds-Averaged Navier-Stokes (RANS) models, with k, ϵ, and ω being the turbulence kinetic energy, the eddy dissipation rate, and the specific turbulence dissipation rate, respectively. In the SST model, a blending function is utilised so that the model can switch from the $k-\omega$ model in the inner region of the boundary layer to the $k-\epsilon$ model in the outer region and in free shear flows (Menter 1994). The SST model includes two transport equations, one for the turbulence kinetic energy k, and another for the specific turbulence dissipation rate ω.

Turbulence kinetic energy k-equation:

$$\rho\frac{\partial k}{\partial t}+\rho u_j\frac{\partial k}{\partial x_j}=\tau_{ij}\frac{\partial u_i}{\partial x_j}-\beta_k\rho k\omega+\frac{\partial}{\partial x_j}[(\mu+\sigma_k\mu_t)\frac{\partial k}{\partial x_j}] \tag{3.25}$$

Specific turbulence dissipation rate ω equation:

$$\rho\frac{\partial \omega}{\partial t}+\rho u_j\frac{\partial \omega}{\partial x_j}=\frac{\gamma}{v_t}\tau_{ij}\frac{\partial u_i}{\partial x_j}-\beta_\omega\rho\omega^2+\frac{\partial}{\partial x_j}[(\mu+\sigma_\omega\mu_t)\frac{\partial \omega}{\partial x_j}]+(1-F_1)\frac{2\rho\sigma_{\omega2}}{\omega}\frac{\partial k}{\partial x_j}\frac{\partial \omega}{\partial x_j} \tag{3.26}$$

Turbulence viscosity μ_t:

$$\mu_t=\rho\frac{k}{\omega} \tag{3.27}$$

where v_t is the eddy viscosity, and β_k, σ_k, β_ω, σ_ω, and $\sigma_{\omega2}$ are model constants (Menter 1994). F_1 is the blending function, which is set to be unit near the walls, thus activating the standard ω equation, while $F_1=0$ when away from the walls, activating the standard ϵ equation.

In order to describe transitional flows, SST model has been improved by coupling two additional transport equations for intermittency, and transition momentum thickness Reynolds number (Menter et al. 2006). The transport equation for intermittency factor γ describes the intermittent characteristic of transitional flows, while another equation for the transition momentum thickness Reynolds number $\overline{Re_{\theta t}}$ is used to capture the non-local influence of the kinetic energy.

Intermittence γ equation:

$$\frac{\partial\rho\gamma}{\partial t}+\frac{\partial\rho u_j\gamma}{\partial x_j}=P_\gamma-E_\gamma+\frac{\partial}{\partial x_j}[(\mu+\mu_t/\sigma_\gamma)\frac{\partial\gamma}{\partial x_j}] \tag{3.28}$$

where P_γ is the transition source term. This term equals to zero in the laminar boundary layer, and is activated when transition onset after the local strain-rate Reynolds number exceeds the local transition criteria. E_γ is the destruction/relaminarisation source term. This term is deactivated when the flow is fully turbulent. On the other hand, it also ensures the intermittency being zero in the laminar boundary layer or when relaminarisation occurs (Menter et al. 2006).

Transition momentum thickness Reynolds number $\overline{Re_{\theta t}}$ equation:

$$\frac{\partial\rho\,\overline{Re_{\theta t}}}{\partial t}+\frac{\partial\rho u_j\,\overline{Re_{\theta t}}}{\partial x_j}=P_{\theta t}+\frac{\partial}{\partial x_j}\,[\sigma_{\theta t}(\mu+\mu_t)\frac{\partial\,\overline{Re_{\theta t}}}{\partial x_j}] \tag{3.29}$$

where $\overline{Re_{\theta t}}$ is the transported scalar and $P_{\theta t}$ is the source term. This source term is turned off in the boundary layer so that the transported scalar $\overline{Re_{\theta t}}$ can diffuse in from the free stream, while it is activated outside the boundary layer to force the $\overline{Re_{\theta t}}$ to match the local value of $Re_{\theta t}$. $Re_{\theta t}$ is the transition onset based on empirical correlations. σ_γ and $\sigma_{\theta t}$ are empirical constants. More details of the SST-Tran model and the full set of equations can be found in Menter et al. (2006).

The SST-Tran model has been adopted for the flow analyses presented in Chapter 5 and 6 because it has been successfully applied to simulations of flow in the thoracic aorta (Cheng et al. 2014; Tan et al. 2009). Tan et al. (2009) analysed blood flow in a patient-specific thoracic aortic aneurysm by means of CFD simulation. When compared with the velocity data acquired *in vivo* using phase-contrast magnetic resonance imaging (PC-MRI), velocity profiles obtained from the SST-Tran model showed better agreement than those obtained from the laminar flow simulation. The SST-Tran model has also been applied to a patient-specific type B aortic dissection model, and a good agreement with PC-MRI velocity data was found (Cheng et al. 2014). Based on the positive experience from these prior studies, the SST-Tran model was employed in Chapters 5 and 6 to simulate complex blood flows in aortic aneurysms and dissections.

3.4 Physiologically Realistic Boundary Conditions

3.4.1 Inflow and Wall Boundary Conditions

For the models described in Chapter 4, the inlet was located in the descending aorta (See Section 3.5 and Chapter 4), and for all the other cases, the inlet was positioned in the aortic root (See Chapter 5 and 6). Regardless of the inlet location, the preferred boundary condition is a patients-specific velocity profile obtained from *in vivo* measurements, using non-invasive techniques such as PC-MRI or Doppler Ultrasound. However, in many situations, patient-specific flow information is not available, and therefore physiologically realistic flow waveforms along with the assumption of flat, parabolic, or Womersley velocity profiles are commonly used. Using a representative aortic flow waveform extracted from the literature, a flat velocity profile can be easily obtained by dividing the volumetric flowrate at the inlet Q(t) by the inlet area A. The corresponding parabolic profiles or Womersley profiles can also be obtained. The Womersley profile describes fully developed flow in a cylindrical, straight pipe driven by a sinusoidal pressure gradient (Womersley 1955). For a given transient inflow waveform Q(t), the Womersley solution can be expressed as:

$$u(r,t) = \frac{2a_0}{\pi R^2}\left[1-\left(\frac{r}{R}\right)^2\right] + \Re\sum_{n=1}^{N}\left\{\frac{a_n\cos(n\omega_f t) + b_n sin\,(n\omega_f t)}{\pi R^2}\left[\frac{1-J_0(\alpha_n \frac{r}{R} i^{\frac{3}{2}})/J_0(\alpha_n i^{\frac{3}{2}})}{1-2J_1(\alpha_n i^{\frac{3}{2}})/\alpha_n i^{\frac{3}{2}} J_0(\alpha_n i^{\frac{3}{2}})}\right]\right\} \tag{3.30}$$

where a_n and b_n are the Fourier coefficients describing the inlet volumetric flow rate waveform, ω_f is the fundamental frequency of the pulsatile flow, J_0 and $J_1$are Bessel functions of the first kind of order zero and one respectively, α_n can be expressed as $R\sqrt{(n\rho\omega_f)/\mu}$, which is the Womerley number and $\Re$ represents the real part of the respective expression while $i = \sqrt{-1}$. This expression can be used to impose Womersley velocity profiles at the inlet. The assumption of a fully developed straight pipe flow used in the derivation of the Womersley profile makes it more suitable for the descending aorta. Therefore, the Womersley profile was used for flow simulations presented in Section 3.5 and Chapter 4. In Chapter 5, since patient-specific inlet velocity profiles were not available, a physiologically realistic velocity waveform was adopted and imposed as inlet boundary conditions together with a flat velocity profile. For the dissection models presented in Chapter 6, patient-specific velocity waveforms derived from Doppler ultrasound measurements were applied and details of their applications will be described in Chapter 6.

The aortic wall was assumed to be rigid in all CFD simulations presented in this study, where no-slip conditions were applied. The impact of this assumption on the obtained results will be discussed in detail in each chapter.

3.4.2 Outflow Boundary Conditions

The most commonly used outflow boundary conditions for blood flow simulations include 0-pressure, flow split and Windkessel models. Typically, the 0-pressure outlet boundary condition is only suitable for models with one outlet and when the actual pressure values are not of interest. For models with multiple outlets, applying 0-pressure at each outlet tends to over-simplify the problem and thus leads to non-physiological results (Vignon-Clementel et al. 2006), which would affect the validity of pressure-dependent results such as displacement forces. The flow split outlet boundary condition usually defines a fixed flow-split among the outlets, and one of the outlets should be defined as 0-pressure (Tang et al. 2006). The most popular outlet boundary condition for arterial flow simulations is the 3-Element Windkessel model, since it can capture the characteristics of downstream vasculature and thus provide a physiologically realistic prediction of pressure values (Pirola et al. 2017).

Windkessel Model

The concept of Windkessel model was first proposed by Otto Frank in 1899, who described the behaviours of the heart and arterial system as a closed hydraulic circuit. This circuit is filled with water except for a little pocket of air in the chamber. Water is pumped to compress the air which in turn pushes the water out of the chamber. In the arterial system, Windkessel model describes the blood pressure and flow by considering the interactions between the cardiac output and large elastic arteries. As shown in Figure 3.4, large elastic arteries, such as the aorta, expand during systole and recoil during diastole. Pulsatile flow is converted into more smooth flow in a compliant artery, where half of blood goes to the circulation while the other half is stored as ''elastic '' energy during systole and is then released during diastole (Roy et al. 2012).

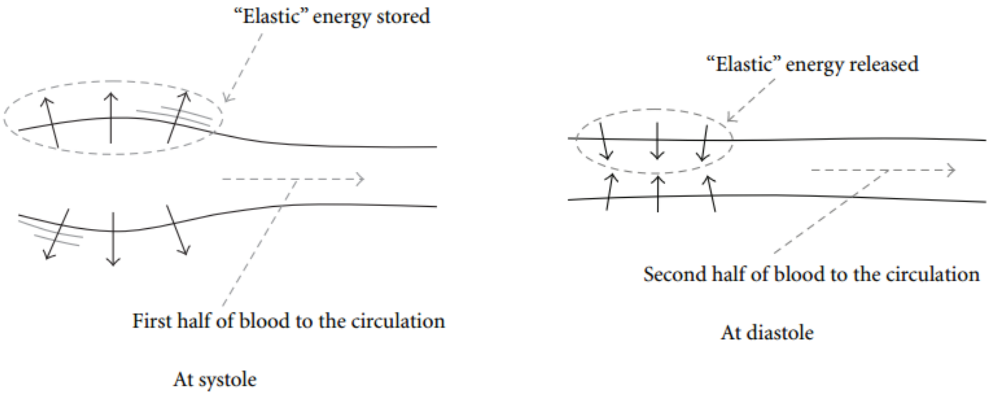

Figure 3.4. Windkessel effect of vessel wall where elastic energy is stored and released by the aorta during systole and diastole, respectively. Figure adopted from Roy et al. (2012).

Windkessel models are lumped-parameter models which describe the arterial system by characterizing the arterial compliance, the peripheral resistance, the total impedance of the aorta and the inertia of the blood flow. As shown in Figure 3.5, three types of Windkessel models have been proposed based on the number of parameters chosen for electrical analogues, known as 2-Element Windkessel (2-EWM), 3-Element Windkessel (3-EWM) and 4-Element Windkessel Models (4-EWM). Among these models, 4-EWM can offer more accurate estimation of the arterial behaviour but the inertance is very hard to predict and thus a preferable model is 3-EWM (Westerhof et al. 2009), which has been proved to be able to provide sufficient accuracy in predicting arterial blood pressure waveform (Vignon-Clementel et al. 2006). In the case of 3-EWM (Figure 3.5 b), R_1 corresponds to the total impedance of the aorta to blood flow in the proximal part, R_2 describes the peripheral resistance of the entire arterial tree and C is the total compliance of the vasculature. Therefore, an explicit relationship between flow rate and pressure combined with these parameters can be expressed as (Xiao et al. 2014):

$$Q\left(1+\frac{R_1}{R_2}\right)+CR_1\frac{\partial Q}{\partial t}=\frac{P-P_{out}}{R_2}+C\frac{\partial P}{\partial t} \tag{3.31}$$

where Q is the outlet volumetric flow rate, P is the pressure at the outlet and P_{out} is the pressure at the distal of the vasculature, which is assumed to be zero.

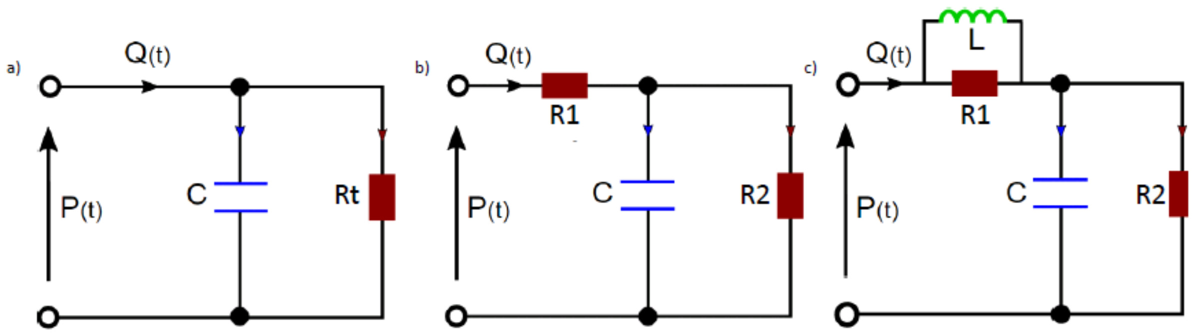

Figure 3.5. Electrical analogues of Windkessel models. (a) 2-EWM; (b) 3-EWM; (c) 4-EWM. Figure modified from Rachid (2017).

To employ 3-EWM as the outlet boundary condition, it is essential to calculate physiologically realistic values of the three parameters, namely, proximal resistance (R_1), distal resistance (R_2) and compliance (C). A detailed procedure is described below.

Step 1 – For each outlet, evaluate the mean pressure $\overline{\mathrm{P}}$ from the blood pressure waveforms acquired from the relevant literature and the mean volumetric flow rate $\overline{\mathrm{Q}}$, which is known for inlet and then calculated by flow-split.

Step 2 – The total resistance was then evaluated as (Les et al. 2010)

$$R_t = \frac{\bar{P}}{\bar{Q}} \tag{3.32}$$

Step 3 – The total resistance can be approximated as

$$R_t = R_1 + R_2 \tag{3.33}$$

Step 4 – The proximal resistance can be evaluated from the equation

$$R_1 = \frac{\rho c}{A} \tag{3.34}$$

where ρ is the density, A is the outlet area and c is the pulse wave velocity (Xiao et al. 2014).

Step 5 – If diameter D is known, the pulse wave speed c (m/s) can be obtained by using an empirical correlation expressed as

$$c = \frac{a}{D^b} \tag{3.35}$$

where a and b are constants and equal to 13.3 and 0.3, respectively, and D is the vessel diameter (Reymond et al. 2009).

Step 6 – The distal resistance R_2 was then calculated from equation (3.33).

Step 7 – Evaluate the total compliance as described by

$$C = \frac{\tau}{R_t} \tag{3.36}$$

where τ is the time constant of the exponential pressure decay during diastole. It is taken to be 1.79s under normal condition and 1.92s for hypertensive subjects (Xiao et al. 2014).

The evaluated parameters were then implemented in a FORTAN code (originally developed by a previous group member, Dr. Harkamaljot Kandail), which was coupled with the flow solver, Ansys CFX. In the code, the aforementioned 3-EMW equation (equation 3.31) is discretised into an algebraic equation by using backward Euler method and is expressed as follows:

$$P_n = \frac{Q_n(R_1+\beta R_1+\beta R_2)-Q_{n-1}+P_{n-1}}{1+\beta} \tag{3.37}$$

where $\beta = \Delta t/CR_2$ and Δt is the chosen time step.

3.5 Comparisons of Two Most Commonly Used Outlet Boundary Conditions

In this section, an idealised fenestrated stent-graft model was used to test the influence of outlet boundary conditions. For the same boundary condition (BC) at the inlet, two types of outlet BCs were tested and compared: fixed flow split and 3-EWM. Moreover, the methodology for parameter estimation for 3-EWM is validated by quantitatively comparing the predicted outlet flow and pressure data against published data in the literature.

3.5.1 Model Geometry and Boundary Conditions

An FSG model with six outlets (superior mesenteric outlet, coeliac outlet, two renal outlets and two iliac outlets) was created using SolidWorks (Dassault Systems, Velizy, France) based on the dimensions reported by Suess et al. (2016). Computational mesh was generated by using ANSYS ICEM CFD (v15.0, ANSYS Inc., Canonsburg, PA). Since the stent-graft geometry contains multiple junctions and branches, unstructured mesh was adopted with tetrahedral elements in the core and 6 layers of prism elements in the near wall region. Grid independent tests have been carried out and the number of elements adopted in the final analysis for the FSG model was approximately 4.7 million. The schematic of the computational model is shown in Figure 3.6, where the respective flow waveform was adopted from the literature (Taylor et al. 2002). This waveform was represented by Fourier series, and the corresponding Womersley solution (Womersley 1955) (see Section 3.4.1) was used to derive velocity profiles imposed at the inlet. In terms of outlet boundary conditions, the flow split and 3-EWM outflow BCs were applied in turn, in order to determine their quantitative effects on predicted flow features. In addition, the stent-graft wall was assumed to be rigid.

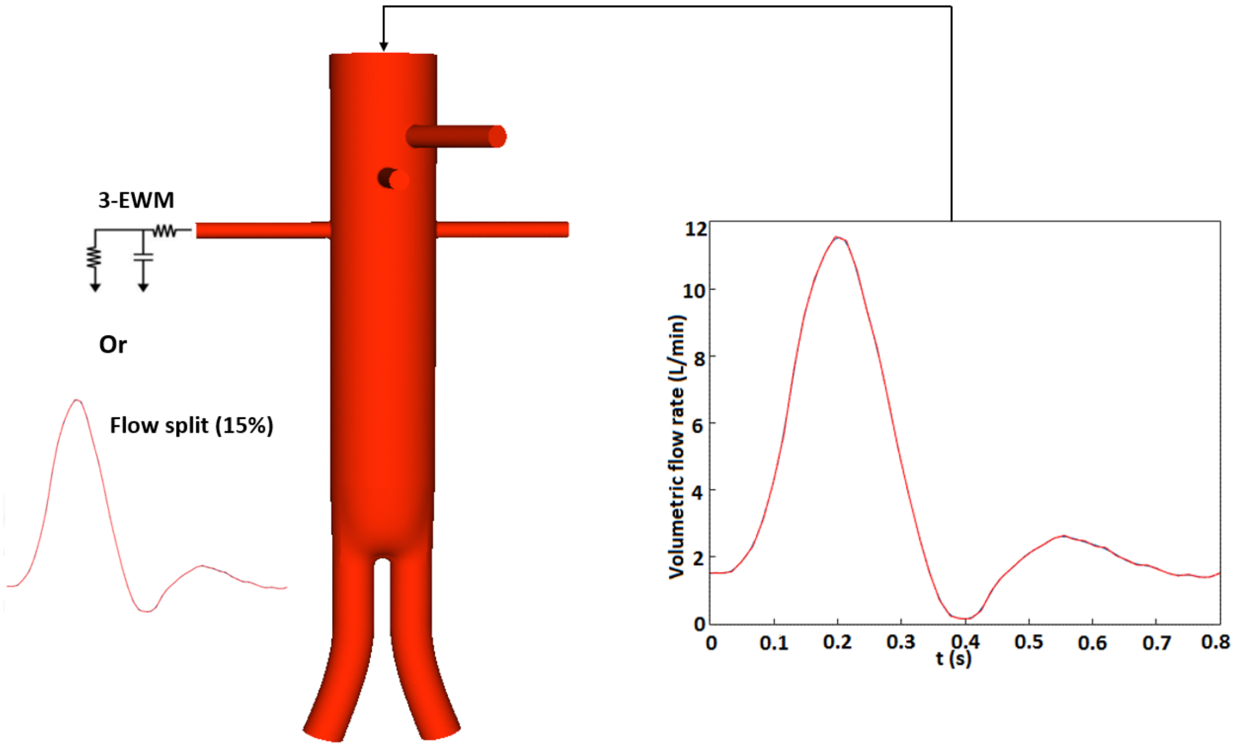

Figure 3.6. Schematic of the computational model employed in this study. Volumetric flow rate waveform was prescribed at the inlet with the assumption of Womersley velocity profile, while two different outlet boundary conditions: 3-EWM and flow split were applied at all outlets in order to directly compare the results.

Flow split outlet BC: A fixed percentage of the inlet flow is assumed to leave through each outlet. Based on data reported in the literature, the following flow division is assumed: coeliac accounts for 20% of the supracoeliac aortic flow; 15% of inflow goes to each of the superior mesenteric artery (SMA), the left and right renal arteries; and the remaining 35% of mass flow rate stays in the infrarenal aorta and is equally divided by the two iliac arteries, namely, 17.5% for each (Moore and Ku 1994). In order to implement flow split, the right iliac outlet was defined as a 0-pressure outlet.

3-EMW outlet BC: To calculate the 3-EWM parameters, pressure waveforms at each outlet were adopted from the literature (Xiao et al. 2014) and the corresponding cycle-averaged pressures were evaluated. The cycle-averaged inlet volumetric flow rate could also be calculated based on the flow waveform shown in Figure 3.6, based on which the mean flow at each outlet was obtained according to the specified flow division. Finally, the central resistance (R_1), peripheral resistance (R_2), and compliance (C) of each outlet were calculated as previously described (see Section 3.4.2) and reported in Table 3.3.

Table 3.3. Estimated values of central resistance (R_1), peripheral resistance (R_2) and compliance (C) for all the outlets.

	Renal outlet	Iliac outlet	SMA outlet	Coeliac outlet
R_1 (10^7 Pa.s/m^3)	29.13	3.05	20.43	15.03
R_2 (10^8 Pa.s/m^3)	10.71	11.90	11.79	8.94
C (10^{-10} m^3/Pa)	13.15	14.66	12.93	17.14

3.5.2 CFD Model Details

The conservation of mass and momentum equations for an incompressible, Newtonian fluid were used to describe the pulsatile blood flow. Blood was assumed to have a constant density of 1060 kg/m^3 and dynamic viscosity of 0.004 Pa·s. In addition, flow was assumed to be laminar. All numerical solutions were obtained using ANSYS CFX 15 (ANSYS, Canonsburg, PA, US), with the root mean square convergence criterion being set to be 1x10^{-5}. A high order advection scheme and second-order implicit backward Euler scheme were chosen for spatial and temporal discretisation, respectively. A fixed time-step of 0.001 s was used based on sensitivity tests on time-step size. All numerical simulations were carried out for three cardiac cycles in order to reach a period solution and results from the last cycle were analysed using ANSYS CFD-Post 15 (ANSYS, Canonsburg, PA, US) and CEI Ensight 10 (CEI Inc, Apex, NC, US).

3.5.3 Comparison of Numerical Results against Known Values

Quantitative comparisons of the predicted mean outlet flow rate were made with the known flow data in the literature (Taylor et al. 2002) for both BCs (Table 3.4). Comparisons of the predicted pressure values were only made for the 3-EWM outlet BC, and results are summarised in Table 3.5 for the minimum (diastolic), maximum (systolic) and mean pressures in each outlet together with the pressure data of Xiao et al. (2014), which were used for parameter estimation.

With both types of outlet BCs, the predicted mean flow rates in all arteries were in good agreement with the values reported in the literature with a maximum discrepancy of 3.1%. Although the mean pressure values were well predicted with the 3-EWM BC, the model predicted lower peak systolic pressure and higher diastolic pressure compared to the target values. There are several possible reasons for this discrepancy: (a) the rigid wall assumption in the CFD model, (b) the lack of a complete set of flow and pressure waveforms for all branches, which resulted in many parameters being either calculated analytically or estimated from the literature. Nevertheless, results obtained with the 3-EWM BC are acceptable since physiologically realistic behaviour of pressure and flow were well captured.

Table 3.4. Comparison of mean flow rates in each artery obtained with two different outlet boundary conditions, together with the corresponding percentage difference from the target values.

	Mean volumetric flow rate (L/min)		
	(Taylor et al. 2002)	3-EWM BC	Flow Split BC
Renal outlet	0.530	0.522 (1.5%)	0.529 (0.1%)
Iliac outlet	0.617	0.636 (3.1%)	0.621 (0.6%)
SMA outlet	0.530	0.524 (1.1%)	0.532 (0.4%)
Coeliac outlet	0.706	0.696 (1.4%)	0.725 (2.7%)

Table 3.5. Minimum, maximum and mean pressures in each branch artery with 3-EWM outlet BC.

	Renal artery		Iliac artery		Coeliac artery		SMA	
	CFD results	(Xiao et al. 2014)	CFD results	(Xiao et al. 2014)	CFD results	(Xiao et al. 2014)	CFD results	(Xiao et al. 2014)
Min P (mmHg)	76.95	66.47	77.20	66.46	77.25	66.53	77.23	67.28
Max P (mmHg)	106.90	114.56	111.77	121.53	107.14	115.68	107.18	116.26
Mean P (mmHg)	88.55	90.19	89.95	94.17	89.24	91.23	89.21	91.70

3.5.4 Comparison of Two Outlet Boundary Conditions

The predicted pressure variations at each outlet are shown in Figure 3.7, while the corresponding volumetric flow rates are given in Figure 3.8.

Figure 3.7 shows that the shape of the predicted pressure waveforms at the outlets are very different for the two outlet BCs. Since normal blood pressure for a healthy adult should be within 80 – 120±10 mmHg, it is obvious that pressures obtained with the flow split BC are physiologically incorrect. On the other hand, the 3-EWM BC reproduced very well not only the shape of the pressure waveform but also physiologically relevant values. Regarding the volumetric flow rate at each outlet (Figure 3.8), the flow split BC produced waveforms that were all in the same shape as the inlet flow waveform. However, it is known that renal flow waveform should always be antegrade due to the low peripheral resistance of the kidney (Nichols et al. 2011), while the iliac artery commonly experiences retrograde flow during part of diastole (Les et al. 2010). Specifically, the coeliac and SMA draw flow anteriorly while renal arteries pull flow laterally and due to the constant antegrade flow in the renal arteries, flow in the infrarenal aorta would be drawn at the beginning of diastole, thus causing flow reversal. Moreover, flow in the renal arteries should be higher than that in the iliac arteries during diastole. All these features were well captured by the 3-EWM BC.

Near Wall Haemodynamic (NWH) Parameters: NWH parameters have been shown to have an effect on the development of atherosclerosis. For example, low wall shear stress (WSS) is known to promote thrombus formation and induce intimal hyperplasia (Suess et al. 2016). More specifically, low WSS has been found to not only be responsible for the delay in nutrient supply and metabolic wastes removal (Malek et al. 1999), but also for causing formed elements, such as monocytes, thrombocytes and granulocytes, to move to peripheral parts of the arterial flow (Joris et al. 1983). On the other hand, high WSS values have been associated with platelet activation in blood (Nobili et al. 2008), activity of which can potentially promote local thrombus formation. High WSS has also been related to degenerative lesions of the vessel wall and subsequent vessel enlargement (Ekaterinaris et al. 2006), with WSS values higher than 40 Pa being linked to direct endothelial damage (Fry 1969). Time-averaged WSS (TAWSS) is derived from WSS over the entire cardiac cycle. Oscillating shear index (OSI) has been evaluated to identify areas with varying shear directions and OSI values of >0.3 have been suggested to be atherogenic. In addition, relative residence time (RRT) has been used to relate the amount of time that solutes and particles of the blood may spend near the vessel wall. Table 3.6 summarises the threshold values for NWH parameters that are shown to be atherogenic (Suess et al. 2016).

Definitions of TAWSS and OSI are given below.

$$TAWSS = \frac{1}{T}\int_0^T |\tau_\omega| dt \tag{3.38}$$

where T is the period of the cardiac cycle and τ_ω is the instantaneous wall shear stress.

$$\mathrm{OSI} = 0.5\left(1 - \frac{\left|\int_0^T \tau_\omega dt\right|}{\int_0^T |\tau_\omega| dt}\right) \tag{3.39}$$

Residence time is a relative concept since all non-adherent particles in the flow are moving and, thus, have zero “residence time” at any location (Himburg et al. 2004). As proposed to by Himburg et al. (2004), the residence time can be expressed in terms of the Cartesian distance $\delta(y)$, which is the travel distance of a fully entrained particle at a small distance y from the wall during a cardiac cycle. The residence time, t_r, of such a particle therefore is proportional to δ^{-1}. Near the wall, the excursion of the particle is small enough so that the spatial variation in shear can be neglected, and $\delta(y)$ can be expressed as:

$$\delta(y) = \left|\int_0^T u(y) dt\right| = \frac{y}{\mu}\left|\int_0^T \tau_\omega dt\right| = \left(\frac{Ty}{\mu}\right)(1 - 2 * OSI) * TAWSS \tag{3.40}$$

where μ is the dynamic viscosity. Since the term $\frac{Ty}{\mu}$ is a constant for any arbitrarily small value of y, hence

$$t_r \sim \delta^{-1} \sim [(1 - 2 * OSI) * TAWSS]^{-1} \tag{3.41}$$

The RRT as proposed by Himburg et al. (2004) can be expressed as

$$\mathrm{RRT} = \frac{1}{(1-2*OSI)*TAWSS} \tag{3.42}$$

It should be noted that RRT is not the exact residence time as it is calculated based on TAWSS and OSI. This variable could be a useful measure of the shear environment for correlative purposes regarding the level of the shear and its oscillatory character.

Table 3.6. Reported ranges of NWH parameters that are atherogenic.

Parameter	Atherosclerosis-promoting range (Suess et al. 2016)
TWASS	<0.4 Pa
OSI	>0.3
RRT	>10 m^2/N

Figures 3.9, 3.10 and 3.11 show the predicted TAWSS, OSI and RRT distributions with the two BCs. Although no significant differences in the overall patterns were observed, there were minor differences in OSI and RRT distributions, especially in the region below the renal branches. The similarity in TAWSS distribution can be explained by the fact that WSS results depend on the flow rate, geometry and flow split among the branches, which were either the same (inlet flow rate and geometry) or differed very little (flow rates in branches) for the two BCs. Since TAWSS represents the magnitude of WSS over one cardiac cycle and OSI characterizes the cyclic variation of WSS, OSI values are between 0 for unidirectional flow and 0.5 for purely oscillatory flow. As a result, regions with high TAWSS usually have low OSI values, which seemed to be the case here where the branches had consistently moderate values for TAWSS along its length, while relatively low OSI values were found in branches. The main stent-graft, especially in the infrarenal region, exhibited high levels of OSI, which was caused by flow reversal. As infrarenal flow reversal was more pronounced with the 3-EWM BC, the area with higher OSI was also larger than that with the flow split BC. For the same reason, areas of higher RRT were also larger with the 3-EWM BC.

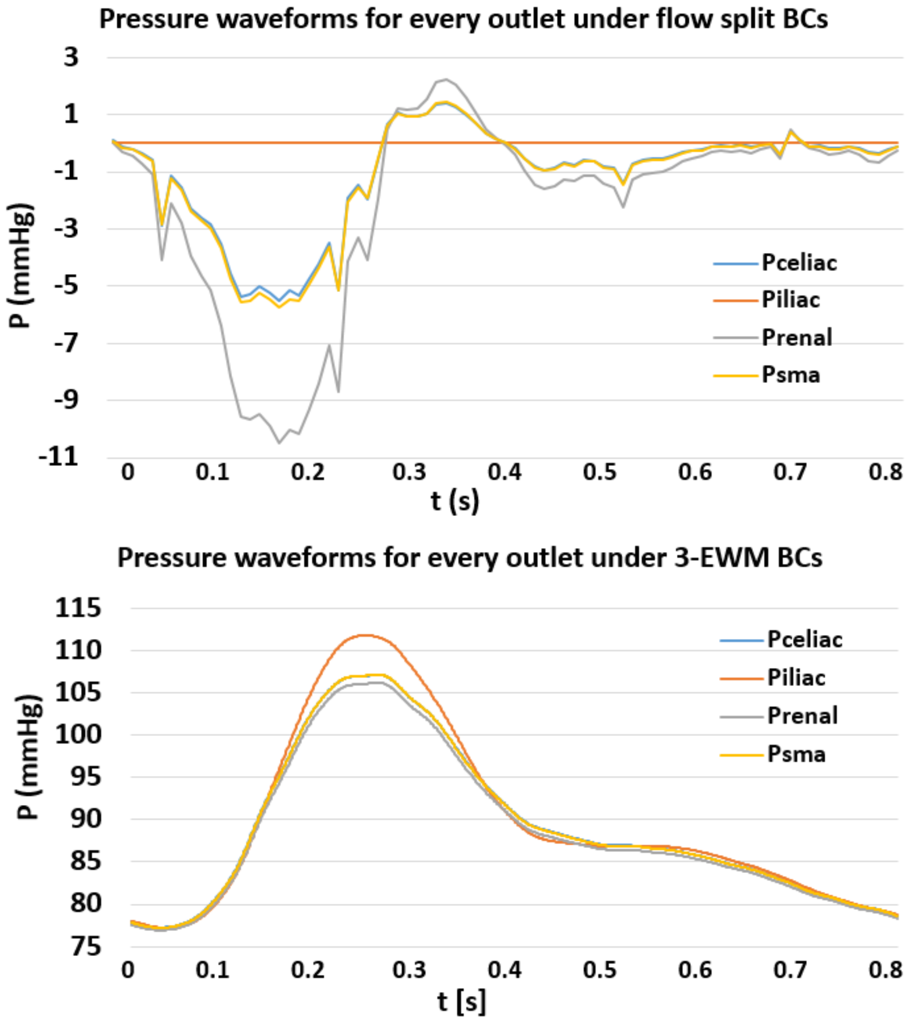

Figure 3.7. Predicted pressure waveforms for every outlet with two outlet boundary conditions. Top: flow split BC; bottom: 3-EWM BC.

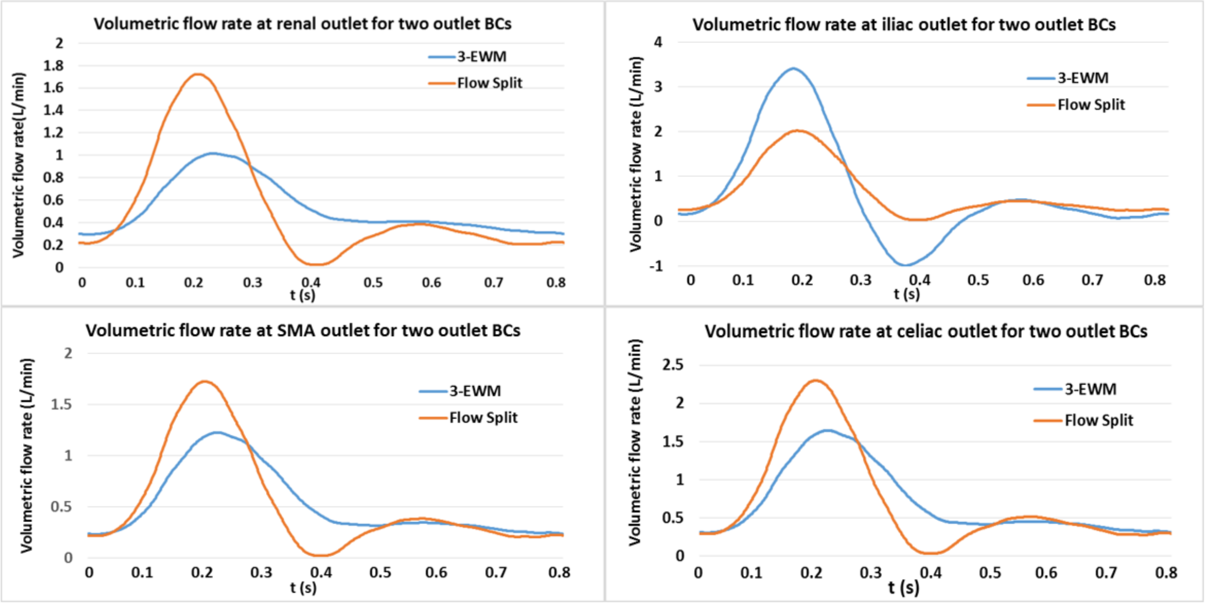

Figure 3.8. Predicted flow rate waveforms for each outlet with two different boundary conditions. Retrograde iliac flow during part of diastole was only predicted by the 3-EWM BC.

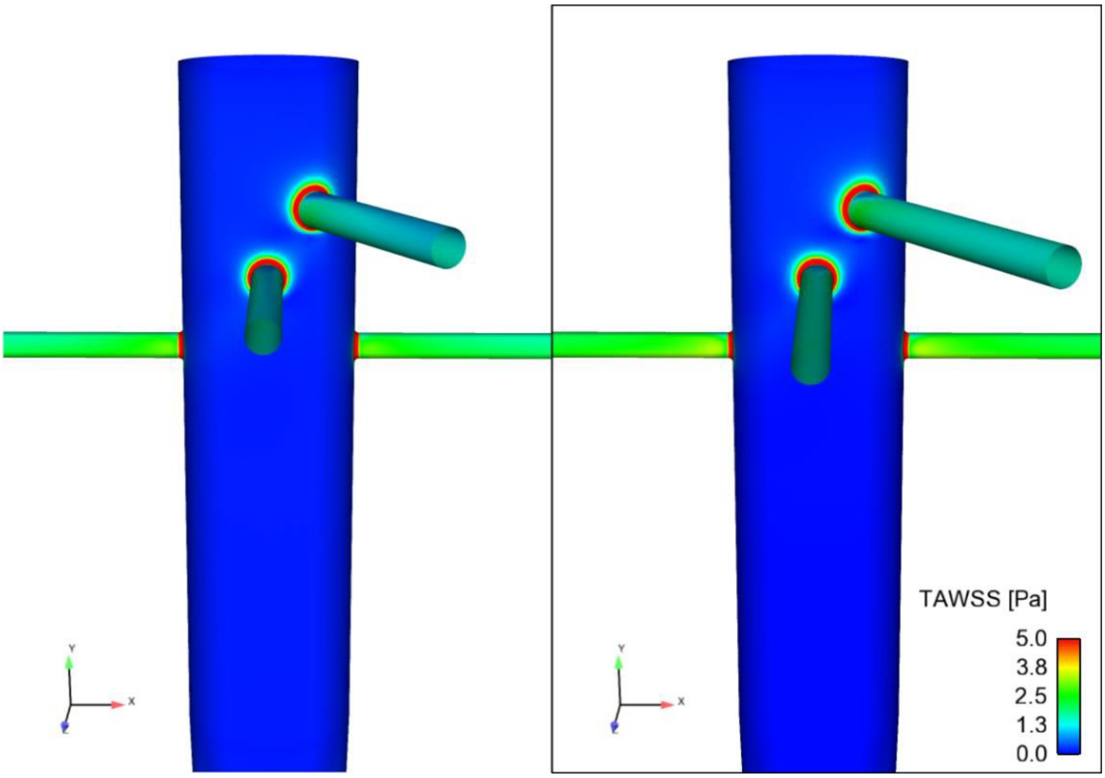

Figure 3.9. Comparison of time-averaged wall shear stress (TAWSS) distributions between two boundary conditions: left for 3-EWM and right for flow split.

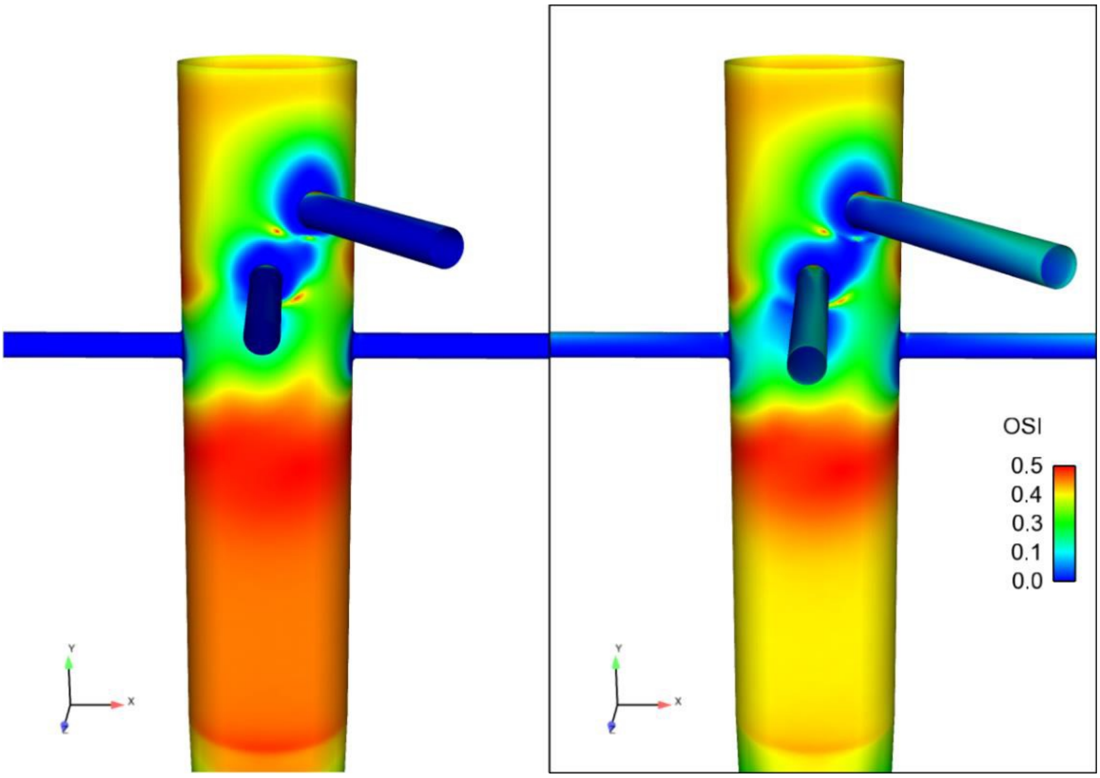

Figure 3.10. Comparison of oscillating shear index (OSI) distributions between two boundary conditions: left for 3-EWM and right for flow split.

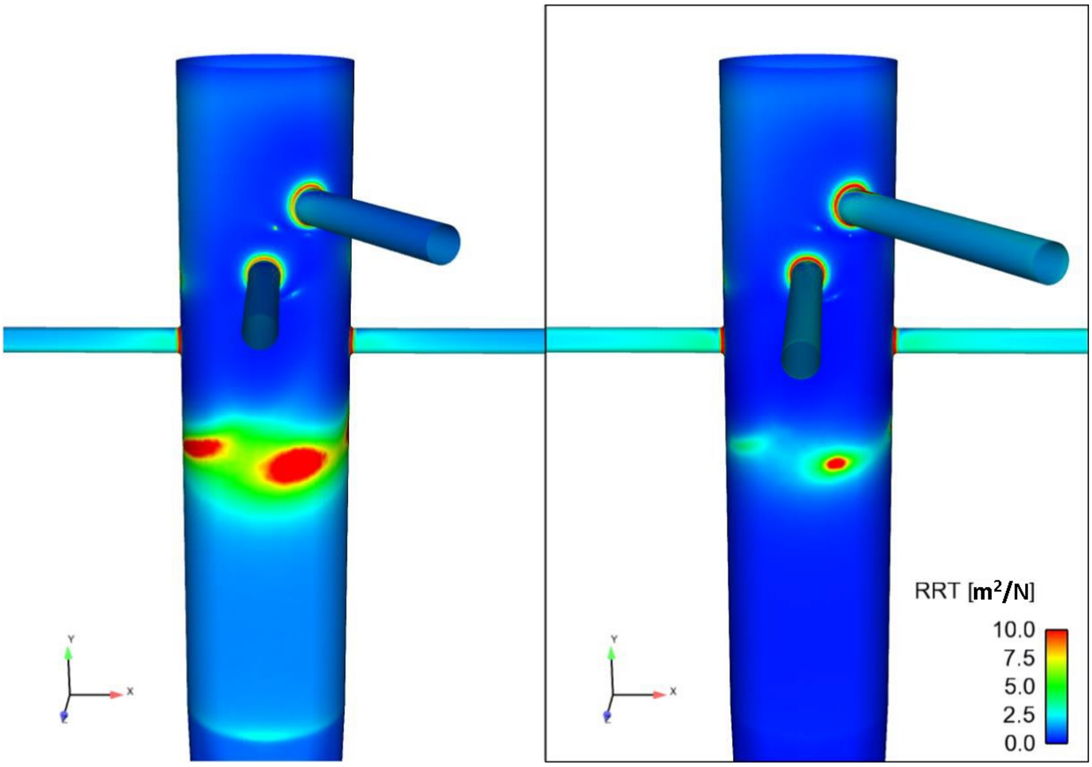

Figure 3.11. Comparison of relative residence time (RRT) distributions between two boundary conditions: left for 3-EWM and right for flow split.

3.6 Summary

The governing equations for blood flow were described in this chapter, which can be solved numerically together with appropriate boundary conditions. Essential components required for physiologically realistic CFD simulations of blood flow were described, including realistic 3-D geometries, highly resolved mesh, together with physiological boundary conditions. In terms of outlet boundary conditions, two most commonly used boundary conditions: fixed flow split and 3-EWM, were compared through CFD simulations of an idealised FSG model. The results demonstrated that the 3-EWM is capable of reproducing physiological flow and pressure waveforms and their values were in good agreement with the target values, justifying the use of 3-EWM as outlet BCs in all flow simulations presented in this thesis.

Chapter 4

Application 1: Evaluating the Haemodynamic Performance of Thoracoabdominal Branch Endoprosthesis (TAMBE)

4.1 Introduction

The most common challenge in device design for endovascular aortic repair (EVAR) of thoracoabdominal aortic aneurysms (TAAAs) is the variability of the visceral branch anatomy. Customized devices, such as fenestrated stent-graft (FSG), are not only more expensive than off-the-shelf designs, but also require longer time to make, thus not suitable for emergency use. Therefore, manufactures are constantly working on developing novel devices with a ''few-sizes-fit-most'' approach. Since the first report on endovascular repair of TAAAs using branched stent-graft (BSG) by Chuter *et al.* (2001), off-the-shelf multi-branched stent-grafts have been developed. Zenith t-branch *(Cook Medical)* was the first commercialized off-the-shelf device; it has four downward-going external cuffs, and has been reported with excellent clinical outcomes (Greenberg et al. 2008). The GORE® EXCLUDER® Thoracoabdominal Branch Endoprosthesis (TAMBE) is the latest multi-branched stent-graft which offers extensive anatomical applicability.

The first successful implantation of TAMBE was reported in 2014 and the clinical experience with this device is still limited (Oderich and Silveira 2016). Based on multicentre data, Oderich et al. (2019) found that TAMBE demonstrated high rates of technical success and favourable short-term (30 days) outcomes, though long-term durability has not been determined yet. TAMBE has four portals sewn on the main endograft, allowing placement of preloaded guidewires to facilitate visceral vessel catheterization. The bridging stent-graft used to connect with the target vessel varies in length and take-off angle (TOA) based on patient's anatomy. Previous computational studies have shown that misaligned visceral stent-grafts could influence local flow patterns and shear stress magnitude and distribution (Georgakarakos et al. 2014; Kandail et al. 2015). These arose two questions on using TAMBE for EVAR: a) long-term durability, and b) the effect of variable geometrical configurations adapted by the visceral stent-grafts on its overall performance. Answering these questions may help to assess the reliability of TAMBE, which may aid surgeons in assessing the risk of future complications, such as migration and endoleaks as well as in-stent thrombosis. This chapter aims to address the aforementioned questions by providing a detailed evaluation of the haemodynamic performance of

TAMBE through CFD simulations. Analysis of results has been performed to include: a) flow patterns, with a particular attention to recirculation zones in the renal branches, b) outflow in visceral and iliac arteries, c) near wall haemodynamic (NWH) parameters, and d) displacement forces experienced by the stent-grafts.

4.2 Methodology

4.2.1 Model Geometry

As described in section 2.2.3, TAMBE has four inner portals with either antegrade or retrograde orientation for the renal arteries. Considering the ease of implantation and relevant clinical guidance (Prof M. Hamady, St Mary's Hospital, London), the antegrade orientation was chosen for this study. Idealised 3-D models of TAMBE were created using SolidWorks (Dassault Systems, Velizy, France). As shown in Figure 4.1, the main stent-graft endoprosthesis has a total length of 160 mm, including a tapered segment with a length of 56 mm. The proximal sealing zone has a length of 35 mm, after which the geometry gradually tapers from the proximal diameter of 37 mm to the distal diameter of 20 mm. In this study, the geometry of the main stent-graft was slightly modified, where the proximal sealing zone was extended to 65 mm while the tapering length was reduced to 26 mm. This modification was inevitable for idealised TAMBE models as a tapering length longer than 26 mm would cause overlapping regions between the renal branches and the main stent-graft endoprosthesis. This modification is believed to have a negligible influence on the haemodynamic parameters of interest. Additionally, inner portals for all the visceral vessels have the same length of 10 mm, but the SMA and coeliac portals are positioned 10 mm above the two renal tunnels. The diameters were 8 mm for the coeliac and SMA, 6 mm for the renal, and 9.5 mm for the iliac. All the visceral arteries were artificially extended to ensure that the flow was fully developed before it reached model outlets.

In order to account for variable configurations of bridging stent-graft, three different TOAs between the main endograft and the renal branch centreline axis were simulated: 90°, representing the most common flat renal anatomy, and 45° and 110° representing a downward and upward renal configuration, respectively. In addition, three different renal branch lengths were simulated as summarised in Table 4.1. Due to the lack of patient-specific data or reported representative geometric dimensions, both the renal TOAs and branch lengths were provided by the clinical collaborator. In reality, the renal anatomy can vary extensively, and the dimensions used in this study only represented some common clinical scenarios. Since the abdominal aorta is located along the curved and non-planar lumber vertebrae and the deployed stent-graft would follow the curvature, the effect of nonplanarity on the performance of TAMBE was also considered by creating an additional non-planar model with an anterior/posterior neck angle (APA) of 20° using the baseline geometry (TOA = 90°, renal branch length = 45 mm). APA is the angle between the y-axis and a line that is perpendicular to the inlet surface in the sagittal plane (Kandail et al. 2014). Schematics of all the simulated TAMBE models are shown in Figure 4.2.

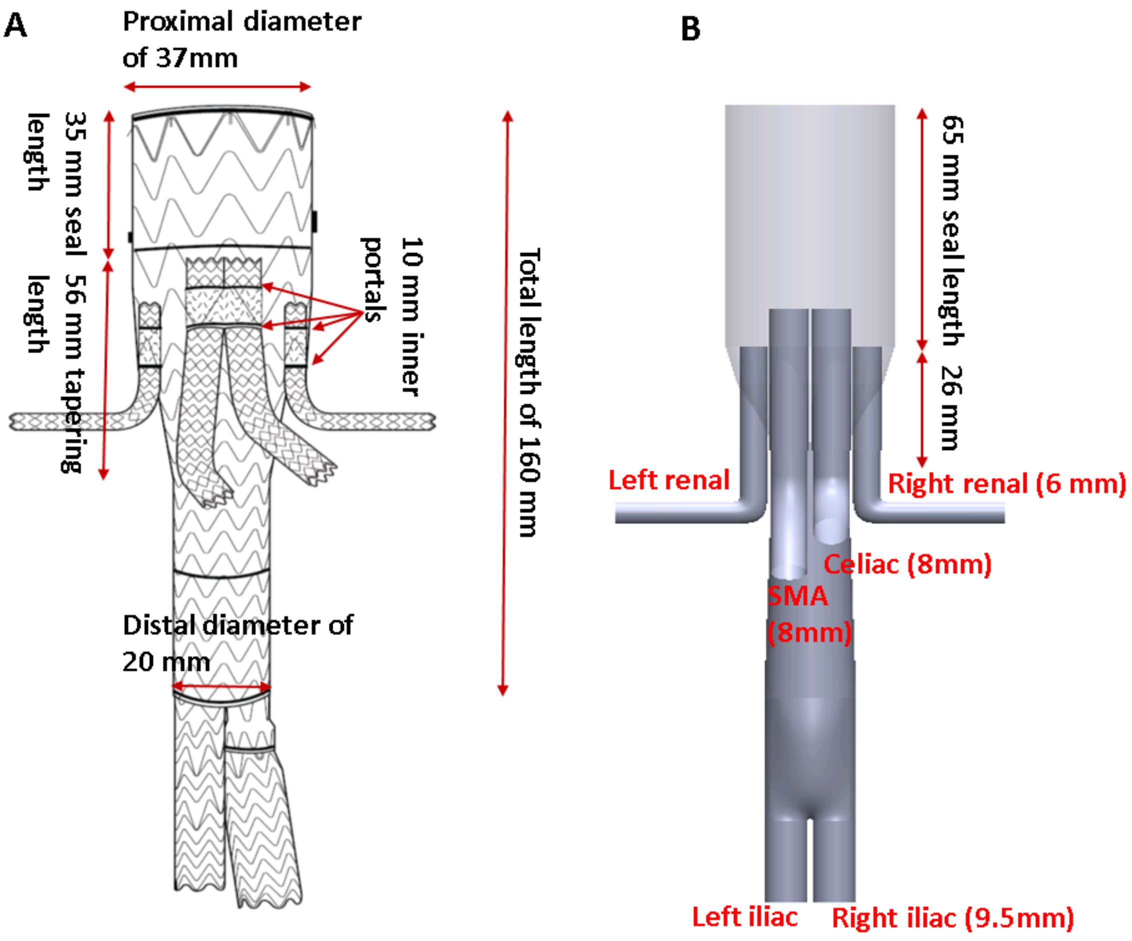

Figure 4.1. (A) Original TAMBE geometry with key dimensions labelled. (B) The modified TAMBE geometry adopted in this study.

Table 4.1. TOAs and lengths of the renal branches for all the simulated geometries.

	Renal TOAs (degree)	Renal branch lengths (mm)
TAMBE model 1	90	45
TAMBE model 2	45	45
TAMBE model 3	110	45
TAMBE model 4	90	70
TAMBE model 5	90	90
Non-planar TAMBE model	90	45

4.2.2 Computational Details

Unstructured meshes were generated for all the TAMBE models by using ANSYS ICEM CFD (ANSYS, Canonsburg, PA, USA). Each mesh consisted of tetrahedral elements in the core and 6 layers of prism elements in the near wall region. Grid independent tests were conducted, starting with a mesh containing around 3 million elements and the number of elements adopted in the final simulation was approximately 7 million. Results were considered grid independent when velocity fields and wall shear stress (WSS) differed by less than 2% between the adopted mesh and a finer mesh.

A physiologically realistic volumetric flow rate waveform extracted from the literature (Taylor et al. 2002) was imposed at the model inlet along with Womersley velocity profiles (Womersley 1955). A schematic of the computational model and the imposed inflow waveform can be found in Figure 4.3. Regarding outlet boundary conditions, a three-element Windkessel model (3-EWM) was coupled with each outlet to incorporate the effect of downstream vasculature.

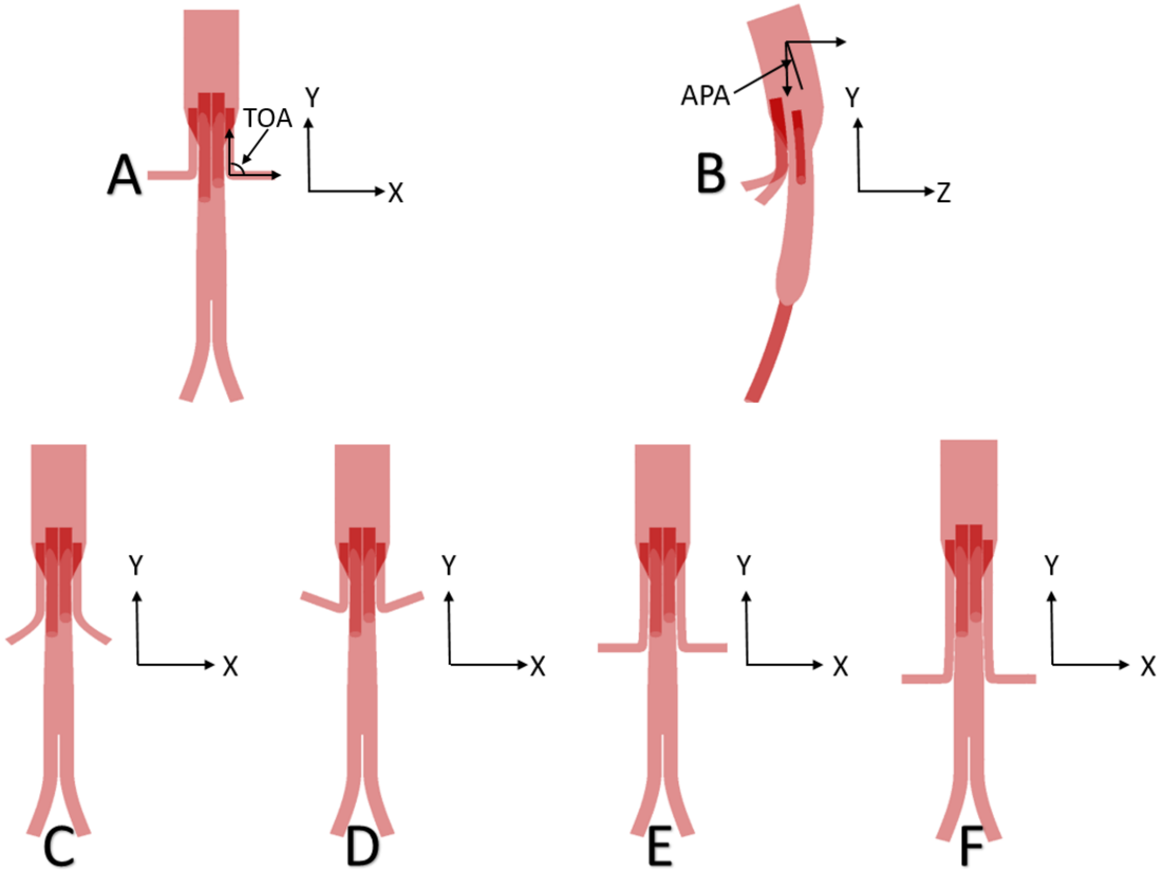

Figure 4.2. Schematic of all the analysed TAMBE geometries: (A) TAMBE model 1, (B) non-planar TAMBE model, (C) TAMBE model 2, (D) TAMBE model 3, (E) TAMBE model 4, and (F) TAMBE model 5. All the planar models are shown in the coronal plane, while the non-planar model is shown in the sagittal plane. The renal take-off angle (TOA) is defined as the angle between main stent-graft endoprosthesis and the renal stent-graft centreline axis. APA refers to anterior/posterior neck angle that is defined as the angle between the y-axis and a line that is perpendicular to the inlet surface in the sagittal plane.

The stent-graft wall was assumed to be rigid, where no-slip boundary conditions were specified. In order to evaluate the effect of geometric variations on the haemodynamic performance, the same set of boundary conditions was applied to all computational models. Blood was assumed to be Newtonian and incompressible with a density of 1060 kg/m^3 and viscosity of 0.004 Pa.s. The conservation equations of mass and momentum were numerically solved for laminar blood flow. All numerical solutions were obtained using ANSYS CFX 15 (ANSYS, Canonsburg, PA, US), which is a coupled solver and the equations for velocity and pressure are solved together in a single system. A high order advection scheme and second order implicit backward Euler scheme were chosen for spatial and temporal discretisation. Numerical convergence was controlled by setting the root mean square residual to be 1×10^{-5}. A uniform time step of 0.001 s was chosen, and all numerical simulations were carried out for three cardiac cycles to reach periodic solutions. Results from the last cycle were used for analysis.

4.2.3 Evaluation of Key Haemodynamic Parameters

Flow patterns inside the stented visceral branches were examined by visulaisation of instantaneous velocity streamlines. Important flow phenomenon, such as flow separation and recirculation were highlighted as they would lead to low and oscillatory WSS, which is considered to be atherogentic (Suess et al. 2016). NWH parameters, such as TAWSS, OSI, and RRT and their relations to atherosclerotic formation have already been defined and explained in Section 3.5.4. In this chapter, an additional metric, endothelial cell activation potential (ECAP), as proposed by Di Achille et al. (2014), was evaluated to identify regions that might be prone to thrombus formation. ECAP is defined as the ratio of OSI to TAWSS, so it can be used to identify regions that simultaneously exposed to high OSI and low TAWSS. It should be mentioned that the 99th percentile values of ECAP were used to avoid any unrealistically high values at isolated spots.

Upon implantation stent-grafts are subjected to time-dependent displacement forces as a result of blood pressure and frictional force exerted by the blood flow. It is important to calculate displacement forces acting on the stent-graft body as they are the main driver for device migration (Kandail et al. 2014). The displacement force was calculated by integrating pressure and WSS over the entire surface of the endograft. It is defined as (Kandail et al. 2014):

$$F_{d,i} = \int_{A,i} \rho dA + \int_{A,i} \left(-\mu \frac{\partial \overrightarrow{v_t}}{\partial \hat{n}}\right) dA \qquad (4.1)$$

where the first term represents the pressure force and the second term represents the WSS force. A is the area of the endograft wall, and i refers to x, y and z in Cartesian coordinates. $\overrightarrow{v_t}$ is the tangential velocity with respect to the unit normal $\hat{n}$ for each wall element and μ is the blood viscosity. The magnitude of displacement force F_d is given by:

$$|F_d| = \sqrt{(F_{d,x})^2 + (F_{d,y})^2 + (F_{d,z})^2} \tag{4.2}$$

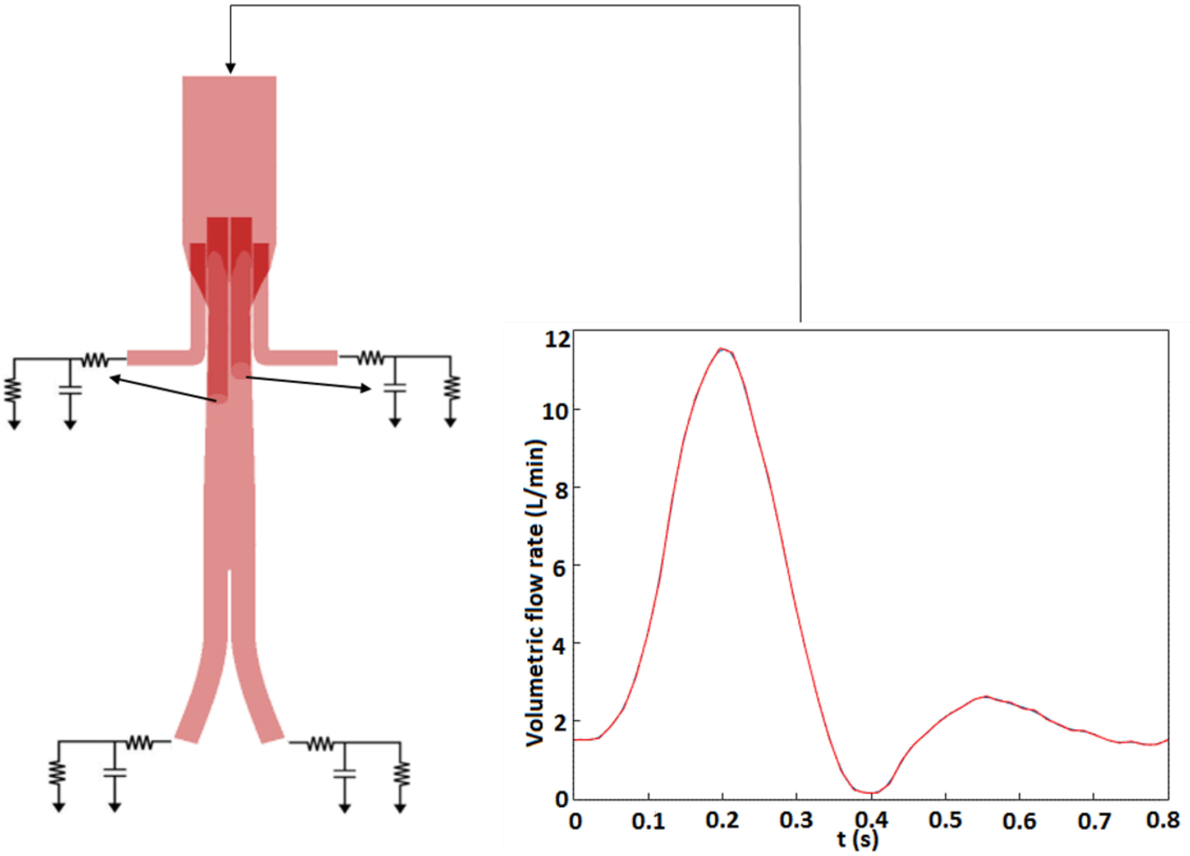

Figure 4.3. Schematic of the computational model employed in this study. Volumetric flow rate waveform extracted from Taylor et al. (2002) was prescribed at the inlet along with Womersley velocity profiles, while a 3-EWM model was applied at all outlets.

4.3 Results

4.3.1 Flow in Branch Vessels

Figure 4.4 shows variations of flow in branch vessels for all the simulated TAMBE models. It is clear that flow waveforms at each branch outlet hardly differed among the 6 models. The cycle-averaged flow rates were 0.51 L/min in the renal artery, 0.54 L/min in the SMA, 0.69 L/min in the coeliac artery, and 0.6 L/min in the iliac artery, accounting for 14.8%, 15.6%, 20%, and 17.4% of the inflow, respectively. Flow division was equal between the left and right renal arteries, as well as between the left and right iliac arteries, as a result of geometric symmetry. Moreover, volumetric flow rates were antegrade throughout the cardiac cycle in all visceral branches (renal, coeliac and SMA), while flow reversal was only observed in the iliac arteries during early diastole.

Instantaneous velocity streamlines near the inner portals and inside the visceral stent-grafts are shown in Figure 4.5 at the time point of maximum flow deceleration (0.28 s). This time point was chosen because flow tends to be most unstable at maximum flow deceleration. It can be seen that velocities were much higher in the branches than in the main stent-graft. Flow was highly disturbed by the inner portals, forming two large and symmetric flow recirculation zones (FRZs) around the entrance to the renal branches (as indicated by yellow stars). Due to the presence of a bend in the visceral stent-grafts, blood flow was skewed towards the inner curvature, causing flow separation and recirculation. Two FRZs were found in the renal branches, with one along the inner curvature (marked by red arrows) and another along the outer curvature (marked by blue arrows). TAMBE model 2 was an exception where the second FRZ was absent.

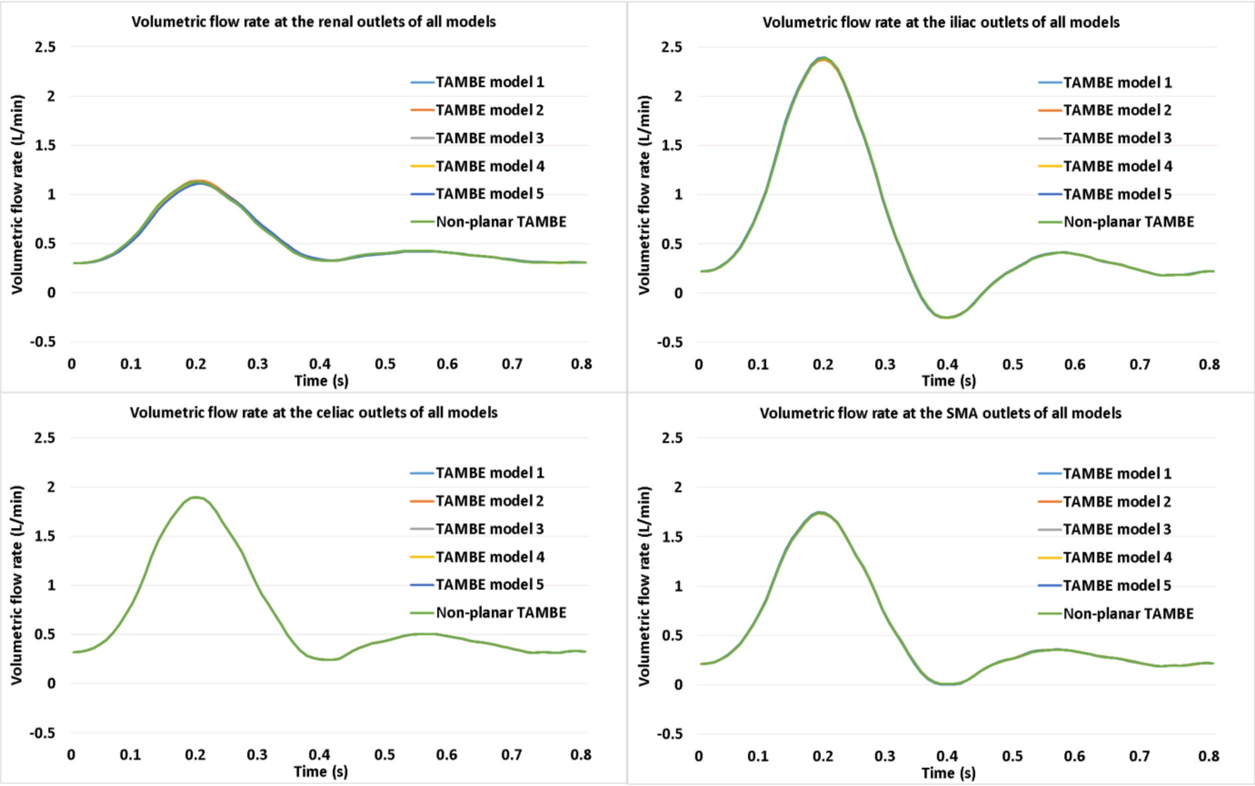

Figure 4.4. Predicted flow rate waveforms in different branches for all the TAMBE models: (A) renal, (B) iliac, (C) coeliac and (D) SMA. It shows that geometric variations hardly altered flow waveforms in the main branches.

4.4.2 Near Wall Haemodynamic Parameters

TAWSS contours are displayed in Figure 4.6 where it is obvious that the magnitude of TAWSS was higher in the visceral branches. Another common feature among all the simulated models was a region of very high TAWSS (> 10 Pa) at the outer curvature of the renal stent-graft, with the exception for TAMBE model 2. This was caused by direct impingement of flow from the vertical straight section of the renal branch. The maximum TAWSS values were evaluated and indicated in the figure where

TAMBE model 3 (TOA = 110°) had the highest peak TAWSS which was more than twice the value in TAMBE model 2 (TOA = 45°), clearly demonstrating the strong influence of TOA on WSS. On the other hand, non-planarity and renal branch length had little effect on the distribution of TAWSS and its peak value. ECAP values were then calculated from the evaluated TAWSS and OSI, in order to identify regions susceptible to thrombus formation. As shown in Figure 4.7 and the corresponding 99th percentile values in Table 4.2, similar ECAP distributions were found for all models, such that all TAMBE stents had a region of high ECAP near the intersection between the bridging stent-grafts and the main stent-graft endoprosthesis, while low ECAP values, up to 0.5 were found on all the visceral stent-grafts. The 99th percentile ECAP values were also comparable among the 6 models, with the maximum difference being 0.18.

4.4.3 Displacement Force

Figure 4.8 shows the magnitude and direction of displacement forces acting on the main stent-graft body for all the TAMBE models. Pressure is the primary contributor to the overall displacement force since the magnitude of WSS is at least two orders of magnitude smaller. Changing the renal branch length and TOA had no effect on displacement force but non-planarity substantially increased its magnitude. As displacement force is a 3D vector, it would also be of interest to examine its direction. For all planar and symmetric TAMBE models (1 to 5), displacement forces were pointing vertically downward in the coronal plane. Non-planarity altered the direction of displacement force which had a cycle-averaged angle of 29° with the y-axis and 61° with the z-axis in the sagittal plane for the non-planar TAMBE model with an APA of 20°.

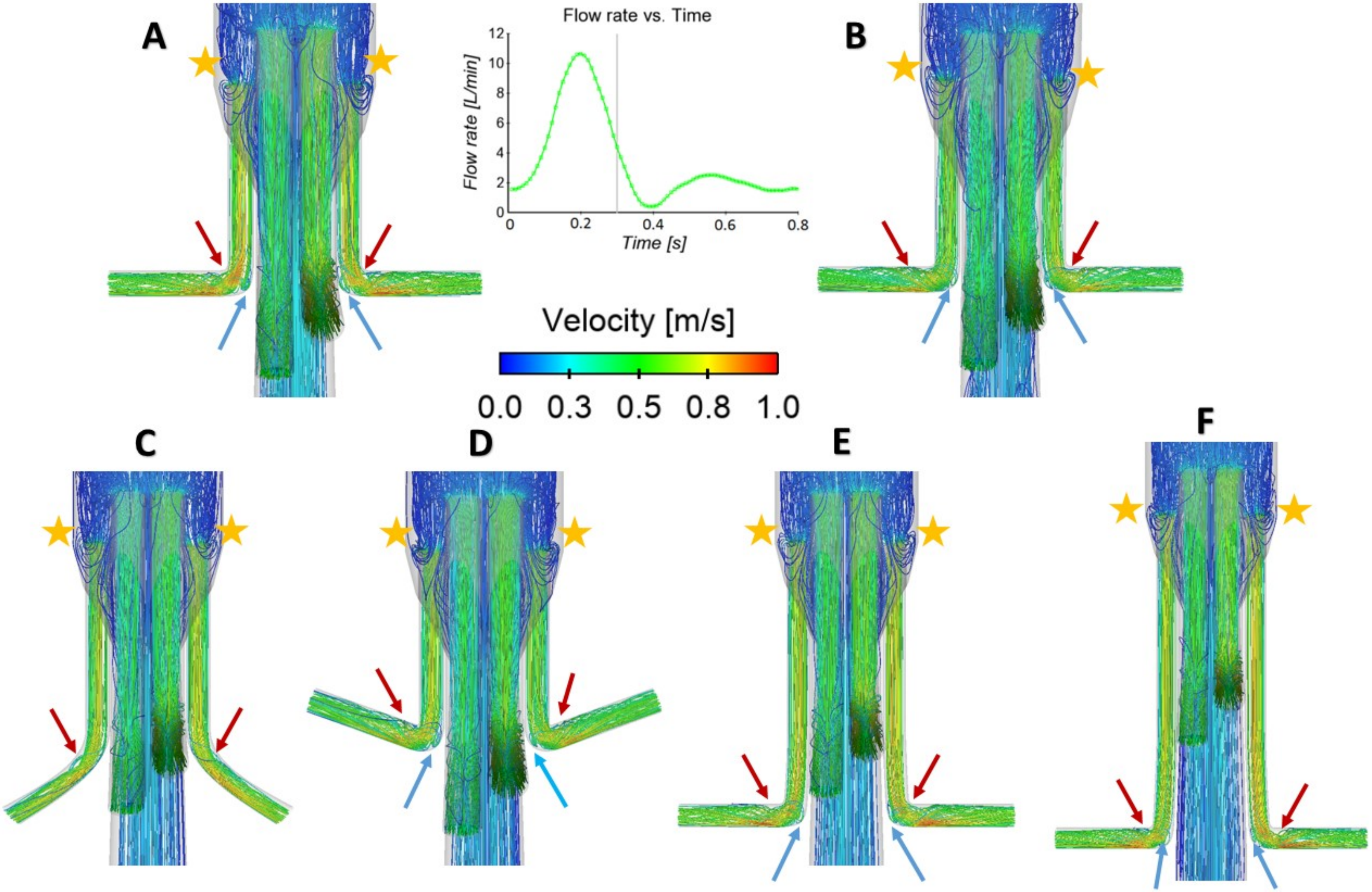

Figure 4.5. Instantaneously velocity streamlines near the inner portals and inside the branch stent-grafts at maximum flow deceleration. (A) TAMBE model 1, (B) non-planar TAMBE model, (C) TAMBE model 2, (D) TAMBE model 3, (E) TAMBE model 4, and (F) TAMBE model 5. All the models are displayed in the coronal plane. Two large and symmetric flow recirculation zones (FRZs) around the entrance to the renal branches are marked by yellow stars. Red and blue arrows indicate the primary and secondary FRZs inside the renal branches, respectively. The secondary FRZ is absent for TAMBE model 2.

4.4 Discussion

TAMBE offers a great potential for adapting to a wide variety of anatomical features of the visceral branches (coeliac, SMA, and renal), especially varying locations of the renal arteries. Previous studies of the anatomy of the visceral arteries confirmed that > 80% of patients with complex AAA or TAAA would be suitable to treatment with TAMBE (Mendes et al. 2014). From 2014 to 2016, thirteen patients treated with TAMBE at multicentres were included in a clinical study to assess the early feasibility of this novel device. Technical success rate was 92% (12/13), with no mortality, aneurysm rupture, conversion to open surgery, dialysis, or spinal cord injury reported. At 30 days, all target vessels (n=52) were patent and no endoleaks occurred. However, its long-term durability has not yet been determined (Oderich et al. 2019). Another critical issue is the durability of bridging stent-grafts for visceral incorporation (Panuccio et al. 2015). Earlier generations of stent-grafts, such as Wallgraft (Boston Scientific, Marlborough, Massachusetts) were related to higher rates of renal occlusion since they are prone to kink (Panuccio et al. 2015). TAMBE incorporates the most advanced GORE VIABAHN Balloon Expandable Endoprosthesis (VBX) which has favourable characteristics, but the long-term durability of VBX stent-graft is still unknown. In order to help assess the effectiveness and long-term durability of TAMBE, a detailed haemodynamic analysis was carried out in this study based on representative geometry and physiologically realistic boundary conditions. Additionally, the effect of variable geometric configurations of renal stent-graft on the haemodynamic performance of TAMBE was evaluated by changing the renal stent-graft length and TOA.

The results showed that TOA and the length of the renal stent-graft had virtually no effect on volumetric flow waveforms in any of the four branches (coeliac, SMA, renal and iliac). Flow distribution among the visceral branch vessels was in line with that reported in the literature (Taylor et al. 2002), with 20% of the supracoeliac aortic flow going into the coeliac artery, 15% into the SMA and 15% into each of the two renal arteries. Since each renal artery usually requires between 20% - 30% of the infra-SMA flow under normal physiological conditions (Williams and Leggett 1989), it can be concluded that normal blood perfusion to the renal arteries was maintained, regardless of geometric variations.

Comparison of flow patterns among the simulated TAMBE models revealed minor quantitative differences except for TAMBE model 2. The gentle bend in the renal branch of TAMBE model 2 allowed flow coming down the vertical segment of the bridging stent-graft to change its direction more gradually, thereby avoiding the occurrence of a second FRZ along the outer curvature. FRZ is characterized by low velocities and flow reversal, which may increase the residence time of blood particles, such as red blood cells and platelets, near the vessel wall (Suess et al. 2016). The presence of a permanent FRZ may trigger thrombus formation, leading to partial or complete occlusion of the visceral stent-graft. Therefore, large and permanent FRZs should be avoided as much as possible.

TAMBE has multiple inner portals which are specially designed to provide better sealing zones between the bridging stent-graft and the main endoprosthesis, and for ease of implantation. However, these inner portals can also cause strong disturbance to the local blood flow, as manifested through the presence of very large FRZs (highlighted in Figure 4.5), indicating an increased risk of subsequent thrombosis in these regions.

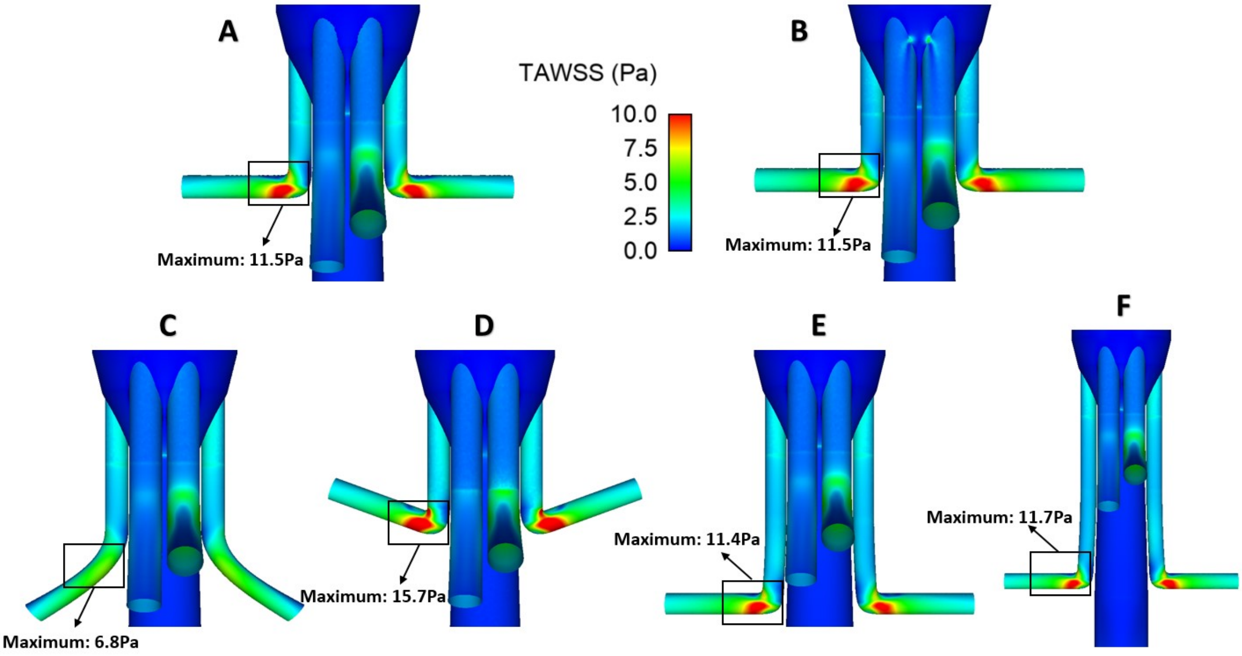

Figure 4.6. Comparison of TAWSS between all the simulated models, with particular attention to the renal stent-grafts. TAWSS values higher than 10 Pa are shown in red and highlighted, together with the maximum TAWSS values. (A) TAMBE model 1, (B) non-planar TAMBE model, (C) TAMBE model 2, (D) TAMBE model 3, (E) TAMBE model 4, and (F) TAMBE model 5. All the models are displayed in the coronal plane.

WSS is an important haemodynamic parameter since it can influence endothelial cell functions, such as proliferation, apoptosis, migration, permeability and remodelling (Lehoux et al. 2006; Li et al. 2005). Healthy arterial WSS ranges between 1 and 7 Pa (Malek et al. 1999). WSS values lower than 0.4 Pa have been associated with intimal hyperplasia and in-stent thrombosis (Malek et al. 1999; Suess et al. 2016), whereas high WSS values are related to endothelial damage, stent material fatigue, thrombogenic and subsequent blockage of the lumen patency (Chatzizisis et al. 2007). WSS changes during the cardiac cycle because of the pulsatile nature of blood flow, as such it is usually analysed by averaging the magnitude of instantaneous WSS over a cardiac cycle to yield a cycle-averaged value, referred to as TAWSS (see equation 3.38 for definition). TAWSS in the visceral stent-grafts was much higher than in the main endoprosthesis due to increased blood velocities. Among the three visceral branches, the renal stent-grafts experienced the highest TAWSS as a result of their small portal diameters. Very high TAWSS values (> 10 Pa) for all the simulated models (except for TAMBE model 2) were found to be concentrated at the proximal region of renal arteries, while values of 5-7 Pa were distributed along the distal renal arteries. Such spatial differentiations in WSS between the proximal and distal renal arteries have been postulated by several studies to induce and increase myointimal hyperplasia (Chen et al. 2009; DePaola et al. 1992; Georgakarakos et al. 2014). Moreover, the maximum TAWSS in TAMBE model 2 was 6.8 Pa, within the normal range, but this was 15.7 Pa in TAMBE model 3, indicating a strong relationship between the maximum TAWSS and TOA.

Table 4.2. Endothelial Cell Activation Potential (ECAP) 99th percentile values for all the simulated TAMBE models.

	99th percentile ECAP values
TAMBE model 1	2.83
TAMBE model 2	3.01
TAMBE model 3	2.91
TAMBE model 4	2.90
TAMBE model 5	2.99
Non-planar TAMBE	2.85

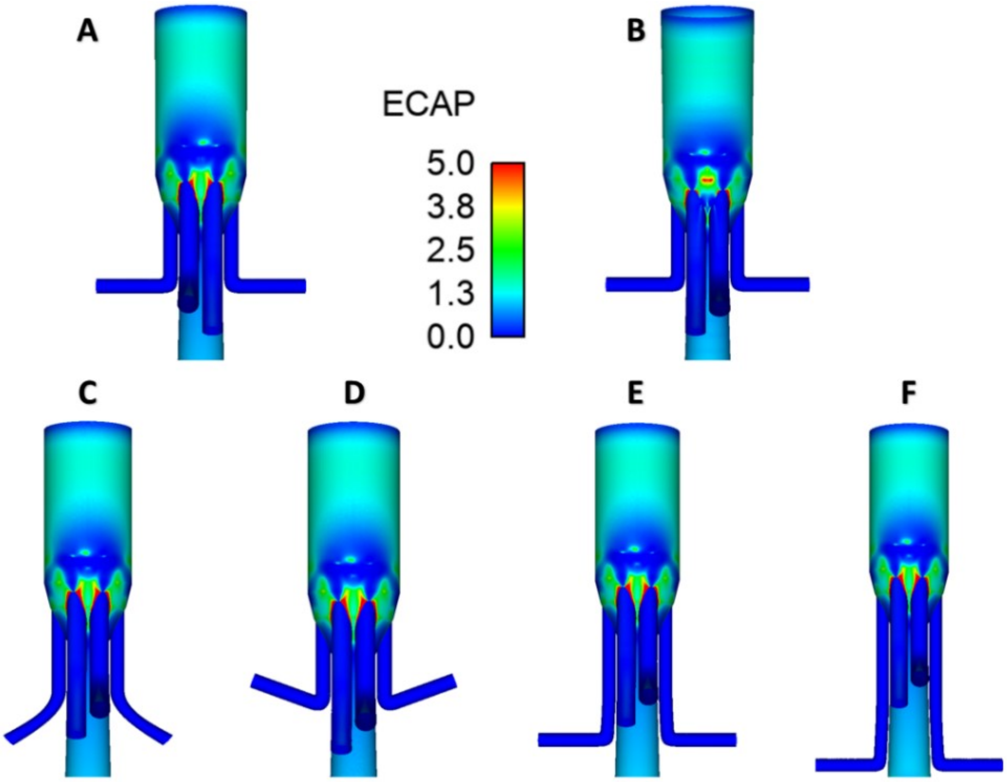

Figure 4.7. ECAP contours for all the simulated TAMBE models in the coronal plane. (A) TAMBE model 1, (B) non-planar TAMBE model, (C) TAMBE model 2, (D) TAMBE model 3, (E) TAMBE model 4, and (F) TAMBE model 5. ECAP is defined as the ratio of OSI to TAWSS, so it can be used to identify regions that simultaneously exposed to high OSI and low TAWSS. Regions where ECAP values higher than 5 (shown in red) were associated with thrombus formation. Similar ECAP distributions were found for all models, with a region of high ECAP (> 5) near the intersection between the bridging stent-grafts and the main stent-graft.

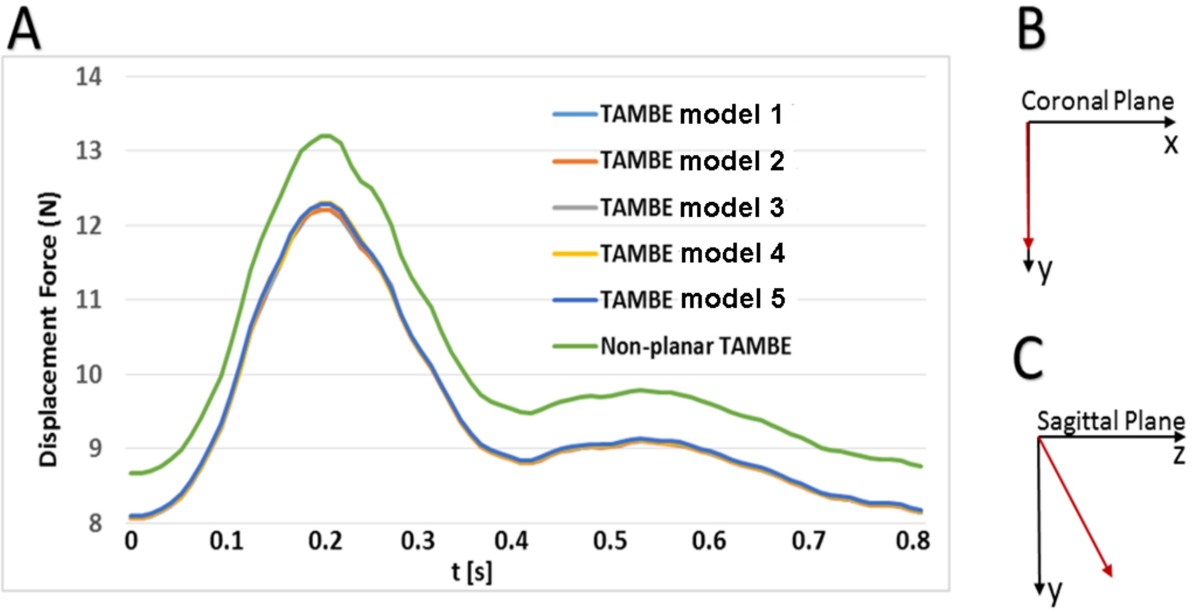

Figure 4.8. (A) Time variation of the magnitude of displacement forces acting on all the TAMBE stent-grafts. (B) Direction of the displacement force for all the planar TAMBE models as indicated by a red arrow in the coronal plane. (C) Direction of the displacement force for the nonplanar TAMBE model as indicated by a red arrow in the sagittal plane.

Spatial distributions of ECAP have been used to find regions that might be prone to thrombosis. As described by Di Achille et al. (2014), locations of thrombus formation in AAA patients correlated well with the regions where ECAP values were greater than 5. Therefore, the colour legend of ECAP was set to range from 0-5 so that the regions shown in red could be considered to have an increased risk of thrombosis. As shown in Figure 4.7, high ECAP values (> 5) were found around the intersections between the inner portals and the main stent-graft. However, thrombus formation in these regions would be expected to cause no adverse clinical consequences. On the other hand, very low ECAP values (< 0.5) were found in all the visceral stent-grafts, even in the regions adjacent to persistent FRZs. This can be explained by the fact that although TAWSS was low in regions of FRZ, OSI values were also low in these regions and as a result, the ECAP values (defined as the ratio of OSI to TAWSS) were very low. Comparisons between different stent-graft configurations indicated that TAMBE model 1 had the lowest 99th percentile ECAP values, but differences among the simulated models were trivial. Therefore, it can be deduced that geometric variations had very little effect on the predicted risk of device-induced thrombosis.

Displacement forces are related to device migration and future complications, such as type I endoleaks. Results obtained in this study showed that variations in renal stent-graft length and TOA did not alter the magnitude of displacement forces. However, non-planarity increased the magnitude of displacement forces throughout the cardiac cycle. This was also observed by another similar study

(Kandail et al. 2015). As reported by Melas et al. (2010), the threshold value was 26.97 N for self-expanding stent-grafts and 34.25 N for balloon-expandable devices, to dislocate the proximal portion of a planar stent-graft (with hooks and barbs) by more than 20 mm. Lower values of 13.58 N for self-expanding stent-grafts and 14.72 N for balloon-expandable devices were required to dislocate a stent-graft without hooks and barbs. The maximum displacement force experienced by the planar stent-grafts included in this study was up to 12.24 N, which was well below the threshold values cited above. TAMBE stents are equipped with hooks and barbs and the preferred branch component is a specially designed balloon-expandable covered stent-graft. The Non-planar TAMBE model experienced a maximum displacement force of 13.14 N, which was also well below the threshold value of 32 N reported to dislocate a non-planar stent-graft (Rahmani et al. 2016). Based on these results, it can be deduced that varying the geometric configuration of the visceral stent-grafts had no effect on the magnitude of displacement forces. Even though non-planarity increased the magnitude of cycle-averaged displacement force, it was still at low risk of distal migration.

Limitations

First, idealised and simplified TAMBE geometries were adopted in this study due to limited clinical data on this novel device. In the future, numerical simulations of patient-specific TAMBE models will be carried out. Second, the lumen surface of the main stent-graft endoprosthesis and bridging stent-graft was assumed to be smooth. This is a major assumption since stent wires are attached at the graft surface, and their shape and pattern can alter the near wall haemodynamics, especially the local WSS. Third, ECAP values were evaluated to identify regions that might be prone to thrombosis without directly modelling the actual process of thrombus formation. Fourth, stent-graft wall was assumed to be rigid. This can be justified since the stent-graft wall is made up of graft fabric supported by a metal framework, which is very stiff and thus the influence of wall compliance on flow is considered to be minimal (Kleinstreuer et al. 2008). Finally, current numerical simulations were mainly focused on the haemodynamic performance of TAMBE under a normal resting condition. Exercise scenarios were not included here since these have been addressed by others (Kandail et al. 2016; Les et al. 2010). However, it is worth mentioning that exercise would increase the peak Reynolds number, where disturbance and turbulence in blood flow might occur. The effect of turbulence on the haemodynamic performance of TAMBE has not been examined and should be considered in future studies.

4.5 Summary

All the TAMBE models examined here can maintain normal blood perfusion to the visceral branches based on the predicted cycle-averaged volumetric flow rate. Persistent FRZs were found in the renal stent-grafts as a result of sudden change in the direction of blood flow. However, ECAP values were not high enough to induce thrombosis in the renal branches. Although high ECAP values were observed around the intersections between the inner portals and the main stent-graft endoprosthesis, thrombosis in these regions would not lead to adverse clinical consequences. A positive relationship between the take-off angle (TOA) of renal stent-grafts and the maximum TAWSS was found, where a sharp bend in the renal anatomy greatly increased the maximum TAWSS, indicating a higher risk of device failure in this configuration. Finally, geometric variations did not alter the magnitude of displacement forces. Even though non-planarity increased the magnitude of displacement forces, they were still below the threshold for device migration.

Chapter 5

Application 2: Evaluating the Haemodynamic Performance of a Novel Branched Stent-Graft for Thoracic Endovascular Aortic Repair (TEVAR)

5.1 Analysis of Blood Flow in an Idealised Model of Dual-Branched Stent-Graft for Endovascular Repair of the Aortic Arch

5.1.1 Introduction

Thoracic endovascular aortic repair (TEVAR) has been developed over two decades and has become one of the most popular choices for treating descending thoracic aortic diseases. In recent years, its application has been extended more proximally in the aorta, if there is a suitable landing zone, to treat pathology in the aortic arch and ascending aorta. However, in the aortic arch, the curvature of the arch and proximity of the ostia of the three arch vessels to each other make it difficult to obtain a landing zone with sufficient length to ensure firm fixation of the device, rendering the use of branched or fenestrated stent-grafts (BSG or FSG) (Ishimaru 2004). As mentioned in the previous chapter, BSGs are conceptually more appealing than FSGs as they are adaptable to a wide range of anatomical configurations. BSGs for arch repair can be manufactured as either single- or double-branched endografts with or without inner tunnels (van Bakel et al. 2018). A single-branched stent-graft requires two bypass connections between the upper vessels, e.g., bypass between the innominate artery (IA) and the left common carotid artery (LCCA) or between the left subclavian artery (LSCA) and the left common carotid (LCCA), while double-branched endografts are developed for zone 0 (Z0) deployment with two bridging stents connected to IA and LCCA (Czerny et al. 2018; Haulon et al. 2014; Spear et al. 2016). Van Bakel et al. (2018) computationally compared different endograft designs for Z0 aortic arch repair, including two single-branched stent-grafts and two dual-branched stent-grafts, and their results indicated that dual-branched stent-grafts offered better haemodynamic performance than single branch alternatives. Hence, only dual-branched stent-grafts were included in this study.

Insertion of a BSG may increase the complexity of the flow (Kandail et al. 2015). Detailed knowledge of the haemodynamic performance of dual-branched thoracic endografts is important for assessing the risk of post-intervention complications and long-term durability of the device. The most common and potentially life-threatening post-TEVAR complications include endoleaks, distal migration of the device, and thrombus formation within the stent-graft. Among all types of endoleaks, type I endoleaks occur more frequently in TEVAR, resulting from poor sealing between the device and the aortic wall (Resch et al. 2001). Distal migration of the device can also result in type I endoleak, thereby increasing the risk of aneurysm rupture. Thrombus formation within the stent-graft can reduce or even block blood perfusion to the supra-aortic branches, which may lead to ischaemia. All these complications are associated with abnormal flow behaviour and flow induced forces. For example, high values of shear stress may cause platelet activation, whereas low wall shear stress and long residence time can promote platelet adhesion and thrombus formation (Menichini and Xu 2016; Nesbitt et al. 2009). Large displacement forces acting on the stent-graft are the main cause for device migration (Kandail et al. 2014). However, there is a lack of complete evaluation of these parameters, along with the assessment of long-term durability of BSG for arch repair in the literature. The present work therefore consisted of numerical studies of blood flow in idealised 3-D models of the aortic arch and its three upper vessels, before and after the introduction of a dual-branched stent-graft. The BSG contains a main body and two inner tunnels connected to the IA and LCCA, respectively. As off-the-shelf BSGs are only manufactured in a small range of sizes that may not completely fit the patients' anatomies, the main aim of this work was to evaluate the haemodynamic consequences of endovascular repair of the aortic arch using BSGs and to study the influence of inner tunnel diameters on the flow characteristics. Moreover, occlusion of the LSCA and consequent bypass of this vessel through the LCCA was considered. These were then coupled with physiologically realistic boundary conditions. Haemodynamic performance was evaluated in terms of flow pattern, wall shear stress and flow-induced displacement forces.

5.1.2 Methodology

5.1.2.1 Model Geometries and Mesh Generation

An idealised arch model was created based on the physiological dimensions reported by Finlay et al. (2012) and used as a reference geometry. As shown in Figure 5.1, this model encompassed part of the ascending aorta, the aortic arch with its three branches (IA, LCCA and LSCA), and part of the descending aorta. Dual branched stent-graft models were hypothetically constructed with two equal-diameter inner tunnels within the main graft body. These inner tunnels lead into the IA and the LCCA, providing sufficient blood perfusion to these supra-aortic branches. The diameters of inner tunnels were 8 mm, 10 mm and 12 mm and the corresponding models were stent-graft 1, stent-graft 2, and stent-graft 3, respectively. All the 3-D models were constructed using SolidWorks (Dassault Systems, Velizy, France), and the key dimensions are summarised in Table 5.1. It should be mentioned that in reality, the aortic arch is highly twisted and non-planar with large variations in some key geometric dimensions such as the arch radius and angle. However, including these geometric variations could cause other confounding factors as the main aim of this study was to investigate the effects of varied inner tunnel diameters on the haemodynamic performance of BSG. The effects of twisted and non-planar arch models will be considered in the following section (Section 5.2) based on patient-specific geometries. In all three stent-graft models, the LCCA and LSCA were artificially extended by 20 mm to ensure that the resolved flow field was not influenced by the location of inlet and outlet boundary conditions. The geometric dimensions were checked and approved by a clinical collaborator who has extensive knowledge and experience of stent-graft devices for TEVAR.

As can be seen in Figure 5.1, in the case of stent-graft 1, the two inner tunnels had smaller diameters than the native vessels and were therefore connected in diverging configurations. In the other two stent-graft models, a diverging tunnel configuration was used for the IA and a converging one for LCCA. All the geometric models were then discretised into a fine unstructured grid using ANSYS ICEM CFD (ANSYS, Canonsburg, PA, USA). To ensure adequate resolution of the near wall flow parameters, 10 prismatic layers were created near the wall, which were combined with tetrahedral elements away from the wall, and local mesh refinement was performed in regions adjacent to curvature and abrupt changes. Grid independent tests were carried out and the number of elements adopted for the final analysis was approximately 3.2 million for the arch model without BSG and 10 million for the more complicated geometries with the dual-branched device.

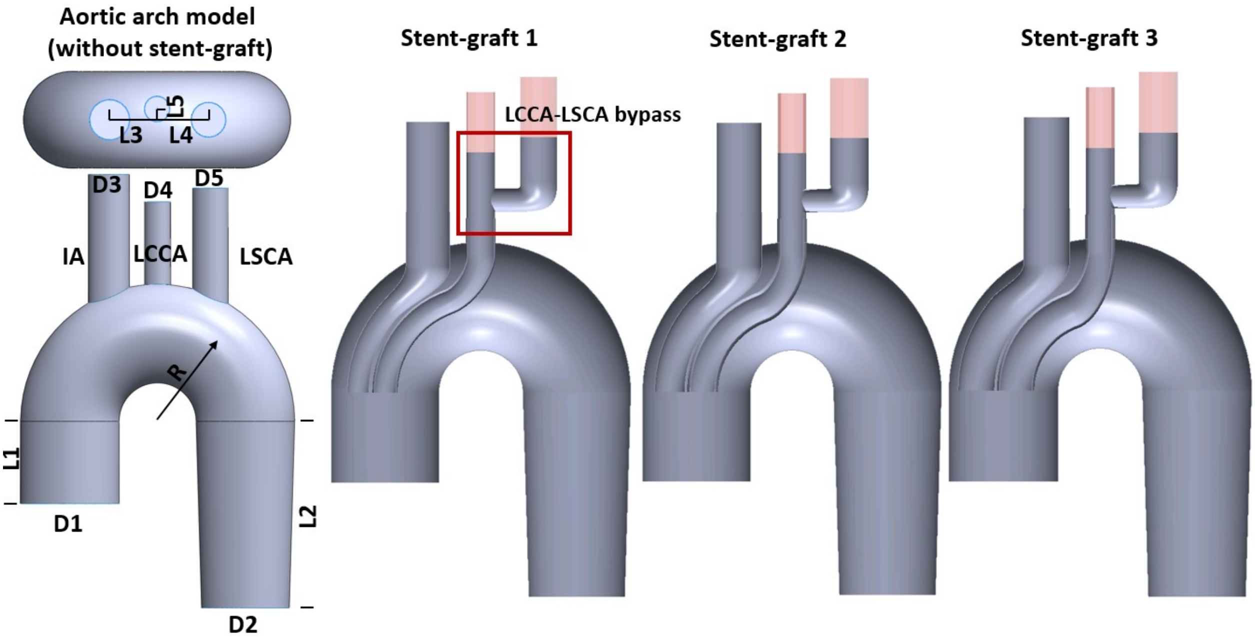

Figure 5.1. The aortic arch model (left) and the three stent-graft models with an inner tunnel diameter of 8 mm, 10 mm, and 12 mm, for stent-graft 1, stent-graft 2, and stent-graft 3, respectively. The LCCA-LSCA bypass procedure was included in all three stent-graft models as highlighted by a red square in stent-graft 1. The LCCA and LSCA were artificially extended by 20 mm so that the resolved flow field was not influenced by the location of outlet boundaries.

5.1.2.2 Boundary Conditions and Numerical Procedures

Each model has 1 inlet and 4 outlets. A flat velocity profile was prescribed at the model inlet along with a realistic velocity waveform (Figure 5.2) adopted from the literature (Tan et al. 2009). The 3-EWM was applied at all the outlets with the model parameters being derived from cycle-averaged outflow and pressure values. The cycle-averaged pressure value at each outlet was evaluated from pressure waveforms adopted from the literature (Olufsen et al. 2000), whereas the cycle-averaged branch outflow was based on a fixed flow split of the inlet flow. The sum of flow exiting through the supra-aortic vessels was assumed to be 30% (Cheng et al. 2015), and flow division among the three branches was determined based on their cross-sectional areas (Zamir et al. 1992). In addition, the walls of the aorta and stent-graft were assumed to be rigid and motionless so that a no-slip boundary condition was specified. The same boundary conditions were applied to all models.

Table 5. 1. Essential geometric dimensions used to construct the computational model.

Geometric parameters	Values (mm)		
Inlet diameter (D1)	36		
Outlet diameter (D2)	32		
Length of the ascending aorta (L1)	30		
Arch angle (degree)	180		
Arch radius (R)	32		
Length of the descending aorta (L2)	68		
IA diameter (D3)	15		
LCCA diameter (D4)	9.5		
LSCA diameter (D5)	13		
Distance between the IA and LCCA (L3)	5.5		
Distance between the LCCA and LSCA (L4)	8		
Distance of LCCA anterior to IA and LSCA (L5)	4		
Geometric variation for the dual-branched stent-graft			
Parameter (mm)	**Stent-graft 1**	**Stent-graft 2**	**Stent-graft 3**
IA inner tunnel diameter	8	10	12
LCCA inner tunnel diameter	8	10	12

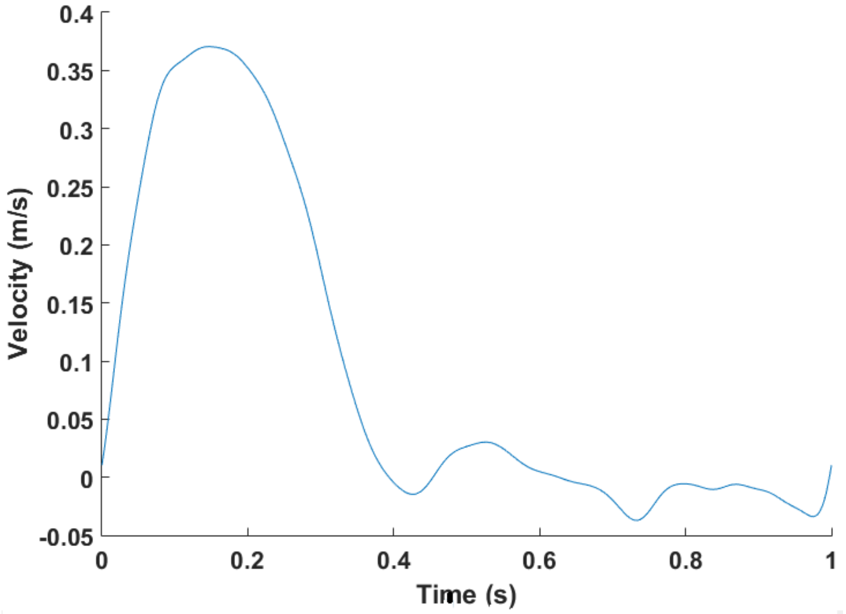

Figure 5.2. Pulsatile velocity waveform adopted from the literature (Tan et al. 2009) was prescribed at the inlet with the assumption of a flat velocity profile.

Blood was assumed to be Newtonian and incompressible, with a density of 1060 kg/m^3 and a constant dynamic viscosity of 0.004 Pa.s. From Figure 5.2, it can be found that the peak systolic velocity prescribed at the inlet was 0.37 m/s and the cycle duration was 1 s. Based on the diameter of the inlet, the peak Reynolds number at the inlet was 3530 and the Womersley number was 23. Therefore, the previously described SST-Tran model (Chapter 3, Section 3.3.1) was employed, with a low inlet turbulence level of 1.5% to represent initial disturbances in the flow (Tan et al. 2009). The Navier-Stokes equations together with the equations needed for the SST-Tran model were solved using a finite-volume based CFD solver, ANSYS CFX 15 (ANSYS, Canonsburg, PA, US). A uniform time-step of 0.001 s was used and the convergence criterion based on the root mean squared residuals was set to be 10^{-5}. All simulations were carried out for three cardiac cycles to reach a period solution, and the results of the last cycle were extracted for further analysis.

5.1.3 Results

5.1.3.1 Flow in the Supra-Aortic Vessels

To assess the effectiveness of BSG for TEVAR, it is essential to understand how it may affect blood flow to the arch vessels. This is important because if perfusion to the arch vessels falls below a certain threshold, some serious complications may occur, such as cerebral ischaemia. Volumetric flow rate waveforms at each outlet of the non-stented model and all BSG configurations are shown in Figure 5.3. From these waveforms, the cycle-averaged volumetric flow rates at the four outlets of all the simulated models were determined, together with the corresponding percentages of flow split, as summarised in Table 5.2. Flow waveforms were quite comparable between different models at each outlet, except for the LSCA, where the volumetric flow rates were lower during systole but higher during early diastole after implantation of the stent-grafts. Additionally, stent-graft 3 with the largest inner tunnels produced constantly higher systolic volumetric flow rates than the other two endografts. These resulted in an obvious increase in blood perfusion to the LSCA of stent-graft 3 (11.3%), compared to stent-grafts 1 & 2, as indicated in Table 5.2. In the aortic arch model without a stent-graft, flow distribution to the IA, LCCA and LSCA was 13.6%, 5.4% and 10.4%, respectively. The insertion of a BSG slightly reduced the amount of flow through the IA, slightly increased flow to the LCCA and LSCA except for stent-graft 1 which has the smallest inner tunnel diameter.

Flow patterns for the aortic arch models with and without stent-graft were compared through the instantaneous velocity streamlines at two characteristic time points, namely, peak systole (0.15 s) and mid-systolic deceleration (0.29 s). Figure 5.4 shows that in the absence of stent-graft, helical flow started to develop in the aortic arch at peak systole, which became more obvious and extended to the descending aorta at mid-systolic deceleration. Insertion of the branched stent-graft disturbed flow in the arch with the presence of high velocity flow in the inner tunnels, but hardly affected flow in the descending aorta. The most obvious difference between the models with and without stent-graft was flow in the arch vessels, where flow was highly disturbed by the dual branched stent-graft especially in the entrance regions. Comparisons among the three stent-graft models suggested that most flow disturbance was caused by stent-graft 1 which has the smallest inner tunnel diameter.

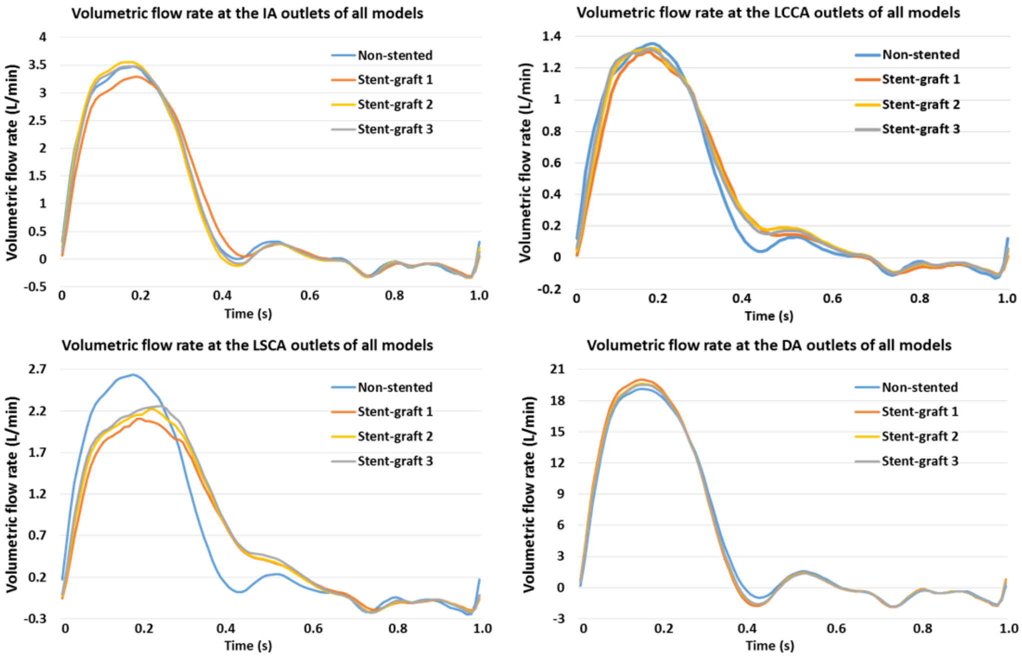

Figure 5.3. Predicted flow rate waveforms over one cardiac cycle for all the simulated models at different outlets.

Table 5.2. Comparison of mean flow at each outlet in the non-stented aortic arch and 3 stented models, along with the respective percentages of flow split.

	Cycle-averaged flow rate (L/min)			
	IA	LCCA	LSCA	DA
Non-stented	0.88 (13.6%)	0.35 (5.4%)	0.67 (10.4%)	4.57 (70.6%)
Stent-graft 1	0.87 (13.4%)	0.35 (5.4%)	0.66 (10.2%)	4.59 (70.9%)
Stent-graft 2	0.86 (13.3%)	0.37 (5.7%)	0.69 (10.7%)	4.55 (70.3%)
Stent-graft 3	0.86 (13.3%)	0.37 (5.7%)	0.73 (11.3%)	4.51 (69.7%)

For more detailed comparisons of flow, a cross-sectional view of the stent-graft model in the sagittal plane was plotted with velocity contours along with in-plane velocity vectors as shown in Figure 5.5. Blood flow accelerated when entering the inner tunnels due to the reduced cross-sectional area, which was more prominent in stent-graft 1. Moreover, there were gaps in between the two inner tunnels as well as between the tunnels and the endograft body, where blood velocities appeared to be quite low. Looking at the arch branches, flow recirculation zones (FRZ) could be observed in the LCCA and the bypass graft, as highlighted by red arrows. FRZs correspond to low WSS, which could increase the possibility of thrombus formation and should be minimised or avoided whenever possible (Kandail et al. 2015). Changing the inner tunnel diameters had a strong influence on local flow patterns inside the arch vessels, where the size and strength of FRZs varied. Stent-graft 3 with the largest inner tunnel diameter performed better with only one FRZ located in the LCCA.

5.1.3.2 Wall Shear Stress

Predicted TAWSS distributions in the models with and without stent-grafts are shown in Figure 5.6. It can be seen from Figure 5.6a that the inclusion of the branched stent-graft greatly increased the nonuniformity and magnitude of TAWSS in the arch vessels. The high velocity flow through the inner tunnels impacted on the branch vessel walls when changing its direction, resulting in very high WSS (> 10 Pa) which may lead to other complications. In all three stent-graft models, the maximum TAWSS (as indicated by the black arrows) was found at the anastomosis between the bypass graft and the LCCA, with stent-graft 1 showing the highest value of 50.9 Pa. On the other hand, insertion of the branched stent-graft resulted in very low WSS values (< 0.4 Pa), which were observed around the ostia of the supra-aortic vessels of all three stent-graft models (Figure 5.6b).

5.1.3.3 Displacement Forces Acting on the Branched Stent-Grafts

Figure 5.7 shows the magnitude of displacement forces experienced by the branched stent-grafts over one cardiac cycle. The displacement force was calculated by taking an area integral of the net pressure and WSS over the entire wall of the branched stent-graft (equation 4.1). More than 99% of the overall displacement force was attributed to the pressure as the magnitude of WSS was much smaller. Stent-graft 1 with the smallest inner tunnels exhibited the highest cycle-averaged displacement force of 20.1 N, along with the maximum peak value of 24.9 N, as summarised in Table 5.3.

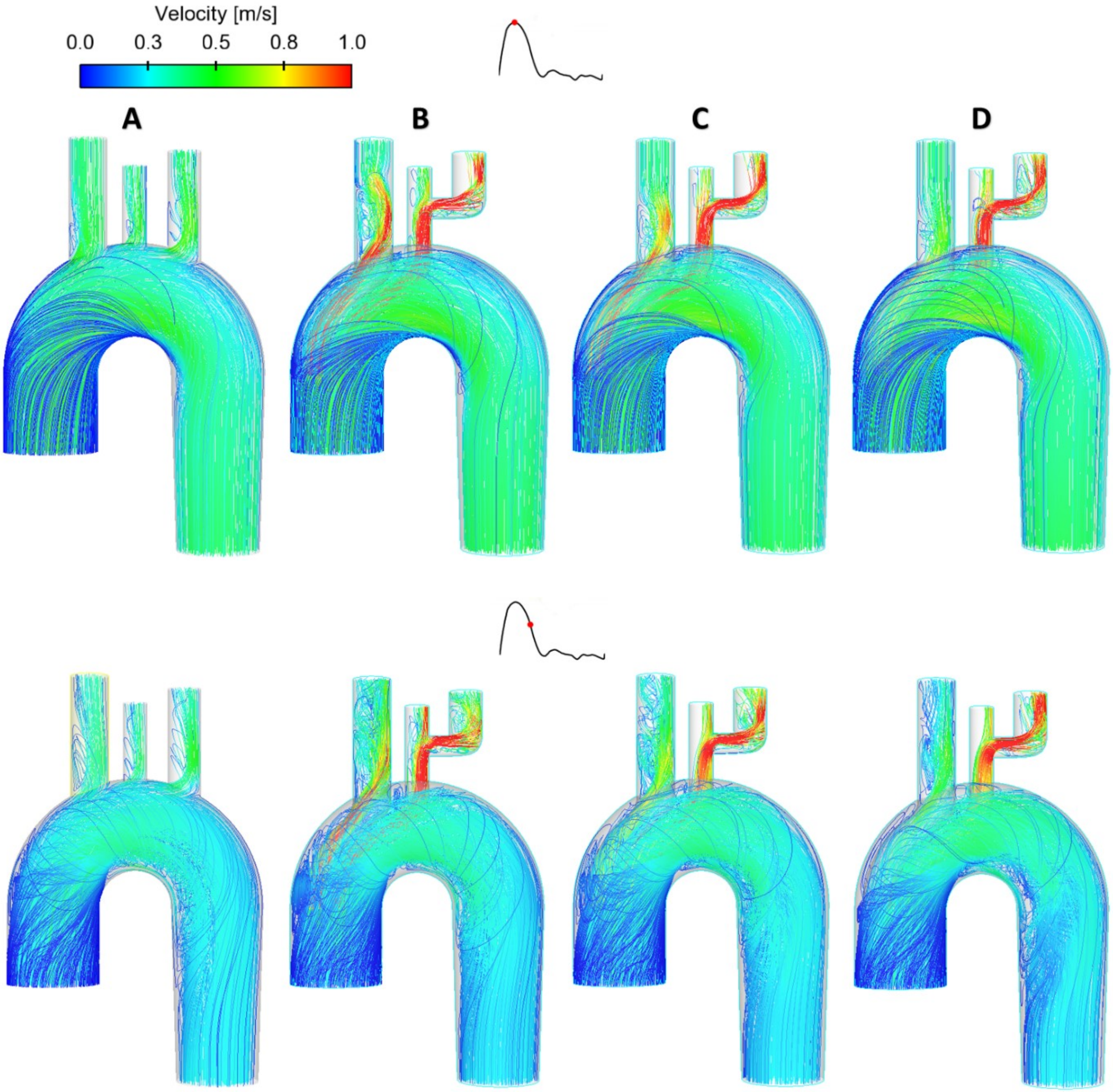

Figure 5.4. Comparison of instantaneous velocity streamlines between the non-stented (A), stent-graft 1 (B), stent-graft 2 (C), and stent-graft 3 (D) models at two characteristic time points: peak systole (top), and mid-systolic deceleration (bottom).

5.1.4 Discussion

Endovascular repair of aortic arch diseases provides a minimally invasive and efficient means of treatment, especially for high risk patients with other comorbidities (Haulon et al. 2014). The implantation of endografts in the arch considerably alters certain haemodynamic characteristics of the region, the effects of which are of great interest. However, not all parameters can be measured directly *in vivo,* therefore the aim of this study was to analyse blood flow in an idealised prototype of dual-branched stent-graft for endovascular repair of the aortic arch using CFD methods. A physiologically representative arch model, together with physiologically realistic boundary conditions, was adopted as a reference case. Three stent-graft models with different inner tunnel diameters were built, with the BSG consisting of a main body with two inner tunnels for cannulation of the IA and LCCA, and a bypass of the LSCA through the LCCA.

Volumetric flow rate waveforms were evaluated at each outlet of all the simulated models, along with the respective cycle-averaged volumetric flow rates and percentages of flow split. In the reference case, flow divisions among the IA, LCCA, and LSCA were 13.6%, 5.4% and 10.4%, respectively. After incorporation of a BSG, blood perfusion to the IA was slightly reduced in all models. In these models, the inner tunnel for the cannulation of IA had a smaller diameter than the IA itself, forming a diverging configuration, which may increase energy loss and reduce blood perfusion. On the other hand, in stent-grafts 2 and 3, a converging tunnel for the LCCA helped increase blood perfusion to both the LCCA and LSCA, while in stent-graft 1, a diverging connection to the LCCA caused a slightly reduction in the LSCA flow. These results indicated that a converging configuration with the inner tunnels being slightly larger than the original arch vessels would be beneficial as far as supra-aortic blood perfusion is concerned. Moreover, stent-graft 3 achieved higher blood perfusion to the LSCA than stent-graft 2 as a result of a more convergent diameter tunnel for the LCCA, suggesting a strong dependence of flow division on the diameter of inner tunnel with larger diameter leading to higher blood flow.

Helical blood flow patterns were observed in all four models at the time-point of mid-deceleration. These findings are consistent with blood flow patterns in a healthy aorta, as reported by several authors: blood flow ranges from axial during the first part of the systole, to helical in its mid-to-late portion, with complex flow recirculation at the end of the systole and throughout diastole (Kousera et al. 2013; Tan et al. 2009). Helical flow has been associated with increased oxygen transport and lipid washout (Liu et al. 2009; Wen et al. 2011). As shown in Figure 5.5, persistent FRZs were identified in the arch vessels of all the stent-graft models. Within FRZ, flow is disturbed, causing regions of low WSS which has been widely accepted as atherogenic (Suess et al. 2016). Low WSS is also known to promote thrombus formation, which may lead to partial or even complete occlusion of the arch vessels, preventing blood perfusion to the upper part of the body, and thus resulting in ischaemia. By comparing three BSG configurations, multiple FRZs were observed in stent-graft 1 that consisted of diverging tunnels for both the IA and LCCA. Increasing the diameter of the inner tunnels reduced the number of FRZs, as only one was found in the LCCA of stent-graft 3. Based on these results, should an off-the-shelf BSG be used, choosing a device with larger inner tunnels than the corresponding arch vessels would be preferred in order to minimise the formation of FRZ.

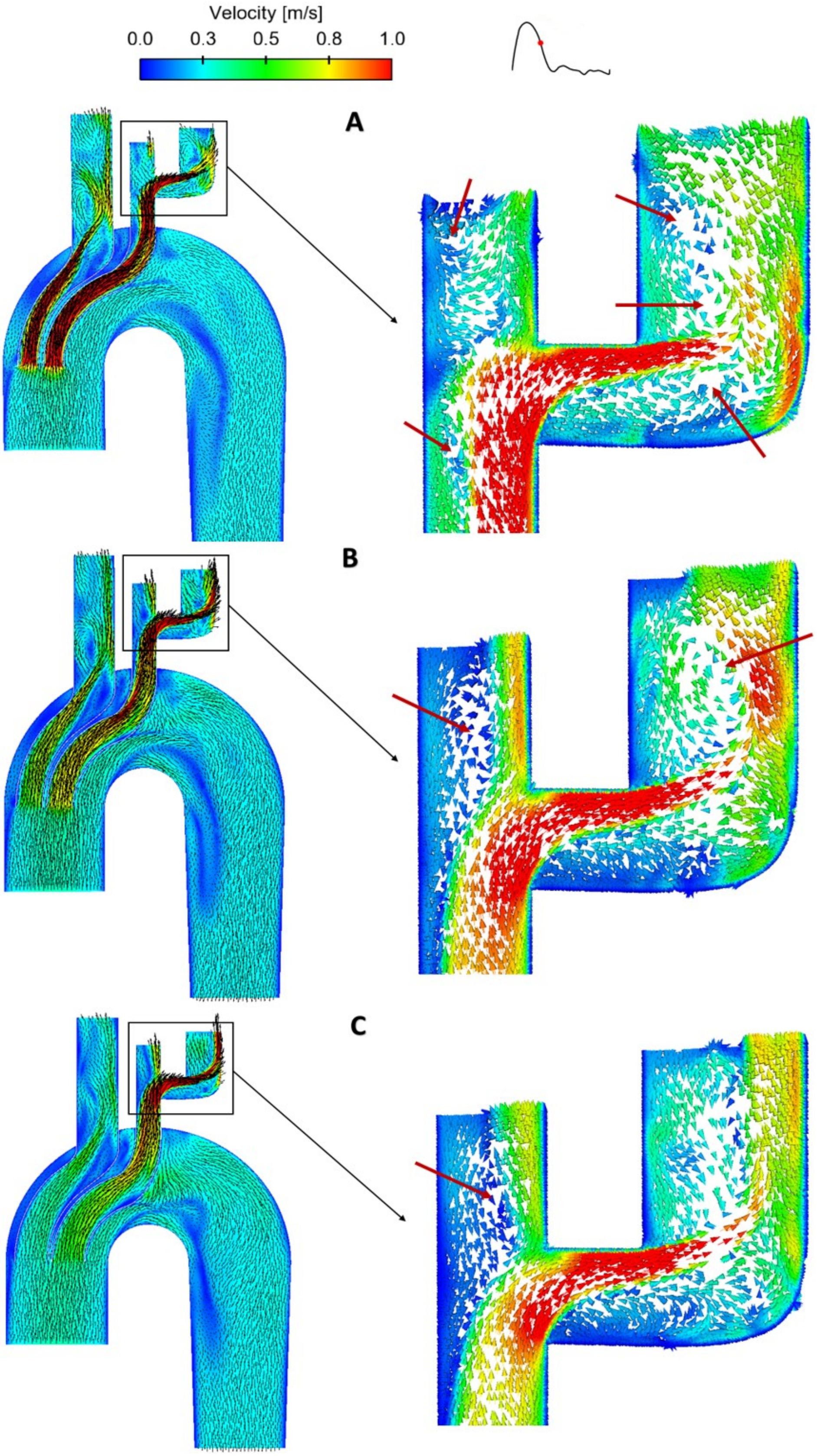

Figure 5.5. Comparison of velocity contours in the sagittal plane along with in-plane velocity vectors between the three BSG models: (A) Stent-graft 1, (B) Stent-graft 2, and (C) Stent-graft 3, at mid-systolic deceleration (0.29 s). Detailed flow patterns are shown by local enlargement of the LCCA-LSCA bypass (right column). FRZs in the bypass graft are indicated by red arrows.

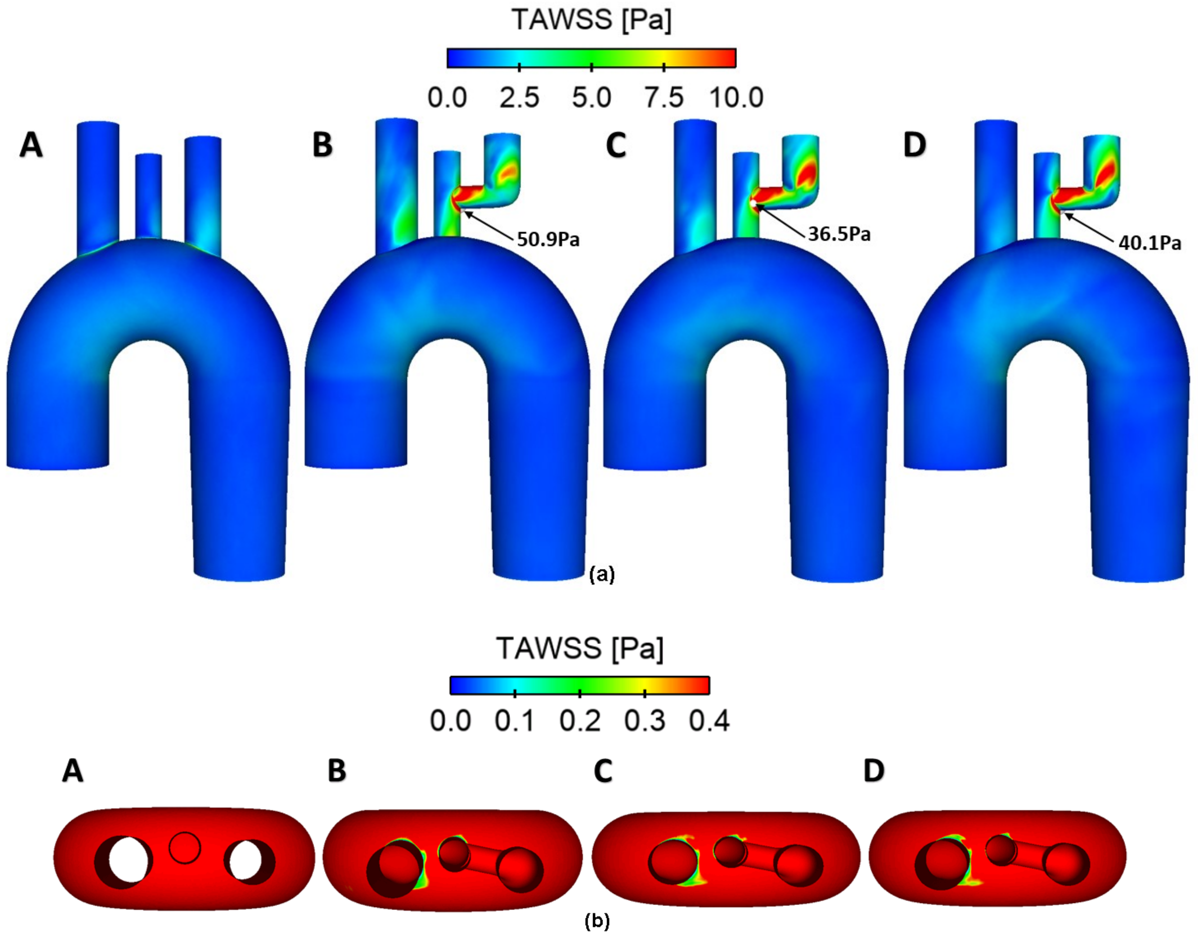

Figure 5.6. Comparison of TAWSS in the four models: (A) non-stented aortic arch (reference case), (B) stent-graft 1, (C) stent-graft 2, and (D) stent-graft 3. TAWSS distributions are displayed in different views to identify areas with (a) very high (>10 Pa) and (b) very low (< 0.4Pa) values. The maximum TAWSS on the walls of all stented geometries are highlighted by the black arrows.

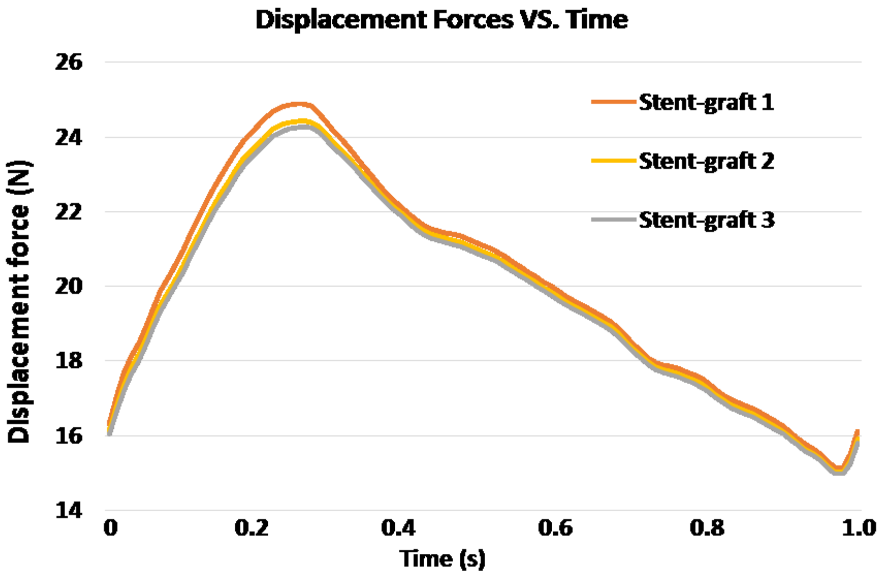

Figure 5.7. Comparison of resultant displacement forces acting on the stent-graft models. Time dependence of displacement forces follows the pressure waveform very closely.

Table 5.3. Cycle-averaged and maximum displacement forces acting on all the stent-graft models.

	Cycle-averaged DF (N)	Maximum DF (N)
Stent-graft 1	20.1	24.9
Stent-graft 2	19.8	24.4
Stent-graft 3	19.7	24.3

Another important influence of BSG is to drastically increase the magnitude of WSS as higher TAWSS were found in all three stent-graft models, especially on the arch vessel walls. Regions of extremely high TAWSS (>10 Pa) were observed on the distal wall of the LSCA and on the bypass graft due to highly skewed flow. In the non-stented model, the maximum TAWSS on the aortic wall was 5.8 Pa, within the normal range of 1-7 Pa (Malek et al. 1999), which was found at the intersection between the LSCA and the arch. However, the maximum TAWSS was significantly increased after inclusion of a BSG, reaching 50.9 Pa, 36.5 Pa, and 40.1 Pa, for stent-graft 1, stent-graft 2 and stent-graft 3, respectively. The maximum TAWSS in all the BSG models were found at the anastomosis between the bypass graft and the LCCA, raising concerns about the long-term durability at this site since high WSS values are related to graft material fatigue and late device failure (Chatzizisis et al. 2007). The high WSS concentration on the vessel walls also require further investigation as high WSS values are related to arterial wall thickening and even rupture (Torii et al. 2013). For the stent-graft models, the highest maximum TAWSS was observed in stent-graft 1, where both inner tunnels were connected with the arch vessels in a diverging configuration. A converging diameter tunnel for the LCCA clearly reduced the maximum TAWSS values. Stent-graft 3 had a slightly higher maximum TAWSS value than stent-graft 2, which might result from a more convergent diameter tunnel for the LCCA causing higher blood velocities. On the other hand, extremely low TAWSS (< 0.4 Pa) was observed in regions around the entrance to the arch vessels of all the BSG models, indicating the potential risk of thrombus formation in these areas because TAWSS values of < 0.4 Pa have been suggested to be thrombogenic (Suess et al. 2016). Variations in inner tunnel diameters hardly affected the regions of low TAWSS.

The evaluated displacement forces had a maximum value of 20.1 N in stent-graft 1, which was well below the threshold value of 34.25 N required to force a planar stent-graft to dislocate at the proximal end (Melas et al. 2010). Although all the idealised BSG models examined here were at low risk of distal migration, non-planarity can increase the magnitude of displacement force and its effect was not included in the idealised models.

5.1.5 Summary

The major limitation of this work was that all the models were ideally constructed based on representative anatomical features, and these models were simplified by neglecting the torsion and non-planarity of the aortic arch, which would strongly impact the numerical results presented here. In reality, there are large variations in the anatomy of human aorta, and the quantitative results presented here will deviate from those for a specific patient. Nevertheless, the geometric models used in this study are physiologically representative and should be valid for a comparative analysis. Moreover, they allow the effect of geometric variations to be isolated and examined without the influence of other confounding factors.

The overall results revealed that all the stent-graft models examined here were capable of ensuring sufficient blood perfusion to the arch vessels and were at low risk of device migration. Comparisons among the three models indicated that stent-graft 1 was the worst performer by all measures. Therefore, when choosing an off-the-shelf device, preference should be given to BSGs with inner tunnels of larger diameters than those of the respective vessels.

5.2 Patient-Specific Analysis of Aortic Flow before and after Thoracic Endovascular Repair with a Dual-Branched Stent-Graft[1]

From the numerical results presented in the preceding section, it is clear that dual-branched stent-graft is capable of maintaining sufficient blood perfusion to the arch branches, though its implantation altered local haemodynamic characteristics. The obtained results from the idealised models have shed some lights on the influence of inner tunnel diameter on BSG's haemodynamic performance, however, the main limitation was the simplification in the geometry. In this section, the haemodynamic performance of a double-branched thoracic endograft is evaluated by means of patient-specific CFD analysis.

5.2.1 Introduction

One of the difficulties with endografts used for aortic arch repair is that when the proximal landing zone approaches an increasingly curved portion of the arch, the risk of misalignment increases as the rigid wall of the stent-graft finds it harder to follow the inner curvature of the aortic arch. This may result in a wedge-shaped gap between the aortic wall and the under surface of the graft, known as bird-beak configuration (Van Bogerijen et al. 2014). To overcome this challenge, current endografts incorporate the flexibility and compliance of the arterial wall and often utilise proximal and distal stents to ensure better fixation. One such example is the Relay thoracic stent-graft system developed by Bolton Medical (Sunrise, FL, US), which was designed to conform into the tight aortic curvature in order to avoid the bird-beak configuration (Yunoki et al. 2014).

---

[1] The content of this section is published in *Medicine in Novel Technology and Devices* (Zhu et al. 2020).

It is well recognised that blood flow in aortic aneurysms is highly disturbed, with the presence of flow recirculation and strong vortices (Allen et al. 2013; Markl et al. 2004). Insertion of a branched stent-graft may further increase the complexity of the flow (Kandail et al. 2015). In order to provide a non-invasive evaluation of aortic flow patterns, CFD has been employed for its ability to offer comprehensive insights into spatial-temporal variations of the flow (Taylor and Figueroa 2009). When applied to patient-specific aorta geometry reconstructed from medical images together with physiological boundary conditions, CFD allows quantitative assessment of cardiovascular flow with good accuracy (Cheng et al. 2014, 2016; Singh et al. 2016).

This study aimed to provide the first detailed evaluation of the haemodynamic performance of double-branched thoracic endografts in a patient-specific setting. Pre- and post-intervention geometries were reconstructed from the CT images acquired before and after the TEVAR procedure. These were then coupled with physiologically realistic boundary conditions. Haemodynamic performance was evaluated in terms of flow pattern, wall shear stress (WSS) related indices and displacement forces. By comparing pre- and post-intervention flow distributions, it would be possible to assess the level of blood perfusion through the arch branches. Quantitative analysis of WSS-related indices would help predict the likelihood of thrombus formation within the endograft, whilst quantification of displacement force experienced by the endograft would allow us to evaluate the risk of device migration.

5.2.2 Methodology

5.2.2.1 Model Geometries and Mesh Generation

The studied branched device (Bolton Medical, Sunrise, FL, US) comprises a main covered stent-graft to take the pressure off the vessel wall of the aortic arch and two attached tunnels to channel the blood directly into the innominate artery (IA) and left common carotid artery (LCCA). Patient 1 was treated with an endograft with 2 inner branches of equal diameters (15 mm) while the inner branch to the LCCA of patient 2 had a smaller diameter (9 mm) compared to the IA (17 mm). For both patients, the left subclavian arteries (LSCA) were covered at the roots, and a separate bypass procedure was performed to supply blood to the LSCA from the LCCA. CT images for both patients were acquired (1.25 mm slice thickness and 0.675 mm/pixel in-plane resolution) with a Discovery CT750 HD scanner (GE Healthcare, Chicago, IL, US), at voltages of 100 KV and 120 KV, for the pre- and post-intervention scans, respectively.

As detailed in Chapter 3 Section 3.2.2, the multislice transverse images were processed using image analysis software MIMICS 20.0 (Materialise HQ, Leuven, Belgium), with luminal surface being segmented based on the local signal intensity. The representative CT images and reconstructed luminal surfaces of the pre- and post-intervention models are presented in Figure 5.8. In the reconstructed models, the presence of stent wires was ignored and the inner surface of the stent-graft was assumed to be smooth. Blooming artefacts due to the presence of thin stent wires were not a major concern here as the stent mesh was not very dense and the lumen diameter is fairly large.

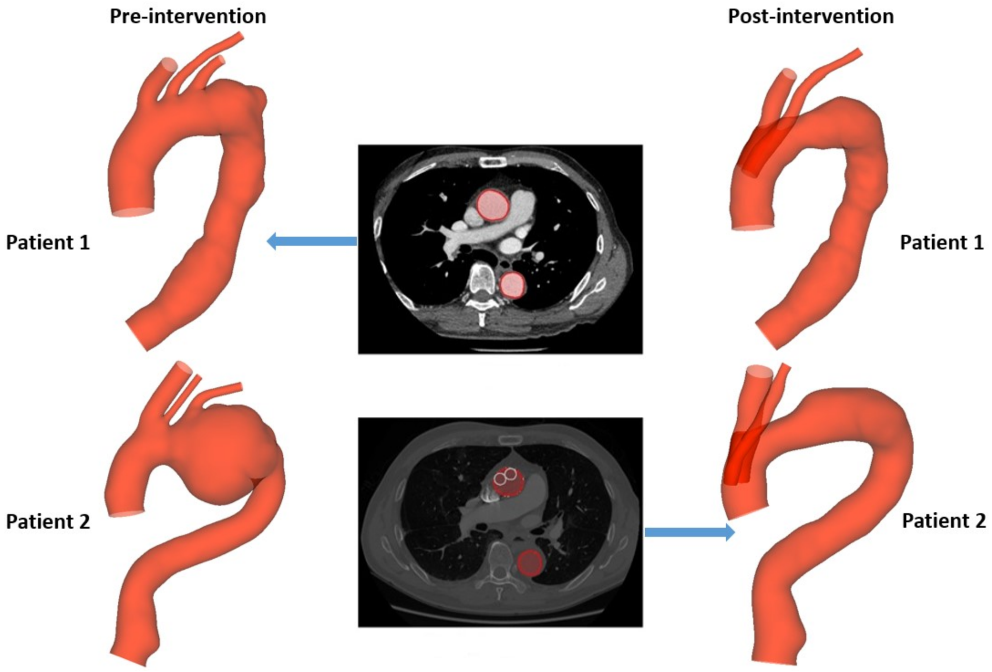

Figure 5.8. Two patient-specific models reconstructed from pre- and post-intervention CT images.

The 3D geometries were then imported into ANSYS ICEM CFD (ANSYS, Canonsburg, PA, US) to generate computational mesh, which consisted of tetrahedral elements in the core region and locally refined hexahedral elements in the sheared boundary layer for accurate prediction of haemodynamic wall parameters. The boundary layer was divided into a minimum of 10 prismatic elements to ensure that the dimensionless height of the near wall elements, y+, was less than 1. Mesh sensitivity tests were carried out, starting with a mesh containing approximately 1 million elements. The final adopted meshes consisted of around 3 and 8.5 million elements for the pre- and post-intervention aortas, respectively. Results were considered to be grid independent when differences in velocity and WSS were less than 2% between the adopted mesh and a finer mesh. A fixed timestep of 0.001s was chosen based on a similar sensitivity test on timestep size.

5.2.2.2 Boundary Conditions and Numerical Approaches

Physiological boundary conditions were employed in order to produce clinically relevant results. Since patient-specific flow information was not available, velocity waveform acquired from a patient with thoracic aortic aneurysm was adopted (Tan et al. 2009) and scaled according to the inlet area of each patient, yielding a cycle-averaged inlet velocity of 0.1 m/s for both patients. This corresponds to a cardiac output of 5 L/min for patient 1and 3.4 L/min for patient 2, both are within the physiological range (Critchley and Critchley 1999). A schematic of the computational model and the applied inflow waveform can be found in Figure 5.9.

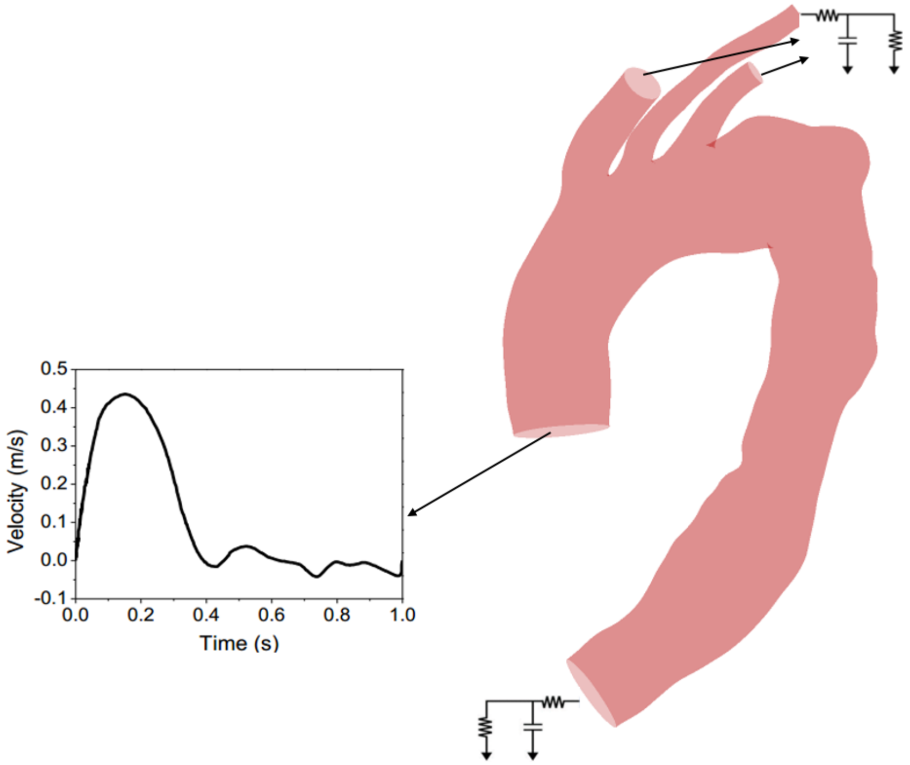

Figure 5.9. Schematic of the computational model employed in this study. Velocity waveform was prescribed at the inlet along with the assumption of a flat velocity profile, while a 3-element Windkessel model was applied at all outlets.

At the model outlets, a 3-element Windkessel model (3-EWM) was applied in order to provide physiological outflow boundary conditions. The assumption of rigid stent-graft walls was made where no-slip boundary conditions were imposed. To calculate the 3-EWM parameters, pressure waveforms at each outlet were adopted from the literature (Olufsen et al. 2000) and the corresponding cycle-averaged pressures were evaluated as: 105 mmHg, 104 mmHg, 103 mmHg, and 103 mmHg, for the IA, LCCA, LSCA and descending aorta (DA), respectively. For the post-intervention model, the outlet boundary conditions were modified to account for the fact that the LSCA was covered at the root and its blood supply was rerouted from the LCCA via a separate bypass procedure. As shown in Figure 5.10, the total downstream resistance at the LCCA outlet was calculated by combining the pre-intervention resistance for the LCCA ($R_{Pre-LCCA}$) and LSCA ($R_{Pre-LSCA}$) (Mohrman and Heller 2006):

$$1/R_{Post-LCCA} = 1/R_{Pre-LCCA} + 1/R_{Pre-LSCA} \tag{5.1}$$

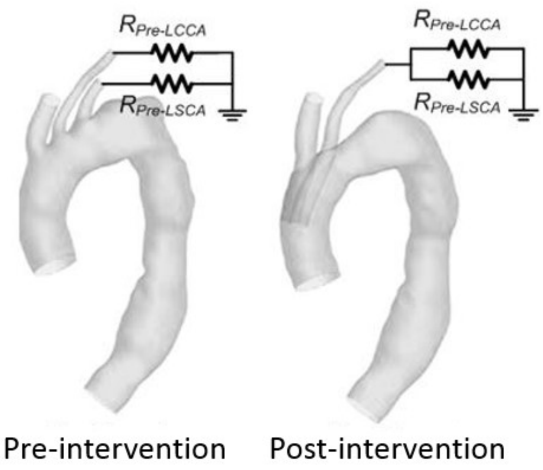

Figure 5.10. Schematic diagram showing resistance at LCCA and LSCA in the pre- and post- intervention models.

The obtained resistance and compliance values are summarised in Table 5.4, which also included the values used for the idealised models (Section 5.1). It should be noted that Windkessel parameters were the same for all the idealised models due to the same outlet dimensions.

The conservation of mass and momentum equations for an incompressible, Newtonian fluid were used to describe the pulsatile blood flow. In addition, the hybrid k-ε/k-ω correlation-based SST-Tran was applied to capture transitional/turbulent flow characteristics (Menter et al. 2006). Blood was assumed to have a constant density of 1060 kg/m^3 and dynamic viscosity of 0.004 Pa·s. The governing equations were solved by means of ANSYS CFX 15 (ANSYS, Canonsburg, PA, US), which is a finite volume based CFD code. Spatial and temporal discretisations were performed by adopting the second order accurate advection scheme and the second order implicit backward Euler scheme, respectively. Convergence of simulations was controlled by setting the residual tolerance as 1×10^{-5}. Each simulation was performed for three cardiac cycles when solutions for both velocity and pressure became periodic, and the differences in systolic pressure between the second and third cardiac cycle were less than 2% at every outlet. Numerical results of the last cycle were analysed using ANSYS CFD-Post 15 (ANSYS, Canonsburg, PA, US) and CEI Ensight 10 (CEI Inc, Apex, NC, US).

5.2.2.3 Haemodynamic Indices

WSS refers to the tangential force generated by blood flow on the endothelial luminal surface. Owing to its strong association with thrombus formation and aneurysm growth and the fact that these processes are much slower compared to the pulsatile cycle period, WSS is usually evaluated in terms of TAWSS as defined by equation (3.38). Based on TAWSS and OSI (as defined by equation (3.39)), ECAP can be calculated as the ratio of OSI to TAWSS, to identify regions that might be prone to thrombosis (Di Achille et al. 2014). In addition, circumferential wall shear stress (CWSS) and shear range index (SRI) were evaluated to quantify the extent of local derangement at the vessel wall (Barker et al. 2010).

$$SRI = \frac{\max[CWSS_{max}(\theta,t) - CWSS_{min}(\theta,t)]}{TACWSS} \tag{5.2}$$

where $CWSS_{max}(\theta, t)$ and $CWSS_{min}(\theta, t)$ represent the maximum and minimum WSS along the circumference of a cross-section, respectively. $TACWSS$ is the temporal and circumferential averaged WSS at a given cross-section. The displacement force was also evaluated for the post-operative models based on the equations (4.1) and (4.2).

Table 5.4. Windkessel parameters for all model outlets, include the idealised models simulated in Section 5.1.

		Patient 1			Patient 2		
		R1 [10^{8} Pa s m^{-3}]	R2 [10^{8} Pa s m^{-3}]	C [10^{-9} m^{3} Pa^{-1}]	R1 [10^{8} Pa s m^{-3}]	R2 [10^{8} Pa s m^{-3}]	C [10^{-9} m^{3} Pa^{-1}]
Pre	IA	0.40	8.94	1.92	0.39	10.86	1.59
	LCCA	1.86	31.51	0.54	3.92	79.01	0.22
	LSCA	1.23	22.32	0.76	2.30	50.00	0.34
	DA	0.08	2.27	7.62	0.07	3.43	5.11
Post	IA	0.49	8.86	1.92	0.26	10.99	1.59
	LCCA	2.21	11.60	1.30	2.73	29.34	0.56
	DA	0.08	2.27	7.62	0.07	3.43	5.11
Idealised models (Pre- and Post-operation)							
				IA	LCCA	LSCA	DA
R1 [10^{8} Pa s m^{-3}]				0.35	1.01	0.49	0.06
R2 [10^{8} Pa s m^{-3}]				8.84	21.62	11.44	1.72
C [10^{-9} m^{3} Pa^{-1}]				1.95	0.79	1.50	10.02

5.2.3 Results

5.2.3.1 Anatomical Features

As shown in Figure 5.8, the pre- and post-intervention geometries differed mainly in the arch for both patients. In the post-intervention model, two built-in tunnels were attached to the main graft body, through which separate stents were retrogradely inserted into the IA and LCCA, with entry to the LSCA being blocked from its origin. Lumen diameters were measured at eight selected locations to evaluate changes in aorta morphology after the intervention, and the results are summarised in Table 5.5. All locations were matched between the pre- and post-intervention geometries by measuring the distance along the respective centreline, which could be achieved in Mimics.

Table 5.5. Comparison of lumen diameters (mm) between the pre- and post-intervention models.

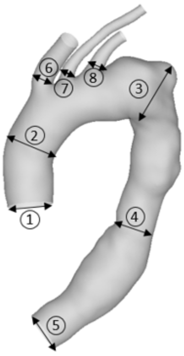

Patient 1			**Patient 2**	
Pre-intervention (mm)	**Post-intervention (mm)**		**Pre-intervention (mm)**	**Post-intervention (mm)**
32	**32**	**①**	**27**	**27**
35	**35**	**②**	**28**	**28**
47	**37**	**③**	**69**	**33**
30	**30**	**④**	**23**	**23**
29	**29**	**⑤**	**31**	**31**
14	**15**	**⑥**	**14.6**	**15.7**
7.5	**8.5**	**⑦**	**5.3**	**8.5**
9.5	**-**	**⑧**	**6.7**	**-**

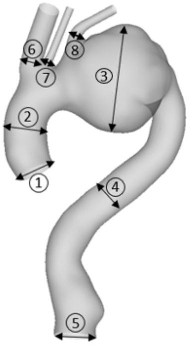

Comparisons showed that, apart from the obvious reduction in diameters in the regions where the aneurysms were located, there was no change in the ascending and descending aortas for both patients. Diameters of the IA and LCCA root were larger after intervention, with patient 2 showing a more pronounced increase in LCCA diameter.

5.2.3.2 Flow Patterns

Instantaneous velocity streamlines in the pre- and post-intervention models were compared at three characteristic time points, namely, peak systole (0.15 s), mid-systolic deceleration (0.29 s) and diastole (0.74 s). As shown in Figure 5.11. (A) & (B), aortic flow patterns for both patients altered significantly after intervention in response to changes in lumen morphology. Blood flow was more organised post-intervention as the aneurysm was repaired. Blood velocities increased in the ascending aorta and the arch due to the presence of the inner tunnels. Flow in the LCCA increased in order to meet the demand of both LCCA and LSCA. As expected, the diastolic phase was dominated by slow and recirculating flow in both pre- and post-intervention aortas.

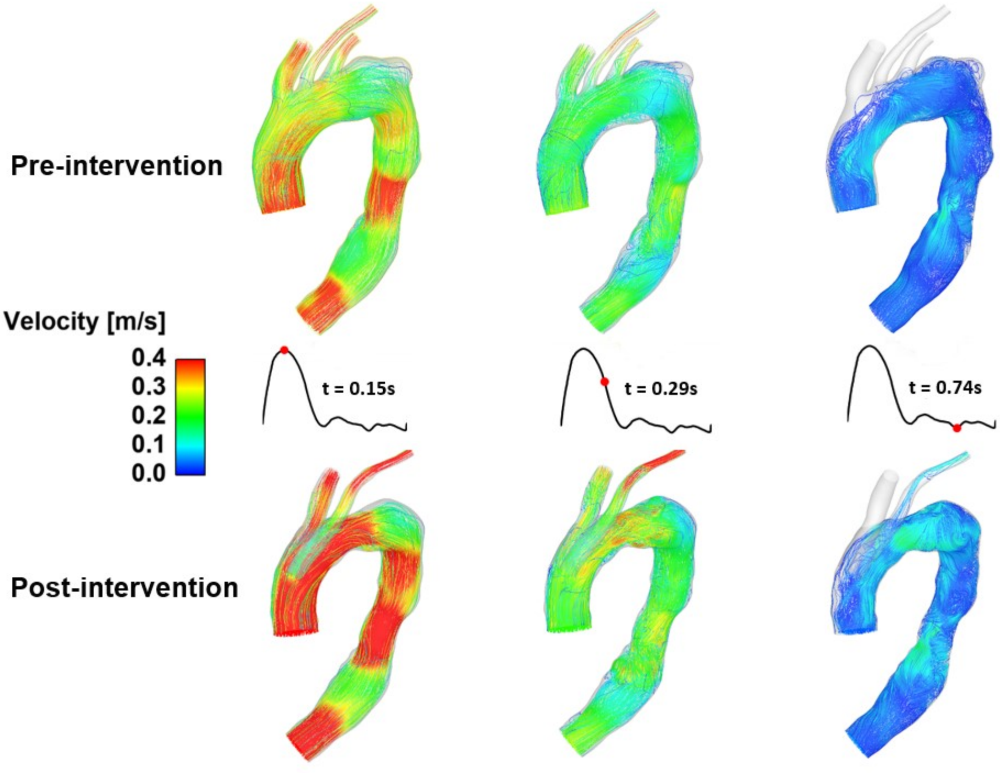

(A) Patient 1

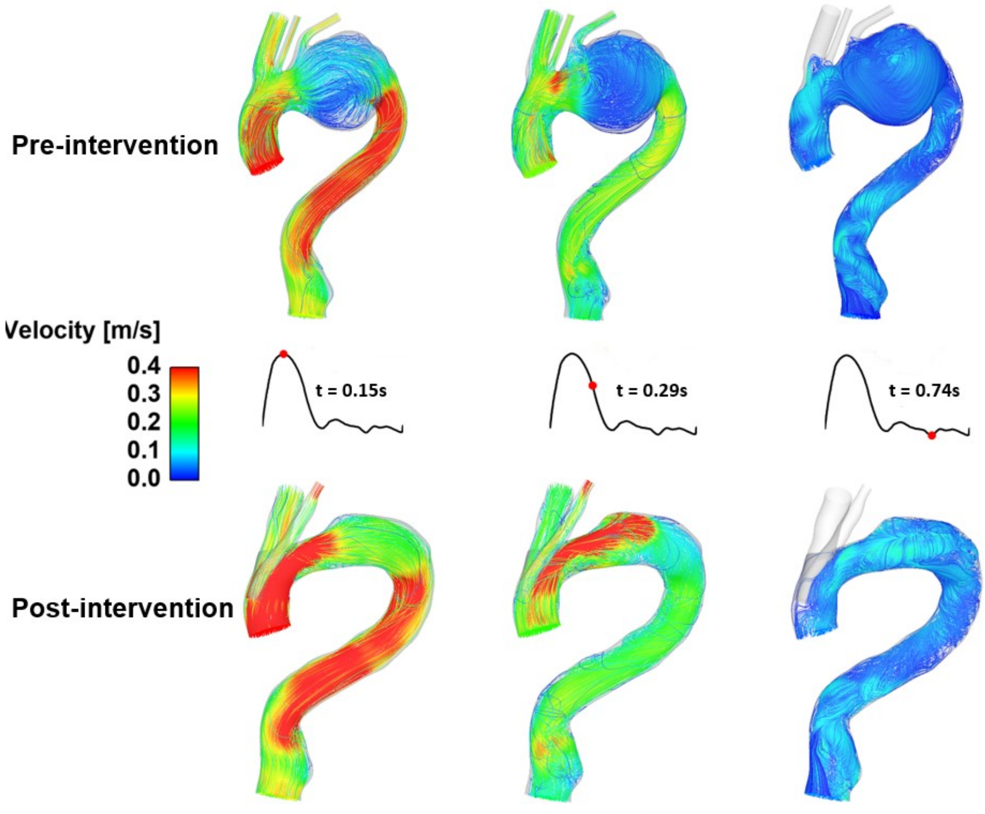

(B) Patient 2

Figure 5.11. Comparisons of instantaneous velocity streamline in pre- and post- intervention models of (A) patient 1 and (B) patient 2, at three characteristic time points of a cardiac cycle, namely, peak systole (0.15 s), mid-systolic deceleration (0.29 s), and diastole (0.74 s). Blood flow was found to be more organised after intervention as a result of repaired aneurysm.

Eight cross-sectional planes were selected along the centreline of each aorta (P1-P4), the IA (P5 & P6) and the LCCA (P7 & P8) for detailed comparisons of flow and WSS. Through-plane velocity contours along with in-plane velocity vectors at these planes were compared before and after intervention, as illustrated in Figure 5.12. A-C, where the right hand side of each cross-sectional image corresponds to the inner curvature of the aorta and vortical flow structures are indicated by red arrows. For both patients, flow in the proximal ascending aorta (P1) hardly changed after the intervention, but this was completely different at P2 where the presence of the inner tunnels caused part of the aortic flow to be channelled into the IA and LCCA after intervention, while entry to the LSCA was blocked. Insertion of the stent-graft reduced the lumen area and thus accelerated blood flow in the posterior region but blocked flow in the anterior part. This stagnant region is likely to be thrombosed over time which may further obstruct the lumen. It can be seen clearly at P2 that patient 1 had a device with equal diameter inner tunnels, while patient 2 had a smaller inner branch to the LCCA. Patient 1 had a much higher blood velocity in the inner IA channel than LCCA when compared to patient 2. Geometric variations in the aneurysm sac (P3) changed local flow patterns after intervention, where vortical flow could be seen in systole. Flow in the descending aorta (P4) was similar before and after intervention.

Flow patterns in the arch branches were compared at two locations: (1) proximal region of the IA (P5) and LCCA (P7); and (2) distal region of the IA (P6) and LCCA (P8). It can be seen that velocity was higher in the IA than LCCA in the pre-intervention models of both patients, but more obvious for patient 1. These were the same for the post–intervention models, but only in the proximal regions (P5, P7). For both patients, blood flow in the LCCA (P7, P8) accelerated distally due to vessel tapering. The effect of tapering was more obvious in the LCCA than in IA.

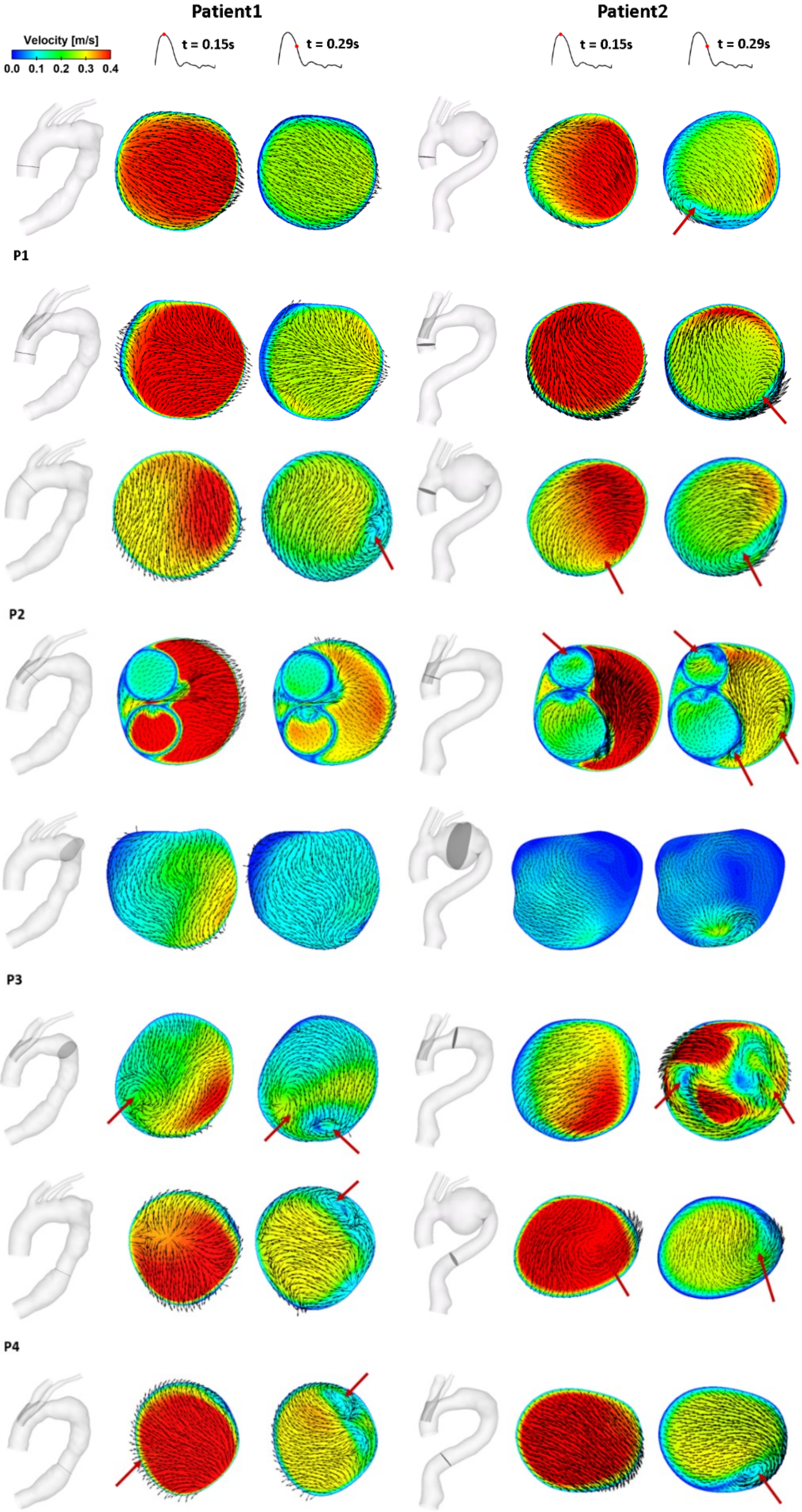

Figure 5.12 A. Comparison of axial velocity contours along with in-plane velocity vectors before and after intervention in the aortas of patient 1(left) and patient 2 (right) at peak systole (0.15 s) and mid-systolic deceleration (0.29 s). P1-P4 are cross-sectional planes selected along the centreline of each aorta. After intervention, flow patterns were clearly altered at P2 due to the presence of inner tunnels and at P3 which is located in the aneurysm sac. Red arrows indicate vortical flow structures.

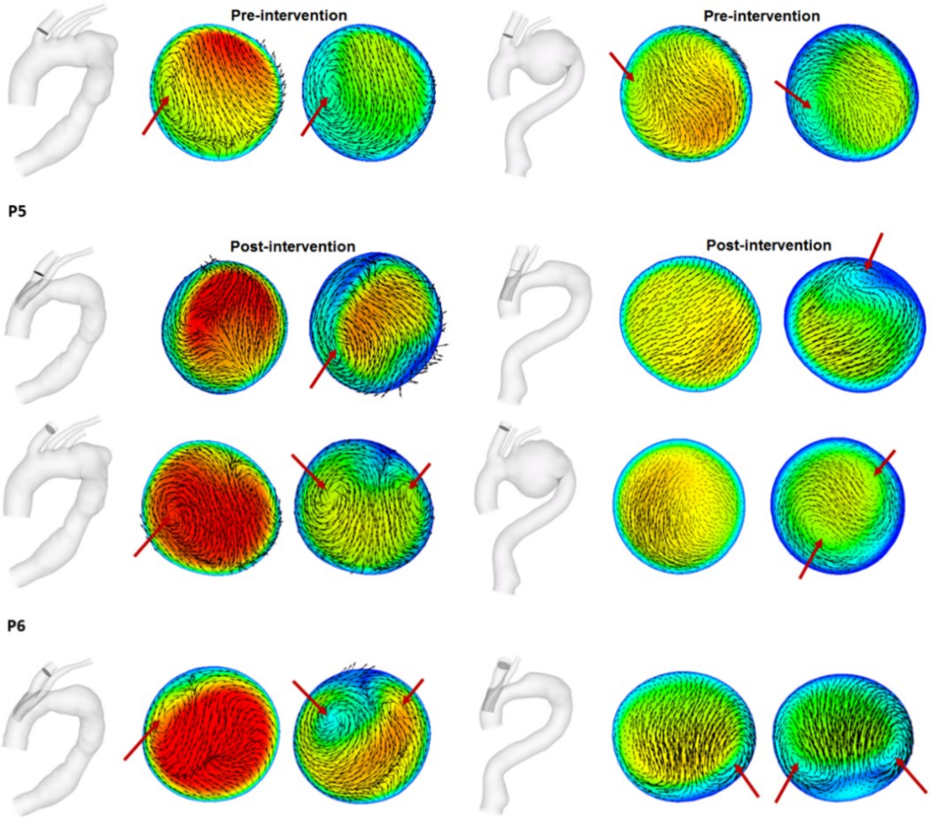

Figure 5.12 B. Comparison of axial velocity contours along with in-plane velocity vectors before and after intervention in the IA of patient 1(left) and patient 2 (right). P5 and P6 are cross-sectional planes selected at the proximal and distal IA.

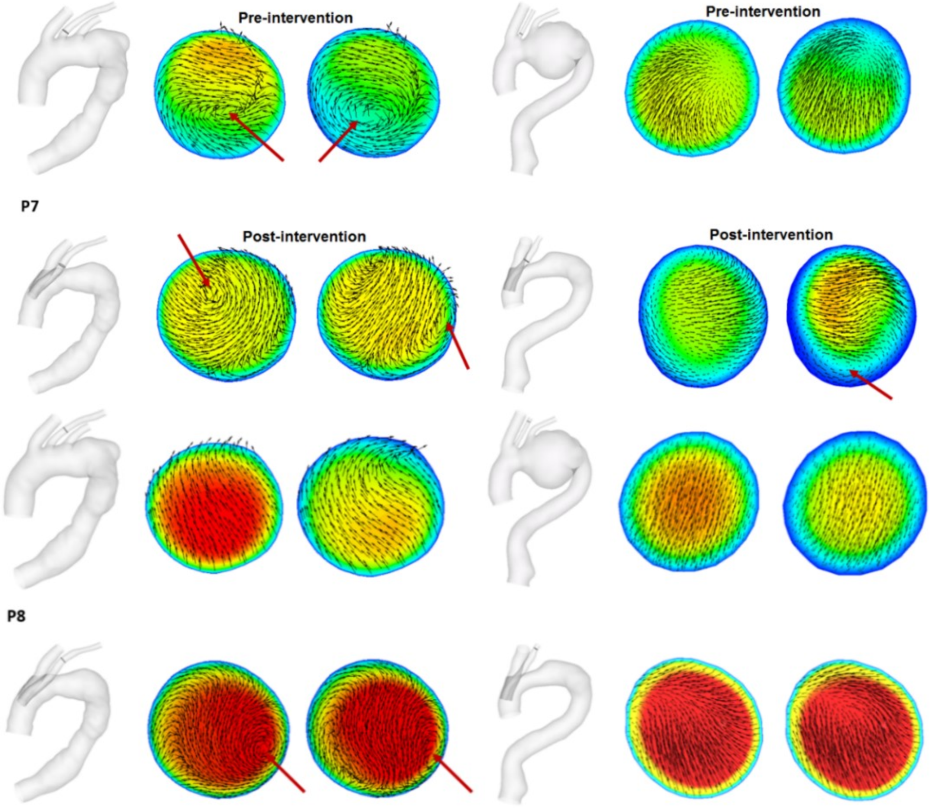

Figure 5.12 C. Comparison of axial velocity contours along with in-plane velocity vectors before and after intervention in the LCCA of patient 1(left) and patient 2 (right). P7 and P8 refer to cross-sectional planes located at the proximal and distal LCCA. Vortical flow structures are indicated by red arrows.

5.2.3.3 Wall Shear Stress

Figure 5.13 shows the predicted TAWSS contours, and it is clear that after intervention the magnitude of TAWSS increased throughout the aorta for both patients, as a result of accelerated flow in the arch and the distal LCCA. More detailed comparisons are shown in Figure 5.14, where the mean circumferential WSS was plotted as a function of time at the pre-defined locations (P1-P8). For both patients, although temporal variations of circumferential WSS exhibited similar shapes before and after intervention, implantation of the branched stent-graft increased the magnitude of WSS in the systolic phase except for the proximal LCCA (P7) of patient 2, where higher WSS was found in the pre-intervention model. The proximal LCCA of patient 2 was significantly enlarged by the endograft (as shown in Table 5.5), leading to lower WSS values in this region in the post-intervention model. During diastole, however, the results were comparable except for P3 of both patients, where the post-intervention WSS was higher throughout the cardiac cycle. Extremely low circumferential WSS values (< 0.5) were observed at P3 of patient 2 due to the large aneurysm sac. The repaired aneurysm in the post-intervention model resulted in a dramatic reduction in arch diameter (from 69 mm to 33 mm) leading to greatly increased WSS magnitudes over the cardiac cycle.

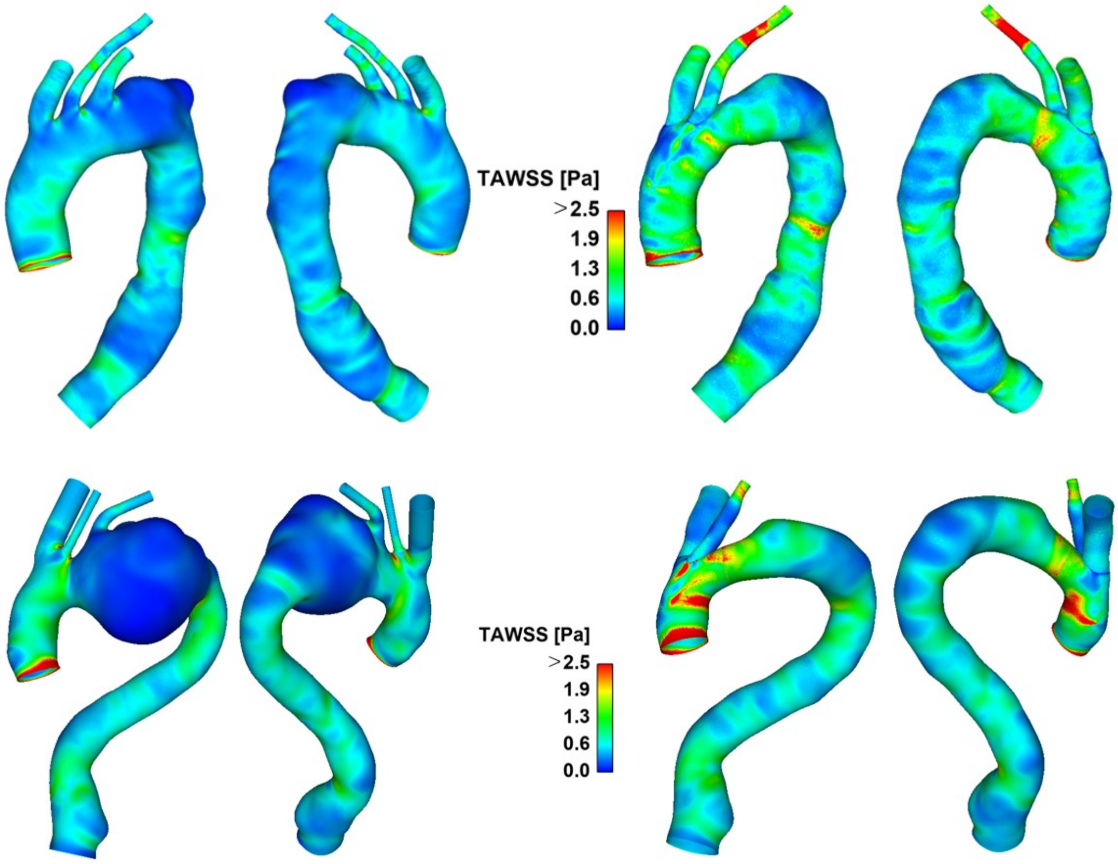

Figure 5.13. Comparison of TAWSS before (left) and after (right) intervention for patient 1 (top) and patient 2 (bottom). Regions with TAWSS values higher than 2.5 Pa are shown in red. Higher TAWSS values were observed in the post-intervention models of both patients.

Patient 1

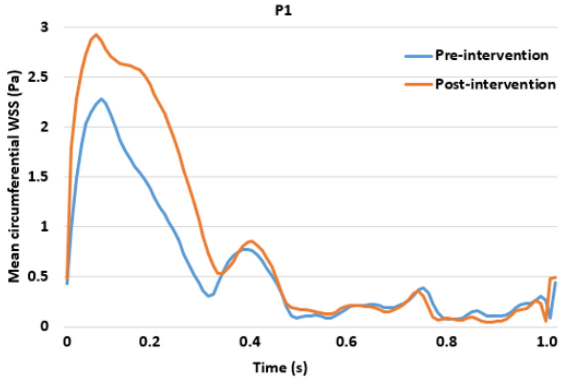

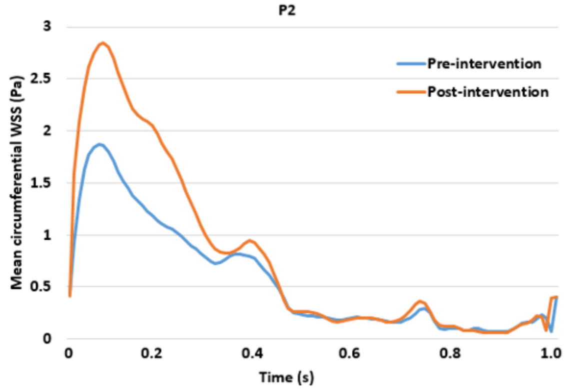

Patient 2

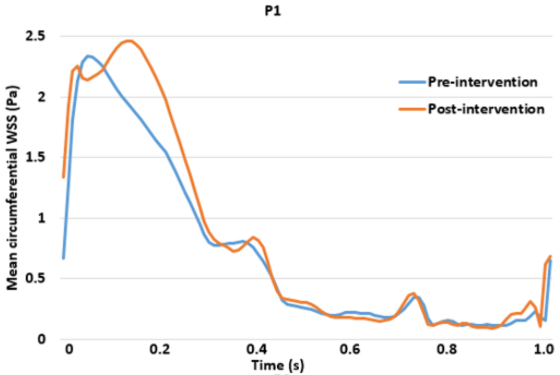

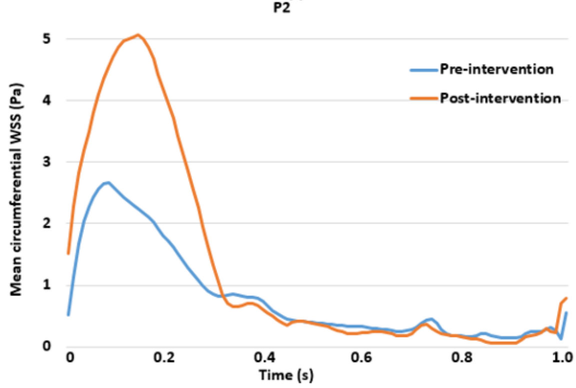

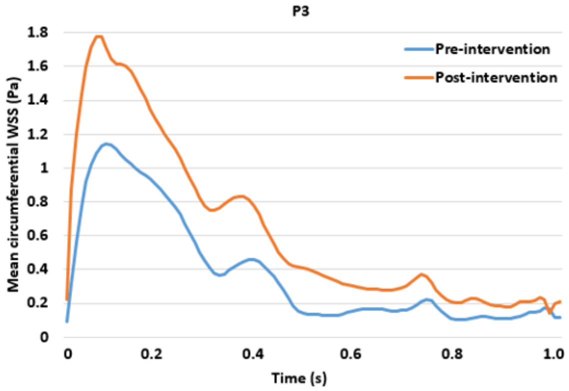

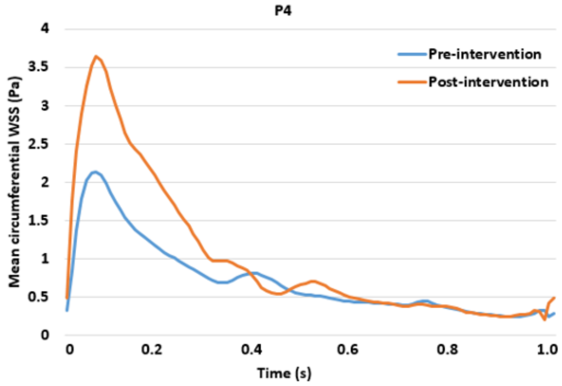

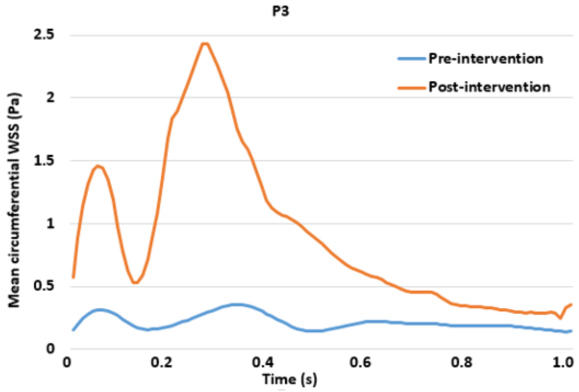

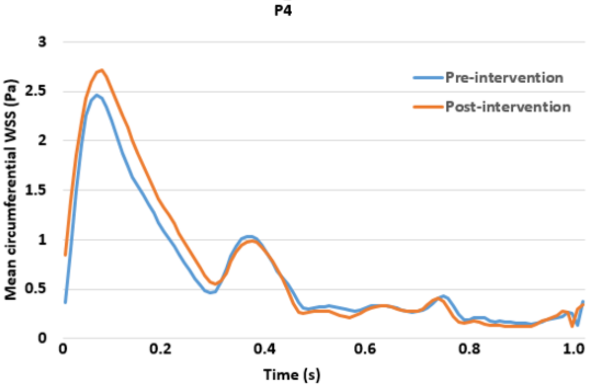

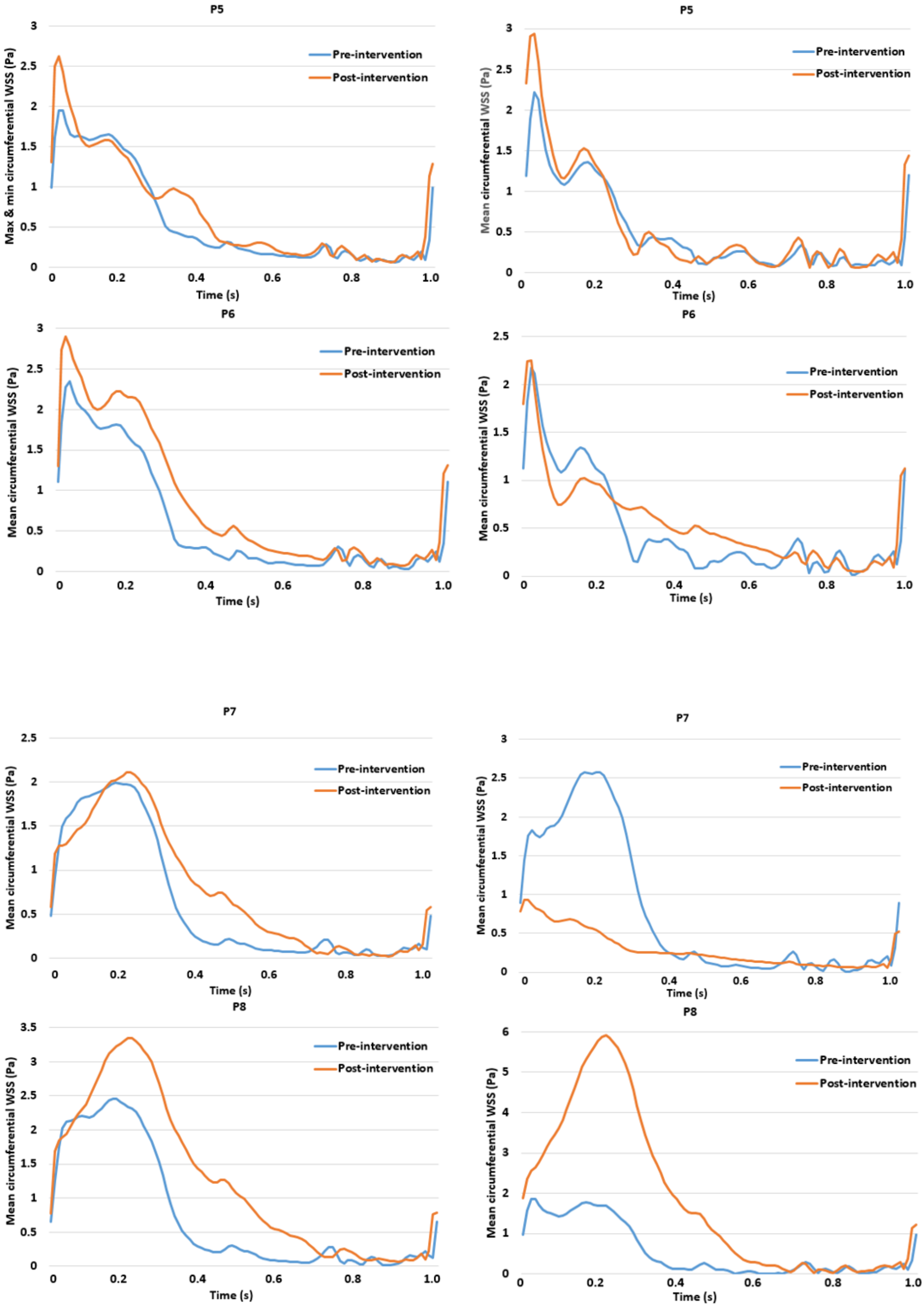

Figure 5.14. Comparison of circumferential-averaged wall shear stress (CWSS) at different planes before and after intervention for patient 1 (left) and patient 2 (right) over a cardiac cycle. The CWSS was evaluated as the spatial-averaged WSS along the intersection lines between the cross-sectional planes and the aortic walls (P1-P4) and the arch vessel walls (P5-P8).

Figure 5.15 shows the circumferential WSS (CWSS) ranges and their variations during a cardiac cycle, with the maximum range of CWSS being highlighted in red. This range determines the value for SRI, which can be used to quantify the degree of asymmetry in WSS caused by disorganised flow near the arterial wall. For both patients, it was obvious that WSS varied more drastically after intervention with much wider ranges, especially along the main aorta (P1-P4). This was largely attributed to the increased non-uniformity in blood flow caused by the inner tunnels. However, one exception was at P4 of patient 2 where there was little change before and after intervention. WSS ranges also increased in the arch vessels (P5-P8) after intervention except at P7 of patient 2, where WSS was more uniform after intervention.

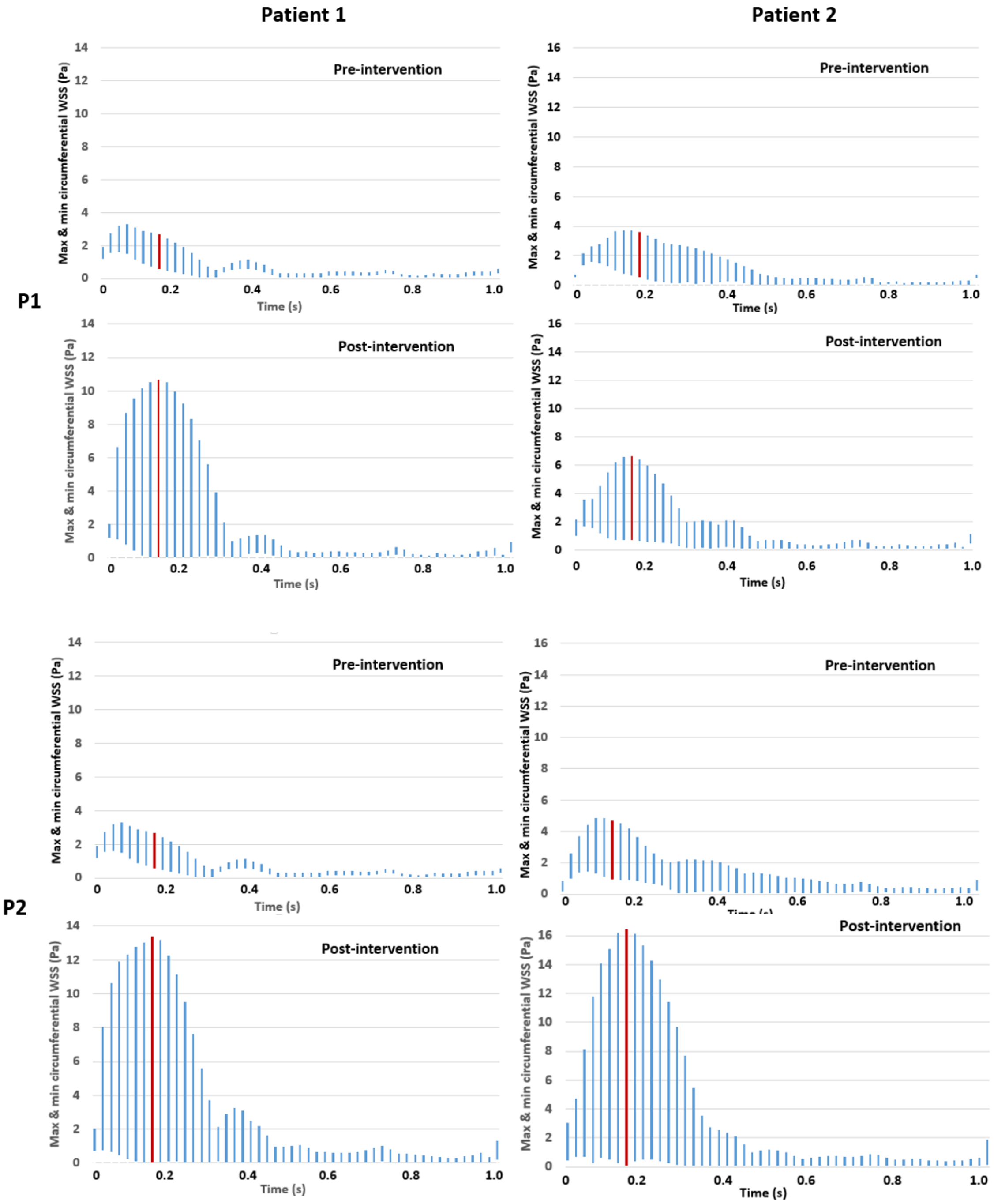

P3

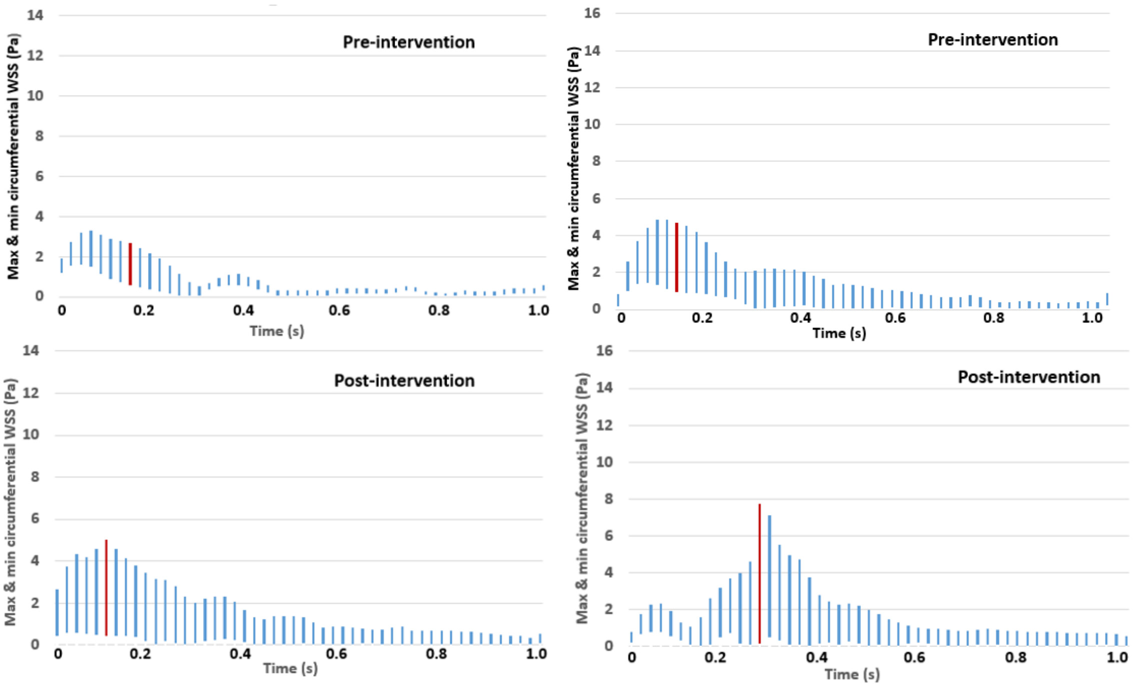
Pre-intervention
Max & min circumferential WSS (Pa)
0
2
4
6
8
10
12
14
0
0.2
0.4
0.6
0.8
1.0
Time (s)
Pre-intervention
Max & min circumferential WSS (Pa)
0
2
4
6
8
10
12
14
16
0
0.2
0.4
0.6
0.8
1.0
Time (s)
Post-intervention
Max & min circumferential WSS (Pa)
0
2
4
6
8
10
12
14
0
0.2
0.4
0.6
0.8
1.0
Time (s)
Post-intervention
Max & min circumferential WSS (Pa)
0
2
4
6
8
10
12
14
16
0
0.2
0.4
0.6
0.8
1.0
Time (s)

P4

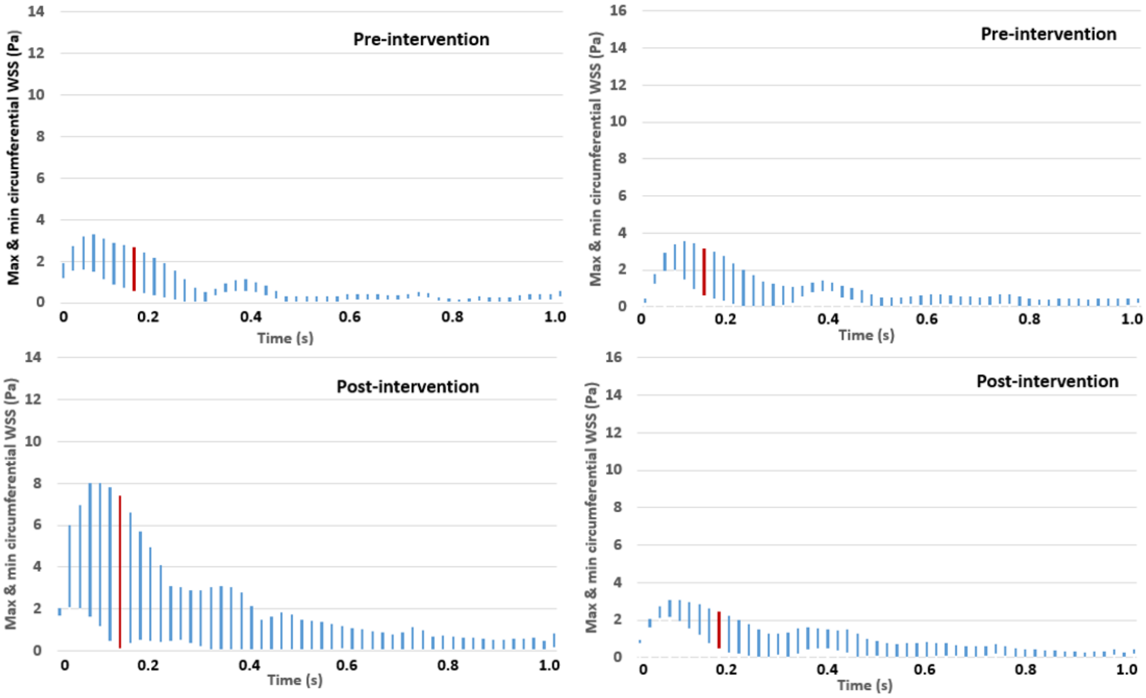
Pre-intervention
Max & min circumferential WSS (Pa)
0
2
4
6
8
10
12
14
0
0.2
0.4
0.6
0.8
1.0
Time (s)
Pre-intervention
Max & min circumferential WSS (Pa)
0
2
4
6
8
10
12
14
16
0
0.2
0.4
0.6
0.8
1.0
Time (s)
Post-intervention
Max & min circumferential WSS (Pa)
0
2
4
6
8
10
12
14
0
0.2
0.4
0.6
0.8
1.0
Time (s)
Post-intervention
Max & min circumferential WSS (Pa)
0
2
4
6
8
10
12
14
16
0
0.2
0.4
0.6
0.8
1.0
Time (s)

P5

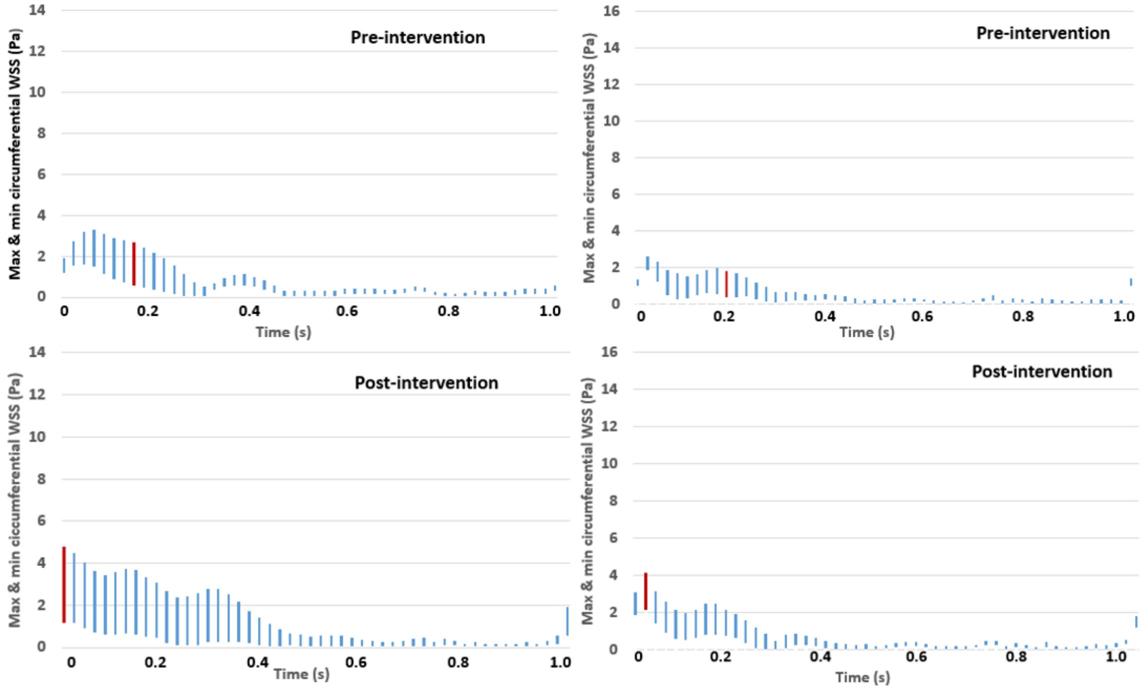
Pre-intervention
Pre-intervention
Post-intervention
Post-intervention
Max & min circumferential WSS (Pa)
Max & min ciccumferential WSS (Pa)
Max & min circumferential WSS (Pa)
Max & min circumferential WSS (Pa)
0
2
4
6
8
10
12
14
16
0
0.2
0.4
0.6
0.8
1.0
Time (s)

P6

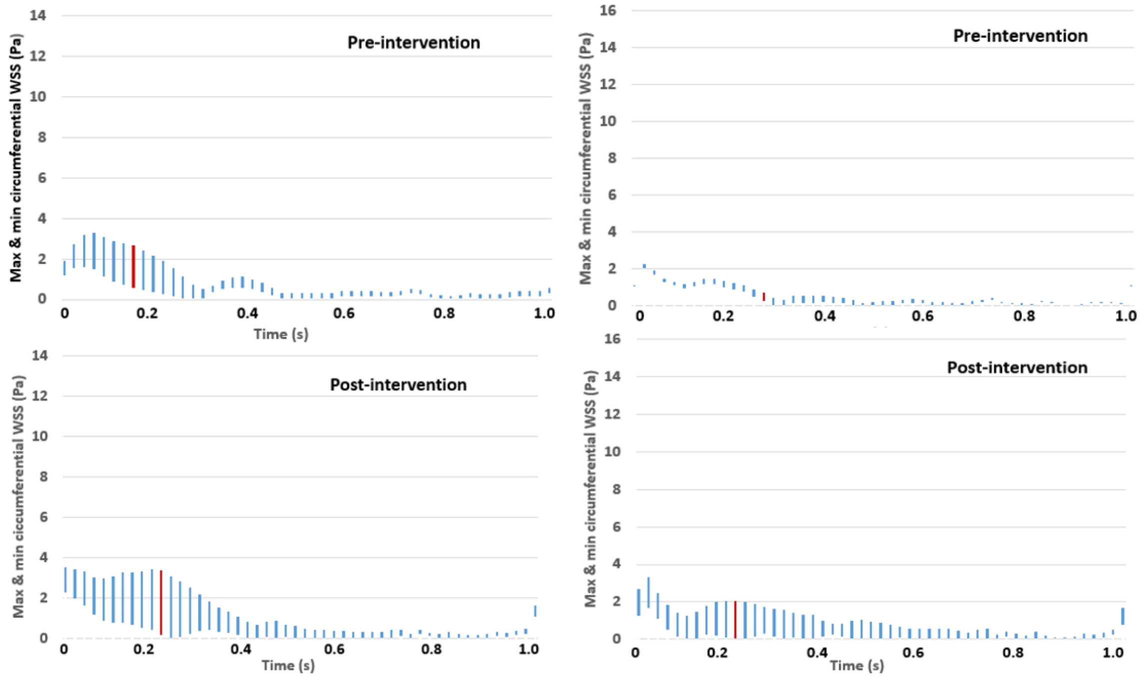
Pre-intervention
Pre-intervention
Post-intervention
Post-intervention
Max & min circumferential WSS (Pa)
Max & min circumferential WSS (Pa)
Max & min ciccumferential WSS (Pa)
Max & min circumferential WSS (Pa)
0
2
4
6
8
10
12
14
16
0
0.2
0.4
0.6
0.8
1.0
Time (s)

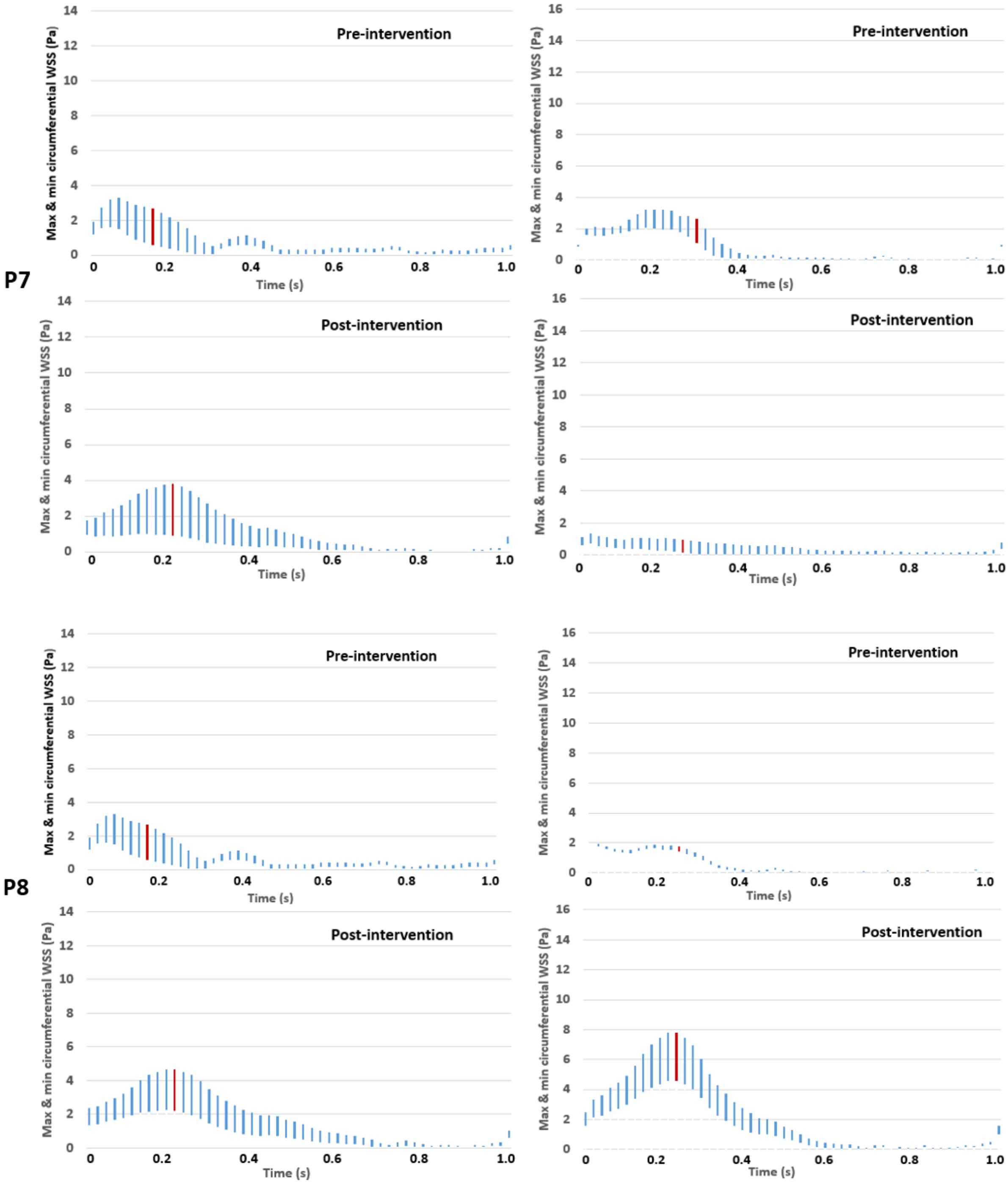

Figure 5.15. Comparison of CWSS range in a cardiac cycle before and after intervention for patient 1 (left) and patient 2 (right). CWSS range at each time-step was calculated as a difference between the maximum and minimum CWSS along the intersection lines between the cross-sectional planes and the aorta (P1-P4), the IA (P5 & P6), and the LCCA (P7 & P8). The maximum ranges of CWSS over a cardice cycle were then identified and highlighted in red.

In order to compare the degree of WSS asymmetry before and after intervention, values for SRI were calculated and the results are summarised in Table 2. For patient 1, it is clear that SRI in the aorta increased significantly after intervention, especially at P2 where SRI was nearly 6 times of its pre-intervention value. However, one exception was in the distal LCCA (P8) where SRI was lower in the post-intervention model. For patient 2, SRI values increased in the ascending aorta and arch vessels after intervention but decreased in the distal arch (P3) and the descending aorta (P4).

Table 5.6. Comparison of SRI at different locations before and after intervention for both patients.

		P1	P2	P3	P4	P5	P6	P7	P8
Patient 1	Pre-intervention	3.51	2.88	6.15	5.25	2.50	2.14	3.21	2.51
	Post-intervention	12.66	16.44	7.04	7.08	5.19	3.66	3.69	1.94
Patient 2	Pre-intervention	4.24	4.64	9.13	3.78	2.91	0.87	2.04	0.64
	Post-intervention	7.23	12.44	8.38	2.69	3.46	3.72	2.73	1.77

5.2.3.4 Endothelial Cell Activation Potential (ECAP)

Figure 5.16 shows ECAP distributions on the post-intervention aortas of both patients where the ECAP values higher than 5 are shown in red. Regions with higher ECAP values are indicated by red circles, which can be found around the attached areas of the inner tunnels and main stent graft of patient 1 and in the supra-aortic vessels of patient 2.

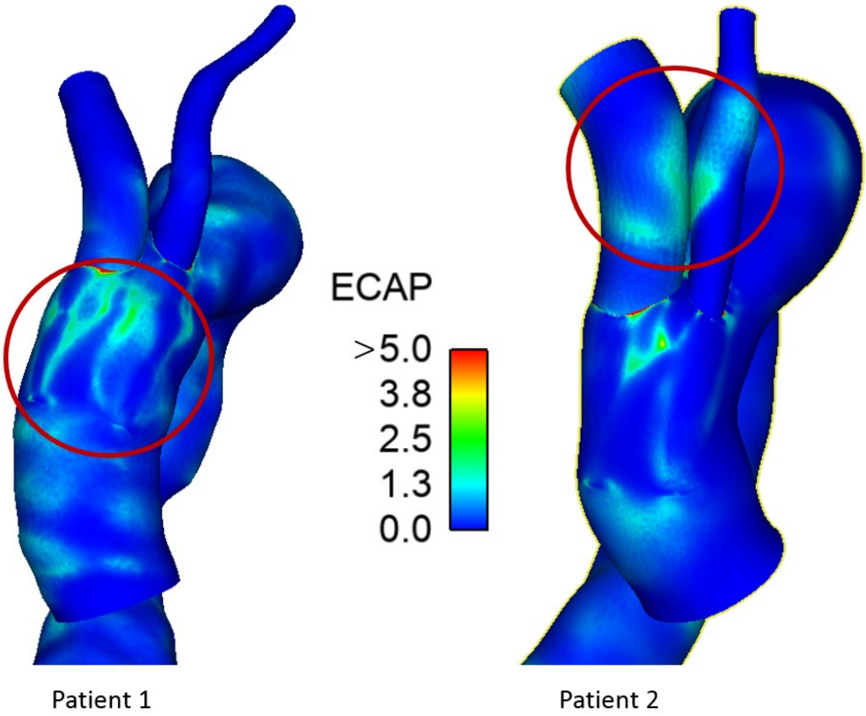

Figure 5.16. Comparisons of ECAP distributions between the post-intervention aortas of patient 1(left) and patient 2 (right). Regions highlighted by the red circles had higher ECAP values.

5.2.3.5 Displacement Forces

As shown in Figure 5.17, the magnitude of displacement forces acting on the branched endografts was evaluated for both patients and plotted over a cardiac cycle. The maximum and cycle-averaged values were 21.91 N and 17.85 N for patient 1 and 21.57 N and 17.86 N for patient 2, respectively, as summarised in Table 5.7. The magnitude of displacement force was dominated by pressure as the effect of WSS was less than 1% in these cases.

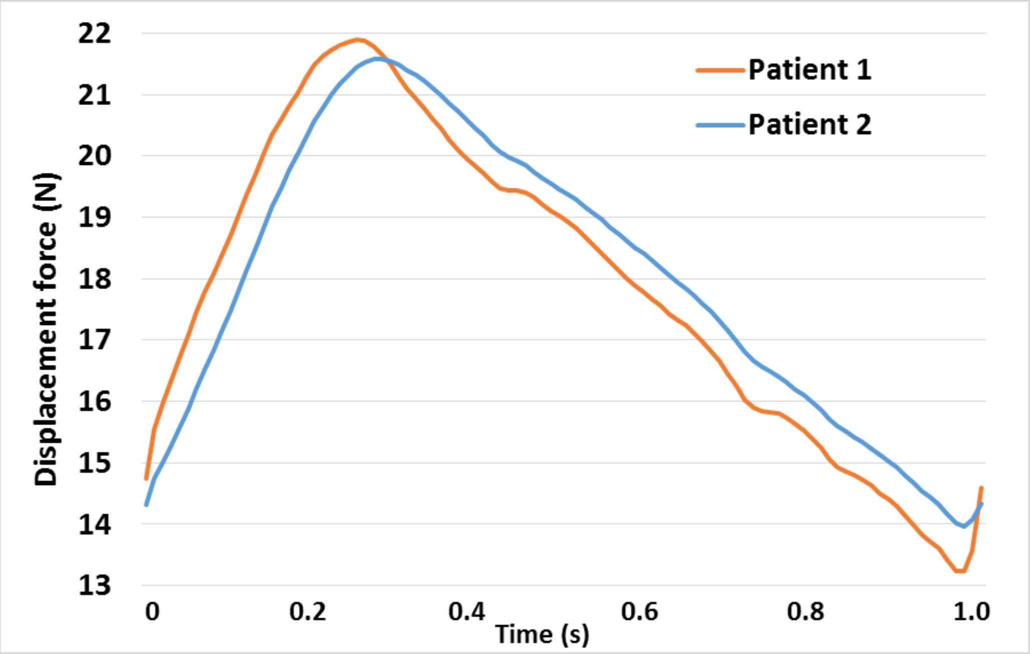

Figure 5.17. The magnitude of displacement forces experienced by the double-branched stent-grafts of both patients. The displacement force is exerted by blood flow as it passes through the endograft and time dependence of displacement forces follows the pressure waveform very closely.

Table 5.7. Cycle-averaged and maximum displacement forces acting on all the stent-graft models.

	Cycle-averaged DF (N)	Maximum DF (N)
Patient 1	17.85	21.91
Patient 2	17.86	21.57

5.2.4 Discussion

Endovascular treatment of thoracic aortic aneurysms faces great challenges especially when it involves the aortic arch owing to the complex anatomy. The Bolton Medical's Relay device is appealing for complex aortic arch diseases since it is specially designed for the tight aorta curvature. In order to help assess the functionality of this device, a detailed haemodynamic analysis was performed in this study based on patient-specific anatomical data and physiologically realistic boundary conditions (Pirola et al. 2017).

Two patients with thoracic aortic aneurysms were included in this study. Results from the pre- and post-intervention models were analysed so that changes in flow conditions could be determined. In the absence of patient-specific information on blood flow, cycle-averaged volumetric flow rate of 5 L/min and 3.4 L/min were applied at the inlets of patient 1 and patient2, respectively, with 30% of these leaving the aortic arch through the supra-aortic branches (Cheng et al. 2015). Flow divisions among the IA, LCCA and LSCA were 18%, 5% and 7%, respectively, in the pre-intervention model of patient 1 and 22%, 3% and 5% for patient 2. After intervention, the coverage of LSCA at its root caused flow redistribution, resulting in 0.91 L/min flow through the IA (18%) and 0.62 L/min through the LCCA (12%) of patient 1, while 0.75 L/min through the IA (22%) and 0.27 L/min through the LCCA (8%) of patient 2. For both patients, blood perfusion to the IA was maintained after intervention. The increased flow into the LCCA after intervention was needed as part of it would be diverted into the LSCA through the bypass.

Changes in flow patterns between the pre- and post-intervention models were assessed based on instantaneous velocity streamlines, axial velocity contours and in-plane velocity vectors. As shown in Figures 5.11 and 5.12, the large flow recirculation zone (FRZ) observed in the pre-intervention aneurysm sacs were absent in the post-intervention models. FRZ is characterized by low velocities and flow reversal, which may favour thrombus formation, leading to partial or complete obstruction of the vessel (Kandail et al. 2015). Therefore, FRZs should be avoided as much as possible. For both patients, away from the regions covered by the stent-grafts, flow in the proximal ascending aorta and the descending aorta were hardly affected by the intervention. In the supra-aortic branches, blood flow was slightly more uniform in the proximal segments due to the smoother transition from the arch in the post-intervention models. Flow in the LCCA of both patients were increased and locally accelerated flow were more obvious in the distal LCCA, since the distal diameters were smaller compared to the slightly oversized stent-grafts in the proximal regions, which were intended to prevent from device migration.

Owing to increased blood velocities in the distal ascending aorta and the arch, WSS in the post-intervention aortas was much higher than in the pre-intervention models for both patients, as can be seen in Figures 5.13 and 5.14 for TAWSS and the mean CWSS, respectively. WSS is known to influence endothelial cell functions and gene expression, and is associated with vascular remodelling (Levick 2013; Malek et al. 1999; Reneman et al. 2006). More specifically, low WSS (< 0.4 Pa) has been reported to promote thrombus formation and induce intimal thickening. With regards to the circumferential distribution of WSS, which was measured using SRI (Table 5.6), the post-intervention ascending aortas of both patients showed significantly higher values of SRI, where blood flow were skewed by the presence of inner tunnels. For patient 1, increased SRI values were also observed in the arch, descending aorta and supra-aortic branches, except for the distal LCCA where flow was more uniform and accelerated, which led to higher mean CWSS and lower SRI values. In contrast to patient 1, SRI values in the distal arch and descending aorta of patient 2 were reduced after intervention where the mean CWSS values were higher than in the pre-intervention model.

ECAP distributions on the aortic wall can be used as a sign to recognise regions that might be prone to thrombosis. As described by Di Achille et al. (2014), locations of thrombus in aneurysm patients correlated well with regions where ECAP values were greater than 5. It was noted from Figure 5.16 that patient 1, whose endograft has equal inner tunnel diameters (15 mm), had high ECAP values around the anastomosis between the inner branches and the main stent-graft. These regions are expected to be thrombosed quickly after TEVAR, which would not cause adverse clinical consequences. However, the regions with relatively high ECAP values were observed in the arch vessels of patient 2, whose endograft has smaller inner LCCA tunnel (9 mm) than the IA branch (17 mm), which might increase the risk of thrombus formation in these two branches. Similar results were reported by (Van Bakel et al. 2018), who computationally compared different endograft designs for zone 0 aortic arch repair, including two designs similar to the device used in this study. By comparing the two designs, they also found that endograft with a smaller LCCA inner tunnel diameter showed higher risk of thrombosis in the supra-aortic vessels, though not significant.

Device migration and future complications, such as type I endoleaks, are associated with pressure and wall shear stress experienced by the stent-graft as blood flows through. It has been suggested that a threshold value of approximately 32 N would be needed to dislocate a non-planar stent-graft (Rahmani et al. 2016), which is well above the maximum displacement forces of 21.91 N and 21.57 N experienced by the branched endografts of patient 1 and patient 2, respectively. Based on these results, it can be deduced that the endografts considered in this study would be at low risk of distal migration.

5.2.5 Comparisons between the Idealised Models and the Patient-Specific Models

It should be mentioned that in the patient-specific models the two inner tunnels of the Bolton device are fixed on the anterior wall of the main endograft, whereas in the idealised models, the LCCA inner tunnel was suspended in the lumen, so that the orientation of the two inner tunnels on the transverse plane is different between the patient-specific and the idealised models. Nevertheless, both models revealed that blood flow was highly disturbed after implantation of a BSG, with increased blood velocities and WSS in the post-intervention models, especially in the arch vessels. Analysis using the idealised models suggested that inner tunnels should have larger diameters than the native vessels to avoid adverse haemodynamic consequences. These results were confirmed by the patient-specific analysis since for both patients, whose endografts have larger inner tunnels than those of the respective vessels, presented with sufficient blood perfusion, less FRZs and relatively lower TAWSS.

5.2.6 Summary

Two thoracic aneurysmal patients treated with Relay thoracic endografts were analysed in detail in terms of flow patterns and WSS related parameters. It was found that blood flow to the supra-aortic branches was sufficient in both cases. Implantation of the device increased TAWSS in the aortic arch due to accelerated blood flow. Elevated TAWSS may help reduce the risk of thrombus formation, but increased spatial variation of WSS and haemodynamic derangement may have a detrimental effect in the long term. This highlights the need for clinical and radiological longitudinal follow up. Moreover, the displacement forces experienced by the endografts were evaluated and the values were below the threshold for device migration. Finally, branched endograft with a smaller LCCA inner tunnel diameter may increase the risk of thrombosis in the supra-aortic branch. In conclusion, the overall haemodynamic performance of this novel branched endograft is promising, but more patient-specific cases and follow-up studies will be needed to assess the durability of the device.

The numerical study presented in this chapter offered valuable insights into the haemodynamic performance of the branched endograft, but there were some limitations. First, the walls were assumed to be rigid. While this is a reasonable assumption for the relatively stiff endograft, the native aortic wall is compliant and subject to translational motion and radial expansion. Second, only two patient cases were analysed, limiting the wider applicability of the findings. Flow patterns and WSS within the IA and LCCA are expected to be influenced by various factors, including inlet velocity profile in the ascending aorta, length and angles between the branches and the aortic arch. Although the main device features are by and large fixed, future studies of more patient cases will be needed to examine a wide variety of anatomical scenarios. Third, inflow and outflow boundary conditions were based on flow and pressure data extracted from the literature as patient-specific flow information was not available for this retrospective study. Finally, there was no direct validation of the results as follow-up data of the two patients are not available. Nevertheless, the same computational methods have been adopted in our previous studies, demonstrating a good overall agreement with available in vivo measurements (Cheng et al. 2014; Menichini et al. 2018; Pirola et al. 2019).

Chapter 6

Application 3: Computational Analysis of Haemodynamic Conditions of the Aorta after Surgical Repair of Type A Aortic Dissections

6.1 Introduction

Acute aortic dissection can be lethal, especially when the ascending aorta is involved (Nienaber et al. 2016). Acute type A aortic dissection (ATAAD) usually requires immediate open surgery as delayed diagnosis and treatment would increase mortality rate (Pacini et al. 2013). The standard surgical approach for ATAAD is to replace the ascending aorta with a synthetic graft. Following surgical repair, 12% of patients were reported to be at risk of aortic rupture due to further dilatation of the residual dissected aorta (Halstead et al. 2007). Progressive aortic dilatation is quite common in patients with a patent false lumen (FL) after repair of ATAAD, with a reported occurrence of 49% between 1 and 167 months (Zierer et al. 2007).

Patients who have increased risk of developing aneurysmal dilatation would benefit from early interventions to prevent sudden aortic rupture and late death (Cheng et al. 2013). Certain anatomical features of the dissected aorta have been reported to correlate with late adverse outcomes; these include FL patency, maximum aortic diameter, FL area, as well as the size and location of entry tears (Chang et al. 2008; Evangelista et al. 2012; Kunishige et al. 2006; Marui et al. 1999; Onitsuka et al. 2004; Sueyoshi et al. 2004). However, neither of these variables could reliably predict FL dilatation. On the other hand, haemodynamic parameters have been widely used to predict the progression of vascular diseases. In the case of aneurysms, high pressure has been reported to cause increased circumferential tension, which may reduce the volume of smooth muscle cells and elastic fibres, and result in the accumulation of collagen fibres within the aneurysmal wall, thereby accelerating the rate of wall enlargement (Rinaudo et al. 2014). Other studies suggested that increased wall shear stress (WSS) could have a direct impact on endothelial cell functions, resulting in formation, progression and final rupture of aortic aneurysms (Sakamoto et al. 2010; Malek et al. 1999).

Although recent advances in clinical imaging technology, such as 4-dimensional magnetic resonance imaging (4D-MRI), have allowed blood velocities and wall motion to be measured directly, non-invasive measurement of pressure and WSS *in vivo* is still challenging. CFD is a numerical approach that is able to provide detailed flow patterns and reliable estimation of WSS and pressure when used with appropriate boundary conditions. It has been increasingly employed as a tool to gain better insights into the haemodynamics within the human body and its association with the aetiology and progression of cardiovascular diseases (Cheng et al. 2013). Previous CFD studies of aortic dissection mainly focused on the Stanford type B aortic dissection (TBAD), aimed at depicting the detailed flow phenomena and haemodynamic conditions in patient-specific dissection models (Chen et al. 2013; Cheng et al. 2010, 2014; Ko et al. 2017), or examining the influence of morphological variations on haemodynamic changes (Cheng et al. 2013; C. Karmonik et al. 2011; Simon et al. 2016; Tang et al. 2012; Wan Ab Naim et al. 2014). Several studies also reported that CFD could assist in predicting progressive aneurysmal dilatation in TBAD (Cheng et al. 2015; Shang et al. 2015; Tse et al. 2011; Xu et al. 2017).

Surgical repair of TAAD with replacement of the ascending aortic segment often leaves re-entry tears in the arch and descending aorta unattended, which may lead to late progressive aortic dilatation. The aim of this study was to examine if CFD simulations could identify patients at risk of further aortic dilatation and help understand the underlying mechanisms. Patient-specific dissection geometries were reconstructed from post-surgery computed tomography angiography (CTA) images and divided into two groups, patients with stable aortic diameters, and those with progressive aortic dilatation. These were then coupled with physiologically realistic boundary conditions. Haemodynamic results including flow patterns, WSS, and pressures were compared.

6.2 Methodology

6.2.1 Data Acquisition and Geometry Reconstruction

This retrospective study was based on the validated database of patients with repaired TAAD at the Royal Brompton and Harefield hospitals. All patients underwent a minimum of 2 follow-up CTA examinations following surgical repair with a time interval between 1 and 5 years (2.5 ± 1.3 years). All studies were reviewed by a radiologist with over 10 years' experience of cardiovascular imaging and patients were classified as stable (minimal or no change in the diameter of the residual dissected aorta) and unstable (significant progressive dilatation). Out of 40 patients, 23 were excluded from CFD simulations due to inadequate image quality or coverage. A total of 17 patients were finally analysed and divided into two groups: stable (N = 9) and unstable (N = 8).

All patient-specific geometries were reconstructed from the first set of CTA images using a semi-automatic threshold-based segmentation tool available in Mimics 20.0 (Materialise, Leuven, Belgium). The regions of interest had to be manually segmented based on local greyscale intensities. The segmented 2D masks were then integrated to generate a 3D fluid domain, which was smoothed to eliminate any reconstruction errors. Details of the reconstruction of the aortic lumen were already described in Chapter 3. For every patient, the computational model was created from the aortic sinotubular junction to the level of diaphragm. Three main arch branches were also included in the reconstructions, as shown in Figure 6.1. A transparent view for each model is provided, which allows visualisation of the location and shape of the tears. The location of the proximal entry tear is highlighted by a red circle in the transparent view.

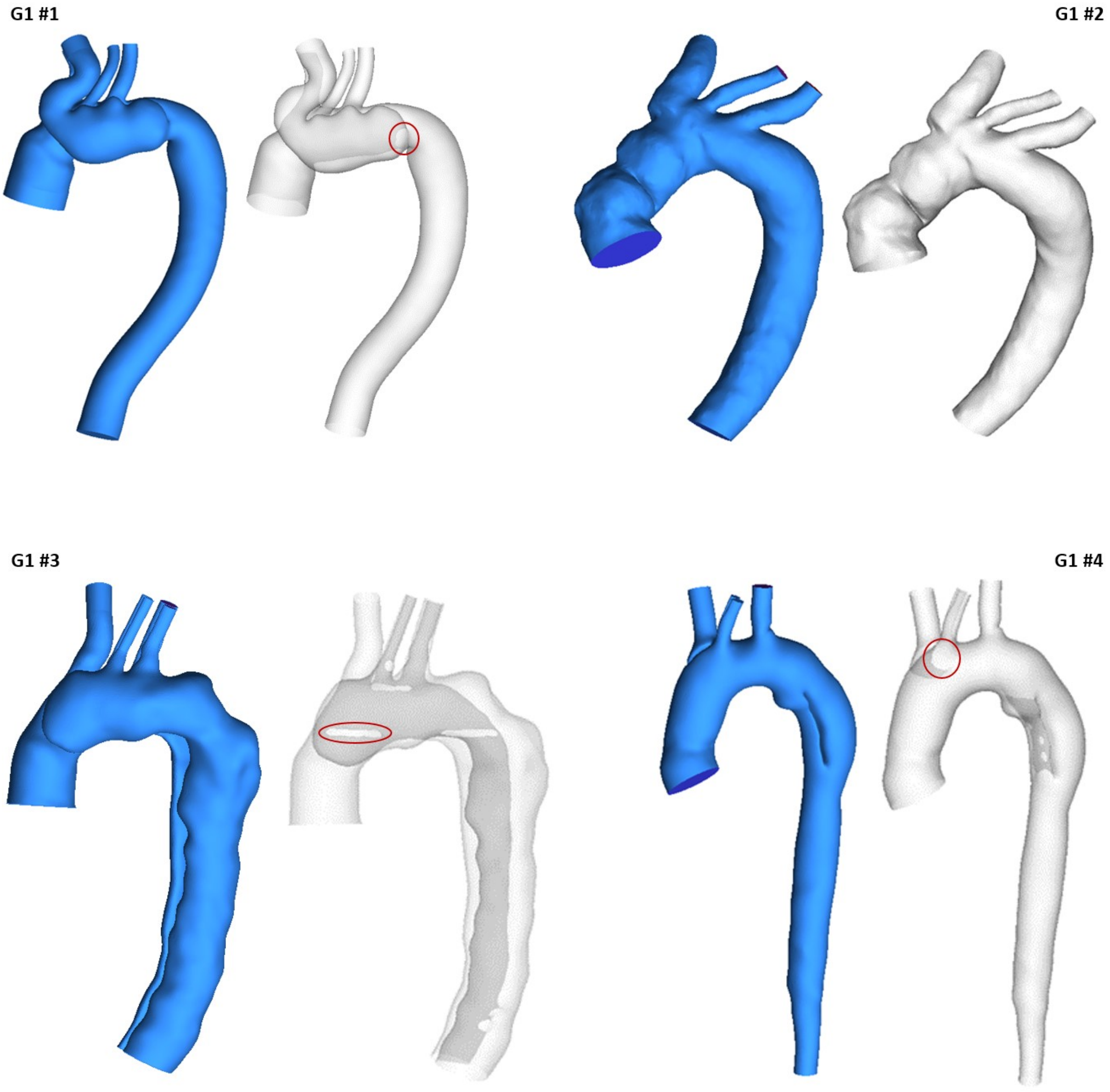

G1 #5

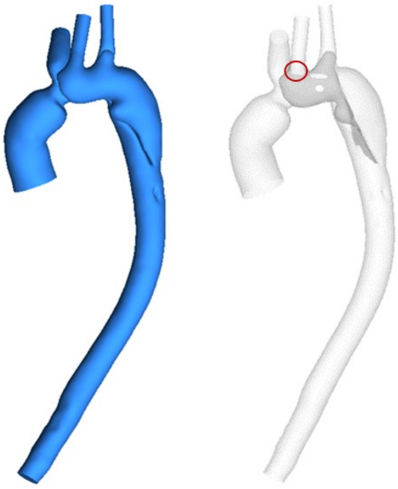

G1 #6

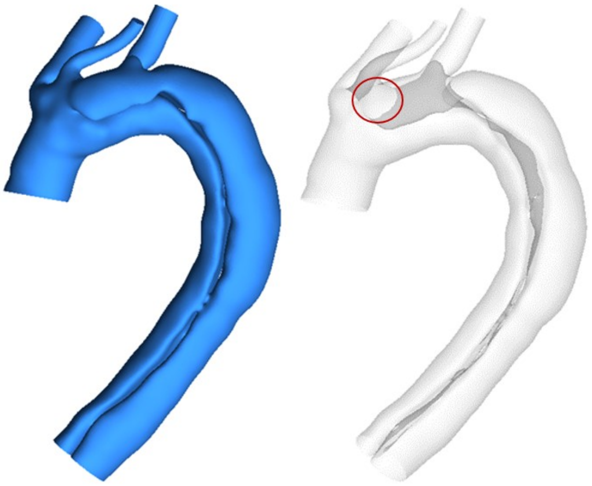

G1 #7

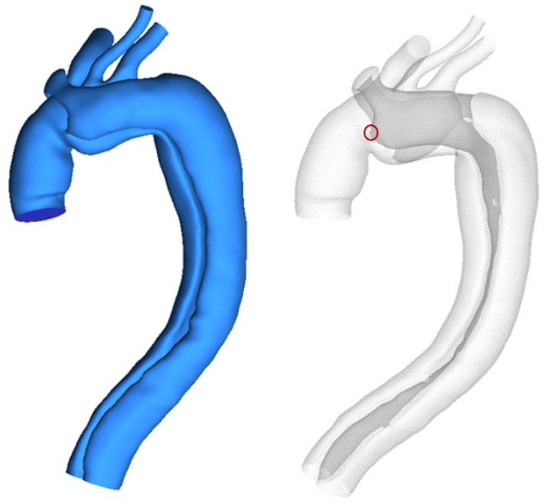

G1 #8

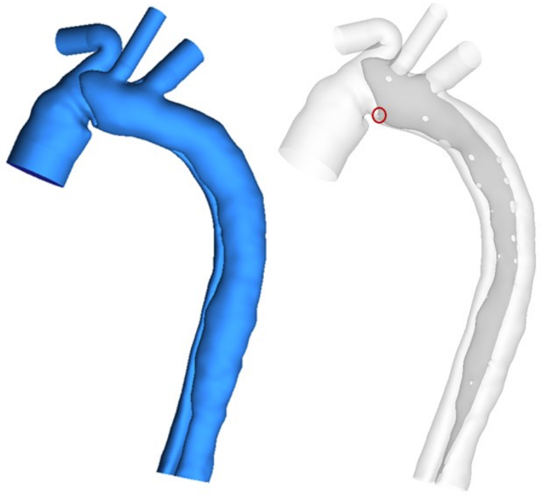

G1 #9

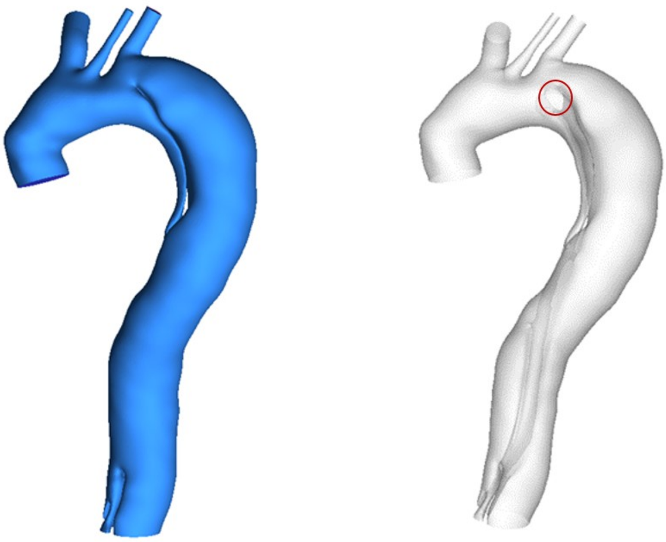

G2 #1

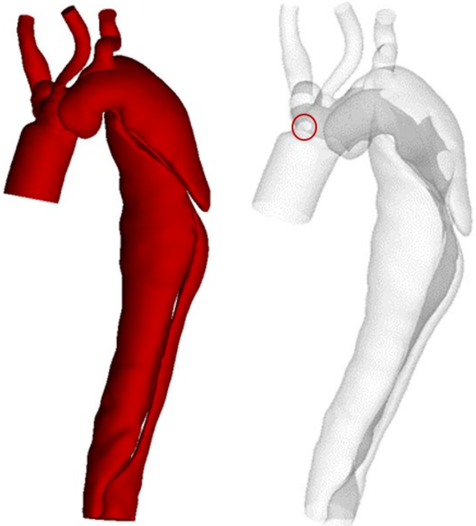

G2 #2

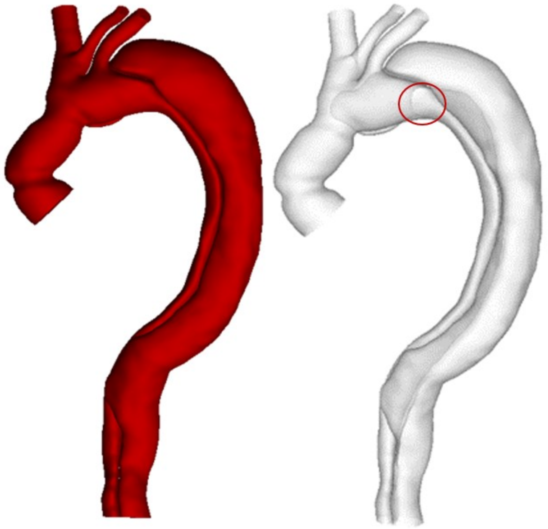

G2 #3

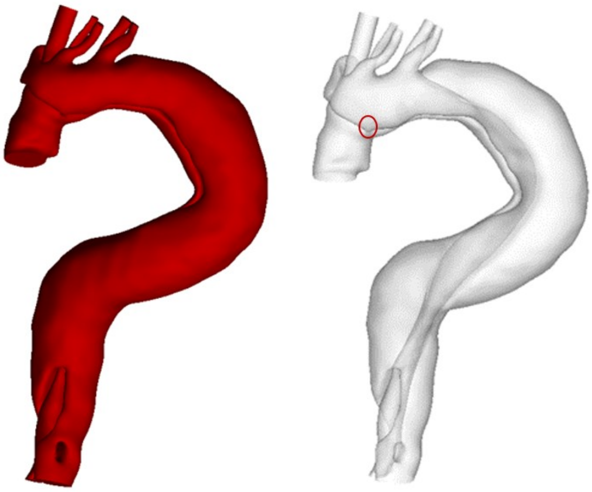

G2 #4

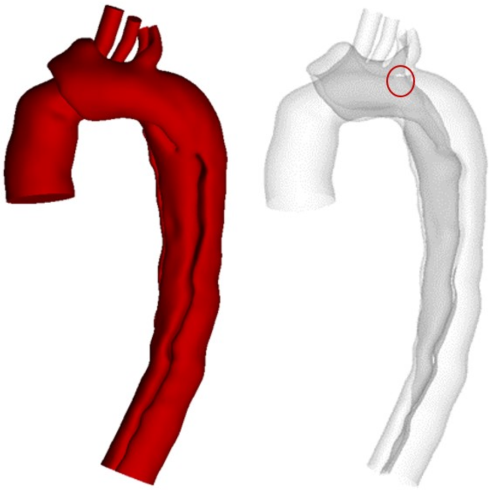

G2 #5

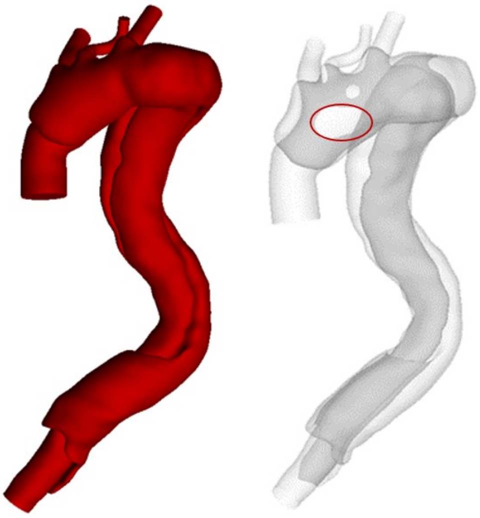

G2 #6

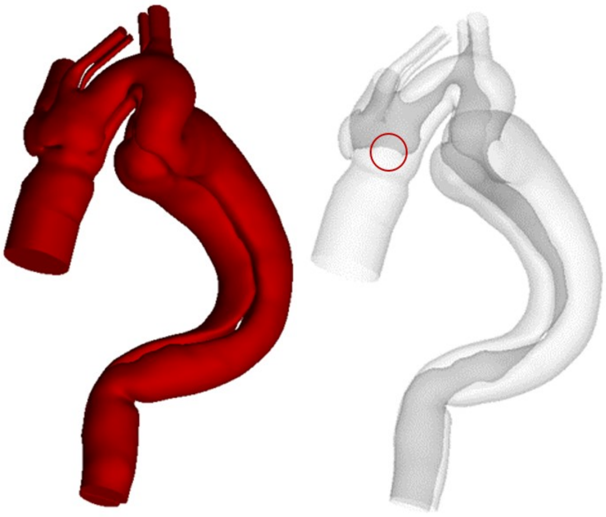

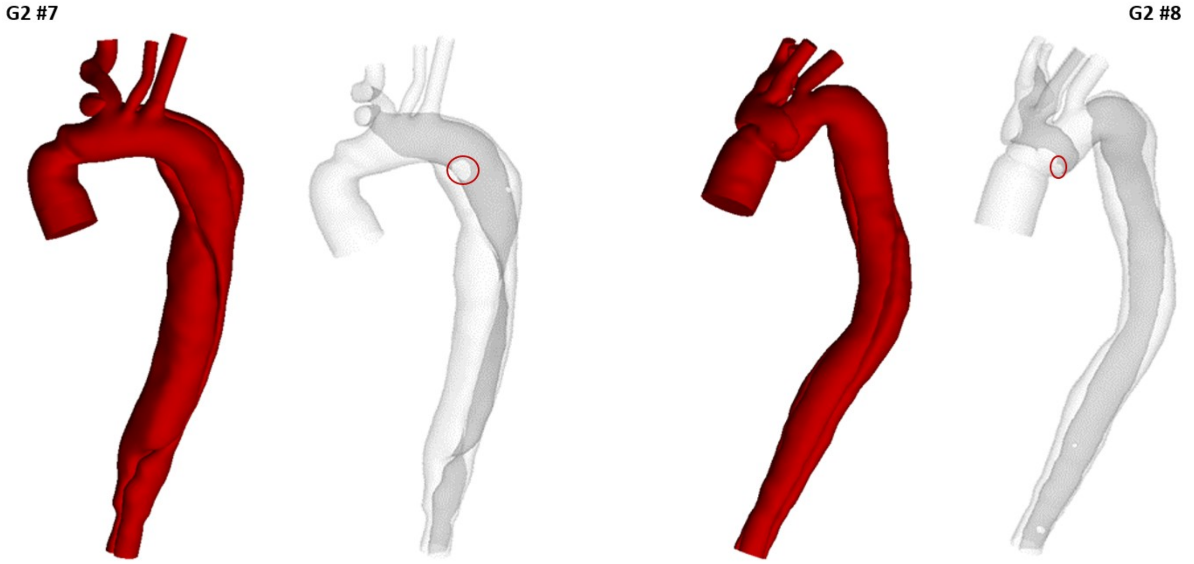

Figure 6.1. Geometries of the 17 aortic dissection models. Patients with stable aortic diameters (Group 1) are shown in blue while those with unstable aortic diameters (Group 2) are displayed in red. A transparent view is given in the right for each model where the primary entry tears are indicated by red cycles.

All the 3D geometries were then imported into ANSYS ICEM CFD (ANSYS, Canonsburg, PA, US) for mesh generation. Each computational mesh consisted of tetrahedral elements in the core and a minimum of 10 layers of prismatic cells in the fluid boundary layer. Local mesh refinement was performed in regions around the tears and great curvature. Grid independent tests were conducted, and the number of elements adopted in the final analysis ranged from 3 to 7.4 million, depending on geometric complexity and size of the model.

6.2.2 Boundary Conditions

Doppler Ultrasound Measurements of Blood Velocity

Doppler ultrasound offers a non-invasive and safe method for measuring the rate of blood flow in a wide range of blood vessels by bouncing high-frequency sound waves off moving objects, such as red blood cells. Medical ultrasound instruments operate by the transmission of a short pulse of ultrasound along a beam, followed by reception of ultrasound which is scattered by the tissue. Doppler ultrasound can estimate how fast blood flows by measuring the rate of change in its frequency, Δf, which is defined as

$$\Delta f = 2\,(v \cos\theta) f_0 / c \tag{6.1}$$

where Δf is also called the Doppler shift, v is the magnitude of blood velocity, θ is the angle between ultrasound beam and direction of motion, f_0 is the frequency of ultrasound transmitted, and c is the speed of propagation of ultrasound in blood. Since f_0 and c are generally known, measurements of the Doppler shift Δf allows calculation of blood velocity, v, if the angle θ can be accurately determined (Gill 1985).

As shown in Figure 6.2, physiological boundary conditions were applied in order to generate results that are clinically relevant. In this study, although Doppler ultrasound measurements of patient-specific velocity waveforms (Figure 6.2 A) were available, this information could not be directly employed due to the absence of diastolic velocity data. Furthermore, velocity data were acquired at the left ventricular outflow tract (LVOT) rather than at the model inlet. Considering the above limitations, *in vivo* measured flow waveform acquired at a similar location in the ascending aorta of a type B aortic dissection patient was adopted as a template (Pirola et al. 2019), and the corresponding maximum velocity was recorded as shown in Figure 6.2 B. This flow waveform was then scaled in both directions by making use of patient-specific heart rate and maximum velocity measured by Doppler ultrasound, so that the applied flow waveform (Figure 6.2 C) contained some patient-specific features. The scaled flow waveform was specified at the corresponding model inlet along with the assumption of a flat velocity profile. With regard to outlet boundary conditions, a total of 21% of inlet flow was assumed to exit through the arch vessels (Pirola et al. 2019), where flow split was calculated based on their cross-sectional areas (Zamir et al. 1992).This information was used to calculate parameters in a 3-EWM which was implemented at each model outlet (Figure 6.2 D). The assumption of rigid vessel walls was made where no-slip boundary conditions were specified. This assumption was not unreasonable given the reduced compliance of dissected aortic walls.

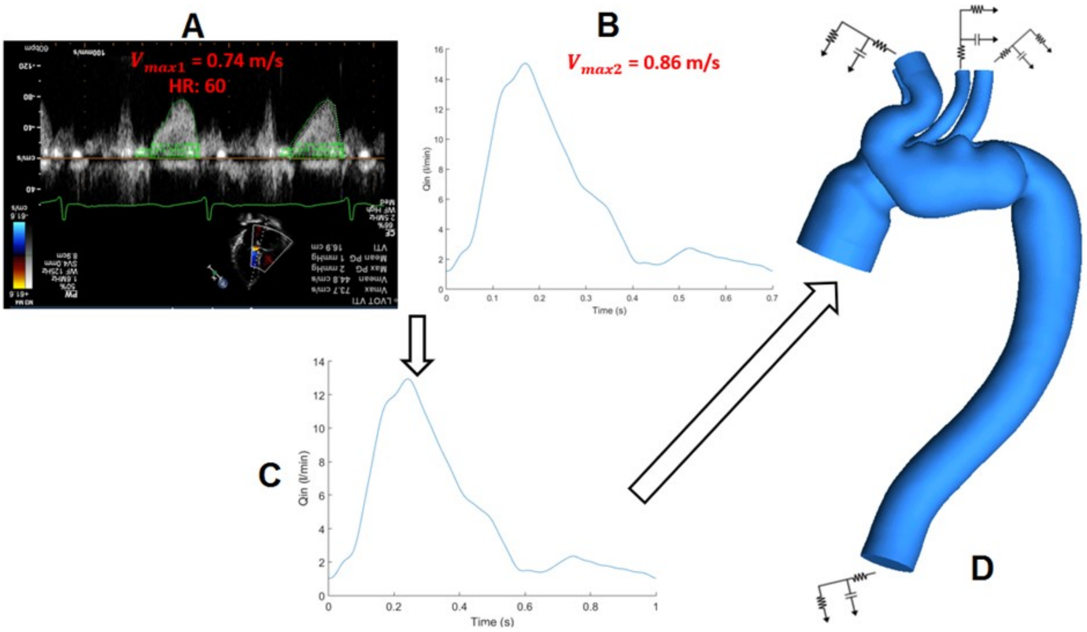

Figure 6.2. (A) Velocity measurements acquired by Doppler ultrasound; (B) Flow waveform at the inlet of the ascending aorta of a type B dissection taken from the literature (Pirola et al. 2019); (C) Scaled flow waveform based on patient-specific heart rate and maximum inlet velocity; (D) Schematic of the computational model employed in this study.

6.2.3 Computational Details

Blood flow was simulated by solving the Navier-Stokes equations with a finite volume based solver ANSYS CFX 15 (ANSYS, Canonsburg, PA, US). Cycle-averaged Reynolds numbers were in the range of 589 and 1585, while the peak values were between 1620 and 4035, which were calculated based on the inlet diameter and the mean and peak velocities of the reconstructed aorta models, respectively. Flow in a dissected aorta is likely to become transitional or turbulent induced by geometric features, such as a narrow tear or highly compressed TL. In order to capture any possible flow turbulence, the SST-Tran model (Menter et al. 2006) was applied in this study. Details of the model were described in Chapter 3. As the SST-Tran model requires a turbulence intensity value to be defined at the inlet, a relatively low value of 1.5% was adopted based on previous studies of aortic flow (Tan et al. 2008, 2009).

Blood was assumed to be incompressible and Newtonian with a constant density of 1060 kg/m^3 and dynamic viscosity of 0.004 Pa.s. A fixed time step of 0.001 s was chosen, and a maximum root-mean-square residual of 1×10^{-5} was specified as a convergence criterion. The period of one cardiac cycle ranged from 0.46 s to 1 s based on the patients' heart rate. All simulations were performed for three cardiac cycles which were sufficient to achieve a periodic solution, and results obtained in the last cycle were used for detailed analysis. Flow patterns, TAWSS as well as pressure were calculated and analysed using CEI Ensight 10 (CEI Inc, Apex, NC, US).

Statistical Analysis

Statistical analysis was carried out using SSPS (IBM Corporation). The Mann-Whitney U test was chosen to determine if two independent samples have the same distribution. All results were presented as mean ± standard deviation with the corresponding p-value. A $p\text{-value} < 0.05$ was deemed statistically significant.

6.3 Results

6.3.1 Anatomical Features

Using the validated database of patients with surgically repaired TAAD, 9 patients with stable aortic diameters (Group 1) and 8 with progressive aortic dilatation (Group 2) with adequate imaging were identified. As already shown in Figure 6.1, the reconstructed geometries of repaired TAAD are highly complex with substantial individual differences. One of the patients (G1#2) with a stable aorta had a fully thrombosed FL at follow up. Out of the 16 cases with a patent FL, in 14 cases the remnant FL started from the distal ascending aorta, involving the arch vessels in 9/14. In 2 cases (G1#9 and G2#2), the patent segment of the FL originated from the distal arch at the level of the LSCA. Three patients in group 1 had a shorter FL that merged with TL at the distal arch in one patient (G1#1), and in the mid-thoracic aorta of the other two (G1#4 and G1#5). A summary of key geometric parameters can be found in Table 6.1.

Distance between the primary tear and the origin of LSCA was estimated by measuring the respective aortic centreline. In 5/16 cases, the primary tear was located distally to the LSCA as indicated by the negative values while in the other 11 patients, the primary tear was observed in the proximal arch. Residual primary entry tears varied in size and shape from patient to patient, the smallest and largest tears were 2.6 mm^2 and 585 mm^2, respectively, both in group 1. Number of re-entry tears was found to vary from 0 to 18 in group 1, much higher than in group 2 (ranged 0-4). In the patient with no re-entry fenestration distal to the proximal tear (G1#1), the residual FL involved the aortic arch and extended to the IA. In all 16 dissected patients, the TL was compressed by the FL; the FL: TL volume ratio ranged from 1.1 - 13.2 in group 1, and 1.8 – 6.8 in group 2. The overall FL: TL volume ratio was higher in group 2 with 7/8 (88%) patients had a value greater than 2, while only 2/8 (25%) patients in group 1 had a value greater than 2. In addition, tortuosity, defined as the ratio between the distance along the aortic centreline and the linear distance, was calculated for the entire aorta, and for the ascending and descending aortas separately. No obvious difference was found between the two groups.

Table 6.1. A summary of key geometric parameters.

	Group 1 (Stable)									**Group 2 (Unstable)**							
Parameters	**#1**	**#2**	**#3**	**#4**	**#5**	**#6**	**#7**	**#8**	**#9**	**#1**	**#2**	**#3**	**#4**	**#5**	**#6**	**#7**	**#8**
Primary tear size																	
Area (mm^2)	**119**	**N/A**	**113**	**363**	**432**	**281**	**2.6**	**4.6**	**585**	**43**	**260**	**8.8**	**341**	**522**	**49**	**116**	**50**
Number of re-entry tears	**0**	**N/A**	**5**	**4**	**3**	**8**	**6**	**18**	**5**	**4**	**0**	**2**	**1**	**1**	**2**	**1**	**3**
Distance between primary tear and LSCA (mm)	**-30**	**N/A**	**38**	**34**	**33**	**37**	**32**	**35**	**-6**	**70**	**-33**	**39**	**-8**	**34**	**56**	**-29**	**29**
Max. distance between tears (mm)	**N/A**	**N/A**	**149**	**80**	**39**	**109**	**88**	**51**	**109**	**38**	**N/A**	**284**	**43**	**13**	**79**	**23**	**264**
Max. aortic diameter (mm)	**36**	**34**	**47**	**42**	**36**	**39**	**41**	**34**	**49**	**49**	**46**	**46**	**41**	**49**	**47**	**43**	**38**
Dissection involved arch vessels (Y/N)	**Y**	**N/A**	**Y**	**Y**	**Y**	**N**	**N**	**Y**	**Y**	**N**	**N**	**Y**	**Y**	**N**	**Y**	**N**	**Y**
Inlet diameter (d_1) (mm)	**35**	**33**	**33**	**38**	**32**	**32**	**26**	**43**	**30**	**33**	**33**	**24**	**39**	**32**	**31**	**30**	**33**
Arch diameter (d_2) (mm)	**24**	**28**	**38**	**36**	**31**	**35**	**35**	**22**	**43**	**30**	**43**	**34**	**36**	**35**	**26**	**30**	**36**
Curvature ratio (d_1/d_2)	**1.5**	**1.2**	**0.9**	**1.1**	**1.0**	**0.9**	**0.7**	**1.5**	**0.7**	**1.1**	**0.8**	**0.7**	**1.1**	**0.9**	**1.2**	**1.0**	**0.9**
Tortuosity																	
Entire aorta (inlet to diaphragm)	**2.0**	**2.7**	**2.1**	**2.4**	**2.4**	**2.3**	**2.4**	**1.6**	**2.2**	**2.1**	**2.9**	**2.4**	**2.0**	**2.7**	**3.0**	**1.9**	**2.2**
Ascending aorta (inlet to LSCA)	**1.1**	**1.3**	**1.2**	**1.1**	**1.2**	**1.1**	**1.2**	**1.2**	**1.2**	**1.1**	**1.2**	**1.3**	**1.3**	**1.3**	**1.2**	**1.3**	**1.1**
Descending aorta (LSCA to diaphragm)	**1.3**	**1.3**	**1.1**	**1.2**	**1.1**	**1.3**	**1.3**	**1.2**	**1.2**	**1.1**	**1.4**	**1.5**	**1.1**	**1.3**	**1.5**	**1.1**	**1.3**
Volume ratio of FL/TL	**1.1**	**N/A**	**2**	**7.2**	**1.9**	**1.4**	**1.5**	**1.2**	**13.2**	**6.8**	**2.5**	**4.9**	**2.8**	**2.2**	**1.8**	**3.1**	**2.8**

6.3.2 Flow Patterns

As shown in Figure 6.3, instantaneous velocity streamlines at the time points of peak systole and mid-systolic deceleration were plotted for all the patient-specific models. Although the flow patterns varied significantly among patients, common flow characteristics could still be observed. Due to the complicated geometries of AD, flow patterns were very complex with helical flow, flow separation and recirculation. Blood flow accelerated when passing through regions with reduced lumen areas, especially when it entered the FL through the primary tear, a high-speed jet formed and impacted on the opposing aortic wall. Blood velocities in the FL were lower than that in the TL, which was more obvious in group 2, corresponding to the relatively higher FL: TL volume ratio. In group 1, very low flow was observed in the FL of patient G1#1, having only one major tear located in the distal FL so that very little flow could retrogradely enter the FL. In group 2, the lowest FL velocities were observed in patient G1#3, who presented with the smallest entry tear size (8.8 mm^2) but the largest distance between the primary tear and the first re-entry tear (284 mm). Although patient G2#5 had the largest entry tear (522 mm^2) in group 2, blood flow could barely enter FL since the orientation of this entry tear was almost parallel to the direction of flow. Several haemodynamic studies on type B aortic dissection found that FL flow had a positive correlation with entry tear size (Cheng et al. 2013, 2015). However, this might not be true for TAAD since most entry tears were found in the arch rather than in the more erect descending aorta. The almost static flow was observed in patient G2#8, who presented with a disconnected FL (ascending and descending FL) and a large distance between the proximal tear and the distal tear (264 mm). This means that little flow could enter the top region of the descending FL.

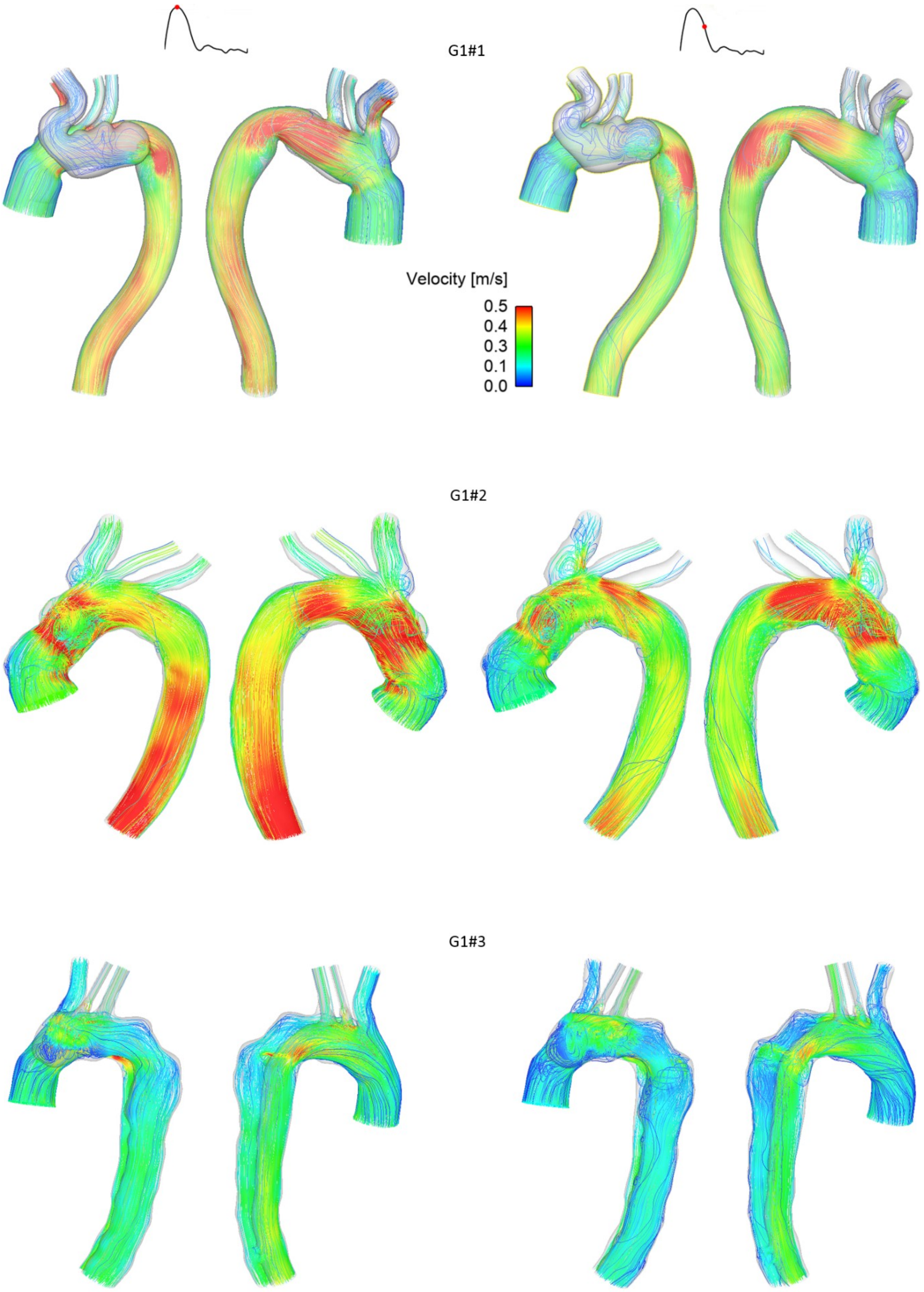
G1#1
Velocity [m/s]
0.5
0.4
0.3
0.1
0.0
G1#2
G1#3

G1#4

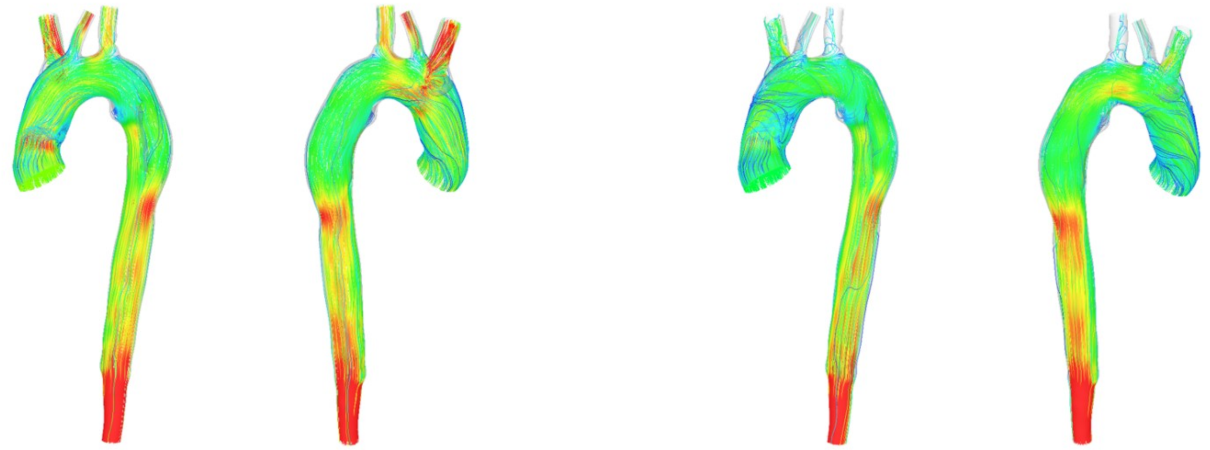

G1#5

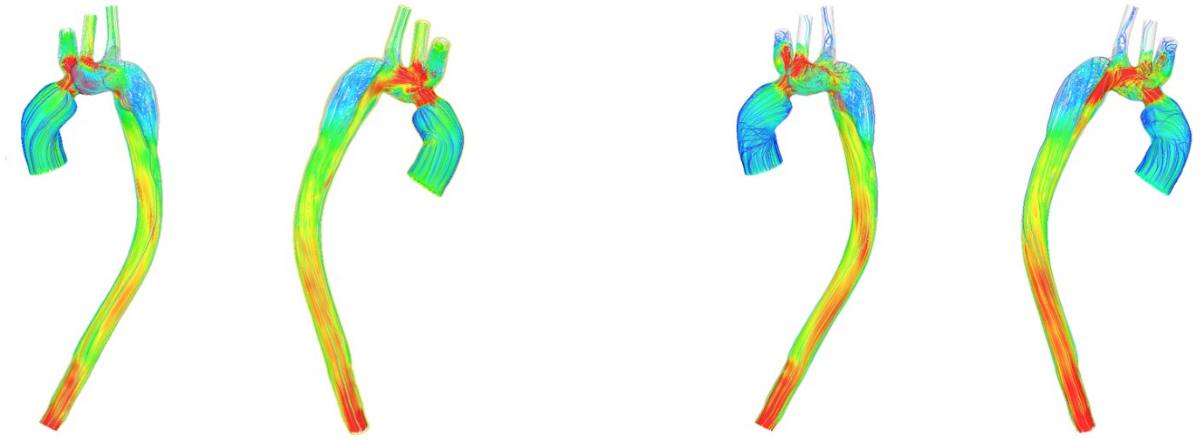

G1#6

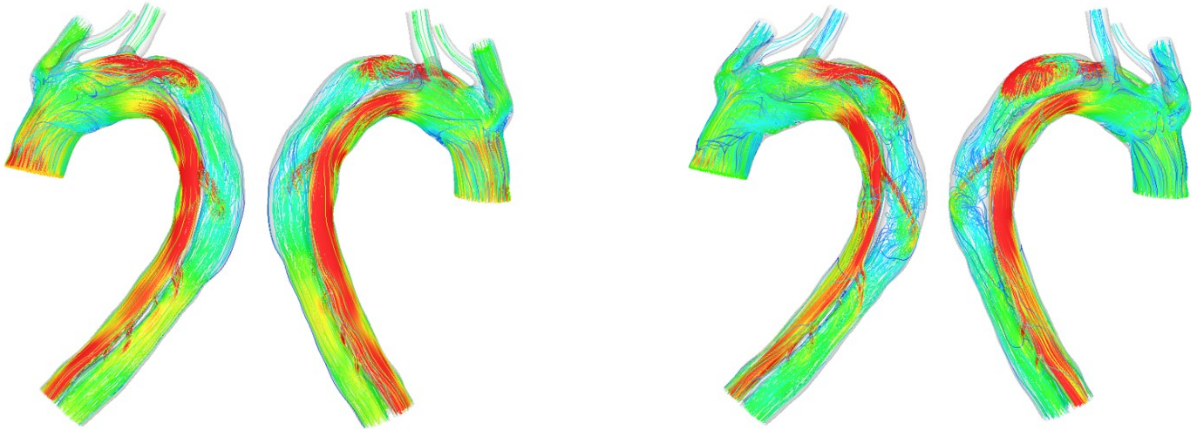

G1#7

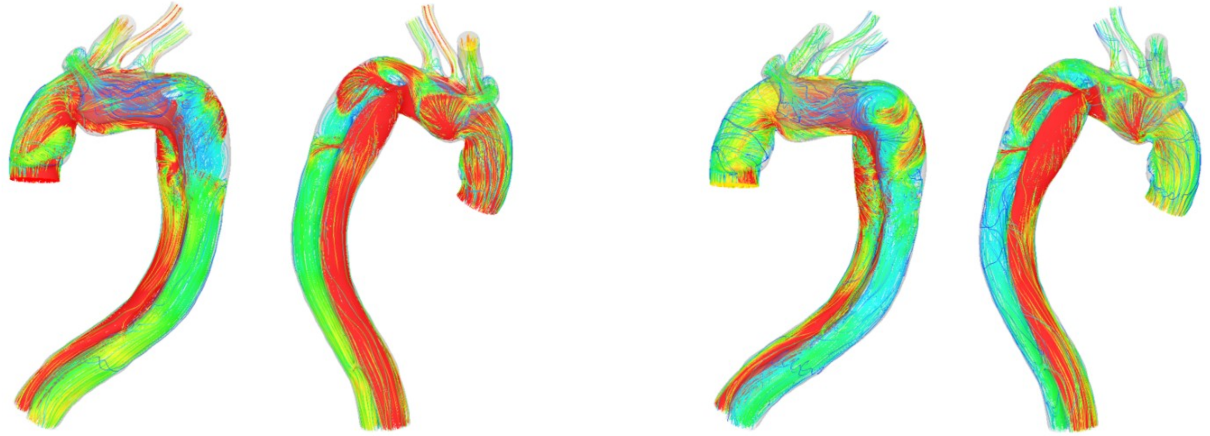

G1#8

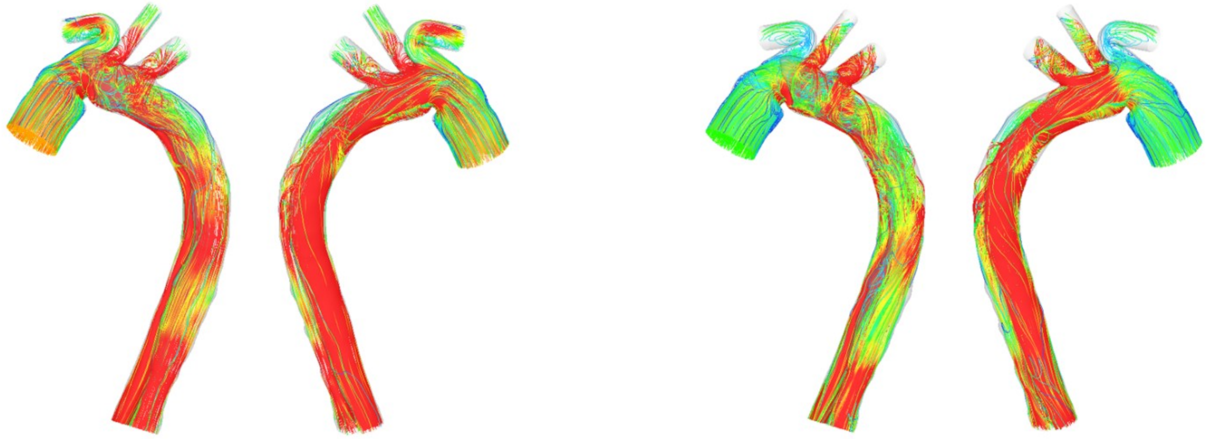

G1#9

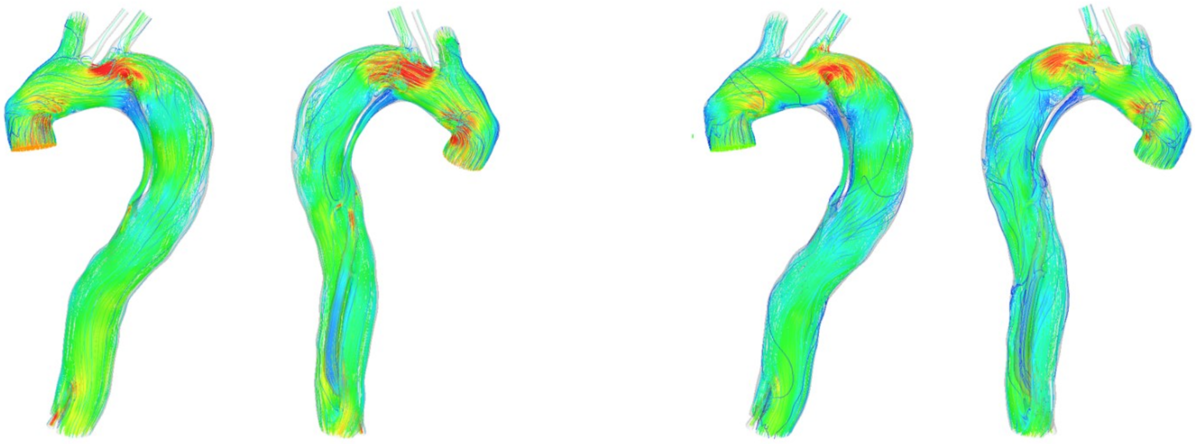

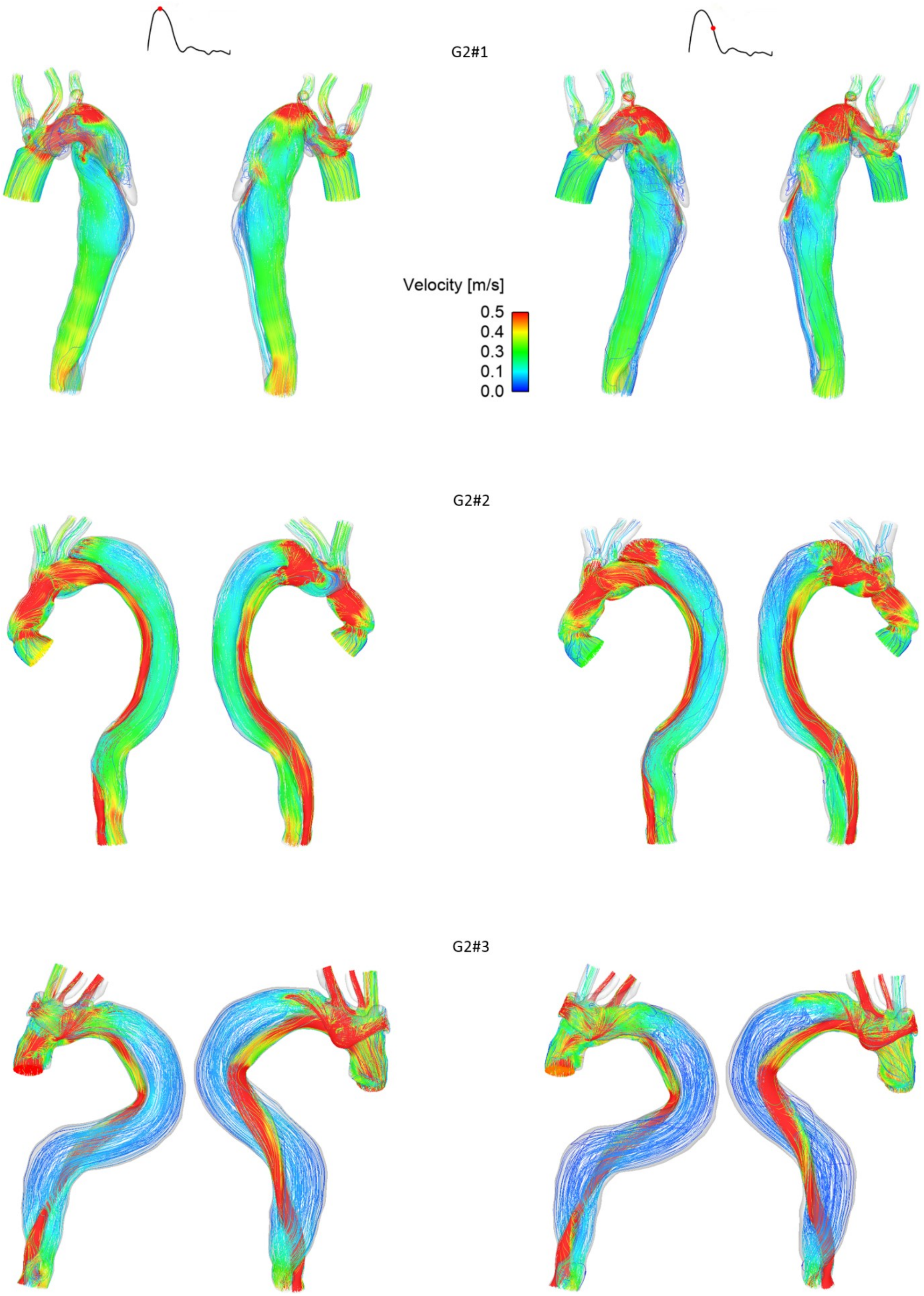
G2#1
Velocity [m/s]
0.5
0.4
0.3
0.1
0.0
G2#2
G2#3

G2#4

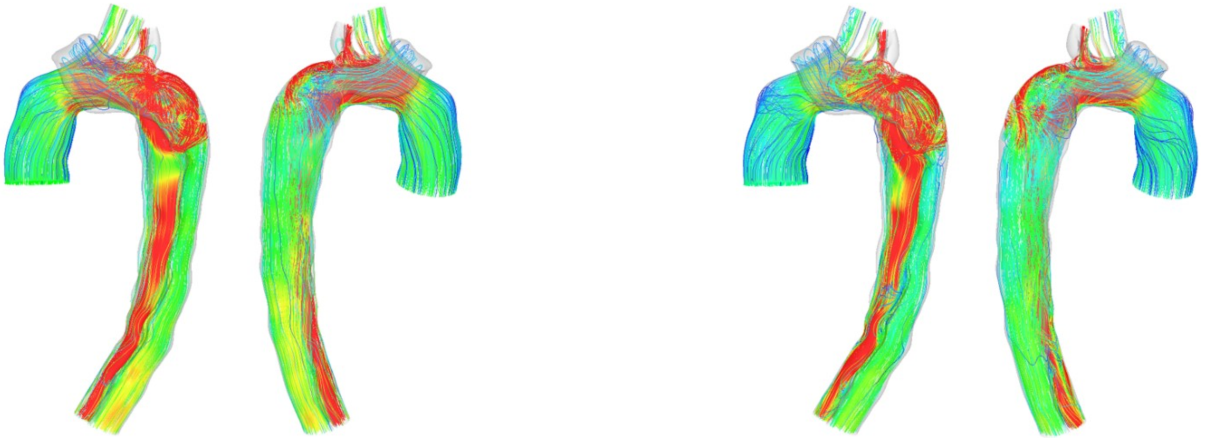

G2#5

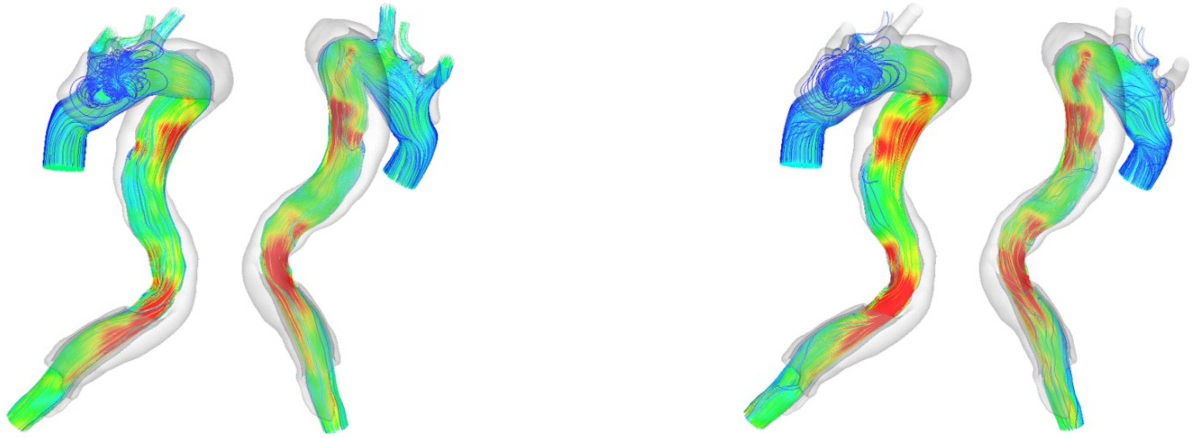

G2#6

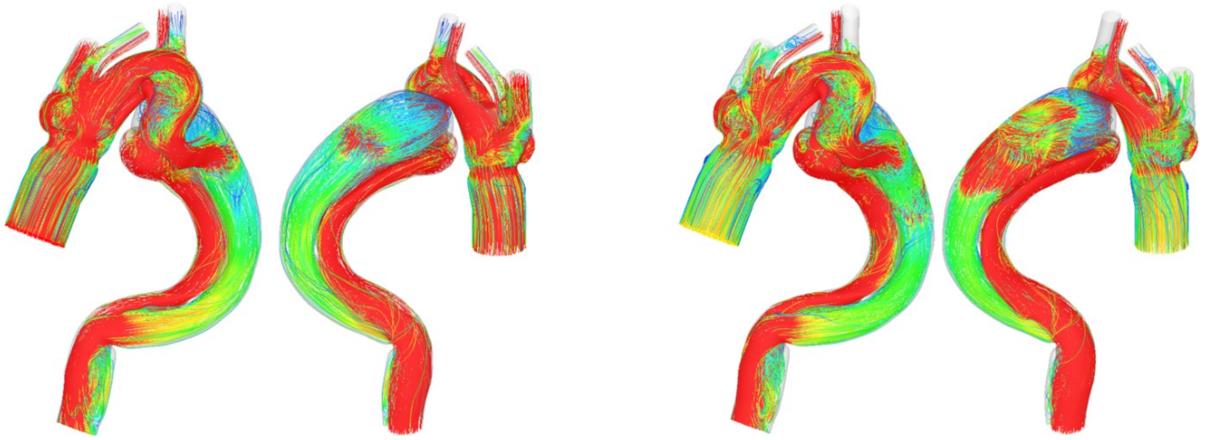

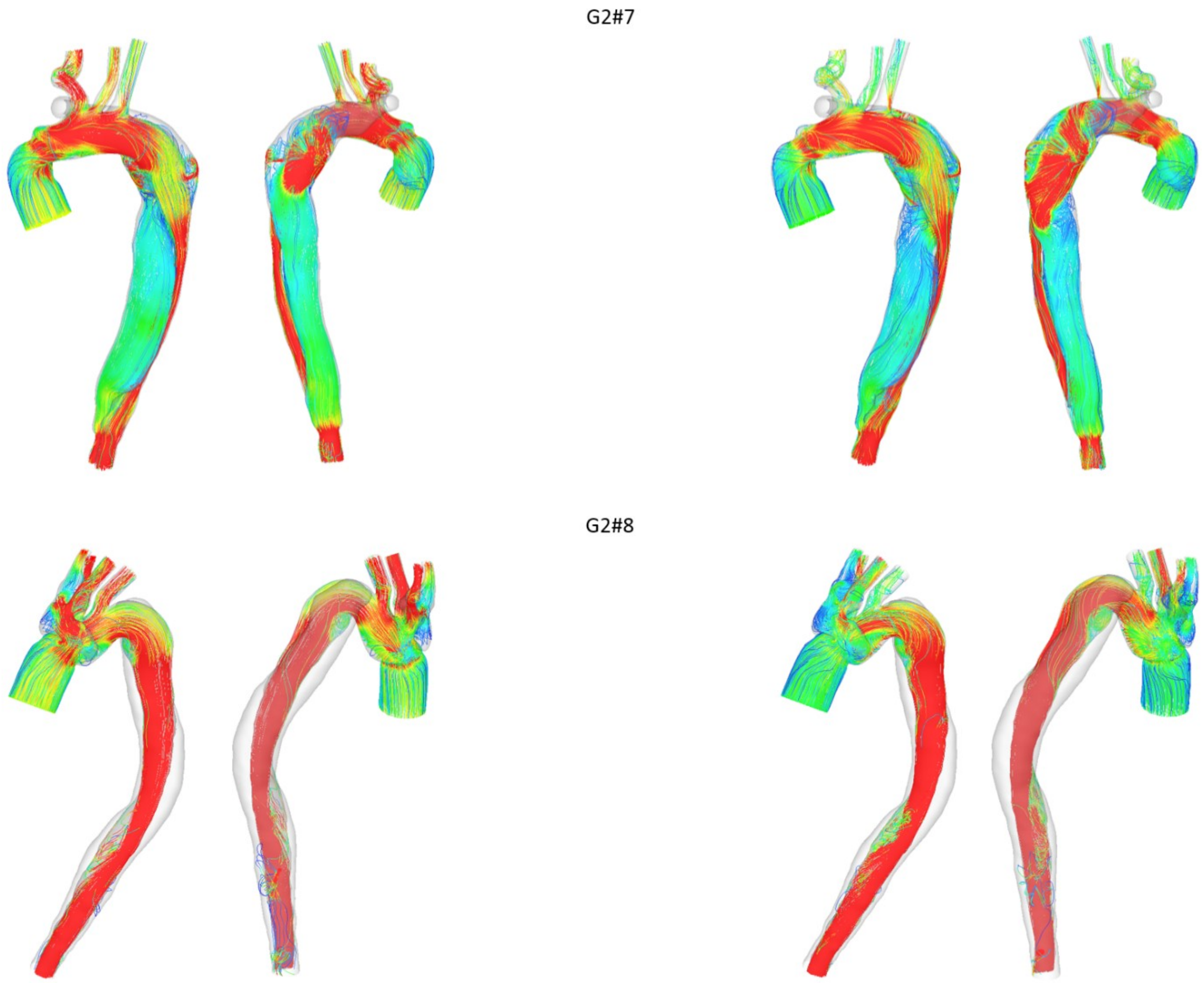

Figure 6.3. Instantaneous velocity streamlines for all the 17 models at two characteristic time points: peak systole (left) and mid-systolic deceleration (right).

6.3.3 Wall Shear Stress

Figure 6.4 shows the predicted TAWSS distributions in all the cases, where regions with TAWSS > 2.5 Pa are shown in red colour. Overall, TAWSS was higher in the TL than in the FL, as a result of accelerated blood flow in the narrowed TL. High TAWSS values were found at the throat of narrowed section where blood flow was accelerated and velocity was high, or in the regions surrounding the tears, with the maximum TAWSS on the edge of the primary tears in most cases. As shown in Figure 6.3, high TAWSS along the edge of tear could be explained by the high velocity of blood flow through the tear into the FL. The jet of fluid from the TL impinged directly on the adventitial bound surface of the FL, causing high wall shear stress on the anterior and posterior surface, or the site opposite the tear in the FL. Figure 6.5 illustrates the comparison of maximum TAWSS on the aortic wall between the two groups. In group 1, the peak values varied from 5.62 – 25.4 Pa, lower than group 2, with a variation from 5.19 to 45.31Pa. In group 1, two relative high values of peak TAWSS, 25.4Pa and 24.9 Pa, were both found in the regions around the entry tears, which were measured as 2.6 mm^2 and 4.6

mm^2 in area, respectively. These small entry tears might lead to relatively high TAWSS. In group 2, very low peak TAWSS was found for patient G2#5, whose entry tear located in a transverse position and therefore very low flow could enter into the FL with small velocities.

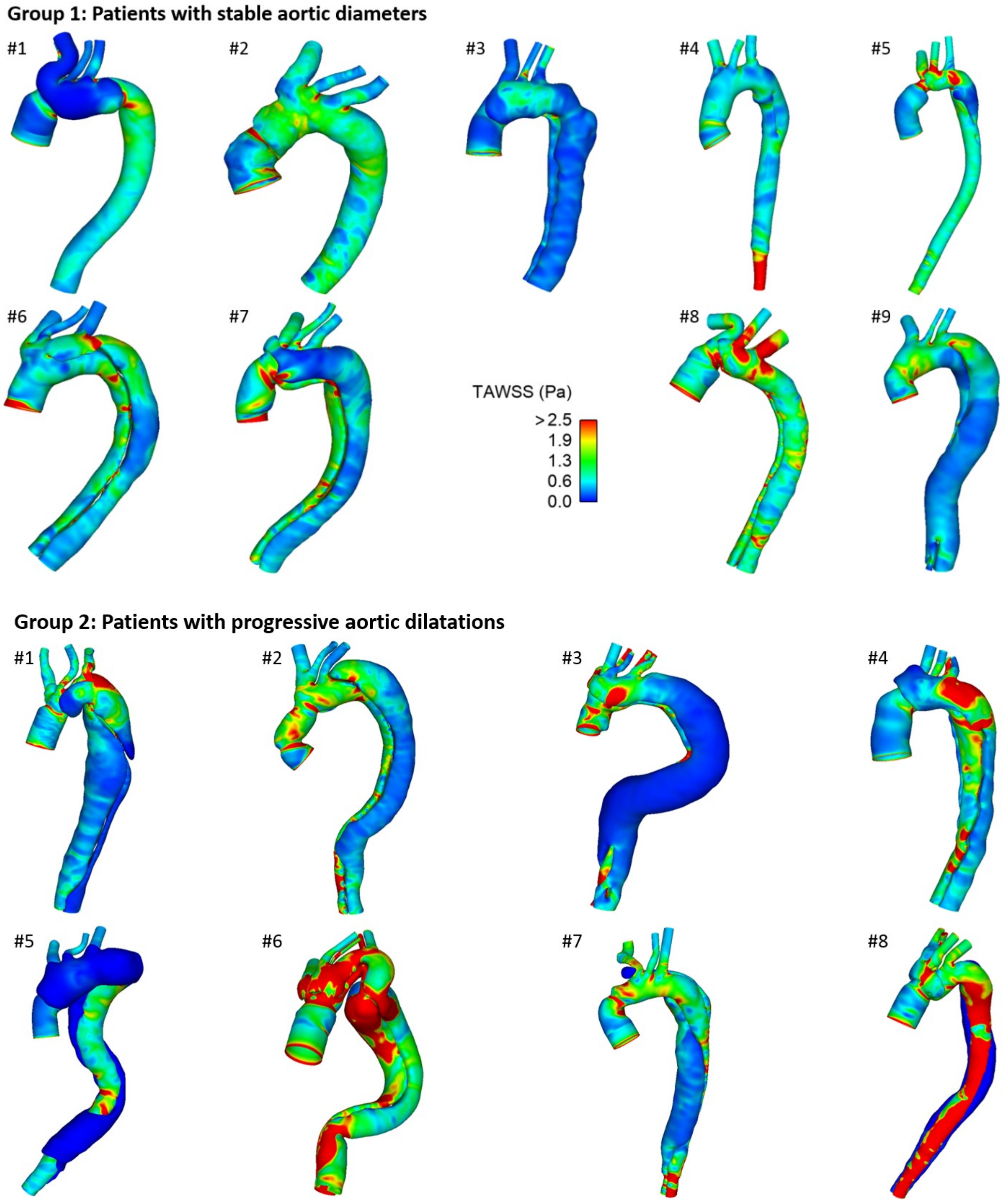

Figure 6.4. TAWSS contours in the aortic dissection models of the 17 subjects. Regions with TAWSS higher than 2.5 Pa are shown in red.

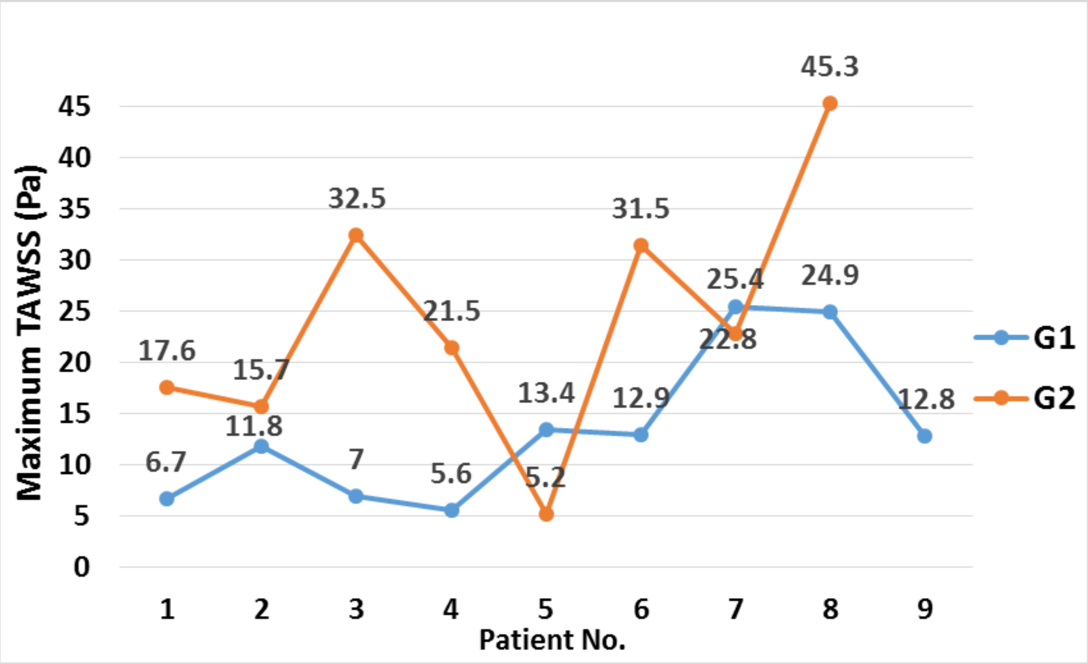

Figure 6.5. Comparison of the maximum TAWSS on the aortic wall between two groups.

6.3.4 Pressure Difference between True and False Lumen

In order to calculate pressure difference between the true and false lumen, eight cross-sectional planes were selected along the centrelines of the dissected aorta, with P1 being 2 cm from the origin of LSCA and P2 – P8 being evenly spaced below P1 with an interval of 3 cm. Pressure variations over a cardiac cycle at the selected cross-sectional plane are shown in Figure 6.6 for two representative cases, one from each group. It can be seen that pressures in the TL and FL were almost identical for the patient in group 1. However, notable differences between TL and FL pressures can be seen for the patient in group 2 especially in the proximal region where pressure was higher in the TL than FL during systole. The evaluated TL and FL pressures were further analysed by examining the pressure difference (P_{TL} - P_{FL}), and results for all the cases are shown in Figure 6.7, where a positive value indicates higher TL pressure while a negative value indicates higher FL pressure. It should be mentioned that fewer cross-sectional planes could be created in 3/8 patients in group 1 due to their short FL. It was clear that pressure differences were much higher for the patients in group 2 than in group 1. The maximum TL and FL pressure differences at all cross-sectional planes were then evaluated and the absolute values ($|P_{TL} - P_{FL}|$) are shown in Figure 6.8 for all the patients. The results clearly indicated that the maximum pressure difference was much higher for group 2.

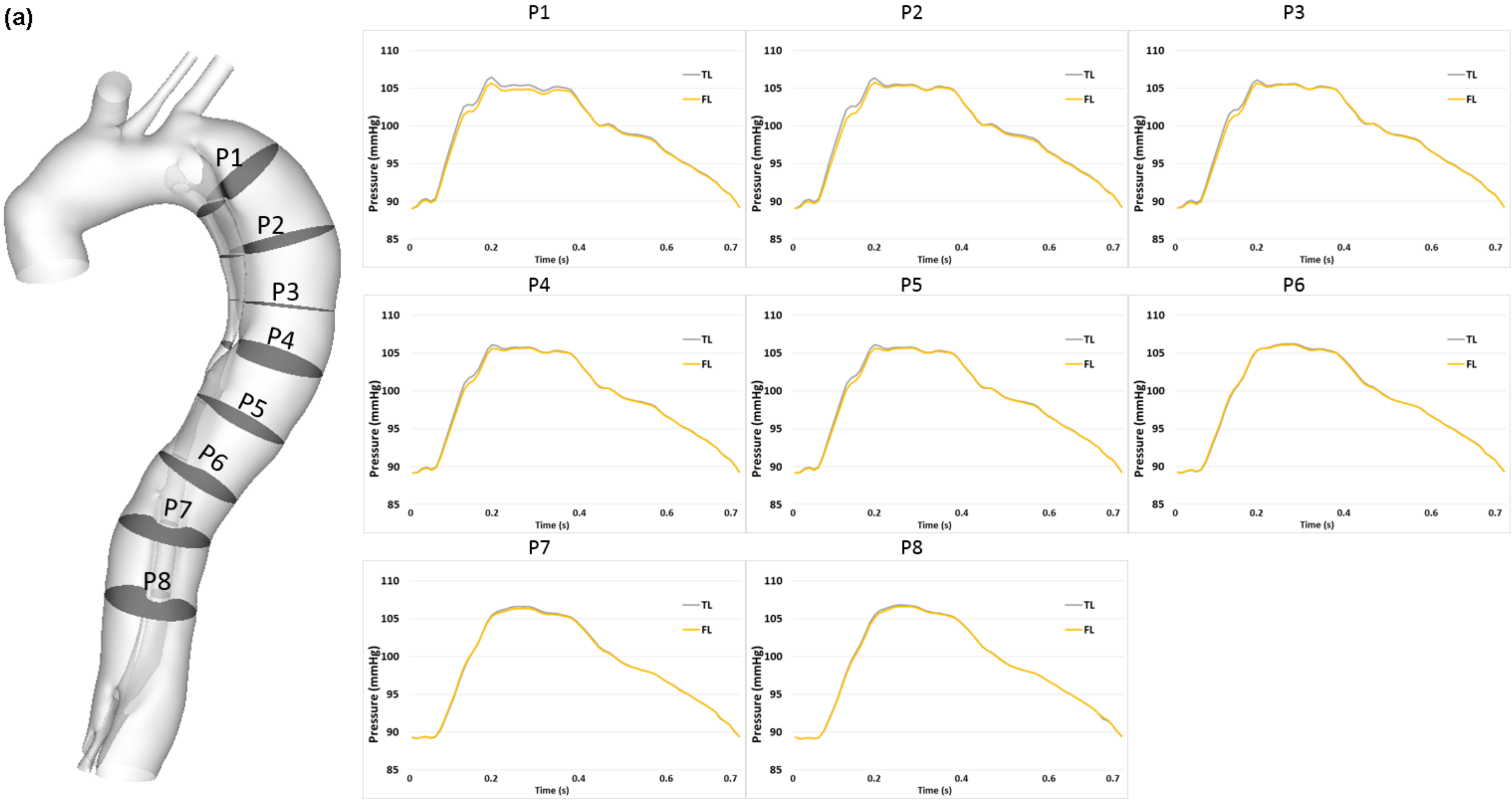
(a)
P1
P2
P3
P4
P5
P6
P7
P8
P1
P2
P3
P4
P5
P6
P7
P8
Pressure (mmHg)
110
105
100
95
90
85
Time (s)
0
0.2
0.4
0.6
0.7
TL
FL

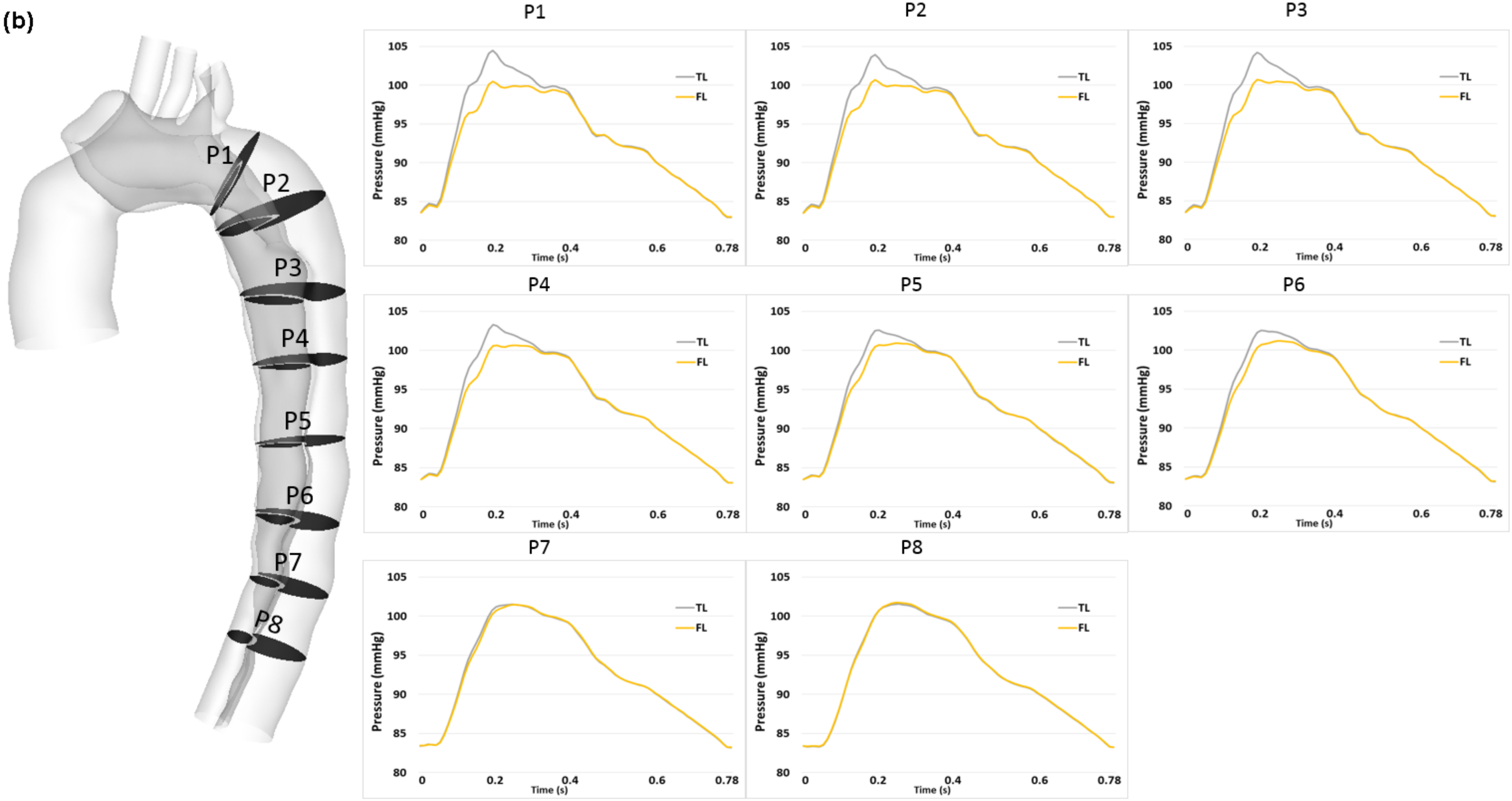

Figure 6.6. Pressure variations in the TL and FL along the dissected aorta for two selected cases: patient G1#9 from group 1 (a) and patient G2#4 from group 2 (b). P1-P8 refer to eight cross-sectional planes along the centrelines of the dissected aorta. P1 is 2 cm distal from the origin of LSCA and P2-P8 are evenly spaced below P1 with an interval of 3 cm.

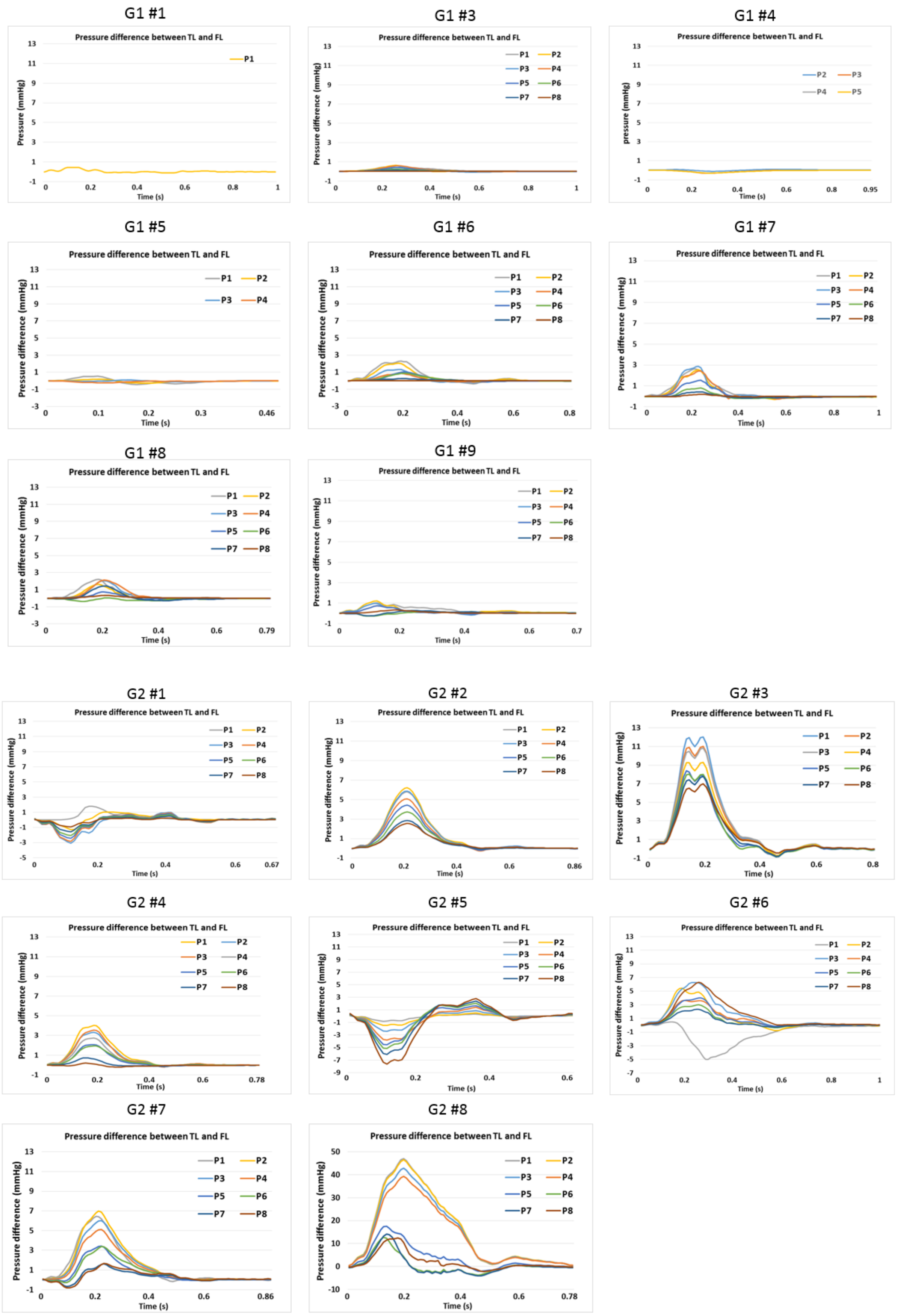

Figure 6.7. Pressure difference between the true and false lumen (P_{TL} - P_{FL}) at the selected cross-sectional planes along the aorta.

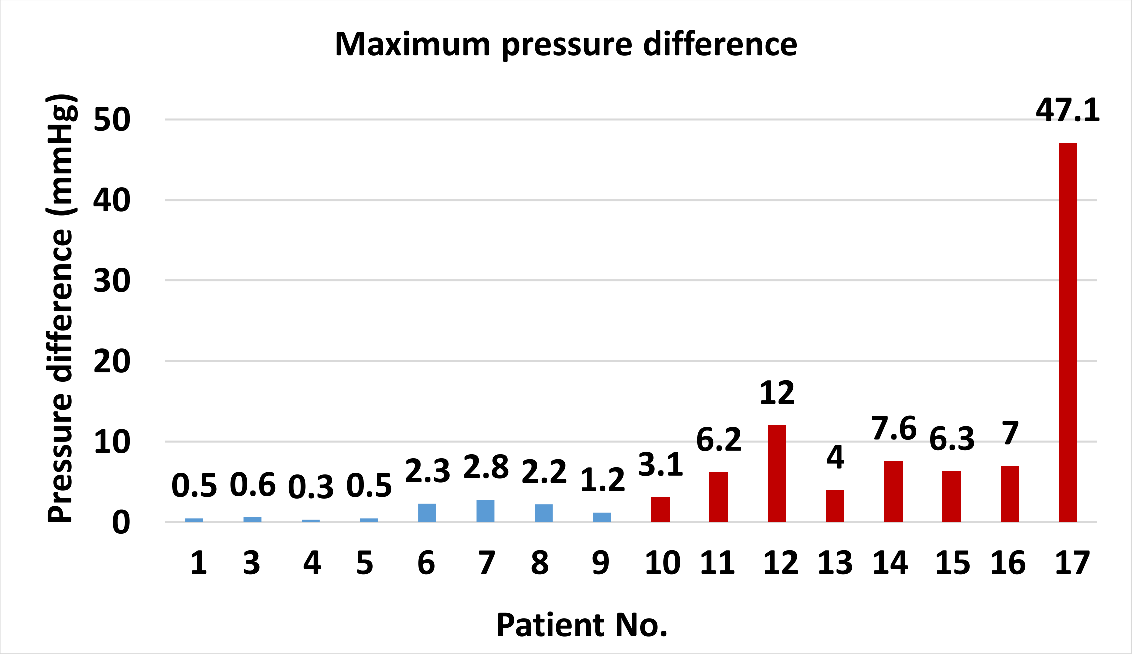

Figure 6.8. The maximum pressure difference between the true and false lumens (absolute values) for all the patients. Group 1 (blue), group 2 (red).

6.3.5 Statistical Analysis

Statistical analyses of the evaluated geometric and haemodynamic parameters were performed, and the results are summarised in Table 6.2. The number of re-entry tears was the only geometric parameter that showed statistically significant difference between the two groups ($p = 0.02$), with patients in the stable group having far more re-entry tears than patients in the unstable group. The maximum aorta diameter was larger for the unstable group but the difference was not statistically significant. In terms of haemodynamic parameters, the maximum TL and FL pressure difference was found to be significantly higher ($p = 0.001$) for patients in group 2. No significant differences between the two groups were found in the other morphological and haemodynamic parameters examined.

6.3.6 Turbulence Intensity

The turbulence intensity, also referred to as turbulence level, is defined as

$$Tu = \frac{u'}{U} \tag{6.2}$$

where U is the mean velocity and u' is the root-mean-square of the turbulent velocity fluctuations that can be expressed as:

$$u' = \sqrt{\frac{1}{3}\left(u_x'^2 + u_y'^2 + u_z'^2\right)} = \sqrt{\frac{2}{3}k} \tag{6.3}$$

where k is the turbulence kinetic energy and therefore the turbulence intensity can be expressed as:

$$Tu = \frac{\sqrt{\frac{2}{3}k}}{U} \tag{6.4}$$

Table 6.2. Summary of geometric and haemodynamic parameters for the two groups with stable aortic diameters (Group 1) and progressive aortic dilatation (Group 2).

	Group 1 (Stable)	**Group 2 (Unstable)**	**Mann-Whitney U test**
Geometric Parameters	**Mean ± SD**	**Mean ± SD**	**Mean ± SD**
Primary tear size			
Area (mm^2)	**237.5 ± 212.2**	**173.7 ± 183.3**	**0.6**
Number of re-entry tears	**6 ± 5**	**2 ± 1**	**0.02**
Distance between primary tear to LSCA (mm)	**30.6 ± 10.3**	**37.3 ± 18.7**	**0.8**
Max. distance between tears (mm)	**89.3 ± 34.7**	**106.3 ± 107.9**	**0.3**
Maximum aortic diameter (mm)	**39.8 ± 5.5**	**44.9 ± 3.9**	**0.07**
Inlet diameter (d_1) (mm)	**32.6 ± 3.3**	**31.9 ± 4.2**	**0.6**
Arch diameter (d_2) (mm)	**32.4 ± 6.8**	**33.8 ± 5.1**	**0.8**
Curvature ratio (d_1/d_2)	**1.1 ± 0.3**	**1.0 ± 0.2**	**0.6**
Tortuosity			
Entire aorta (inlet to diaphragm)	**2.2 ± 0.3**	**2.4 ± 0.4**	**0.6**
Ascending aorta (inlet to LSCA)	**1.2 ± 0.1**	**1.2 ± 0.1**	**0.2**
Descending aorta (LSCA to diaphragm)	**1.2 ± 0.1**	**1.3 ± 0.2**	**0.4**
Volume ratio of FL/TL	**3.7 ± 4.3**	**3.4 ± 1.7**	**0.14**
Haemodynamic Parameters			
Flow into FL (%)	**39.8 ± 26.5**	**30.9 ± 25.5**	**0.5**
Max. TAWSS (Pa)	**13.4 ± 7.3**	**24 ± 12.3**	**0.07**
Max. pressure difference (mmHg)	**1.3 ± 1**	**11.7 ± 14.6**	**0.001**

Iso-surfaces of the turbulence intensity (Tu) levels during peak and mid-systolic deceleration in patient G2#6 are illustrated in Figure 6.9. It should be noted that the intensity levels presented here were based on instantaneous local velocities rather than the mean values in order to portray realistic levels. The red and blue iso-surfaces in the figure represent different values of Tu. Since the turbulence intensity is proportional to the kinetic energy (k) and inversely proportional to the velocity, the maximum Tu values were found during mid-systolic deceleration when k had high values but the velocity was decelerating. The Tu levels of approximately 8% were found in the entire descending aorta during mid-systolic deceleration, while very high turbulence intensity (>50%) were observed at both peak systole and mid-systolic deceleration phases in the proximal descending aorta. About 8% turbulence intensity was also found in part of the ascending aorta and in the proximal descending TL.

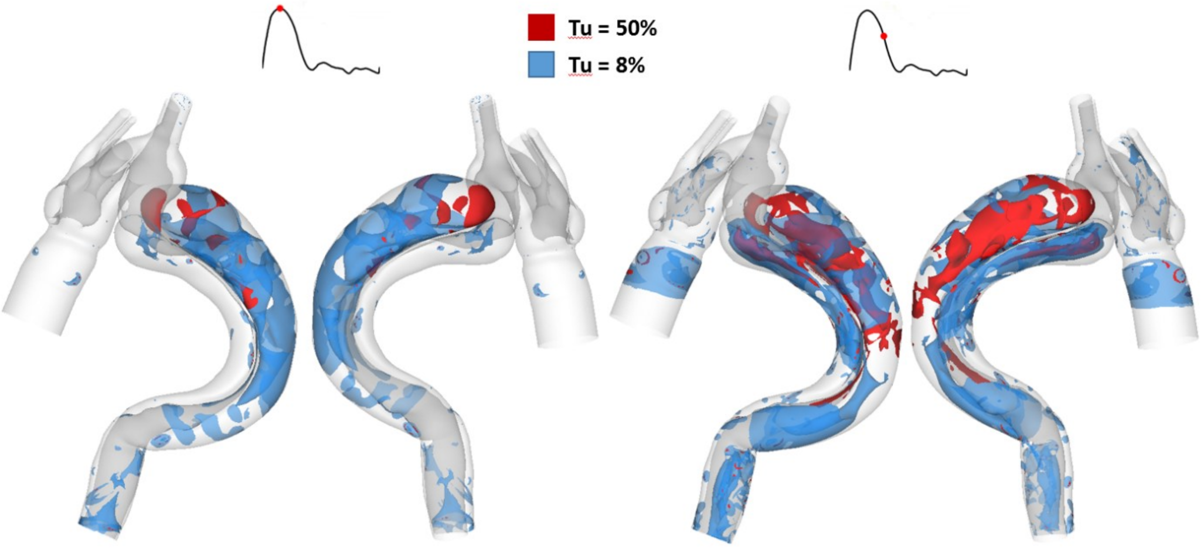

Figure 6.9. Turbulence intensity (Tu) iso-surfaces in patient G2#6 at peak systole (left) and mid-systolic deceleration phase (right). Tu levels of approximately 8% are shown in blue while much higher Tu levels of approximately 50% are displayed in red.

6.4 Discussion

TAAD is a life-threatening cardiovascular disease that usually requires urgent open surgery since the mortality rate of untreated patients is about 50% within the first 48 hours (Anagnostopoulos et al. 1972). The standard surgical approach for TAAD is supra-commissural replacement of the ascending aorta with synthetic tube grafts (Guilmet et al. 1979). A known problem with this procedure is that the residual aorta may still contain dissected segments, which would increase the risk of late adverse events such as progressive aneurysmal dilatation and rupture (Halstead et al. 2007; Marui et al. 1999; Onitsuka et al. 2004; Sueyoshi et al. 2004). With a persistent patent FL, 20% - 50% of patients were reported to die at 5 years and 40% - 70% at 10 years (Bernard et al. 2001; Gysi et al. 1997; Yu et al. 2004). This study was designed to evaluate blood flow in patient-specific aortas after surgical repair of TAAD, in an attempt to identify haemodynamic features that might predict progressive aortic dilatation. In addition to haemodynamic analysis, morphological features of the dissected aortas were also examined.

The study cohort contained 17 patients (9 stable and 8 unstable), among these one patient (G1#2) had a fully thrombosed FL after surgery, while all the other patients (n=16) maintained a patent FL. Analysis of morphological features indicated that patients with a stable aortic diameter had a significantly larger number of re-entry tears. The influence of the number of re-entry tears on haemodynamic conditions has been reported in previous studies, where the lack of distal tears was found to increase the FL pressure (Karmonik et al. 2011; Tang et al. 2012; Tsai et al. 2008; Wan Ab Naim et al. 2014). Wan Ab Naim et al. (2014) among others, concluded that the presence of extra re-entry tears could reduce the pressure difference between the true and false lumen and thus prevent FL expansion and TL collapse. A clinical study also showed that communications between the TL and FL through multiple distal re-entry tears might help prevent TL collapse and should therefore be considered as a positive prognostic indicator (Quint et al. 2003).

Previous studies on TBAD showed that larger entry tears were correlated with higher FL flow (Cheng et al. 2013, 2015), which could lead to rapid aneurysmal expansion (Shang et al. 2015). However, neither entry tear size nor FL flow was significantly different between the two groups in this study. Aortic geometries included in the present study are more complex than those reported in previous TBAD models, as most of the entry tears were located in the ascending aorta or arch rather than distal to the LSCA. Therefore, the amount of flow entering the FL would depend not only on the entry tear size but also its orientation relative to the flow direction. Moreover, it has been reported that patients presented with multiple distal tears have increased FL flow (Dillon-Murphy et al. 2016). This may explain why some patients with very small entry tears but multiple communication tears were found to have relatively high flow in the FL.

Another morphological parameter of interest is the maximum aortic diameter. Although the results showed that the maximum aortic diameter was larger in patients with progressive aortic dilatation than in patients with a stable aortic diameter, the evidence was weak based on the analysis of this relatively small cohort. In fact, clinicians mainly rely on the maximum aortic diameter to predict aortic dilatation and its risk of rupture in the current practice. However, previous studies on aortic dissection challenged the reliability of using this criterion and suggested that maximum diameter alone was not a reliable predictor of late complications (Bernard et al. 2001; Neri et al. 2005; Rudenick et al. 2010). For this reason, it would be worth considering factors in addition to sizing criteria, e.g. haemodynamics related parameters when assessing the risk of aortic dilatation in patients with TAAD. Blood flow was found to be highly disturbed in all dissected models with varying extent of flow recirculation in both true and false lumens, especially in regions surrounding the tears. Large recirculation regions have been associated with thrombus formation, while partial thrombosis in the FL might occlude distal tears, impede outflow and therefore increase the risk of death from further aortic dilatation and rupture (Tsai et al. 2007). Another potentially important feature is turbulence, which is likely to occur in the flow jet through a tear, where the peak Reynolds number can exceed 8200 (Cheng et al. 2010). Turbulent flow within the aneurysm has been reported to cause extra stresses on the aneurysmal wall, increasing the rate of wall dilatation (Berguer et al. 2006; Khanafer et al. 2007). In order to capture potential turbulent flow in the post-surgery TAAD models, the SST-Tran model was adopted which allowed turbulence intensities to be evaluated. An example is given in Figure 6.9, showing high turbulence intensities (>50%).

Areas of high wall shear stress stimulate the endothelial cells to produce plasmin, nitric oxide and transforming growth factor-β causing matrix breakdown by expression of plasmin, matrix-metalloproteinases and smooth muscle cells apoptosis (Lehoux et al. 2006; Li et al. 2005; Slagger et al. 2005). This has been associated with endothelial damage and degenerative lesions of the dissected wall, leading to wall weakening and eventual rupture (Ekaterinaris et al. 2006). Regions of elevated TAWSS were observed in the opposing FL wall as a result of direct impingement of jet flow when passing through the tear. Elevated TAWSS in the false lumen has been reported to cause wall weakening and subsequent increase in luminal diameter (Rudenick et al. 2010). In most of the cases, the maximum TAWSS was found along the edge of the primary tear, which could lead to further degeneration and erosion in this area, perhaps indicating the vulnerability of this region to further increase in tear size. Results obtained in this study showed that patients with unstable aneurysmal expansion had higher maximum TAWSS on the aortic wall although this finding was not statistically significant. It was noted that two outliers in group 1 had relative high maximum TAWSS due to the existence of very small entry tears. Small tears have been reported to result in higher tear velocities (Rudenick et al. 2013) and therefore increased WSS.

Pressure difference between the true and false lumen is a key factor in driving the deformation of intimal flap. Previous small case series also reported that higher pressure difference was associated with further aneurysmal dilatation in type B dissections (Cheng et al. 2015; Tse et al. 2011), but no similar studies on TAAD could be found in the literature. Results in this study demonstrated that patients with progressive aortic dilatation following TAAD repair had significantly higher luminal pressure difference compared to the stable group. Although the sample size is relatively small (n=17), this is the first time such a correlation has been identified for TAAD. It is also of interest to note that pressure difference between the true and false lumen is influenced by the number and size of tears (Dillon-Murphy et al. 2016; Tsai et al. 2008). As mentioned before, multiple tears along the length of type B aortic dissection could lead to an equalisation of pressure between two lumens. In the study carried out by Rudenick et al. (2013) a smaller tear was found to cause a greater luminal pressure difference, whereas larger tears corresponded to equalized true and false lumen pressures. This phenomenon was not observed in the results presented here, for example 2 patients in group 1 (G1#7 and G1#8) with very small entry tears did not present with large pressure imbalance between the true and false lumen. The effect of small entry tears on luminal pressure difference might be counteracted by multiple re-entry tears. In contrast, a large primary entry tear in a patient (G2#5) was associated with a significantly higher pressure difference as flow entering the FL appeared to be unidirectional with no exit to relieve the pressure. As reported in the literature (Zhang et al. 2014), in the case of blind end of the FL, absence of a distal tear or a side branch to shunt pressure from the FL may result in pressure difference between TL and FL.

Limitations of the study

The main limitation of this study is the small sample size that may limit wider applicability of the findings. Further validation of the CFD technique and its ability to predict risk of aortic dilatation post-surgical repair will be required. With regards to the computational model, the rigid wall assumption may miss some complex flow structures caused by expansion and contraction of the vessel wall (Alimohammadi et al. 2015). This assumption can be relaxed by performing a fluid-structure interaction (FSI) simulation, which couples the flow model with a compliant wall model. However, building a compliant wall model of aortic dissection requires information on wall thickness and material properties which are difficult to measure *in vivo*. Additionally, FSI simulations are computationally expensive, which will limit its use in comparative studies involving a large cohort of patients. Even with the fluid model alone, the computational time was still considerable with each simulation taking approximately 5-7 days using a workstation (Intel i7 processer, 32GB RAM). Future refinements of the modelling approach should address this issue. Finally, patient-specific pressure data were not available due to retrospective nature of the study, which may influence the patient specificity of the predicted pressure values but should not affect the evaluated pressure difference. It is also worth mentioning that flow divisions among the arch vessels can vary from patient to patient, and with physical and mental activities. In this study, however, a fixed flow distribution of 21% (Pirola et al. 2019) was assumed to exit through the arch vessels of all the simulated models due to the lack of patient-specific data. This assumption was reasonable for comparative studies as it would not cause any other confounding factors. Nevertheless, patient-specific data would be desirable if they are available for future studies.

6.5 Summary

This study suggests that large pressure difference between the true and false lumen may be an important predictor of progressive aortic dilatation following surgical repair of TAAD, whereas the presence of multiple re-entry tears along the length of the dissection might help equalize the true and false lumen pressure, thereby reducing the risk for unstable aortic dilatation. Although not statistically significant between the two groups, larger maximum aortic diameter as well as higher maximum TAWSS on the aortic wall might also be related to rapid aneurysmal expansion. These findings are promising and point to a potential role of haemodynamic factors in predicting the risk of progressive aortic dilatation following TAAD repair. Further large cohort studies are warranted to validate these findings.

Chapter 7

Biomechanical Analysis of Type A Aortic Dissection after Surgical Repair and Fluid-Solid Interaction Simulation

7.1 Introduction

In Chapter 6, detailed haemodynamic features in surgically repaired TAADs were evaluated and it was found that luminal pressure imbalance, as well as higher maximum TAWSS might be associated with progressive aortic dilatation. On the other hand, biomechanical factors also play an important role in aortic remodelling, such that elevated wall stress has been reported to lead to the development of aneurysm or dissection (Nathan et al. 2011). Based on fluid-solid interaction (FSI) simulation of a patient-specific thoracic aortic aneurysm, Tan et al. (2009) suggested that the maximum wall stress at the inner wall of the aneurysm might contribute to further dilation, weakening of the wall, and its risk for rupture. In fact, as the aorta expands, the aortic wall loses elasticity, and stresses in the dilated region would increase significantly (Thubrikar et al. 1999). If the local stresses exceed the mechanical strength of the material, rupture may occur. In this chapter, finite element analysis (FEA) was carried out to evaluate biomechanical properties of patient-specific TAAD models described in the preceding chapter. Due to the time constraint, wall models were built and analysed for 4 selected cases only (2 from each group). Comparisons of results were made between the two patients in the stable group (G1#3 & G1#9) and two with progressive aortic dilatation (G2#4 & G2#5), in order to examine differences and to identify potential biomechanical predictors of late aneurysmal dilatation.

Blood flow simulation followed by structural analysis describe the haemodynamic and biomechanical conditions of the dissected aorta, separately. In reality, the aorta expands and contracts in response to the pulsation of blood pressure, necessitating the use of fluid- structure interaction (FSI) to account for the dynamic effects of moving wall on blood flow and the respective effects of blood flow on wall motion. Tan et al. (2009) found that velocity profiles obtained from FSI simulations were in better agreement with *in vivo* MRI data than those from the rigid wall flow model alone. FSI simulations have also been performed on type B aortic dissections, and the obtained results were compared with those from rigid wall models (Alimohammadi et al. 2015; Qiao et al. 2019). These studies demonstrated that although spatial distributions of TAWSS obtained with FSI and rigid wall models had similar trend, there were marked differences in the predicted OSI. To gain more detailed knowledge of how compliance may influence intraluminal haemodynamics, a preliminary FSI analysis was performed on one of the TAAD models (G1#5) described in the previous chapter. The obtained results are compared with those from the rigid wall model of the same patient.

7.2 Methodology

7.2.1 Geometry Reconstruction and Mesh Generation

Wall models were built for 5 of the 17 post-surgical type A dissection geometries described in Chapter 6 (G1#3, G1#5, G1#9, G2#4 and G2#5), 4 of which were for FEA and another one was for FSI (G1#5). In terms of FEA, 2 patients with stable aortic diameters (G1#3 & G1#9) were randomly selected to be compared with 2 patients with unstable aortic diameters (G2#4 & G2#5). FSI simulation was performed on a patient with a stable aortic diameter (G1#5) whose FL merged with TL in the mid-thoracic aorta. The shorter FL and intimal flap reduced the computational complexity and time needed for the computationally intense FSI simulation. The inner and outer wall surfaces were created separately to construct the solid domain including the intimal flap. The 3-D fluid domain reconstructed in the preceding chapter was used as the inner wall surface, while the outer wall surface was created by uniformly extruding the undissected equivalent of the inner wall by 1.4 mm for the aorta (Van Puyvelde et al. 2016) and by 0.65 mm for the Dacron graft (Nagano et al. 2007), as shown in Figure 7.1. Moreover, for the wall models built for FEA, 5-6 pairs of intercostal artery branches were added along the descending aorta to restrict any possible swing of the model. All geometries were then exported into ANSYS ICEM CFD (ANSYS, Canonsburg, PA, US) to generate computational mesh for the solid domain. For each geometry, the wall model (solid domain) was discretised into unstructured tetrahedral meshes comprising approximately 2.8 and 0.3 million elements for the aorta and graft, respectively, as shown in Figure 7.2. For the FSI simulation, the fluid domain of patient G1#5 was meshed with a tetrahedral core and 10 prismatic layers at the wall comprising of around 4 million elements (Figure 7.3).

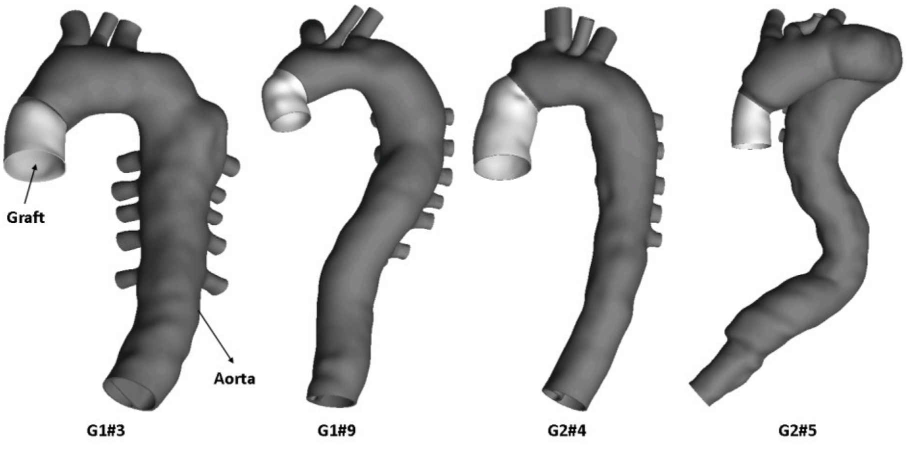

Figure 7.1. Reconstructed patient-specific models for the four cases selected for FEA. Graft (light grey) and the aorta (dark grey) are indicated by arrows.

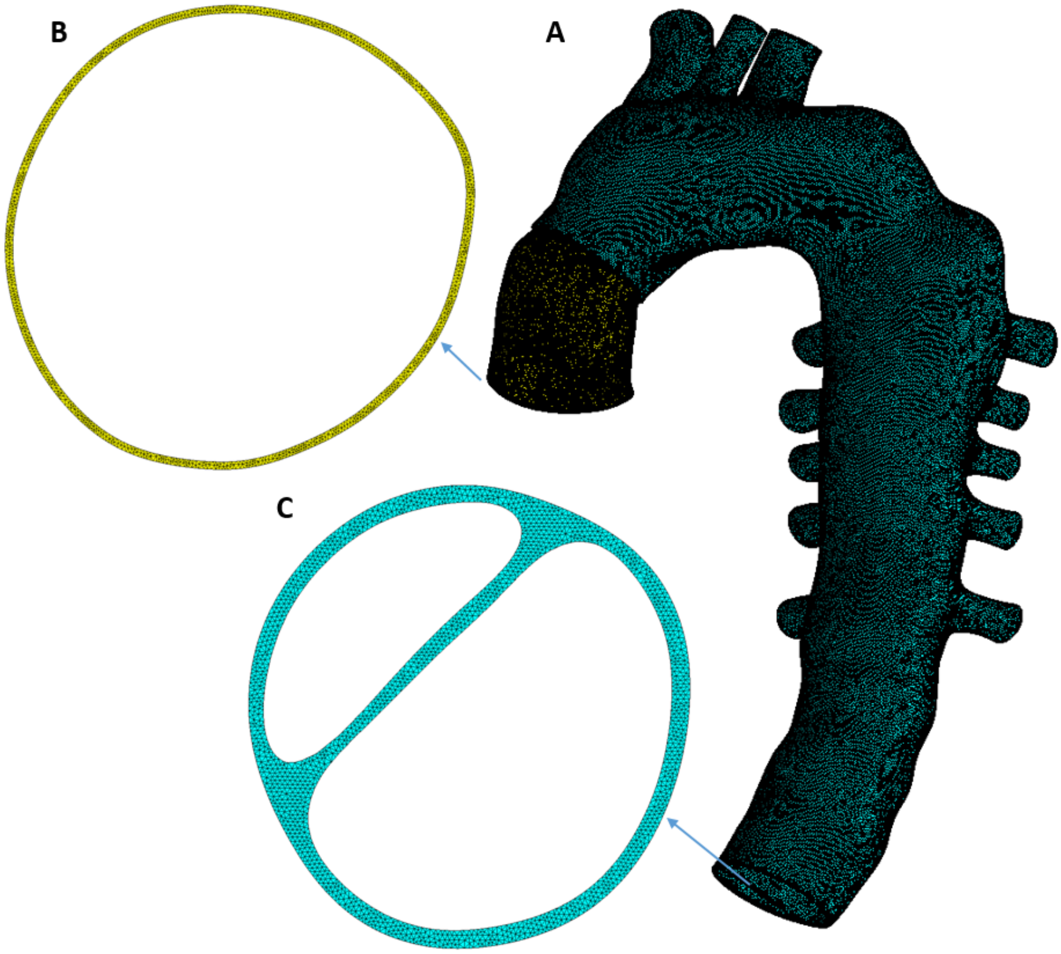

Figure 7.2. Tetrahedral mesh elements for the dissected wall model (solid domain) are shown for (A) 3D geometry, (B) inlet, and (C) Outlet.

7.2.2 Finite Element Modelling

The mechanical behaviour of the wall follows its constitutive equation, which describes the intrinsic behaviour of a material under loading by relating the stress to the strain. A strain measures deformation representing the displacement between particles in the body relative to a reference length. Hooke's law is the most basic constitutive relation, describing the behaviour of a linear elastic material as:

$$[\sigma] = [D][\varepsilon] \tag{7.1}$$

where $[\sigma]$ is the stress tensor, $[\varepsilon]$ is the total strain vector, and $[D]$ is the elastic stiffness matrix represented by the Young's modulus E and the Poisson's ratio ν. E is the stiffness of a material that measures a material's ability to resist stretch, while ν is defined as the negative of the ratio of transverse to axial strain. Although linear elastic models based on simplified measures of the Young's modulus and the Poisson's ratio may give a good approximation in some cases, they do not capture the non-linear behaviour of the aortic wall.

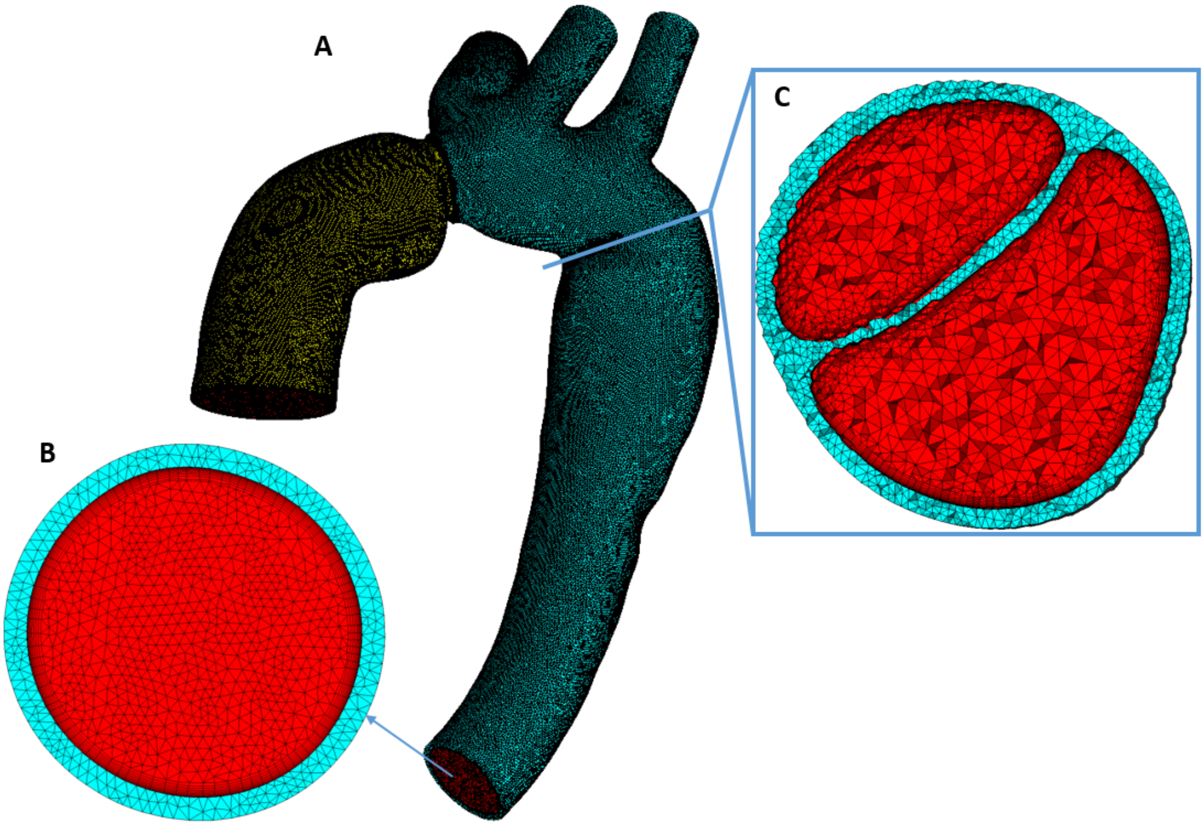

Figure 7.3. Detailed mesh elements are shown for (A) the FSI model, (B) outlet cross-sectional plane, and (C) cut plane. It can be seen clearly from (B) and (C) that the solid domain (light blue) was discretised into tetrahedral elements, while the fluid domain (red) was meshed with a tetrahedral core and prismatic layers at the wall.

In this study, a linear elastic model was used to describe the graft material, assuming it to be incompressible, homogenous and isotropic. The Dacron graft used to replace the ascending aorta is made of polyethylene terephthalate (PET), with a reported Poisson's ratio of 0.3 and Young's modulus of 7800 kPa (Weltert et al. 2009). For the dissected aortic wall and intimal flap, a non-linear, hyperplastic material model was adopted. Based on a finite strain constitutive model proposed by Raghavan and Vorp for abdominal aortic aneurysms (AAA) (Raghavan and Vorp 2000), the stress and stretch along either longitudinal or circumferential direction can be described by the following equation:

$$T = [2\alpha + 4\beta(\lambda^2 + 2\lambda^{-1} - 3)][\lambda^2 - \lambda^{-1}] \qquad (7.2)$$

where T is the stress calculated as the applied force normalized by the deformed cross-sectional area, and $\lambda = \varepsilon + 1$ is the stretch. α and β are model parameters representing the mechanical properties of the AAA wall. Additionally, Raghavan and Vorp found no significant difference in α or β values between the longitudinal and circumferential samples, supporting their combination into a single equation with mean values of 174 kPa and 1881 kPa for α and β, respectively. Using ANSYS Workbench (ANSYS, Canonsburg, PA, US), the experimental $T - \lambda$ curve derived from equation (7.2) was fitted to a well-defined nonlinear five-parameter Mooney-Rivlin material model expressed using the strain energy density function as:

$$W = c_{10}(I_1 - 3) + c_{01}(I_2 - 3) + c_{20}(I_2 - 3)^2 + c_{11}(I_1 - 3)(I_2 - 3) + c_{02}(I_2 - 3)^2 \qquad (7.3)$$

where W is the strain energy, and I_1, I_2 are the first and second invariants of the strain tensor respectively. c_{10}, c_{01}, c_{20}, c_{11}, and c_{02} are material constants that describe the deviatoric deformation of the vessel wall and they were calculated by curve-fitting the $T - \lambda$ data. The obtained values are summarised in Table 7.1.

Table 7.1. Calculated constants of the Mooney-Rivlin material model.

c_{10}	c_{01}	c_{20}	c_{11}	c_{02}
0.34 MPa	-0.17 MPa	8.15 MPa	-10.48 MPa	4.26 MPa

The boundary conditions were then applied including nodal surface loads and displacement constraints. A static load corresponding to the patient's pulse pressure was applied perpendicular to the inner surface of each model. Due to the absence of patient-specific pressure data, a typical pulse pressure of 40 mmHg for a healthy subject from the literature was used for all models (Olufsen et al. 2000). Zero-displacement constraints were applied at the model inlet, at the distal ends of the innominate, left common carotid, left subclavian, and all intercostal arteries, as well as in the mid-descending aorta. FEA of the wall models was performed with ANSYS Static Structural solver (ANSYS Inc.).

7.2.3 Fluid-Solid Interaction

As shown in Figure 7.4, for flow analysis, the boundary conditions at the inlet of the TAAD were the same as in the fluid-only simulation where a scaled patient-specific flow waveform was imposed along with the assumption of a flat velocity profile. It was assumed that a total of 21% of inlet flow would exit through the three arch vessels (Pirola et al. 2019), where the flow division was calculated based on their cross-sectional areas (Zamir et al. 1992). A 3-EWM was imposed at each outlet. With regards to structural analysis, displacement constraints were applied at the inlet and at all outlets. An external pressure that equals to the diastolic pressure was applied at the outer surface (Alimohammadi et al. 2015), based on the assumption that the reconstructed TAAD geometry was in its diastolic configuration. Additional constraint was applied on the inner wall surface by specifying an elastic support to increase its stiffness, so as to avoid highly distorted mesh during the simulation.

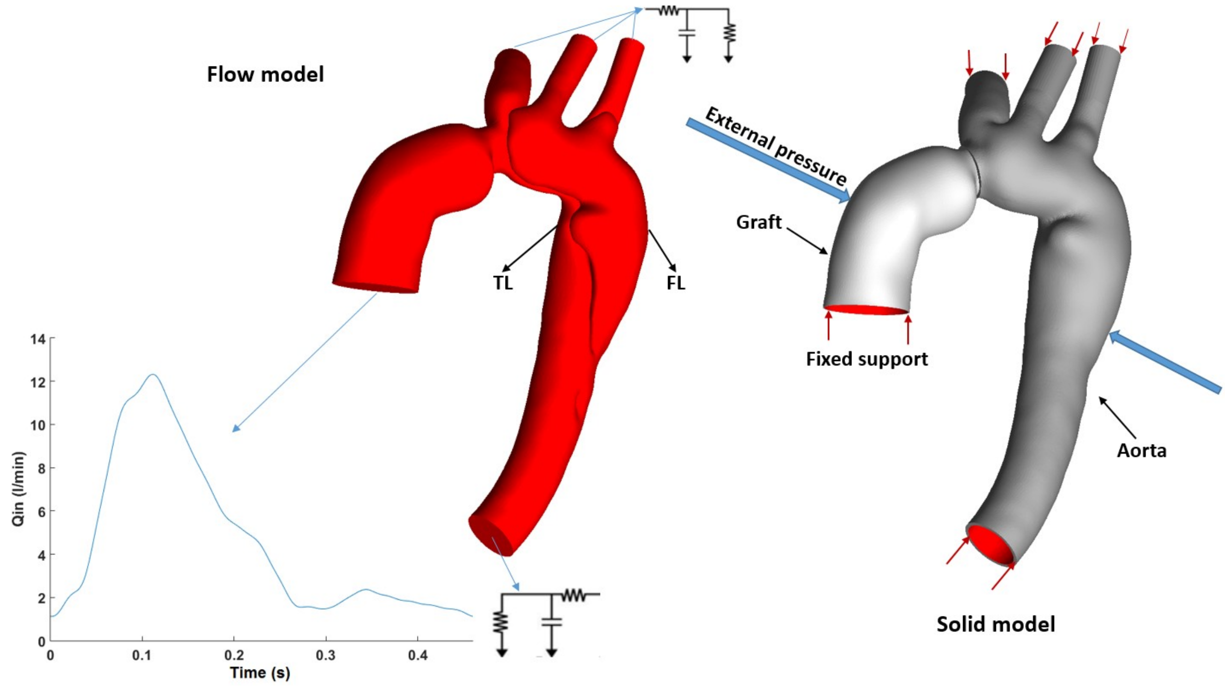

Figure 7.4. Schematic of the computational model employed for FSI simulation. For flow analysis, patient-specific flow waveform was prescribed at the inlet, while a 3-EWM was applied at all outlets. For structural analysis, zero-displacement constraints were set at inlet and at all outlets. In addition, an external pressure corresponding to the diastolic pressure was applied on the outer walls to recoil the geometry from its diastolic configuration.

The wall model of patient G1#5 was solved using ANSYS Transient Structure solver, while the pulsatile blood flow was solved using ANSYS CFX solver, with more details described in Chapter 6. The two-way FSI simulation was then performed using ANSYS Multi-field solver (ANSYS, Canonsburg, PA, US), which couples ANSYS Structure and ANSYS CFX through a sequence of multi-field time-steps, consisting of ‘’stagger’’ (or coupling) iterations. The outer surface of the lumen in the fluid domain corresponding to the inner surface of the structural domain (as shown in red in Figure 7.4) was selected as an interface where data exchange occurred at every time-step. ANSYS CFX provided the fluid-induced wall forces to the structural domain, and ANSYS Structure sent back the total mesh displacement information. Within each multi-field time-step, the iterations were repeated until a maximum number of 10 stagger iterations was reached or until the data transferred between solvers and all field equations were converged. In the fluid model, the maximum RMS residual of 10^{-5} was specified and approximately 15-100 iterations were needed to reach convergence at each time-step. In the structural model, the maximum RMS residual was set as 10^{-3} with a total of 15 iterations. A coupled time-step of 0.005 s was specified and three cardiac cycles were simulated to reach a periodic solution.

7.3 Results

7.3.1 Comparison of Biomechanical Properties of Different Wall Models

Displacement: Predicted wall displacement patterns are shown in Figure 7.5. In all cases, the aorta segment replaced by the synthetic graft was static with almost zero displacement, whereas noticeable displacements could be observed throughout the aorta. High displacement values (>3.5 mm) are shown in red, which were located sporadically around the aortic arch and in the proximal descending aorta of patients G1#3 and G1#9, and in slightly extended regions in patient G2#4. Much larger displacements with values up to 5.2 mm were found in patient G2#5, potentially indicating a more significant expansion of the aorta.

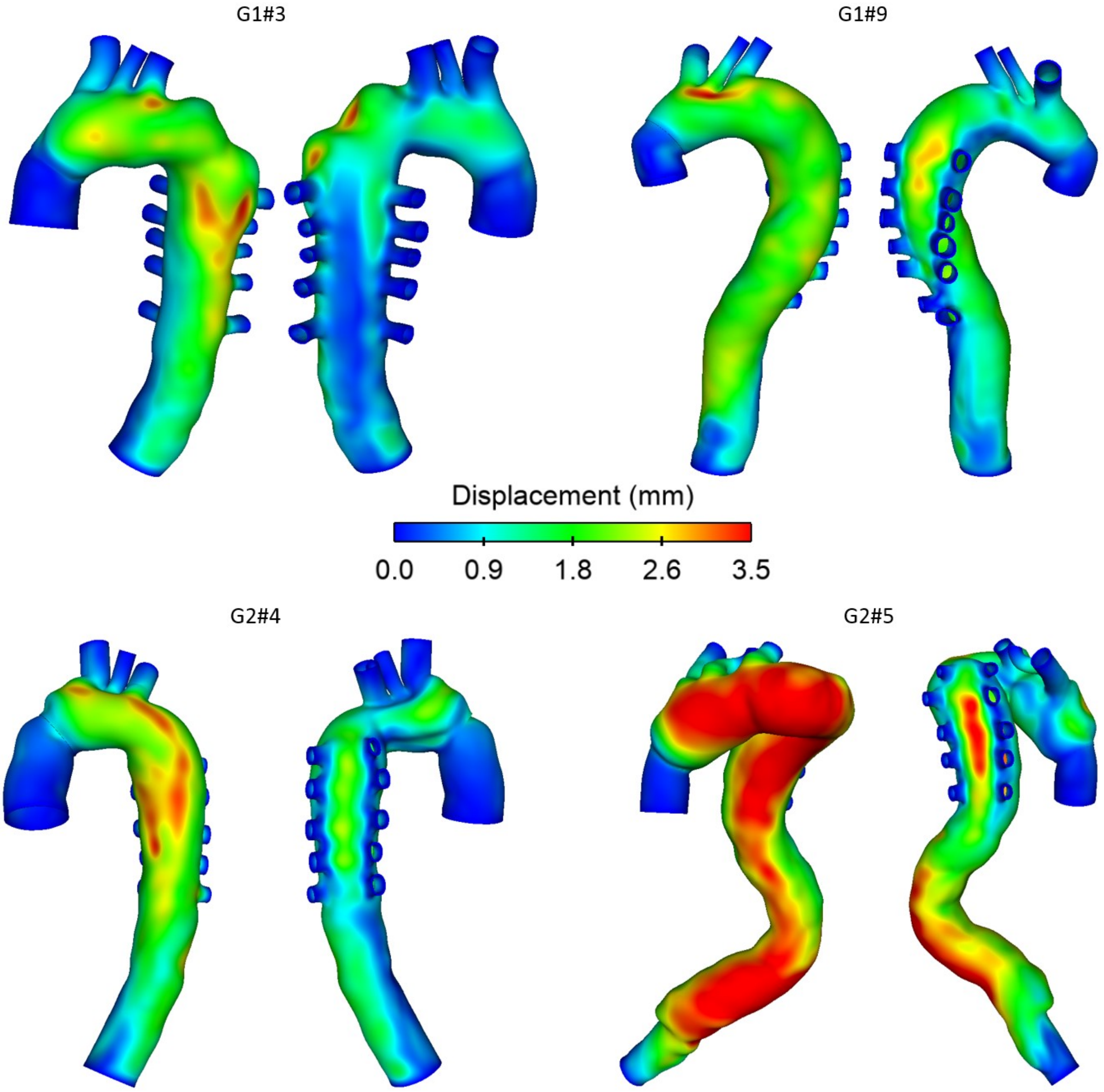

Figure 7.5. Spatial distribution of total displacement in the 4 selected models for FEA. Top: two patients from Group 1; bottom: two patients from Group 2.

Von Mises stress: von Mises stress is an index commonly used to assess the maximum wall stress in the aorta. Spatial distributions of von Mises stress in the four post-surgical TAAD models are shown in Figure 7.6. In all cases, peak stress values were found at the anastomosis between the graft and the aorta (as indicated by the black arrows), which could be attributed to the mismatch in material properties. Away from the graft, high stress values occurred on the edge of tears and at sharp corners, with the maximum values indicated in Figure 7.6. The peak von Mises stress values at the graft-aorta interface were comparable among the 4 models (364 – 394 kPa), but peak stresses away from the graft varied substantially (166 – 350 kPa) with patient G2#5 presenting with the highest value.

7.3.2 Comparison between FSI model and Rigid Wall Model

Flow patterns: Figure 7.7 shows instantaneous velocity streamlines obtained with the FSI simulation and the corresponding rigid-wall model. In general, flow patterns at the systolic and maximum flow deceleration time points were similar, with high velocities through the tears and in regions with narrowed lumen, such as the proximal descending TL. The proximal descending FL, however, was dominated by slow and recirculating flow due to widened luminal area. The merged TL and FL in the mid-descending aorta resulted in a reduced downstream luminal area causing flow acceleration. Flow patterns obtained from the FSI and rigid wall models were qualitatively the same and quantitatively comparable, especially at mid-systolic deceleration. At peak systole, the FSI model produced slightly lower blood velocities in the arch vessels but higher velocities in the distal thoracic aorta compared to the rigid wall model.

Flow exchange between true and false lumen: A more detailed quantitative comparison of volumetric flow rate was made between the rigid and FSI models. Figure 7.8 shows the comparison of volumetric flow rate at the primary entry tear and re-entry tears. Although both models displayed qualitatively similar trends, quantitative differences were observed. Over a cardiac cycle, the percentage of inflow passing through the primary entry tear, re-entry tears 1, 2 and 3 was 13.3%, -12.1%, 0.2% and -1.4%, respectively, in the rigid wall model, and 12.5%, -10.2%, 1%, and -3.3% for the FSI model. It should be noted that a positive value represents flow from the TL to FL, whereas a negative value indicates flow from the FL to TL.

TAWSS: Spatial distributions of TAWSS were compared between the two models, and the results are shown in Figure 7.9. Similar to flow patterns, the FSI and rigid wall models produced qualitatively similar results, with high wall shear stress concentrated in and around the aortic arch and branches, and low wall shear stress in the proximal descending FL. Quantitative comparisons revealed that the FSI model generally predicted slightly lower wall shear stress, with peak TAWSS values being 13 Pa and 13.4 Pa in the FSI model and rigid wall model, respectively.

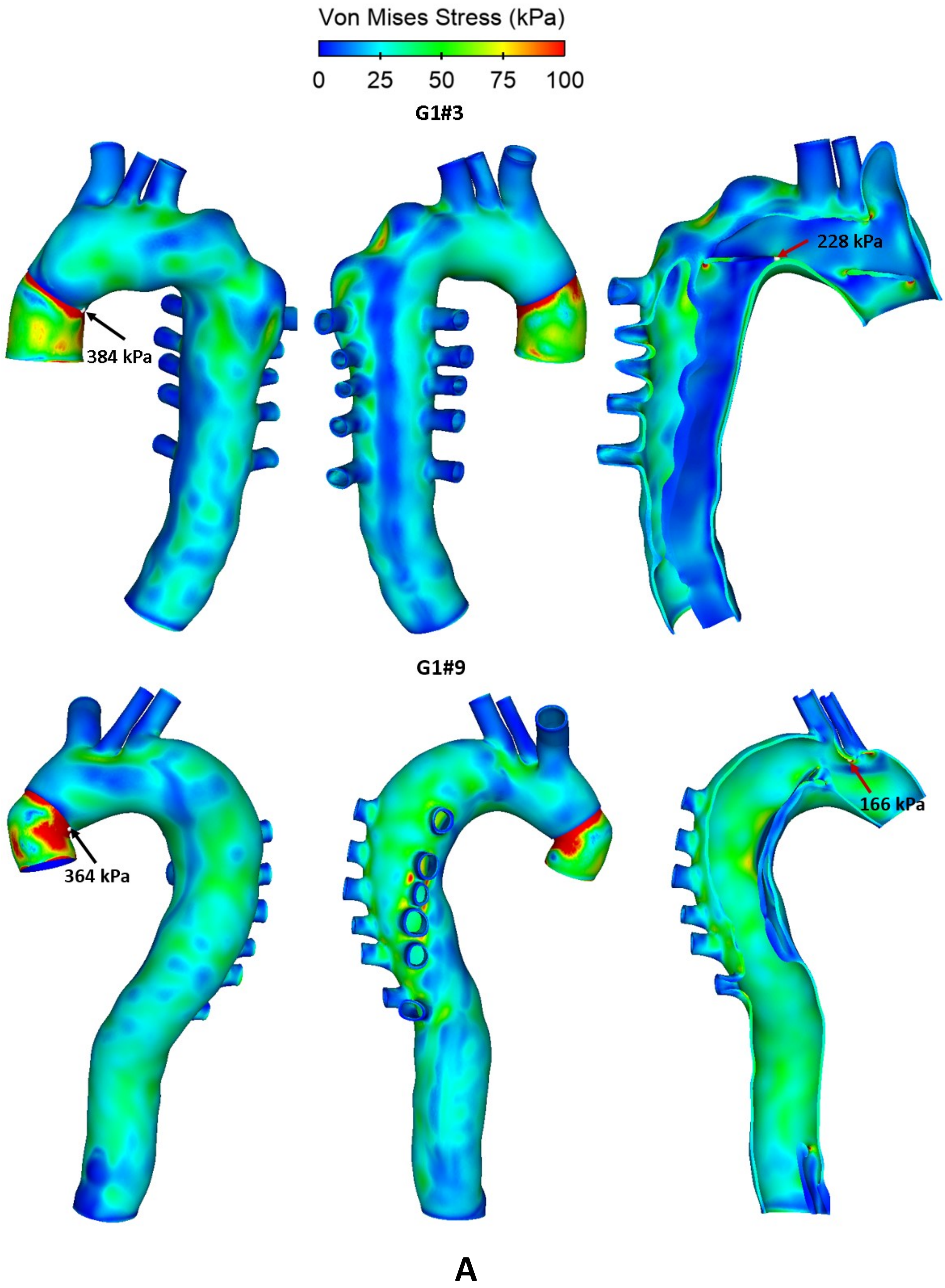
Von Mises Stress (kPa)
0
25
50
75
100
G1#3
384 kPa
228 kPa
G1#9
364 kPa
166 kPa
A

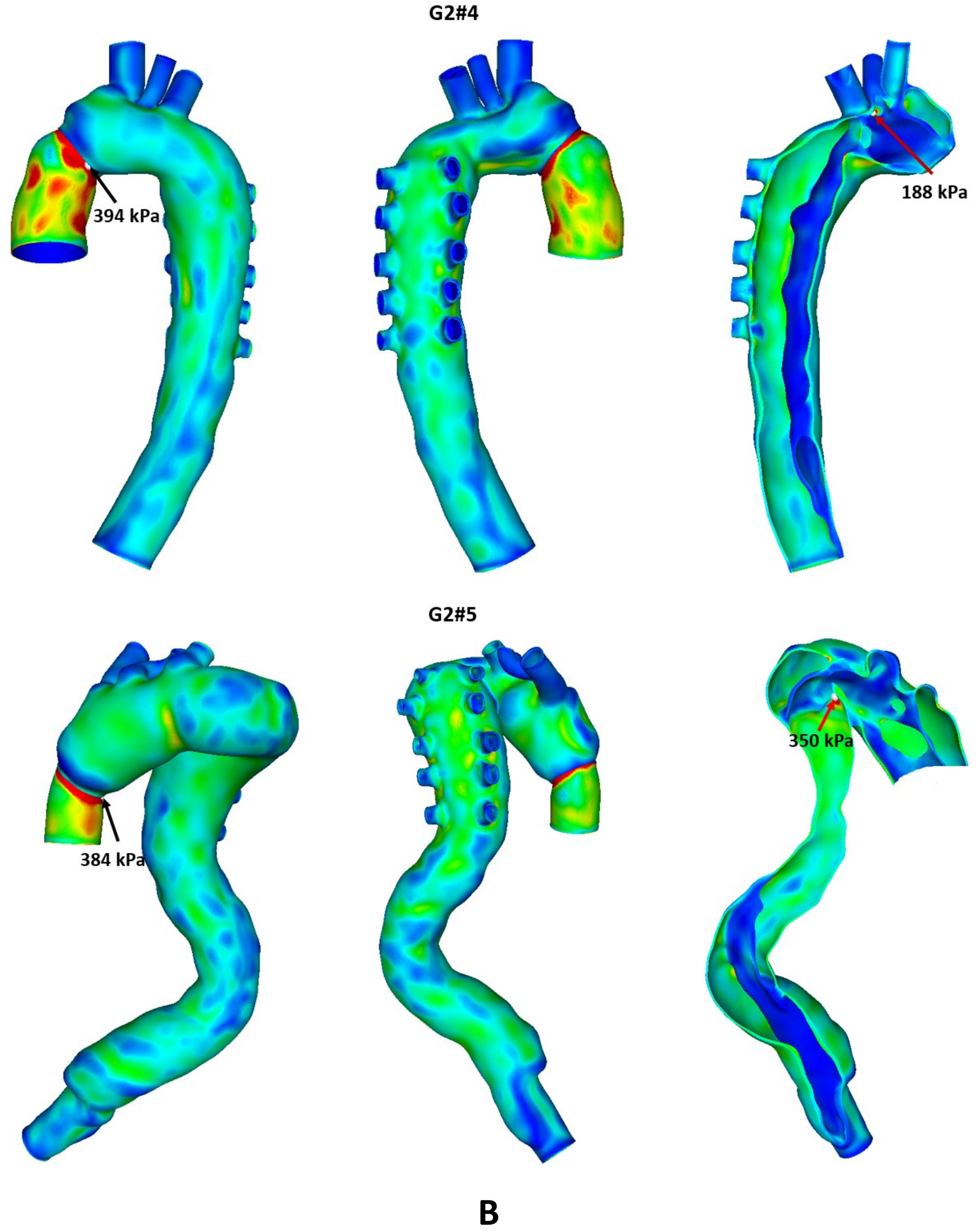

Figure 7.6. Spatial distributions of von Mises stress distributions in all four models. (A) Two patients from Group 1; (B) two patients from Group 2.

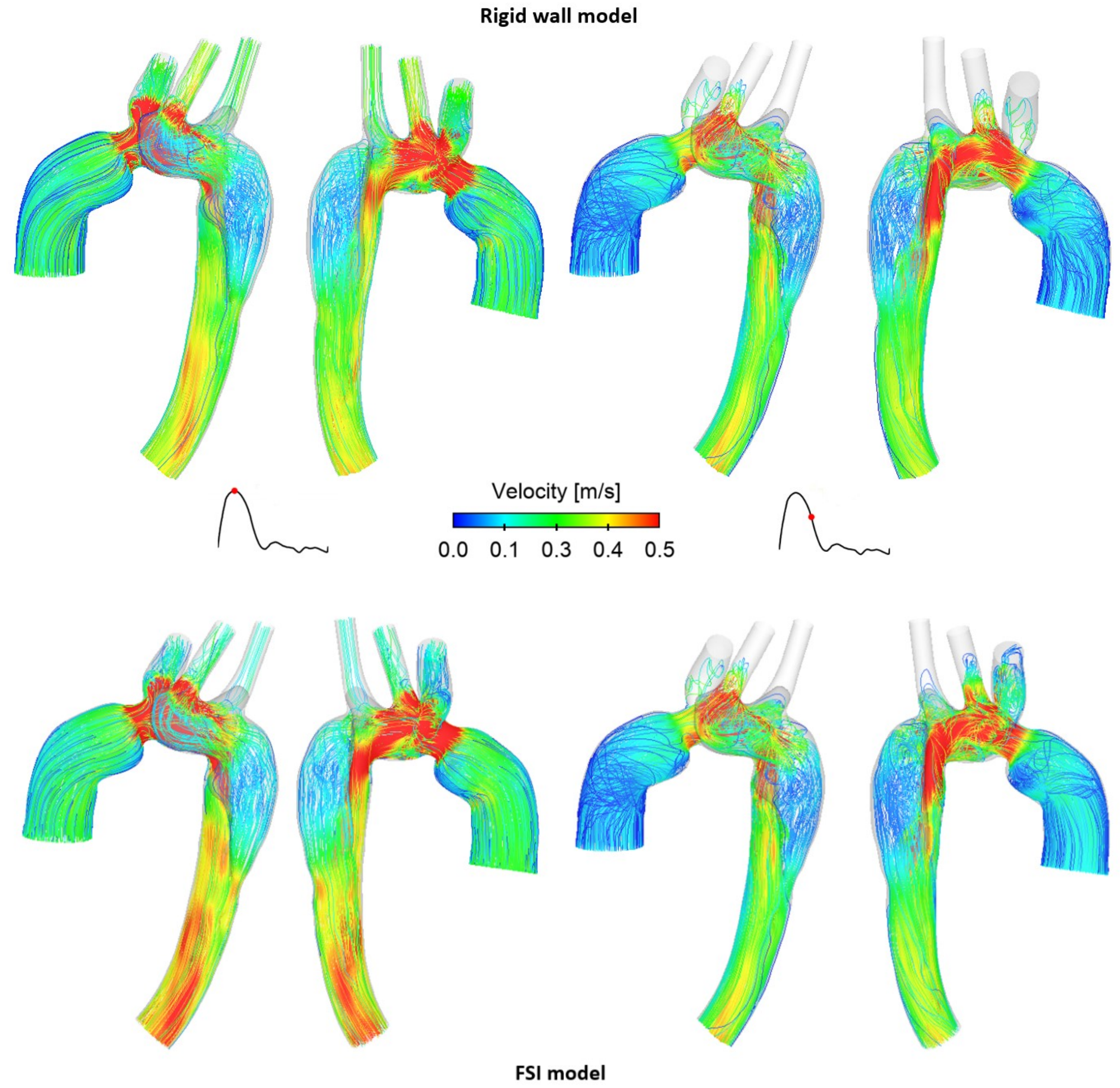

Figure 7.7. Comparison of instantaneous velocity streamlines obtained from the rigid wall model (top) and FSI model (bottom) at peak systole (left) and mid-systolic deceleration (right).

Luminal pressure variations: Figure 7.10 shows the pressure variations in the TL and FL along the dissected aorta obtained from the rigid wall and FSI simulations. Irrespective of the location, incorporating wall compliance resulted in much lower systolic pressure, up to 10 mmHg at peak systole, and slightly higher diastolic pressure in both TL and FL. Nevertheless, the pressure difference between the true and false lumen was close to zero in both the rigid wall and FSI simulations.

7.4 Discussion

Comparison of Biomechanics among the Four Cases

Re-intervention in patients with progressive aortic dilatation after surgical repair of TAAD is typically based on aortic size and the rate of expansion. In Chapter 6, a systematic examination of the flow patterns and haemodynamic factors in dissected aortas was performed, and possible links were identified between certain morphological and haemodynamic parameters and the progression of aneurysmal dilatation. This chapter focuses on examining the role of biomechanical parameters, such as displacement and von Mises stress, in the occurrence of aortic dilatation and late rupture.

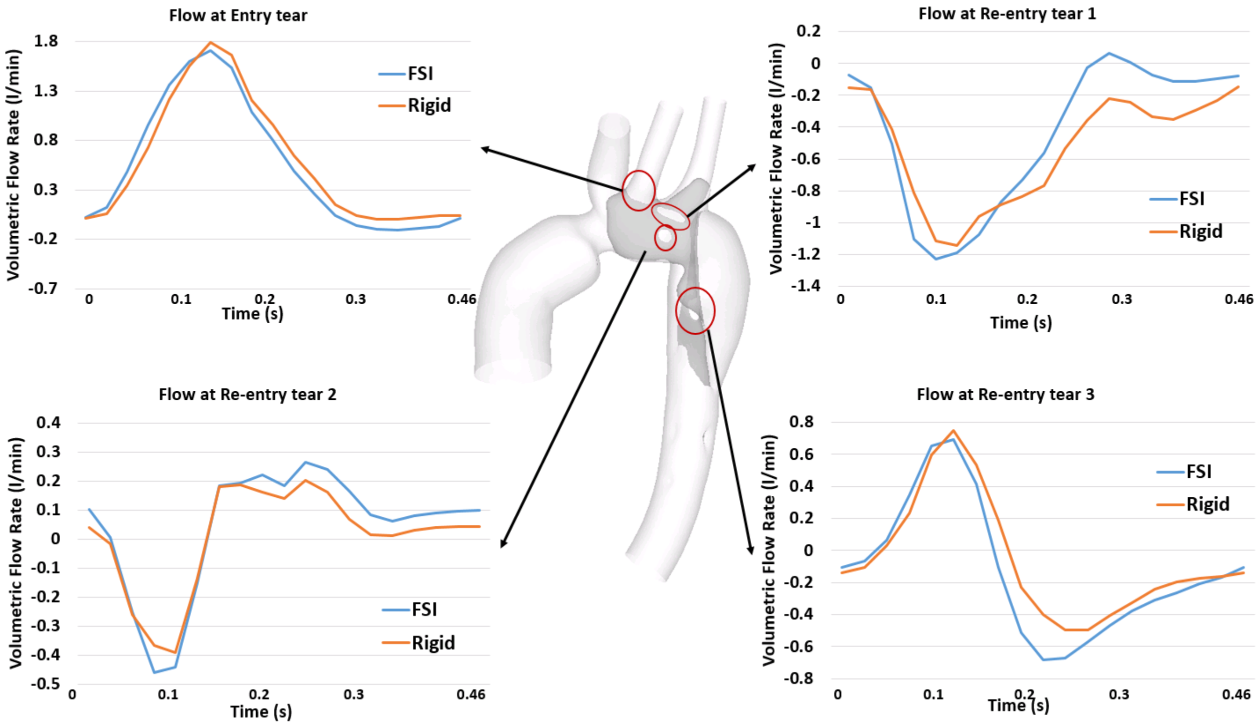

Figure 7.8. Comparison of volumetric flow rate over a cardiac cycle at the four tears. Locations of the entry-tear and three re-entry tears are highlighted by the red cycles.

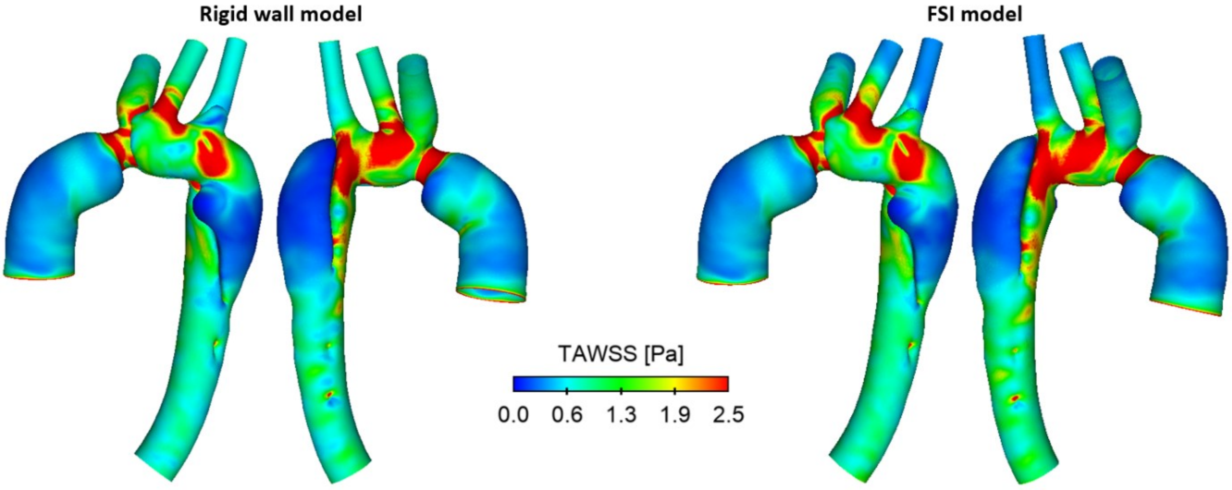

Figure 7.9. Comparison of TAWSS distributions between the rigid wall (left) and FSI (right) models.

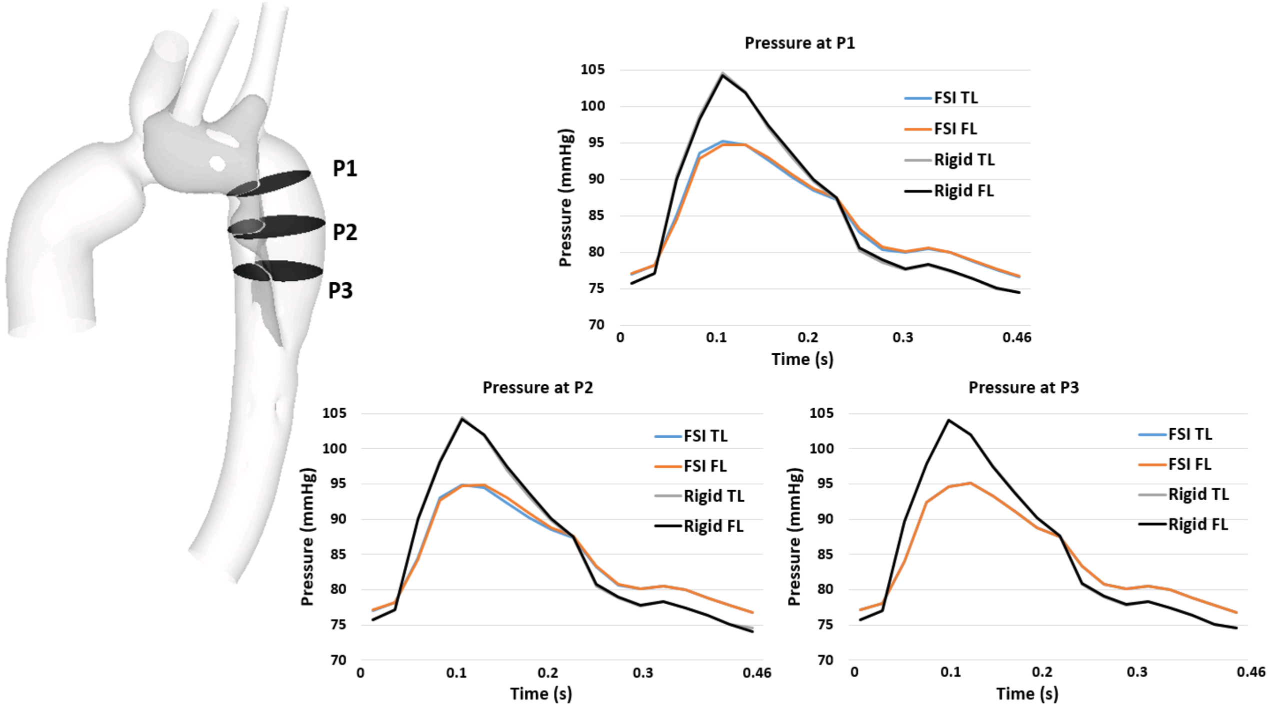

Figure 7.10. Comparison of pressure variations between the rigid wall and FSI models at three selected cross-sections (P1-P3).

Based on the results obtained, patient G2#5 exhibited significantly larger displacements with a peak value of 5.2 mm, which might be attributed to a more tortuous geometry as compared to the other three cases (see details in Chapter 6). The spatial distribution and magnitude of total displacement were comparable among the other three cases, with a maximum displacement of approximate 3.5 mm occurring in the aortic arch and in the proximal descending aorta. The highly distorted geometry of patient G2#5 also resulted in much higher von Mises stress, with a peak value of 350 kPa on the inner arch wall. Peak stresses within the range of 290 kPa and 450 kPa have been reported for aneurysmal aortas (Vorp and Geest 2005). For the other three cases, higher stress levels on the aortic wall concentrated near the tears, with maximum values along the edges of the tears. Some regions of high von Mises stress coincided with the regions experiencing high TAWSS as illustrated in the preceding chapter, indicating potential vulnerability of these regions to further increase in size. The spatial distribution of von Mises stress followed the same pattern for all cases with high stress concentration at the anastomosis between the graft and the native aorta, indicating a potential risk for future tear or rupture at this site.

The approach adopted for FEA involved several assumptions. First, a constant wall thickness was assumed for the aortic wall. This was a major assumption but unavoidable because CT images do not contain sufficient information for extraction of wall thickness. Second, the structural simulations were conducted by applying a static load that was equivalent to the pulse pressure of a healthy subject, whereas in reality the pressure varies both spatially and temporally. Since structural deformation and fluid flow interact with each other, a more in-depth FSI analysis was performed on one patient by coupling pulsatile flow and wall deformation.

Comparison between FSI Model and Rigid Wall Model

Several studies have been published in recent years on FSI simulations of type B aortic dissection (TBAD) (Alimohammadi et al. 2015; Bäumler et al. 2020; Qiao et al. 2019; Qiao et al. 2015; Ryzhakov et al. 2019), in an attempt to understand the effect of wall motion on flow related parameters. Unfortunately, there were large variations in the extent of intimal flap movement incorporated in these models. Qiao et al. (2015) and Ryzhakov et al. (2019) predicted small flap displacements of up to 0.15 mm and 0.13 mm, respectively. In another FSI study conducted by Qiao et al. (2019), the maximum flap displacement was slightly larger than 0.6 mm, which was consistent with *in vivo* measurements of approximately 0.68 ± 0.2 mm in chronic dissections (Karmonik et al. 2012). In a more recent paper on TBAD, Bäumler et al. (2020) simulated much larger flap displacements of up to 13.4 mm, and they found that flap motion could be reduced from 13.4 mm to 1.4 mm by increasing the Young's modulus from 20 kPa to 800 kPa. However, no FSI analysis of TAAD has been reported so far. In this pilot study, the elastic support applied on the inner surface increased its stiffness, which produced a maximum flap displacement of 0.16 mm, similar to the results reported by Qiao et al. (2015) on TBAD. This choice was made due to limitations of the FSI solver employed in this study – the coupled equations were solved using a partitioned approach which is known to have convergence and stability issues when applied to large deformation problems. Despite of this limitation, it is still possible to examine the effect of aortic wall compliance on haemodynamic features in TAAD.

For TAAD with limited flap motion, the effect of wall compliance on flow patterns was negligible, but its quantitative effect on tear flow was not trivial. Accounting for wall compliance reduced the amount of flow entering the FL through the primary entry tear, but increased blood flow into the FL through re-entry tear 2. In addition, blood flow re-entering the true lumen through re-entry tear 1 was reduced by 1.9%, which was redistributed through re-entry tear 3. Rudenick et al. (2015) analysed the effect of wall elasticity on intraluminal haemodynamics based on a lumped-parameter model, and they found that increasing wall elasticity completely altered tear flow dynamics with higher amplitude and increased flow reversal through the tears.

Comparison of TAWSS between the rigid wall model and FSI model revealed little difference in its spatial distribution, but the magnitude of peak TAWSS predicted by the FSI model was slightly lower than (3%) that predicted by the rigid wall model. Similar findings were reported by Tan et al. (2009) on thoracic aortic aneurysm and Alimohammadi et al. (2015) on TBAD. On the other hand, Alimohammadi et al. (2015) observed that rigid wall assumption appeared to have a notable impact on the regions with low TAWSS values. In these regions, the TAWSS values were underestimated by more than 50% due to the near zero velocity values obtained by the rigid wall simulation. However, the absolute differences between the rigid wall and FSI models was small at approximately 0.2 Pa.

Accounting for aortic wall compliance had a clear and strong effect on intraluminal pressures, where the systolic pressure was reduced by up to 10 mmHg in both TL and FL, while the diastolic pressure was slightly increased. Similar findings were reported by Rudenick et al. (2015), who reported that increasing wall elasticity further damped TL and FL pressure waveforms with a lower systolic pressure and higher diastolic pressure. Most of the previous FSI studies did not investigate the influence of wall compliance on intraluminal pressure, for example, Alimohammadi et al. (2015) and Qiao et al. (2019) analysed wall pressure distributions and they found that TL pressure was higher than the FL pressure in the proximal region but lower in the distal region. These findings were consistent with the early numerical studies based on rigid wall assumptions (Cheng et al. 2015; Tse et al. 2011). Most recently, Bäumler et al. (2020) evaluated the maximum pressure difference between the TL and FL with various flap elasticities and they found that the pressure difference decreased as the flap became more compliant. In this study, the patient (G1#5) selected for FSI analysis had a small pressure difference based on the rigid wall simulation and further incorporating wall compliance did not lead to any noticeable change in luminal pressure difference.

Apart from the limitations that have been discussed separately in the finite element analysis above, and in the fluid analysis in Chapter 6, there were several limitations associated with the FSI simulation. First, elastic support was applied on the inner wall surface to increase its stiffness, and thus minimizing mesh distortion at the interface between the fluid and solid domains. Highly distorted mesh was the main problem encountered during simulation leading to non-convergent solutions. As a result of this constraint, limited flap motion was allowed, which may have caused an underestimation of the overall effect of wall compliance on flow. Second, pre-stress of the structural domain was not taken into account which could affect the predicted aortic deformation. Pre-stressed geometry can be determined based on the approach proposed by Hsu and Bazilevs (2011). Third, the constitutive model developed for abdominal aortic aneurysms (Raghavan and Vorp 2000) was employed to simulate the mechanical behaviour of aortic wall since material properties for TAAD are not available in the literature. Bäumler et al. (2020) have shown that the choice of material properties for the wall could affect the haemodynamic results and materiel properties may vary substantially from patient to patient. Additionally, material properties were assumed to be isotropic for the aortic wall and intimal flap. Finally, the FSI simulation took 3 weeks to complete 3 cycles as compared to 5 days required for the rigid wall simulation on a desktop workstation (Intel i7 processer, 32GB RAM). The long computational time for FSI simulations will limit its applicability to a large cohort study.

7.5 Summary

This chapter presents the FE analysis of four post-surgical type A dissection models, and a preliminary FSI simulation to evaluate the effect of wall compliance on predicted haemodynamic parameters.

The results obtained from FEA were compared between the patients with stable aortic diameters (N=2) and those with unstable aortic growth (N=2). Patient G2#5 presented with significantly higher displacements as compared to the two patients with stable aortic diameters (G1#3 & G1#9), but patient G2#4 showed comparable results. Spatial distributions of von Mises stress on the entire wall showed a similar pattern for all patients, with high stresses concentrated around the anastomosis between the graft and the native aorta. High stress values were also found in regions around the tears and at the sharp corners. Again, patient G2#5 displayed the highest peak stress (350 kPa) among the 4 cases examined. Prognostic values of biomechanical parameters on progressive aortic dilatation are still unclear based on the current results, and a large cohort of patients should be included in the future.

The pilot FSI analysis performed on a single patient revealed that the most notable effects of wall compliance on haemodynamics in TAAD were flow distribution among the tears and pressure values in the TL and FL. The latter was particularly noticeable as accounting for wall compliance reduced the systolic pressure by up to 10 mmHg and slightly increased the diastolic pressure, thereby reducing the pulse pressure which is defined as the difference between systolic and diastolic pressure. However, for the selected patient model and under the assumption of a stiff intimal flap, the predicted pressure difference between the TL and FL hardly differed between the FSI and rigid wall simulations. This was mainly due to the fact that the luminal pressure difference in this patient was very small. However, since the quantitative effect of wall compliance on pressures in the TL and FL was similar, it may be reasonable to expect that the predicted luminal pressure difference would not change very much between the rigid wall and FSI simulations. Nevertheless, further FSI studies will be required to test these preliminary findings.

Chapter 8

Conclusions and Recommendations

8.1 Summary of Main Conclusions

Thoracic endovascular aortic repair (TEVAR) is a minimally invasive procedure that avoids open surgery. It has become one of the most popular choices for treating descending thoracic aortic diseases. Recent innovations in TEVAR techniques and devices have extended its application to more complex thoracic aortic aneurysms involving the aortic arch. However, the long-term durability of the new generation of devices is not yet clear. In addition, for complex pathologies involving the ascending aorta, such as TAAD, surgical replacement of the affected ascending aorta remains the gold standard, although the risk of aortic rupture due to further dilatation of the residual dissected aorta remains high. This study aims to facilitate better understating and evaluation of the long-term outcomes of these procedures by providing computational analyses of the post-operative haemodynamic and biomechanical conditions in the aorta. Key contributions of the work presented in this thesis include the following:

(a) Evaluation of the long-term durability of novel multi-branched stent-graft (TAMBE) for endovascular repair of complex TAAAs.
(b) Comparison of flow characteristics and haemodynamic indices in patient-specific TAAs before and after deployment of a novel double-branched stent-graft. The influence of inner tunnel diameter on haemodynamic performance of the device has also been investigated.
(c) Analysis of geometric and haemodynamic parameters in TAAD patients following surgical repair and identification of potential predictors of progressive aortic dilatation.
(d) Analysis of biomechanics and preliminary fluid-solid interaction analysis of post-surgical TAAD models.

Detailed conclusions drawn from each of these aspects are summarised below.

8.1.1 Haemodynamic Assessment of TAMBE

The aim of this study was to assess the detailed haemodynamic performance of a novel EVAR device, namely, thoracoabdominal branch endoprosthesis (TAMBE), by analysing the effects of geometric variations on flow patterns and near wall haemodynamic parameters. Due to the absence of patient-specific data, hypothetical models of TAMBE were constructed where key geometric features, such as take-off angles (TOAs) and length of the renal branch stent-graft were examined, along with non-planarity of the abdominal aorta. The main findings (Chapter 4) are as follows:

- The mean volumetric flow rates were 0.51 L/min in the renal artery, 0.54 L/min in the SMA, and 0.69 L/min in the coeliac artery, accounting for 14.8%, 15.6%, and 20% of the supra-coeliac aortic flow. These predicted values showed that TAMBE is capable of maintaining sufficient perfusion to the visceral arteries, and changing the TOA or length of the renal branch stent-graft did not alter the volumetric flow distribution.
- Due to a sudden change in the direction of blood flow, persistent flow recirculation zones (FRZs) were observed in the bridging renal branches. The presence of inner portals also caused two large FRZs near the entrance to the renal branches. Association of FRZ locations with low endothelial cell activation potential (ECAP) values (< 0.5) suggested that these regions would be at low risk of thrombosis. Similar flow patterns were observed in all the simulated geometries except for TAMBE model 2 with a TOA of 45°, where secondary FRZs were absent.
- High values of time-averaged wall shear stress (TAWSS) were found on the outer curvature of the renal stent-grafts, raising concerns about long-term durability of the device at these locations. Additionally, TOA was found to have a strong influence on the maximum TAWSS, as TAMBE model 3 (TOA = 110°) had the highest peak TAWSS of 15.7 Pa, which was more than twice of the value (6.8 Pa) in TAMBE model 2 (TOA = 45°). TAMBE model 1 with a TOA of 90 showed modest peak TAWSS value of 11.5 Pa, and altering the length of the renal branch stent-graft hardly changed this value.
- Spatial distributions of ECAP were similar for all the simulated models and high ECAP values (> 5) were observed around the intersections between the bridging stent-grafts and the main stent-graft endoprosthesis, suggesting that this region is potentially thrombogenic. Moreover, the 99th percentile ECAP values were comparable between all the TAMBE models, with the maximum difference being 0.18.
- The magnitude of displacement forces was the same for all models except for the non-planar geometry which increased the cycle-averaged displacement force. Nevertheless, the planar TAMBE models included in this study had a maximum displacement force of 12.24N, and 13.14 N for the non-planar TAMBE, both were well below the threshold value of 32 N for device migration.

In summary, geometric variations had a minor effect on the haemodynamic performance of TAMBE, but the high TAWSS along the outer curvature of the renal stent-graft could be a concern, especially for the upward renal configuration. The clinical implication of this study is that TAMBE has the potential to be safely used in endovascular repair of complex TAAAs, despite variable configurations of bridging stent-graft.

8.1.2 Haemodynamic Evaluation of a Novel Double-Branched Stent-Graft

Branched stent-grafts (BSGs) have been developed to treat complex pathology in the aortic arch and ascending aorta. This study aimed to evaluate the haemodynamic performance of a double-branched thoracic endograft by detailed comparison of flow patterns and wall shear stress in the aorta and supra-aortic branches before and after stent-graft implantation. An idealised arch model along with the corresponding BSG models were constructed to investigate the influence of the diameter of inner tunnels on flow characteristics. This was then followed by patient-specific analysis of two TAAs where pre- and post-intervention geometries were reconstructed from the CT images acquired before and after the TEVAR procedure. Based on the results obtained from both idealised and patient-specific models, the main findings are as follows:

- With the idealised models, implantation of a BSG slightly altered blood perfusion to the arch vessels. Insertion of a BSG also increased blood velocities resulting in increased magnitude of WSS. After comparing three different BSG models with various diameters of the inner tunnels, the BSG model with a diverging configuration for both the IA and LCCA was found to have the worst haemodynamic performance, presenting with less blood perfusion to the IA and LSCA, more persistent FRZs in the arch vessels, higher TAWSS, and larger displacement forces. These results suggested that inner tunnels should have larger diameters than the corresponding native vessels.
- After intervention, 12% of inflow passing through the LCCA of patient 1, and 8% for patient 2, increased from 5% and 3%, respectively, in the pre-intervention models. The increased flow into the LCCA after intervention was needed as part of it would be diverted into the LSCA through the bypass. Flow divisions among the IA of patient 1 and patient 2 remained the same between pre- and post- interventions. Therefore, the patient-specific simulations confirmed that there was sufficient blood perfusion through the arch branches.
- A detailed analysis of WSS related indices showed that the presence of inner tunnels caused flow derangement and asymmetric WSS in the ascending aorta, where shear range index was up to 6 times higher than in the pre-intervention model. WSS in the aortic arch increased considerably after intervention as a result of accelerated flow. Elevated TAWSS may help reduce the risk of thrombus formation but increased spatial variation of WSS and haemodynamic derangement may have a detrimental effect in the long term.

- Spatial distributions of ECAP indicated that the patient who received a BSG with a smaller inner LCCA tunnel diameter than that of the IA branch presented higher ECAP values in the arch vessels compared to the patient who received two equal diameter inner tunnels. Since high ECAP values may increase the risk of thrombosis in the supra-aortic branch, having equal diameter inner tunnels may help reduce the associated risk and potential blockage of the arch vessels.
- The maximum flow-induced displacement forces on the branched endografts were around 22N for both patients, which was below the threshold for device migration.

In summary, although no obvious adverse haemodynamic features were found immediately after intervention for the cases analysed, more patient-specific cases and follow-up studies will be needed to assess durability of the device. The clinical implication of this study is when choosing an off-the-shelf device, preference should be given to BSGs with two equal inner tunnel diameters, which are both larger than that of the respective vessels.

8.1.3 Evaluation of Haemodynamic Conditions in Surgical Repaired TAADs

Patients with residual AD following surgical repair of TAAD have increased risk of developing aneurysmal dilatation. In an attempt to help understand the underlying mechanisms, blood flow in 17 patient-specific cases was analyzed and compared between the groups with and without progressive aortic dilatation. The main findings are as follows:

- The number of re-entry tears was the only geometric parameter found to be significantly different between the two groups - patients with progressive aortic dilatation had significant smaller number of re-entry tears ($6 \pm 5\ vs\ 2 \pm 1; P = 0.02$). Although patients with larger maximum aortic diameters might also be prone to unstable aortic dilatation, this parameter was not statistically significant based on the samples analysed ($39.8 \pm 5.5\ vs\ 44.9 \pm 3.9\ mm; P = 0.07$).
- Patients with progressive aortic dilatation had significantly higher pressure difference between the true and false lumen ($1.3 \pm 1\ vs\ 11.7 \pm 14.6\ mmHg; P = 0.001$). Luminal pressure difference was found to be the strongest predictor of unstable aortic expansion.
- High TAWSS values were found in regions surrounding the tears with the maximum TAWSS on the edge of the tears in most cases, perhaps indicating the vulnerability of this region to further increase in tear size. Although patients with progressive aortic dilatation also had higher maximum TAWSS, the difference was not statistically significant ($13.4 \pm 7.3\ vs\ 24 \pm 12.3\ Pa; P = 0.07$).

In summary, this is the first time that luminal pressure difference has been identified as a potential risk indicator for aneurysmal dilatation following surgical repair of TAAD, whilst distal tears equalize the true and false lumen pressures and therefore stabilizing the aorta. Combined haemodynamic and geometrical assessment of the residual aorta may assist appropriate surgical planning at the initial presentation or during post TAAD repair period. Further large cohort studies are warranted to validate these findings.

8.1.4 FE and FSI Analysis of Post-Surgical TAAD

Biomechanics analysis of post-surgical TAAD has not been reported in the literature. In an effort to compliment the haemodynamics analysis presented in Chapter 6, finite element analysis (FEA) was performed on 4 post-surgical TAAD models: two patients with a stable aorta and another two with unstable aortic growth. A preliminary FSI simulation was also performed in order to assess the effect of wall compliance on haemodynamic parameters. Based on the obtained results in Chapter 7, the main findings are as follows:

- Spatial distributions of von Mises stress were comparable between the patients with stable aortic growth and those with unstable aortic growth. The peak values of 364 – 394 kPa were observed at the anastomosis between the graft and the native aorta, indicating a potential risk for future tear or rupture at this site. Away from the graft, high stress concentration was found in regions around the tears and at the sharp corners, co-localised with the areas of high TAWSS. One patient with unstable aortic growth showed significantly larger wall displacement with a peak value of 5.2 mm and greater peak stress in the aortic wall (350 kPa) than the other three patients examined.
- The FSI analysis was performed on a case with small flap displacements of up to 0.16 mm. Despite this limitation, incorporation of wall compliance had clear effects on intraluminal haemodynamics, such that significant quantitative differences were observed in flow divisions among entry and re-entry tears and in intraluminal pressures. Over a cardiac cycle, the percentage of inflow passing through the primary tear and re-entry tears 1 to 3 was 13.3%, -12.1%, 0.2%, and -1.4%, respectively, in the rigid wall model, and 12.5%, -10.2%, 1%, and -3.3% for the FSI model. Accounting for wall compliance also reduced systolic pressure by up to 10 mmHg at peak systole, while slightly increased diastolic pressure in both true and false lumen. However, FSI simulation did not alter the pressure difference between the true and false lumen. Moreover, although TAWSS distributions predicted by the rigid and FSI models were qualitatively similar, FSI simulation predicted slightly lower (3%) maximum TAWSS value of 13 Pa as compared to 13.4 Pa in the rigid wall model.

In summary, prognostic values of biomechanical parameters on progressive aortic dilatation are still unclear. Although the preliminary FSI results presented here shed some lights on the effects of wall compliant on haemodynamic results, further improvement of the FSI model is necessary in order to accommodate physiologically realistic flap motion.

8.2 Limitations

8.2.1 Blood as a Newtonian Fluid

Blood is a combination of red blood cells, white blood cells, platelets and other proteins suspended in plasma, which therefore exhibits non-Newtonian characteristics. In fact, it has been found that blood is a shear-thinning fluid and its non-Newtonian effect becomes more important in small vessels (Cokelet 1972). On the other hand, it is widely accepted that blood behaves in a Newtonian manner in large arteries, where the shear rate is usually greater than 100 s^{-1} (Cho and Kensey, 1991; Perktold et al. 1991). However, as there are regions of flow stagnation in aortic dissection and aneurysm where local shear rate could be less than 10 s^{-1}, the non-Newtonian effect of blood could be important in localized regions. This should be considered in future studies. If information on patient-specific haematocrit is available, the effect of non-Newtonian viscosity of blood could be incorporated readily by using Quemada model (Quemada 1978).

8.2.2 Rigid Wall Assumption

In the simulations of patient-specific TAA and TAAD models presented in Chapters 5 & 6, a rigid wall assumption was applied. FSI simulations could not be performed due to the high computational demand and lack of essential information on the aortic wall (e.g. wall thickness and elastic modulus). In terms of pre- and post-TEVAR models of a TAA, although stent-graft walls are very stiff and the effect of wall compliance on the predicted flow field is expected to be minimal (Kleinstreuer et al. 2008), these effects cannot be ignored while performing haemodynamic simulations in the native aorta. Tan et al. (2009) conducted an FSI simulation on a TAA model to investigate the effect of wall compliance on flow patterns and wall shear stress distributions. Their study demonstrated a marginal difference in the results of the rigid and FSI simulations, though the assumption of a constant wall thickness was adopted. For the post-surgical TAAD models, the situation is further complicated by the intimal flap which can be highly mobile especially in the acute phase. However, building a compliant wall model of AD is very challenging since the wall thickness and material properties vary in different components of the vessel wall and are difficult to measure. Additionally, the complexity of the model will demand extensive computational resources for FSI simulation. In the preliminary FSI study on a post-surgical TAAD model, the wall thickness was assumed to be constant and the mechanical properties were adopted from the experimental data on AAAs. In the future, if the material properties of each layer of dissected wall could be determined experimentally and more advanced imaging modalities can provide better details about the local wall thickness, this assumption would be further relaxed.

8.2.3 Lack of Complete Patient-Specific Pressure and Flow Data

Non-patient-specific inlet and outlet boundary conditions are often used, due to the lack of patient-specific flow and pressure measurement. In the patient-specific analysis of pre- and post-TEVAR of TAAs, a flow waveform acquired from a different subject with the assumption of flat velocity profiles was imposed at all the model inlet. This would obviously affect the predicted flow and wall shear stress related parameters. In fact, even with a patient-specific flow waveform, the assumption of idealised velocity profiles could still have a strong influence on the predicted results, especially for studies focusing on the ascending aorta and aortic arch (Pirola et al. 2018). Therefore, in the simulations of the post-surgical TAAD models, the use of scaled patient-specific flow waveforms along with the assumption of flat velocities profiles might not reflect truly the patient-specific features especially in the ascending aorta. For each outlet, a 3-EWM was applied to account for the behaviour of the distal vascular bed and to predict the physiologically realistic pressure waveforms. However, patient-specific pressure data were not available for estimation of 3-EWM parameters and pressure waveforms in the literature were adopted. It would be highly desirable if a complete set of patient-specific flow and pressure data are available so that the quantitative errors in this study could be reduced. As shown in Figure 8.1, Pirola et al. (2019) have conducted numerical simulations in type B dissection models using patient-specific flow and pressure data. The velocity profiles imposed at the inlet were extracted from the 4D MRI data while calibration of Windkessel parameters for multiple visceral branches were based on Doppler-wire pressure measurements at each branch outlet. Their results showed a good agreement with *in vivo* 4D flow MRI.

8.2.4 Smooth Stent-Graft Walls

Another limitation is that the stent-graft walls were assumed to be smooth without considering the presence of metallic stent wires on the stent-graft surface. Zhang et al. (2014) demonstrated that bare-metal stents significantly altered the CFD results. However, all the stent-graft models included in this thesis are covered with a graft fabric, which might reduce the effect of metallic stent wires. Nevertheless, stent wires sewn on the endograft surface are exposed to blood flow, which would increase local flow disturbance around the exposed struts especially in the first few days following TEVAR.

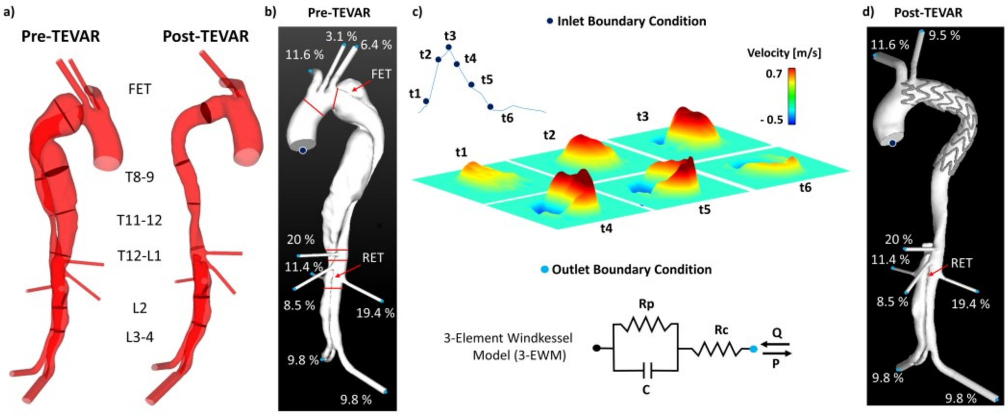

Figure 8.1. Example of incorporating the complete patient-specific pressure and velocity data on type B dissection. (a) *In vivo* pressure measurements. (b) Pre- and (d) post-TEVAR geometric models with flow distributions among all the outlets. (c) Inlet and outlet boundary conditions. Inlet velocity profiles were obtained from the 4D MRI data. Figure adopted from Pirola et al.(2019).

8.2.5 Cohort Size and *in vivo* Validation

Both TAMBE and the dual-branched stent-graft for aortic arch aneurysms are novel designs so patient-specific data were limited or even absent. Haemodynamic performance within the visceral vessels can be affected by various factors, such as length and angles between the branches and the main endoprosthesis. Future studies of more patient cases will be needed to examine a wide variety of anatomical scenarios, though some of these have been assessed using physiologically relevant idealised models.

The study in Chapter 6 has correlated late progressive aortic dilatation with certain geometric and haemodynamic parameters. However, the relatively small sample size might influence the statistical results due to the existence of outliers. These outliers are inevitable but their effects on statistics would be minimal with a large cohort size. Moreover, given the small sample size, current studies were based on a univariate analysis so that each parameter was studied individually. A much larger cohort size would be needed if we want to perform a multivariate analysis, where the effect of multiple parameters can be evaluated simultaneously.

The lack of direct validation of the numerical results is another limitation of this research project. Ideally, non-invasive measurements of blood velocity using 4D flow magnetic resonance imaging (MRI) should be performed to provide *in vivo* data for validation. However, the number of patients treated with TAMBE or dual-branched BSG is very limited, and none of these was available for 4D flow MRI scans by our clinical collaborators. The TAAD study was retrospective, using the validated database of patients at two hospitals. Again, no MR imaging was performed on the patients in this database, as CT is the standard imaging modality for diagnosis of TAAD. Nevertheless, the computational methodology adopted in the present study has been validated in other relevant applications, including type B aortic dissection (Cheng et al. 2014; Menichini et al. 2018; Pirola et al. 2019). All of their studies showed a good overall agreement with available *in vivo* measurements.

8.3 Recommendations for Future Work

8.3.1 Virtual Stent-Graft Deployment

In cases where patient-specific post-operative stent-graft geometries were not available (e.g. TAMBE), or stent wires could not be segmented from medical images (e.g. dual-branched stent-graft) due to the blooming artefacts, parametric models of stent-grafts can be created and deployed into patient-specific pre-operative models using advanced FEA. This procedure is known as ''virtual stent-graft deployment'', and has been increasingly applied to the studies of abdominal aortic aneurysms (De Bock et al. 2012; Perrin et al. 2015), type B aortic dissections (Chen et al. 2018; Ma et al. 2018) and stenotic coronary arteries (Wei et al. 2019). The FEA methods used in these studies can simulate the actual stenting procedure, including compression, bending and release of the stent-graft so that highly realistic post-operative deformed stent-grafts configurations can be obtained, which can then be used to perform CFD analysis. Using FEA methods along with CFD simulations, not only the post-operative haemodynamic performance of stent-grafts can be analysed, but also the structural behaviour of the stent-grafts, as well as the effects of various stent designs can be analysed. For example, Chen et al. (2018) applied this hybrid FEA-CFD approach to predict stent-induced remodelling in type B dissection by analysing both haemodynamic and structural parameters.

8.3.2 Incorporation of Thrombus Formation Model

Thrombus formation and growth was not modelled explicitly in the simulations of TEAVR for TAAs but indirect WSS related indices were used to identify regions at potential risks of thrombosis. More recently, Menichini and Xu (2016) proposed a novel mathematical model for the prediction of thrombosis in aortic dissection based on the analysis of flow patterns and key variables such as shear stress and residence time. Their model has been tested in patient-specific type B dissection geometries and has shown satisfactory agreement with *in vivo* observations (Menichini et al. 2018). Therefore, the thrombus formation model can be coupled with the stent-graft models presented in this thesis, but careful calibration and validation are needed to ensure its suitability for these new applications.

8.3.3 Effect of Aortic Root Motion

Ventricular contraction and relaxation during each heartbeat exert a traction force inducing a spatial movement of the aortic annulus, which is then transmitted to the ascending aorta, aortic arch and arch vessels. The aortic root motion therefore can influence both haemodynamic and biomechanics in different parts of the aorta. For example, Jin et al. (2003) measured both in-plane (perpendicular to lumen) radial expansion-contraction and translational motion of the aorta at the inlet section, which were then prescribed in the computational model. The obtained CFD results from this model showed best agreement with the *in vivo* MR data by capturing the clockwise migration of the peak velocity zone during systole, whereas the results obtained from the rigid wall model and the model including only radial motion failed to reproduce this behaviour. On the other hand, some aortic finite element models were reported to evaluate the aortic root downward motion effects on proximal AA stress levels (Beller et al. 2008; Singh et al. 2016). Aortic root displacement in longitudinal direction significantly increased the longitudinal stress in the ascending aorta. Therefore, the aortic root motion in both transverse and longitudinal directions are expected to be include in future works.

References

Albornoz, G., Coady, M. A., Roberts, M., Davies, R. R., Tranquilli, M., Rizzo, J. A., and Elefteriades, J. A. (2006). “Familial Thoracic Aortic Aneurysms and Dissections-Incidence, Modes of Inheritance, and Phenotypic Patterns.” *Annals of Thoracic Surgery* 82(4):1400–1405.

Alimohammadi, M., Sherwood, J. M., Karimpour, M., Agu, O., Balabani, S., and Díaz-Zuccarini, V. (2015). “Aortic Dissection Simulation Models for Clinical Support: Fluid-Structure Interaction vs. Rigid Wall Models.” *BioMedical Engineering Online* 14(1):1–16.

Allen, B. D., Barker, A. J., Kansal, P., Collins, J. D., Carr, J. C., Malaisrie, S. C., and Markl, M. (2013). “Impact of Aneurysm Repair on Thoracic Aorta Hemodynamics.” *Circulation* 128(17):e341–43.

Anagnostopoulos, C. E., Prabhakar, M. J., and Kittle, C. F. (1972). “Aortic Dissections and Dissecting Aneurysms.” *The American Journal of Cardiology* 30(3):263–73.

Assar, A. N., and Zarins, C. K. (2009). “Ruptured Abdominal Aortic Aneurysm: A Surgical Emergency with Many Clinical Presentations.” *Postgraduate Medical Journal* 85(1003):268–73.

Avrahami, I., Brand, M., Meirson, T., Ovadia-Blechman, Z., and Halak, M. (2012). “Hemodynamic and Mechanical Aspects of Fenestrated Endografts for Treatment of Abdominal Aortic Aneurysm.” *European Journal of Mechanics, B/Fluids* 35:85–91.

Balm, R., Reekers, J. A., and Jacobs, M. J. (2000). “Classification of Endovascular Procedures for Treating Thoracic Aortic Aneurysms.” *Surgical and Endovascular Treatment of Aortic Aneurysms. New York: Futura Publishing Company,* 19–26.

Barker, A. J., Lanning, C., and Shandas, R. (2010). “Quantification of Hemodynamic Wall Shear Stress in Patients with Bicuspid Aortic Valve Using Phase-Contrast MRI.” *Annals of Biomedical Engineering* 38(3):788–800.

Bashir, M. R., Ferral, H., Jacobs, C., McCarthy, W., and Goldin, M. (2009). “Endoleaks after Endovascular Abdominal Aortic Aneurysm Repair: Management Strategies According to CT Findings.” *American Journal of Roentgenology* 192(4):178–86.

Bäumler, K., Vedula, V., Sailer, A. M., Seo, J., Chiu, P., Mistelbauer, G., Chan, F. P., Fischbein, M. P., Marsden, A. L., and Fleischmann, D. (2020). “Fluid – Structure Interaction Simulations of Patient-Specific Aortic Dissection.” *Biomechanics and Modeling in Mechanobiology* (0123456789).

Bavaria, J., Vallabhajosyula, P., Moeller, P., Szeto, W., Desai, N., and Pochettino, A. (2013). “Hybrid Approaches in the Treatment of Aortic Arch Aneurysms: Postoperative and Midterm Outcomes.” *Journal of Thoracic and Cardiovascular Surgery* 145(3 SUPPL.):S85–90.

Beller, C. J., Labrosse, M. R., Thubrikar, M. J., and Robicsek, F. (2008). “Finite Element Modeling of the Thoracic Aorta: Including Aortic Root Motion to Evaluate the Risk of Aortic Dissection.” *Journal* *of Medical Engineering and Technology* 32(2):167–70.

Benedetto, U., Melina, G., Angeloni, E., Codispoti, M., and Sinatra, R. (2013). "Current Results of Open Total Arch Replacement versus Hybrid Thoracic Endovascular Aortic Repair for Aortic Arch Aneurysm: A Meta-Analysis of Comparative Studies." *Journal of Thoracic and Cardiovascular Surgery* 145(1):305–6.

Berguer, R., Bull, J. L., and Khanafer, K. (2006). "Refinements in Mathematical Models to Predict Aneurysm Growth and Rupture." *Annals of the New York Academy of Sciences* 1085:110–16.

Bernard, Y., Zimmermann, H., Chocron, S., Litzler, J. F., Kastler, B., Etievent, J. P., Meneveau, N., Schiele, F., and Bassand, J. P. (2001). "False Lumen Patency as a Predictor of Late Outcome in Aortic Dissection." *American Journal of Cardiology* 87(12):1378–82.

Blum, U., Voshage, G., Lammer, J., Beyersdorf, F., Töllner, D., Kretschmer, G., Spillner, G., Polterauer, P., Nagel, G., Hölzenbein, T., and Thurnher, S. (1997). "Endoluminal Stent–Grafts for Infrarenal Abdominal Aortic Aneurysms." *New England Journal of Medicine* 336(1):13–20.

Borghi, A., Wood, N. B., Mohiaddin, R. H., and Xu, X. Y. (2008). "Fluid-Solid Interaction Simulation of Flow and Stress Pattern in Thoracoabdominal Aneurysms: A Patient-Specific Study." *Journal of Fluids and Structures* 24(2):270–80.

Borst, H. G., Schaudig, A., and Rudolph, W. (1964). "Arteriovenous Fistula of the Aortic Arch: Repair During Deep Hypothermia and Circulatory Arrest." *The Journal of Thoracic and Cardiovascular Surgery* 48(3):443–47.

Borst, H. G., Walterbusch, G., and Schaps, D. (1983). "Extensive Aortic Replacement Using 'elephant Trunk' Prosthesis." *Thoracic and Cardiovascular Surgeon* 31(1):37–40.

Brown, L. C., and Powell, J. T. (1999). "Risk Factors for Aneurysm Rupture in Patients Kept under Ultrasound Surveillance." *Annals of Surgery* 230(3):289–97.

Bungay, P. M., Burfitt, N., Sritharan, K., Muir, L., Khan, S. L., De Nunzio, M. C., Lingam, K., and Davies, A. H. (2011). "Initial Experience with a New Fenestrated Stent Graft." *Journal of Vascular Surgery* 54(6):1832–38.

Buth, J., Harris, P. L., Hobo, R., van Eps, R., Cuypers, P., Duijm, L., and Tielbeek, X., (2007). "Neurologic Complications Associated with Endovascular Repair of Thoracic Aortic Pathology: Incidence and Risk Factors. A Study from the European Collaborators on Stent/Graft Techniques for Aortic Aneurysm Repair (EUROSTAR) Registry." *Journal of Vascular Surgery* 46(6):1103-11.

Buth, J., Harris, P. L., van Marrewijk, C., and Fransen, G. (2003). "The Significance and Management of Different Types of Endoleaks." *Seminars in Vascular Surgery* 16(2):95–102.

Cecconi, M., Manfrin, M., Moraca, A., Zanoli, R., Colonna, P. L., Bettuzzi, M. G., Moretti, S., Gabrielli, D., and Perna, G. P. (2005). "Aortic Dimensions in Patients with Bicuspid Aortic Valve without

Significant Valve Dysfunction." American Journal of Cardiology 95(2):292–94.

Chadwick, J. W., and Lam, E. W. N. (2010). "The Effects of Slice Thickness and Interslice Interval on Reconstructed Cone Beam Computed Tomographic Images." *Oral Surgery, Oral Medicine, Oral Pathology, Oral Radiology and Endodontology* 110(4):e37–42.

Chang, C. P., Liu, J. C., Liou, Y. M., Chang, S. S., and Chen, J. Y. (2008). "The Role of False Lumen Size in Prediction of In-Hospital Complications After Acute Type B Aortic Dissection." *Journal of the American College of Cardiology* 52(14):1170–76.

Chatzizisis, Y. S., Coskun, A. U., Jonas, M., Edelman, E. R., Feldman, C. L., and Stone, P. H. (2007). "Role of Endothelial Shear Stress in the Natural History of Coronary Atherosclerosis and Vascular Remodeling. Molecular, Cellular, and Vascular Behavior." *Journal of the American College of Cardiology* 49(25):2379–93.

Chen, D., Müller-Eschner, M., von Tengg-Kobligk, H., Barber, D., Böckler, D., Hose, R., and Ventikos, Y. (2013). "A Patient-Specific Study of Type-B Aortic Dissection: Evaluation of True-False Lumen Blood Exchange." *BioMedical Engineering Online* 12(1):1–16.

Chen, D., Wei, J., Deng, Y., Xu, H., Li, Z., Meng, H., Han, X., Wang, Y., Wan, J., Yan, T., Xiong, J., and Tang, X. (2018). "Virtual Stenting with Simplex Mesh and Mechanical Contact Analysis for Real-Time Planning of Thoracic Endovascular Aortic Repair." *Theranostics* 8(20):5758–71.

Chen, H. Y., Hermiller, J., Sinha, A. K., Sturek, M., Zhu, L., and Kassab, G. S. (2009). "Effects of Stent Sizing on Endothelial and Vessel Wall Stress: Potential Mechanisms for in-Stent Restenosis." *Journal of Applied Physiology* 106(5):1686–91.

Cheng, S. W. K., Lam, E. S. K., Fung, G. S. K., Ho, P., Ting, A. C. W., and Chow, K. W. (2008). "A Computational Fluid Dynamic Study of Stent Graft Remodeling after Endovascular Repair of Thoracic Aortic Dissections." *Journal of Vascular Surgery* 48(2):303–10.

Cheng, Z., Juli, C., Wood, N. B., Gibbs, R. G. L., and Xu, X. Y. (2014). "Predicting Flow in Aortic Dissection: Comparison of Computational Model with PC-MRI Velocity Measurements." *Medical Engineering and Physics* 36(9):1176–84.

Cheng, Z., Tan, F. P. P., Riga, C. V., Bicknell, C. D., Hamady, M., Gibbs, R. G. J., Wood, N. B., and Xu, X. Y. (2010). "Analysis of Flow Patterns in a Patient-Specific Aortic Dissection Model." *Journal of Biomechanical Engineering* 132(5):1–9.

Cheng, Z., Kidher, E., Jarral, O. A., O'Regan, D. P., Wood, N. B., Athanasiou, T., and Xu, X. Y. (2016). "Assessment of Hemodynamic Conditions in the Aorta Following Root Replacement with Composite Valve-Conduit Graft." *Annals of Biomedical Engineering* 44(5):1392–1404.

Cheng, Z., Riga, C., Chan, J., Hamady, M., Wood, N. B., Cheshire, N. J. W., Xu, X. Y., and Gibbs, R. G. J. (2013). "Initial Findings and Potential Applicability of Computational Simulation of the Aorta in

Acute Type B Dissection." *Journal of Vascular Surgery* 57(2 SUPPL.):35S-43S.

Cheng, Z., Wood, N. B., Gibbs, R. G. J., and Xu, X. Y. (2015). "Geometric and Flow Features of Type B Aortic Dissection: Initial Findings and Comparison of Medically Treated and Stented Cases." *Annals of Biomedical Engineering* 43(1):177–89.

Cho, Y. I., and Kensey, K. R. (1991). "Effects of the Non-Newtonian Viscosity of Blood on Flows in a Diseased Arterial Vessel. Part 1: Steady Flows." *Biorheology* 28(3–4):241–62.

Chuter, T. A. M., Gordon, R. L., Reilly, L. M., Goodman, J. D., and Messina, L. M. (2001). "An Endovascular System for Thoracoabdominal Aortic Aneurysm Repair." *Journal of Endovascular Therapy* 8(1):25–33.

Clare, R., Jorgensen, J., and Brar, S. S. (2016). "Open Versus Endovascular or Hybrid Thoracic Aortic Aneurysm Repair." *Current Atherosclerosis Reports* 18(10).

Coady, M. A., Rizzo, J. A., Hammond, G. L., Mandapati, D., Darr, U., Kopf, G. S., Elefteriades, J. A., Isom, O. W., Robicsek, F., and Griepp, R. B. (1997). "What Is the Appropriate Size Criterion for Resection of Thoracic Aortic Aneurysms?" *Journal of Thoracic and Cardiovascular Surgery* 113(3):476–91.

Coady, M. A., Davies, R. R., Roberts, M., Goldstein, L. J., Rogalski, M. J., Rizzo, J. A., Hammond, G. L., Kopf, G. S., and Elefteriades, J. A. (1999). "Familial Patterns of Thoracic Aortic Aneurysms." *Archives of Surgery* 134(4):361–67.

Cokelet, G. R. 1972. *Chapter 4, in "Biomechanics. Its Foundations and Objectives."* edited by Y. Fung, N. Perrone, and M. Anliker. Prentice-Hall, New Jersey.

Cragg, A., Lund, G., Rysavy, J., Castaneda, F., Castaneda-Zuniga, W., and Amplatz, K. (1983). "Nonsurgical Placement of Arterial Endoprostheses: A New Technique Using Nitinol Wire." *Radiology* 147(1):261–63.

Crawford, E. S. 1990. "The Diagnosis and Management of Aortic Dissection." *Jama* 264(9):2537–41.

Critchley, L. A. H., and Critchley, J. A. J. H. (1999). "A Meta-Analysis of Studies Using Bias and Precision Statistics to Compare Cardiac Output Measurement Techniques." *Journal of Clinical Monitoring and Computing* 15(2):85–91.

Crosetto, P., Reymond, P., Deparis, S., Kontaxakis, D., Stergiopulos, N., and Quarteroni, A. (2011). "Fluid-Structure Interaction Simulation of Aortic Blood Flow." *Computers and Fluids* 43(1):46–57.

Czerny, M., Rylski, B., Morlock, J., Schröfel, H., Beyersdorf, F., Lebes, B. S., Meyrignac, O., Mokrane, F., Lescan, M., Schlensak, C., Hazenberg, C., Bloemert-Tuin, T., Braithwaite, S., van Herwaarden, J., and Rousseau, H. (2018). "Orthotopic Branched Endovascular Aortic Arch Repair in Patients Who Cannot Undergo Classical Surgery." *European Journal of Cardio-Thoracic Surgery* 53(5):1007–12.

Dake, M. D., Miller, D. C., Semba, C. P., Mitchell, R. S., Walker, P. J., and Liddell, R. P. (1994).

“Transluminal Placement of Endovascular Stent-Grafts for the Treatment of Descending Thoracic Aortic Aneurysms.” *New England Journal of Medicine* 331(26):1729–34.

David, T. E., David, C. M., Manlhiot, C., Colman, J., Crean, A. M., and Bradley, T. (2015). “Outcomes of Aortic Valve-Sparing Operations in Marfan Syndrome.” *Journal of the American College of Cardiology* 66(13):1445–53.

De Bock, S., Iannaccone, F., De Santis, G., De Beule, M., Van Loo, D., Devos, D., Vermassen, F., Segers, P., and Verhegghe, B. (2012). “Virtual Evaluation of Stent Graft Deployment: A Validated Modeling and Simulation Study.” *Journal of the Mechanical Behavior of Biomedical Materials* 13:129–39.

De Oliveira, N. C., David, T. E., Ivanov, J., Armstrong, S., Eriksson, M. J., Rakowski, H., Webb, G., De Oliveira, M. Y., and Schaff, H. V. (2003). “Results of Surgery for Aortic Root Aneurysm in Patients with Marfan Syndrome.” *Journal of Thoracic and Cardiovascular Surgery* 125(4):789–96.

DePaola, N., Gimbrone, M. A., Davies, P. F., and Dewey, C. F. (1992). “Vascular Endothelium Responds to Fluid Shear Stress Gradients.” *Arteriosclerosis and Thrombosis* 12(11):1254–57.

Di Achille, P., Tellides, G., Figueroa, C. A., and Humphrey, J. D. (2014). “A Haemodynamic Predictor of Intraluminal Thrombus Formation in Abdominal Aortic Aneurysms.” *Proceedings of the Royal Society A: Mathematical, Physical and Engineering Sciences* 470(2172).

Dietz, H. C., Loeys, B., Carta, L., and Ramirez, F. (2006). “Recent Progress towards a Molecular Understanding of Marfan Syndrome.” *American Journal of Medical Genetics Part C: Seminars in Medical Genetics* 139(1):4–9.

Dillon-Murphy, D., Noorani, A., Nordsletten, D., and Figueroa, C. A. (2016). “Multi-Modality Image-Based Computational Analysis of Haemodynamics in Aortic Dissection.” *Biomechanics and Modeling in Mechanobiology* 15(4):857–76.

Dotter, C. T., Buschmann, R. W., McKinney, M. K., and Rosch, J. (1983). “Transluminal Expandable Nitinol Coil Stent Grafting: Preliminary Report.” *Radiology* 147(1):259–60.

Ekaterinaris, J. A., Ioannou, C. V., and Katsamouris, A. N. (2006). “Flow Dynamics in Expansions Characterizing Abdominal Aorta Aneurysms.” *Annals of Vascular Surgery* 20(3):351–59.

Elsheikh, M., Casadei, B., Conway, G. S., and Wass, J. A. H. (2001). “Hypertension Is a Major Risk Factor for Aortic Root Dilatation in Women with Turner’s Syndrome.” *Clinical Endocrinology* 54(1):69–73.

England, A., and McWilliams, R. (2013). “Endovascular Aortic Aneurysm Repair (EVAR).” *Ulster Medical Journal* 82(1):3–10.

Authors/Task Force members, Erbel, R., Aboyans, V., Boileau, C., Bossone, E., Bartolomeo, R. D., Eggebrecht, H., Evangelista, A., Falk, V., Frank, H., Gaemperli, O., and et al. (2014). “2014 ESC

Guidelines on the Diagnosis and Treatment of Aortic Diseases: Document Covering Acute and Chronic Aortic Diseases of the Thoracic and Abdominal Aorta of the Adult." The Task Force for the Diagnosis and Treatment of Aortic Diseases of the European Society of Cardiology (ESC), *European Heart Journal* 35(41):2873–2926.

Evangelista, A., Salas, A., Ribera, A., Ferreira-González, I., Cuellar, H., Pineda, V., González-Alujas, T., Bijnens, B., Permanyer-Miralda, G., and Garcia-Dorado, D. (2012). "Long-Term Outcome of Aortic Dissection with Patent False Lumen: Predictive Role of Entry Tear Size and Location." *Circulation* 125(25):3133–41.

Fattouch, K., Sampognaro, R., Navarra, E., Caruso, M., Pisano, C, Coppola, G., Speziale, G., and Ruvolo, G. (2009). "Long-Term Results After Repair of Type A Acute Aortic Dissection According to False Lumen Patency." *Annals of Thoracic Surgery* 88(4):1244–50.

Fedak, P. W. M., De Sa, M. P. L., Verma, S., Nili, N., Kazemian, P., Butany, J., Strauss, B. H., Weisel, R. D., David, T. E., Yacoub, M. H., Sundt, T. M., Sellke, F. W., and Pizarro, C. (2003). "Vascular Matrix Remodeling in Patients with Bicuspid Aortic Valve Malformations: Implications for Aortic Dilatation." *Journal of Thoracic and Cardiovascular Surgery* 126(3):797–805.

Ferrer, C., and Cao, P. (2018). "Endovascular Arch Replacement with a Dual Branched Endoprosthesis." *Annals of Cardiothoracic Surgery* 7(3):367–72.

Fillinger, M. F., Raghavan, M. L., Marra, S. P., Cronenwett, J. L., and Kennedy, F. E. (2002). "In Vivo Analysis of Mechanical Wall Stress and Abdominal Aortic Aneurysm Rupture Risk." *Journal of Vascular Surgery* 36(3):589–97.

Finlay, A., Johnson, M., and Forbes, T. L. (2012). "Surgically Relevant Aortic Arch Mapping Using Computed Tomography." *Annals of Vascular Surgery* 26(4):483–90.

Fry, D. L. (1969). "Certain Histological and Chemical Responses of the Vascular Interface to Acutely Induced Mechanical Stress in the Aorta of the Dog." *Circulation Research* 24(1):93–108.

Gao, F., Ohta, O., and Matsuzawa, T. (2008). "Fluid-Structure Interaction in Layered Aortic Arch Aneurysm Model: Assessing the Combined Influence of Arch Aneurysm and Wall Stiffness." *Australasian Physical and Engineering Sciences in Medicine* 31(1):32–41.

Gao, F., Guo, Z., Sakamoto, M., and Matsuzawa, T. (2006). "Fluid-Structure Interaction within a Layered Aortic Arch Model." *Journal of Biological Physics* 32(5):435–54.

GBD 2013 Mortality and Causes of Death Collaborators. (2015). "Global, Regional, and National Age-Sex Specific All-Cause and Cause-Specific Mortality for 240 Causes of Death, 1990-2013: A Systematic Analysis for the Global Burden of Disease Study 2013." *The Lancet* 385(9963):117–71.

Georgakarakos, E., Xenakis, A., Georgiadis, G. S., Argyriou, C., Antoniou, G. A., Schoretsanitis, N., and Lazarides, M. K. (2014). "The Hemodynamic Impact of Misalignment of Fenestrated Endografts:

A Computational Study." *European Journal of Vascular and Endovascular Surgery* 47(2):151–59.

Germain, D. P. (2002). "Clinical and Genetic Features of Vascular Ehlers-Danlos Syndrome." *Annals of Vascular Surgery* 16(3):391–97.

Giles, K. A., Pomposelli, F., Hamdan, A., Wyers, M, Jhaveri, A., and Schermerhorn, M. L. (2009). "Decrease in Total Aneurysm-Related Deaths in the Era of Endovascular Aneurysm Repair." *Journal of Vascular Surgery* 49(3):543–50.

Gill, R. W. (1985). "Measurement of Blood Flow by Ultrasound: Accuracy and Sources of Error." *Ultrasound in Medicine and Biology* 11(4):625–41.

Gopaldas, R. R., Dao, T. K., Lemaire, S. A., Huh, J., and Coselli, J. S. (2011). "Endovascular versus Open Repair of Ruptured Descending Thoracic Aortic Aneurysms: A Nationwide Risk-Adjusted Study of 923 Patients." *Journal of Thoracic and Cardiovascular Surgery* 142(5):1010–18.

Greenberg, R. K., Lu, Q., Roselli, E. E., Svensson, L. G., Moon, M. C., Hernandez, A. V., Dowdall, J., Cury, M., Francis, C., Pfaff, K., Clair, D. G., Ouriel, K., and Lytle, B. W. (2008). "Contemporary Analysis of Descending Thoracic and Thoracoabdominal Aneurysm Repair a Comparison of Endovascular and Open Techniques." *Circulation* 118(8):808–17.

Guilmet, D., Bachet, J., Goudot, B., Laurian, C., Gigou, F., Bical, O., and Barbagelatta, M. (1979). "Use of Biological Glue in Acute Aortic Dissection. Preliminary Clinical Results with a New Surgical Technique." *Journal of Thoracic and Cardiovascular Surgery* 77(4):516–21.

Guo, D. C., Papke, C. L., He, R., and Milewicz, D. M. (2006). "Pathogenesis of Thoracic and Abdominal Aortic Aneurysms." *Annals of the New York Academy of Sciences* 1085:339–52.

Guo, D. C., Hasham, S., Kuang, S. Q., Vaughan, C. J., Boerwinkle, E., Chen, H., Abuelo, D., Dietz, H. C., Basson, C. T., Shete, S. S., and Milewicz, D. M. (2001). "Familial Thoracic Aortic Aneurysms and Dissections Genetic: Heterogeneity with a Major Locus Mapping to 5q13-14." *Circulation* 103(20):2461–68.

Gysi, J., Schaffner, T., Mohacsi, P., Aeschbacher, B., Althaus, U., and Carrel, T. (1997). "Early and Late Outcome of Operated and Non-Operated Acute Dissection of the Descending Aorta." *European Journal of Cardio-Thoracic Surgery* 11(6):1163–70.

Hagan, P. G., Nienaber, C. A., Isselbacher, E. M., Bruckman, D., Karavite, D. J., Russman, P. L., Evangelista, A., Fattori, R., Suzuki, T., Oh, J. K., Moore, A. G., Malouf, J. F., Pape, L. A., Gaca, C., Sechtem, U., Lenferink, S., Deutsch, H. J., Diedrichs, H., Robles, J. M., Llovet, A., Gilon, D., Das, S. K., Armstrong, W. F., Deeb, C. M., and Eagle, K. A. (2000). "The International Registry of Acute Aortic Dissection (IRAD)." *Jama* 283(7):897.

Halak, M., Goodman, M. A., and Baker, S. R. (2006). "The Fate of Target Visceral Vessels After Fenestrated Endovascular Aortic Repair-General Considerations and Mid-Term Results."

European Journal of Vascular and Endovascular Surgery 32(2):124–28.

Hall, J. E. (2010). *Guyton and Hall Textbook of Medical Physiology*. Elsevier Health Sciences.

Halstead, J. C., Meier, M., Etz, C., Spielvogel,D., Bodian, C., Wurm, M., Shahani, R., and Griepp, R. B. (2007). "The Fate of the Distal Aorta after Repair of Acute Type A Aortic Dissection." *Journal of Thoracic and Cardiovascular Surgery* 133(1):127–36.

Harris, P., Brennan, J., Martin, J., Gould, D., Bakran, A., Gilling-Smith, G., Buth, J., Gevers, E., and White, D. (1999). "Longitudinal Aneurysm Shrinkage Following Endovascular Aortic Aneurysm Repair: A Source of Intermediate and Late Complications." *Journal of Endovascular Surgery* 6(1):11–16.

Haulon, S., Greenberg, R. K., Spear, R., Eagleton, M., Abraham, C., Lioupis, C., Verhoeven, E., Ivancev, K., Kölbel, T., Stanley, B., Resch, T., Desgranges, P., Maurel, B., Roeder, B., Chuter, T., and Mastracci, T. (2014). "Global Experience with an Inner Branched Arch Endograft." *Journal of Thoracic and Cardiovascular Surgery* 148(4):1709–16.

He, C. M., and Roach, M. R. (1994). "The Composition and Mechanical Properties of Abdominal Aortic Aneurysms." *Journal of Vascular Surgery* 20(1):6–13.

Himburg, H. A., Grzybowski, D. M., Hazel, A. L., LaMack, J. A., Li, X. M., and Friedman, M. H. (2004). "Spatial Comparison between Wall Shear Stress Measures and Porcine Arterial Endothelial Permeability." *American Journal of Physiology - Heart and Circulatory Physiology* 286(5 55-5):1916–22.

Hiratzka, L. F., Bakris, G. L., Beckman, J. A., Bersin, R. M., Carr, V. F., Casey, D. E., Eagle, K. A., Hermann, L. K., Isselbacher, E. M., Kazerooni, E. A., Kouchoukos, N. T., Lytle, B. W., Milewicz, D. M., Reich, D. L., Sen, S., Shinn, J. A., Svensson, L. G., and Williams, D. M. (2010). "2010 ACCF/AHA/AATS/ACR/ASA/SCA/SCAI/SIR/STS/SVM Guidelines for the Diagnosis and Management of Patients With Thoracic Aortic Disease." *Journal of the American College of Cardiology* 55(14):e27–129.

Holmlund, P. (2013). "Computational Fluid Dynamic Simulations of Pulsatile Flow in Stenotic Vessel Models."

Holzapfel, G. A., Gasser, T. C., and Ogden, R. W. (2000). "A New Constitutive Framework for Arterial Wall Mechanics and a Comparative Study of Material Models." *Journal of Elasticity* 61(1–3):1–48.

Hsu, M. C., and Bazilevs, Y. (2011). "Blood Vessel Tissue Prestress Modeling for Vascular Fluidstructure Interaction Simulation." *Finite Elements in Analysis and Design* 47(6):593–99.

Iba, Y., Minatoya, K., Matsuda, H., Sasaki, H., Tanaka, H., Oda, T., and Kobayashi, J. (2014). "How Should Aortic Arch Aneurysms Be Treated in the Endovascular Aortic Repair Era? A Risk-Adjusted Comparison between Open and Hybrid Arch Repair Using Propensity Score-Matching Analysis."

European Journal of Cardio-Thoracic Surgery 46(1):32–39.

Ishimaru, S. (2004). “Endografting of the Aortic Arch.” *Journal of Endovascular Therapy* 11(SUPPL. 2):6–7.

Isselbacher, E. M. (2005). “Thoracic and Abdominal Aortic Aneurysms.” *Circulation* 111(6):816–28.

Januzzi, J. L., Isselbacher, E. M., Fattori, R., Cooper, J. V., Smith, D. E., Fang, J., Eagle, K. A., Mehta, R. H., Nienaber, C. A., and Pape, L. A. (2004). “Characterizing the Young Patient with Aortic Dissection: Results from the International Registry of Aortic Dissection (IRAD).” *Journal of the American College of Cardiology* 43(4):665–69.

Jeremy, R. W., Huang, H., Hwa, J., McCarron, H., Hughes, C. F., and Richards, J. G. (1994). “Relation between Age, Arterial Distensibility, and Aortic Dilatation in the Marfan Syndrome.” *The American Journal of Cardiology* 74(4):369–73.

Jin, S., Oshinski, J., and Giddens, D. P. (2003). “Effects of Wall Motion and Compliance on Flow Patterns in the Ascending Aorta.” *Journal of Biomechanical Engineering* 125(3):347–54.

Johansson, G., Markström, U., and Swedenborg, J. (1995). “Ruptured Thoracic Aortic Aneurysms: A Study of Incidence and Mortality Rates.” *Journal of Vascular Surgery* 21(6):985–88.

Joris, I., Zand, T., Nunnari, J. J., Krolikowski, F. J., and Majno, G. (1983). “Studies on the Pathogenesis of Atherosclerosis. I. Adhesion and Emigration of Mononuclear Cells in the Aorta of Hypercholesterolemic Rats.” *American Journal of Pathology* 113(3):341–58.

Kallenbach, K., Pethig, K., Leyh, R. G., Baric, D., Haverich, A., and Harringer, W. (2002). “Acute Dissection of the Ascending Aorta: First Results of Emergency Valve Sparing Aortic Root Reconstruction.” *European Journal of Cardio-Thoracic Surgery* 22(2):218–22.

Kandail, H., Hamady, M., and Xu, X. Y. (2015). “Comparison of Blood Flow in Branched and Fenestrated Stent-Grafts for Endovascular Repair of Abdominal Aortic Aneurysms.” *Journal of Endovascular Therapy* 22(4):578–90.

Kandail, H., Hamady, M., and Xu, X. Y. (2016). “Effect of a Flared Renal Stent on the Performance of Fenestrated Stent-Grafts at Rest and Exercise Conditions.” *Journal of Endovascular Therapy* 23(5):809–20.

Kandail, H., Hamady, M., and Xu, X. Y. (2014). “Patient-Specific Analysis of Displacement Forces Acting on Fenestrated Stent Grafts for Endovascular Aneurysm Repair.” *Journal of Biomechanics* 47(14):3546–54.

Karck, M., Chavan, A., Hagl, C., Friedrich, H., Galanski, M., and Haverich, A. (2003). “The Frozen Elephant Trunk Technique: A New Treatment for Thoracic Aortic Aneurysms.” *Journal of Thoracic and Cardiovascular Surgery* 125(6):1550–53.

Karmonik, C., Bismuth, J., Shah, D. J., Davies, M. G., Purdy, D., and Lumsden, A. B. (2011).

“Computational Study of Haemodynamic Effects of Entry- and Exit-Tear Coverage in a DeBakey Type III Aortic Dissection: Technical Report.” *European Journal of Vascular and Endovascular Surgery* 42(2):172–77.

Karmonik, C., Bismuth, J., Davies, M. G., Shah, D. J., Younes, H. K., and Lumsden, A. B. (2011). “A Computational Fluid Dynamics Study Pre-and Post-Stent Graft Placement in an Acute Type B Aortic Dissection.” *Vascular and Endovascular Surgery* 45(2):157–64.

Karmonik, C., Duran, C., Shah, D. J., Anaya-Ayala, J. E., Davies, M. G., Lumsden, A. B., and Bismuth, J. (2012). “Preliminary Findings in Quantification of Changes in Septal Motion during Follow-up of Type B Aortic Dissections.” *Journal of Vascular Surgery* 55(5):1419-1426.e1.

Katzen, B. T., Dake, M. D., MacLean, A. A., and Wang, D. S. (2005). “Endovascular Repair of Abdominal and Thoracic Aortic Aneurysms.” *Circulation* 112(11):1663–75.

Khanafer, K. M., Bull, J. L., Upchurch, G. R., and Berguer, R. (2007). “Turbulence Significantly Increases Pressure and Fluid Shear Stress in an Aortic Aneurysm Model under Resting and Exercise Flow Conditions.” *Annals of Vascular Surgery* 21(1):67–74.

Kimura, N., Tanaka, M., Kawahito, K., Yamaguchi, A., Ino, T., and Adachi, H. (2008). “Influence of Patent False Lumen on Long-Term Outcome after Surgery for Acute Type A Aortic Dissection.” *Journal of Thoracic and Cardiovascular Surgery* 136(5).

Kleinstreuer, C., Li, Z., Basciano, C. A., Seelecke, S., and Farber, M. A. (2008). “Computational Mechanics of Nitinol Stent Grafts.” *Journal of Biomechanics* 41(11):2370–78.

Kleinstreuer, C., Li, Z., and Farber, M. A. (2007). “Fluid-Structure Interaction Analyses of Stented Abdominal Aortic Aneurysms.” *Annual Review of Biomedical Engineering* 9(1):169–204.

Ko, L., Ka. J., Liu, R. W., Ma, D., Shi, L., Simon, C. H., and Wang, D. (2017). “Pulsatile Hemodynamics in Patient-Specific Thoracic Aortic Dissection Models Constructed from Computed Tomography Angiography.” *Journal of X-Ray Science and Technology* 25(2):233–45.

Kolvenbach, R. R., Yoshida, R., Pinter, L., Zhu, Y., and Lin, F. (2011). “Urgent Endovascular Treatment of Thoraco-Abdominal Aneurysms Using a Sandwich Technique and Chimney Grafts - A Technical Description.” *European Journal of Vascular and Endovascular Surgery* 41(1):54–60.

Kolvenbach, R. R., Karmeli, R., Pinter, L. S., Zhu, Y., Lin, F., Wassiljew, S., and Meyer-Gaessner, M. (2011). “Endovascular Management of Ascending Aortic Pathology.” *Journal of Vascular Surgery* 53(5):1431–37.

Konoura, C., Yagi, T., Nakamura, M., Iwasaki, K., Qian, Y., Okuda, S., Yoshitake, A., Shimizu, H., Yozu, R., and Umezu, M. (2013). “Numerical Analysis of Blood Flow Distribution in 4- and 3-Branch Vascular Grafts.” *Journal of Artificial Organs* 16(2):157–63.

Kourliouros, A., Vecht, J., Kakouros, N., Grapsa, J., Nihoyannopoulos, P., Kokotsakis, J., and Athanasiou,

T. (2011). “Frozen Elephant Trunk as an Effective Alternative to Open and Hybrid Two-Stage Procedures for Complex Aortic Disease.” *Hellenic Journal of Cardiology* 52(4):337–44.

Kousera, C. A., Wood, N. B., Seed, W. A., Torii, R., O’Regan, D., and Xu, X. Y. (2013). “A Numerical Study of Aortic Flow Stability and Comparison with in Vivo Flow Measurements.” *Journal of Biomechanical Engineering* 135(1).

Kunishige, H., Myojin, K., Ishibashi, Y., Ishii, K., Kawasaki, M., and Oka, J. (2006). “Predictors of Surgical Indications for Acute Type B Aortic Dissection Based on Enlargement of Aortic Diameter during the Chronic Phase.” *Japanese Journal of Thoracic and Cardiovascular Surgery* 54(11):477–82.

Kuratani, T. (2014). “Best Surgical Option for Arch Extension of Type B Dissection: The Endovascular Approach.” *Annals of Cardiothoracic Surgery* 3(3):292–99.

Kuzmik, G. A., Sang, A. X., and Elefteriades, J. A. (2012). “Natural History of Thoracic Aortic Aneurysms.” *Journal of Vascular Surgery* 56(2):565–71.

Lehoux, S., Castier, Y., and Tedgui, A. (2006). “Molecular Mechanisms of the Vascular Responses to Haemodynamic Forces.” *Journal of Internal Medicine* 259(4):381–92.

Lemaire, S. A., Price, M. D., Parenti, J. L., Johnson, M. L., Lay, A. D., Preventza, O., Huh, J., and Coselli, J. S. (2011). “Early Outcomes after Aortic Arch Replacement by Using the Y-Graft Technique.” *Annals of Thoracic Surgery* 91(3):700–708.

Les, A. S., Shadden, S. C., Figueroa, C. A., Park, J. M., Tedesco, M. M., Herfkens, R. J., Dalman, R. L., and Taylor, C. A. (2010). “Quantification of Hemodynamics in Abdominal Aortic Aneurysms during Rest and Exercise Using Magnetic Resonance Imaging and Computational Fluid Dynamics.” *Annals of Biomedical Engineering* 38(4):1288–1313.

Levick, J. R. (2013). *An Introduction to Cardiovascular Physiology*. Butterworth-Heinemann.

Li, Y. S. J., Haga, J. H., and Chien, S. (2005). “Molecular Basis of the Effects of Shear Stress on Vascular Endothelial Cells.” *Journal of Biomechanics* 38(10):1949–71.

Liu, X., Pu, F., Fan, Y., Deng, X., Li, D., and Li, S. (2009). “A Numerical Study on the Flow of Blood and the Transport of LDL in the Human Aorta: The Physiological Significance of the Helical Flow in the Aortic Arch.” *American Journal of Physiology - Heart and Circulatory Physiology* 297(1):163–70.

Loeys, B. L., Chen, J., Neptune, E. R., Judge, D. P., Podowski, M., Holm, T., Meyers, J., Leitch, C. C., Katsanis, N., Sharifi, N., Xu, F. L., Myers, L. A., Spevak, P. J., Cameron, D. E., Backer, J. D., Hellemans, J., Chen, Y., Davis, E. C., Webb, C. L., Kress, W., Coucke, P., Rifkin, D. B., De Paepe, A. M., and Dietz, H. C. (2005). “A Syndrome of Altered Cardiovascular, Craniofacial, Neurocognitive and Skeletal Development Caused by Mutations in TGFBR1 or TGFBR2.” *Nature Genetics* 37(3):275–81.

Ma, T., Dong, Z. H., Wang, S., Meng, Z. Y., Chen, Y. Y., and Fu, W. G. (2018). “Computational

Investigation of Interaction between Stent Graft and Aorta in Retrograde Type A Dissection after Thoracic Endovascular Aortic Repair for Type B Aortic Dissection.” *Journal of Vascular Surgery* 68(6):14S-21S.e2.

Malek, A. M., Alper, S. L., and Izumo, S. (1999). “Hemodynamic Shear Stress and Its Role in Atherosclerosis.” *Journal of the American Medical Association* 282(21):2035–42.

Markl, M., Draney, M. T., Hope, M. D., Levin, J. M., Chan, F. P., Alley, M. T., Pelc, N. J., and Herfkens, R. J. (2004). “Time-Resolved 3-Dimensional Velocity Mapping in the Thoracic Aorta.” *Journal of Computer Assisted Tomography* 28(4):459–68.

Marui, A., Mochizuki, T., Mitsui, N., Koyama, T., Kimura, F., and Horibe, M. (1999). “Toward the Best Treatment for Uncomplicated Patients with Type B Acute Aortic Dissection: A Consideration for Sound Surgical Indication.” *Circulation* 100(19 SUPPL.):II–275.

Masuda, Y., Yamada, Z., Morooka, N., Watanabe, S., and Inagaki, Y. (1991). “Prognosis of Patients with Medically Treated Aortic Dissections.” *Circulation* 84(5 Suppl):III7-13.

Matsumura, J. S., Lee, W. A., Mitchell, R. S., Farber, M. A., Murad, M. H., Lumsden, A. B., Greenberg, R. K., Safi, H. J., and Fairman, R. M. (2009). “The Society for Vascular Surgery Practice Guidelines: Management of the Left Subclavian Artery with Thoracic Endovascular Aortic Repair.” *Journal of Vascular Surgery* 50(5):1155–58.

Mehta, R. H., Manfredini, R., Hassan, F., Sechtem, U., Bossone, E., Oh, J. K., Cooper, J. V., Smith, D. E., Portaluppi, F., Penn, M., Hutchison, S., Nienaber, C. A., Isselbacher, E. M., and Eagle, K. A. (2002). “Chronobiological Patterns of Acute Aortic Dissection.” *Circulation* 106(9):1110–15.

Melas, N., Saratzis, A., Saratzis, N., Lazaridis, J., Psaroulis, D., Trygonis, K., and Kiskinis, D. (2010). “Aortic and Iliac Fixation of Seven Endografts for Abdominal-Aortic Aneurysm Repair in an Experimental Model Using Human Cadaveric Aortas.” *European Journal of Vascular and Endovascular Surgery* 40(4):429–35.

Mendes, B. C., Oderich, G. S., Macedo, T. A., Pereira, A. A., Cha, S, Duncan, A. A., Gloviczki, P., and Bower, T. C. (2014). “Anatomic Feasibility of Off-The-Shelf Fenestrated Stent Grafts to Treat Juxtarenal and Pararenal Abdominal Aortic Aneurysms.” *Journal of Vascular Surgery* 60(4):839-848.e2.

Mendes, B. C., Rathore, A., Ribeiro, M. S., and Oderich, G. S. (2016). “Off-the-Shelf Fenestrated and Branched Stent Graft Designs for Abdominal Aortic Aneurysm Repair.” *Seminars in Vascular Surgery* 29(1–2):74–83.

Menichini, C., Cheng, Z., Gibbs, R. G. J., and Xu, X. Y. (2018). “A Computational Model for False Lumen Thrombosis in Type B Aortic Dissection Following Thoracic Endovascular Repair.” *Journal of Biomechanics* 66:36–43.

Menichini, C., and Xu, X. Y. (2016). “Mathematical Modeling of Thrombus Formation in Idealized Models of Aortic Dissection: Initial Findings and Potential Applications.” *Journal of Mathematical Biology* 73(5):1205–26.

Menter, F. R. (1994). “Two-Equation Eddy-Viscosity Turbulence Models for Engineering Applications.” *AIAA Journal* 32(8):1598–1605.

Menter, F. R., Langtry, R., and Völker, S. (2006). “Transition Modelling for General Purpose CFD Codes.” *Flow, Turbulence and Combustion* 77(1–4):277–303.

Midulla, M., Moreno, R., Baali, A., Chau, M., Negre-Salvayre, A., Nicoud, F., Pruvo, J. P., Haulon, S., and Rousseau, H. (2012). “Haemodynamic Imaging of Thoracic Stent-Grafts by Computational Fluid Dynamics (CFD): Presentation of a Patient-Specific Method Combining Magnetic Resonance Imaging and Numerical Simulations.” *European Radiology* 22(10):2094–2102.

Miyamoto, Y. (2014). “Elephant Trunk Technique for Hybrid Aortic Arch Repair.” *General Thoracic and Cardiovascular Surgery* 62(3):135–41.

Miyazaki, S., Itatani, K., Furusawa, T., Nishino, T., Sugiyama, M., Takehara, Y., and Yasukochi, S. (2017). “Validation of Numerical Simulation Methods in Aortic Arch Using 4D Flow MRI.” *Heart and Vessels* 32(8):1032–44.

Mohrman, D., and Heller, L. J. (2006). *Cardiovascular Physiology*. McGraw-Hill Medical.

Moore, A. G., Eagle, K. A., Bruckman, D., Moon, B. S., Malouf, J. F., Fattori, R., Evangelista, A., Isselbacher, E. M., Suzuki, T., Nienaber, C. A., Gilon, D., and Oh, J. K. (2002). “Choice of Computed Tomography, Transesophageal Echocardiography, Magnetic Resonance Imaging, and Aortography in Acute Aortic Dissection: International Registry of Acute Aortic Dissection (IRAD).” *American Journal of Cardiology* 89(10):1235–38.

Moore, J. E. and Ku, D. N. (1994). “Pulsatile Velocity Measurements in a Model of the Human Abdominal Aorta under Resting Conditions.” *Journal of Biomechanical Engineering* 116(3):337–46.

Mori, D., and Yamaguchi, T. (2002). “Computational Fluid Dynamics Modeling and Analysis of the Effect of 3-D Distortion of the Human Aortic Arch.” *Computer Methods in Biomechanics and Biomedical Engineering* 5(3):249–60.

Nagano, N., Cartier, R., Zigras, T., Mongrain, R., and Leask, R. L. (2007). “Mechanical Properties and Microscopic Findings of a Dacron Graft Explanted 27 Years after Coarctation Repair.” *Journal of Thoracic and Cardiovascular Surgery* 134(6):1577–78.

Nardi, A., and Avrahami, I. (2017). “Approaches for Treatment of Aortic Arch Aneurysm, a Numerical Study.” *Journal of Biomechanics* 50:158–65.

Nathan, D. P., Xu, C., Gorman, J. H., Fairman, R. M., Bavaria, J. E., Gorman, R. C., Chandran, K. B., and

Jackson, B. M. (2011). "Pathogenesis of Acute Aortic Dissection: A Finite Element Stress Analysis." *Annals of Thoracic Surgery* 91(2):458–63.

Nerem, R. M., Seed, W. A., and Wood, N. B. (1972). "An Experimental Study of the Velocity Distribution and Transition to Turbulence in the Aorta." *Journal of Fluid Mechanics* 52(1):137–60.

Neri, E., Barabesi, L., Buklas, D., Vricella, L. A., Benvenuti, A., Tucci, E., Sassi, C., and Massetti, M. (2005). "Limited Role of Aortic Size in the Genesis of Acute Type A Aortic Dissection." *European Journal of Cardio-Thoracic Surgery* 28(6):857–63.

Nesbitt, W. S., Westein, E., Tovar-Lopez, F. J., Tolouei, E., Mitchell, A., Fu, J., Carberry, J., Fouras, A., and Jackson, S. P. (2009). "A Shear Gradient-Dependent Platelet Aggregation Mechanism Drives Thrombus Formation." *Nature Medicine* 15(6):665–73.

Nichols, W. W., O'Rourke, M. F., Vlachopoulos, C., Hoeks, A. P., and Reneman, R. S. (2011). *McDonald's Blood Flow in Arteries Theoretical, Experimental and Clinical Principles*. CRC press.

Nienaber, C. A., Clough, R. E., Sakalihasan, N., Suzuki, T., Gibbs, R., Mussa, F., Jenkins, M. T., Thompson, M. M., Evangelista, A., Yeh, J. S. M., Cheshire, N., Rosendahl, U., and Pepper, J. (2016). "Aortic Dissection." *Nature Reviews Disease Primers* 2(July).

Nienaber, C. A. and Eagle, K. A. (2003). "Aortic Dissection: New Frontiers in Diagnosis and Management. Part I: From Etiology to Diagnostic Strategies." *Circulation* 108(5):628–35.

Nistri, S., Sorbo, M. D., Marin, M., Palisi, M., Scognamiglio, R., and Thiene, G. (1999). "Aortic Root Dilatation in Young Men with Normally Functioning Bicuspid Aortic Valves." *Heart* 82(1):19–22.

Nkomo, V. T., Enriquez-Sarano, M., Ammash, N. M., Melton, L. J., Bailey, K. R., Desjardins, V., Horn, R. A., and Tajik, A. J. (2003). "Bicuspid Aortic Valve Associated with Aortic Dilatation: A Community-Based Study." *Arteriosclerosis, Thrombosis, and Vascular Biology* 23(2):351–56.

Nobili, M., Sheriff, J., Morbiducci, U., Redaelli, A., and Bluestein, D. (2008). "Platelet Activation Due to Hemodynamic Shear Stresses: Damage Accumulation Model and Comparison to in Vitro Measurements." *ASAIO Journal* 54(1):64–72.

Numata, S., Itatani, K., Kanda, K., Doi, K., Yamazaki, S., Morimoto, K., Manabe, K., Ikemoto, K., and Yaku, H. (2016). "Blood Flow Analysis of the Aortic Arch Using Computational Fluid Dynamics." *European Journal of Cardio-Thoracic Surgery* 49(6):1578–85.

Oderich, G. S., and Silveira, P. G. (2016). "Initial Experience With the GORE ® EXCLUDER ® Thoracoabdominal Branch Endoprosthesis." *Endovascular Today* 15(3):12–16.

Oderich, G. S., Farber, M. A., Silveira, P. G., Tadros, R., Marin, M., Fillinger, M., Makaroun, M., Hemmer, J., and Madden, M., (2019). "Technical Aspects and 30-Day Outcomes of the Prospective Early Feasibility Study of the GORE EXCLUDER Thoracoabdominal Branched Endoprosthesis (TAMBE) to Treat Pararenal and Extent IV Thoracoabdominal Aortic Aneurysms." *Journal of Vascular*

Surgery 70(2):358-368.e6.

Oderich, G. S., Ribeiro, M., de Souza, L. R., Hofer, J., Wigham, J., and Cha, S. (2017). “Endovascular Repair of Thoracoabdominal Aortic Aneurysms Using Fenestrated and Branched Endografts.” *Journal of Thoracic and Cardiovascular Surgery* 153(2):S32-S41.e7.

Olufsen, M. S., Peskin, C. S., Kim, W. Y., Pedersen, E. M., Nadim, A., and Larsen, J. (2000). “Numerical Simulation and Experimental Validation of Blood Flow in Arteries with Structured-Tree Outflow Conditions.” *Annals of Biomedical Engineering* 28(11):1281–99.

Onitsuka, S., Akashi, H., Tayama, K., Okazaki, T., Ishihara, K., Hiromatsu, S., and Aoyagi, S. (2004). “Long-Term Outcome and Prognostic Predictors of Medically Treated Acute Type B Aortic Dissections.” *Annals of Thoracic Surgery* 78(4):1268–73.

Pacini, D., Di Marco, L., Fortuna, D., Belotti, L. M. B., Gabbieri, D., Zussa, C., Pigini, F., Contini, A., Barattoni, M. C., De Palma, R., and Di Bartolomeo, R. (2013). “Acute Aortic Dissection: Epidemiology and Outcomes.” *International Journal of Cardiology* 167(6):2806–12.

Panuccio, G., Bisdas, T., Berekoven, B., Torsello, G., and Austermann, M. (2015). “Performance of Bridging Stent Grafts in Fenestrated and Branched Aortic Endografting.” *European Journal of Vascular and Endovascular Surgery* 50(1):60–70.

Pape, L. A., Awais, M., Woznicki, E. M., Suzuki, T., Trimarchi, S., Evangelista, A., Myrmel, T., Larsen, M., Harris, K. M., Greason, K., Di Eusanio, M., Bossone, E., Montgomery, D. G., Eagle, K. A., Nienaber, C. A., Isselbacher, E. M., and O’Gara, P. (2015). “Presentation, Diagnosis, and Outcomes of Acute Aortic Dissection: 17-Year Trends from the International Registry of Acute Aortic Dissection.” *Journal of the American College of Cardiology* 66(4):350–58.

Patel, H. J., Dake, M. D., Bavaria, J. E., Singh, M. J., Filinger, M., Fischbein, M. P., Williams, D. M., Matsumura, J. S., and Oderich, G. (2016). “Branched Endovascular Therapy of the Distal Aortic Arch: Preliminary Results of the Feasibility Multicenter Trial of the Gore Thoracic Branch Endoprosthesis.” *Annals of Thoracic Surgery* 102(4):1190–98.

Patel, R. P., Katsargyris, A., Verhoeven, E. L. G., Adam, D. J., and Hardman, J. A. (2013). “Endovascular Aortic Aneurysm Repair with Chimney and Snorkel Grafts: Indications, Techniques and Results.” *CardioVascular and Interventional Radiology* 36(6):1443–51.

Peate, I., and Nair, M. (2016). *Fundamentals of Anatomy and Physiology: For Nursing and Healthcare Students, 2nd Edition*. John Wiley and Sons.

Perktold, K., Resch, M., and Florian, H. (1991). “Pulsatile Non-Newtonian Flow Characteristics in a Three-Dimensional Human Carotid Bifurcation Model.” *Journal of Biomechanical Engineering* 113(4):464–75.

Perrin, D., Badel, P., Orgéas, L., Geindreau, C., Dumenil, A., Albertini, J. N., and Avril, S. (2015). “Patient-

Specific Numerical Simulation of Stent-Graft Deployment: Validation on Three Clinical Cases." *Journal of Biomechanics* 48(10):1868–75.

Pirola, S., Cheng, Z., Jarral, O. A., O'Regan, D. P. , Pepper, J. R., Athanasiou, T., and Xu, X. Y. (2017). "On the Choice of Outlet Boundary Conditions for Patient-Specific Analysis of Aortic Flow Using Computational Fluid Dynamics." *Journal of Biomechanics* 60:15–21.

Pirola, S., Jarral, O. A., O'Regan, D. P., Asimakopoulos, G., Anderson, J. R., Pepper, J. R., Athanasiou, T., and Xu, X. Y. (2018). "Computational Study of Aortic Hemodynamics for Patients with an Abnormal Aortic Valve: The Importance of Secondary Flow at the Ascending Aorta Inlet." *APL Bioengineering* 2(2):026101.

Pirola, S., Guo, B., Menichini, C., Saitta, S., Fu, W., Dong, Z., and Xu, X. Y. (2019). "4-D Flow Mri-Based Computational Analysis of Blood Flow in Patient-Specific Aortic Dissection." *IEEE Transactions on Biomedical Engineering* 66(12):3411–19.

Pyeritz, R. E. (2016). "Recent Progress in Understanding the Natural and Clinical Histories of the Marfan Syndrome." *Trends in Cardiovascular Medicine* 26(5):423–28.

Qiao, A., Yin, W., and Chu, B. (2015). "Numerical Simulation of Fluid–Structure Interaction in Bypassed DeBakey III Aortic Dissection." *Computer Methods in Biomechanics and Biomedical Engineering* 18(11):1173–80.

Qiao, Y., Zeng, Y., Ding, Y., Fan, J., Luo, K., and Zhu, T. (2019). "Numerical Simulation of Two-Phase Non-Newtonian Blood Flow with Fluid-Structure Interaction in Aortic Dissection." *Computer Methods in Biomechanics and Biomedical Engineering* 22(6):620–30.

Quemada, D. (1978). "Rheology of Concentrated Disperse Systems II. A Model for Non-Newtonian Shear Viscosity in Steady Flows." *Rheologica Acta* 17(6):632–42.

Quint, L. E., Platt, J. F., Sonnad, S. S., Deeb, G. M., and Williams, D. M. (2003). "Aortic Intimal Tears: Detection with Spiral Computed Tomography." *Journal of Endovascular Therapy* 10(3):505–10.

Rachid, K. (2017). "2-Element, 3-Element and 4 Element Windkessel Models." https://commons.wikimedia.org/wiki/File:2-element,_3 element_and_4_element_Windkessel_models.svg

Raghavan, M. L., and Vorp, D. A. (2000). "Toward a Biomechanical Tool to Evaluate Rupture Potential of Abdominal Aortic Aneurysm: Identification of a Finite Strain Constitutive Model and Evaluation of Its Applicability." *Journal of Biomechanics* 33(4):475–82.

Raghavan, M. L., Webster, M. W., and Vorp, D. A. (1996). "Ex Vivo Biomechanical Behavior of Abdominal Aortic Aneurysm: Assessment Using a New Mathematical Model." *Annals of Biomedical Engineering* 24(5):573–82.

Raghavan, M. L., Kratzberg, J. A., and Golzarian, J. (2005). "Introduction to Biomechanics Related to

Endovascular Repair of Abdominal Aortic Aneurysm.” *Techniques in Vascular and Interventional Radiology* 8(1 SPEC. ISS.):50–55.

Rahmani, S., Grewal, I. S., Nabovati, A., Doyle, M. G., Roche-Nagle, G., and Tse, L. W. (2016). “Increasing Angulation Decreases Measured Aortic Stent Graft Pullout Forces.” *Journal of Vascular Surgery* 63(2):493–99.

Reneman, R. S., Arts, T., and Hoeks, A. P. G., (2006). “Wall Shear Stress - An Important Determinant of Endothelial Cell Function and Structure - In the Arterial System in Vivo: Discrepancies with Theory.” *Journal of Vascular Research* 43(3):251–69.

Resch, T., Koul, B., Dias, N. V., Lindblad, B., and Ivancev, K. (2001). “Changes in Aneurysm Morphology and Stent-Graft Configuration after Endovascular Repair of Aneurysms of the Descending Thoracic Aorta.” *Journal of Thoracic and Cardiovascular Surgery* 122(1):47–52.

Reymond, P., Merenda, F., Perren, F., Rüfenacht, D., and Stergiopulos, N. (2009). “Validation of a One-Dimensional Model of the Systemic Arterial Tree.” *American Journal of Physiology - Heart and Circulatory Physiology* 297(1):208–22.

Rinaudo, A., D’Ancona, G., Lee, J. J., Pilato, G., Amaducci, A., Baglini, R., Follis, F., Pilato, M., and Pasta, S. (2014). “Predicting Outcome of Aortic Dissection with Patent False Lumen by Computational Flow Analysis.” *Cardiovascular Engineering and Technology* 5(2):176–88.

Robinson, P. N., Arteaga-Solis, E., Baldock, C., Collod-Béroud, G., Booms, P., De Paepe, A., Dietz, H. C., Guo, G., Handford, P. A., Judge, D. P., Kielty, C. M., Loeys, B., Milewicz, D. M., Ney, A., Ramirez, F., Reinhardt, D. P., Tiedemann, K., Whiteman, P., and Godfrey, M. (2006). “The Molecular Genetics of Marfan Syndrome and Related Disorders.” *Journal of Medical Genetics* 43(10):769–87.

Roy, D., Kauffmann, C., Delorme, S., Lerouge, S., Cloutier, G., and Soulez, G. (2012). “A Literature Review of the Numerical Analysis of Abdominal Aortic Aneurysms Treated with Endovascular Stent Grafts.” *Computational and Mathematical Methods in Medicine* 2012.

Rudenick, P. A., Bijnens, B. H., García-Dorado, D., and Evangelista, A. (2013). “An in Vitro Phantom Study on the Influence of Tear Size and Configuration on the Hemodynamics of the Lumina in Chronic Type B Aortic Dissections.” *Journal of Vascular Surgery* 57(2):464-474.e5.

Rudenick, P. A., Bijnens, B. H., Segers, P., García-Dorado, D., and Evangelista, A. (2015). “Assessment of Wall Elasticity Variations on Intraluminal Haemodynamics in Descending Aortic Dissections Using a Lumped-Parameter Model.” *PLoS ONE* 10(4):1–17.

Rudenick, P. A., Bordone, M., Bijnens, B. H., Soudah, E., Oñate, E., Garcia-Dorado, D., and Evangelista, A. (2010). “A Multi-Method Approach towards Understanding the Pathophysiology of Aortic Dissections - The Complementary Role of in-Silico, in-Vitro and in-Vivo Information.” *Lecture*

Notes in Computer Science (Including Subseries Lecture Notes in Artificial Intelligence and Lecture Notes in Bioinformatics) 6364 LNCS:114–23.

Ryzhakov, P., Soudah, E., and Dialami, N. (2019). “Computational Modeling of the Fluid Flow and the Flexible Intimal Flap in Type B Aortic Dissection via a Monolithic Arbitrary Lagrangian/Eulerian Fluid-Structure Interaction Model.” *International Journal for Numerical Methods in Biomedical Engineering* 35(11):5–8.

Shahverdyan, R., Majd, M. P., Thul, R., Braun, N., Gawenda, M., and Brunkwall, J. (2015). “F-EVAR Does Not Impair Renal Function More than Open Surgery for Juxtarenal Aortic Aneurysms: Single Centre Results.” *European Journal of Vascular and Endovascular Surgery* 50(4):432–41.

Shang, E. K., Nathan, D. P., Sprinkle, S. R., Vigmostad, S. C., Fairman, R. M., Bavaria, J. E., Gorman, R. C. , Gorman III, J. H., Chandran, K. B., and Jackson, B. M. (2013). “Peak Wall Stress Predicts Expansion Rate in Descending Thoracic Aortic Aneurysms.” *The Annals of Thoracic Surgery* 95(2):593–98.

Shang, E. K., Nathan, D. P., Fairman, R. M., Bavaria, J. E., Gorman, R. C., Gorman, J. H., and Jackson, B. M. (2015). “Use of Computational Fluid Dynamics Studies in Predicting Aneurysmal Degeneration of Acute Type B Aortic Dissections.” *Journal of Vascular Surgery* 62(2):279–84.

Shiga, T., Wajima, Z. I., Apfel, C. C., Inoue, T., and Ohe, Y. (2006). “Diagnostic Accuracy of Transesophageal Echocardiography, Helical Computed Tomography, and Magnetic Resonance Imaging for Suspected Thoracic Aortic Dissection: Systematic Review and Meta-Analysis.” *Archives of Internal Medicine* 166(13):1350–56.

Shirakawa, Y., Kuratani, T., Shimamura, K., Torikai, K., Sakamoto, T., Shijo, T., and Sawa, Y. (2014). “The Efficacy and Short-Term Results of Hybrid Thoracic Endovascular Repair into the Ascending Aorta for Aortic Arch Pathologies.” *European Journal of Cardio-Thoracic Surgery* 45(2):298–304.

Shrestha, M., Martens, A., Behrendt, S., Maeding, I., Koigeldiyev, N., and Haverich, A. (2014). “Is the Branched Graft Technique Better than the En Bloc Technique for Total Aortic Arch Replacement?” *European Journal of Cardio-Thoracic Surgery* 45(1):181–87.

Simon, C. H., Liu, W., Wong, R. H., Underwood, M., and Wang, D. (2016). “The Potential of Computational Fluid Dynamics Simulation on Serial Monitoring of Hemodynamic Change in Type B Aortic Dissection.” *Cardiovascular and Interventional Radiology* 39(8):1090–98.

Singh, S. D., Xu, X. Y., Pepper, J. R., Izgi, C., Treasure, T., and Mohiaddin, R. H. (2016). “Effects of Aortic Root Motion on Wall Stress in the Marfan Aorta before and after Personalised Aortic Root Support (PEARS) Surgery.” *Journal of Biomechanics* 49(10):2076–84.

Singh, S. D., Xu, X. Y., Wood, N. B., Pepper, J. R., Izgi, C., Treasure, T., and Mohiaddin, R. H. (2016). “Aortic Flow Patterns before and after Personalised External Aortic Root Support Implantation in Marfan Patients." *Journal of Biomechanics* 49(1):100–111.

Siu, S. C., and Silversides, C. K. (2010). "Bicuspid Aortic Valve Disease." *Journal of the American College of Cardiology* 55(25):2789–2800.

Slagger, C. J., Wentzell, J. J., Gijsen, F. J. H., Thury, A., van der Waal, A. C., Schaar, J. A., and Serruys, P. W. (2005). "The Role of Shear Stress in the Destabilization of Vulnerable Plaques and Related Therapeutic Implications." *Nature Clinical Practice Cardiovascular Medicine* 2(9):456–64.

Song, S. W., Chang, B. C., Cho, B. K., Yi, G., Youn, Y. N., Lee, S., and Yoo, K. J. (2010). "Effects of Partial Thrombosis on Distal Aorta after Repair of Acute DeBakey Type I Aortic Dissection." *Journal of Thoracic and Cardiovascular Surgery* 139(4):841-847.e1.

Soudah, E., Rudenick, P., Bordone, M., Bijnens, B., García-Dorado, D., Evangelista, A., and Oñate, E. (2015). "Validation of Numerical Flow Simulations against in Vitro Phantom Measurements in Different Type B Aortic Dissection Scenarios." *Computer Methods in Biomechanics and Biomedical Engineering* 18(8):805–15.

Spear, R., Haulon, S., Ohki, T., Tsilimparis, N., Kanaoka, Y., Milne, C. P. E., Debus, S., Takizawa, R., and Kölbel, T. (2016). "Editor's Choice - Subsequent Results for Arch Aneurysm Repair with Inner Branched Endografts." *European Journal of Vascular and Endovascular Surgery* 51(3):380–85.

Stein, P. D., and Sabbah, H. N. (1976). "Turbulent Blood Flow in the Ascending Aorta of Humans with Normal and Diseased Aortic Valves." *Circulation Research* 39(1):58–65.

Suess, T., Anderson, J., Danielson, L., Pohlson, K., Remund, T., Blears, E., Gent, S., and Kelly, P. (2016). "Examination of Near-Wall Hemodynamic Parameters in the Renal Bridging Stent of Various Stent Graft Configurations for Repairing Visceral Branched Aortic Aneurysms." *Journal of Vascular Surgery* 64(3):788–96.

Sueyoshi, E., Sakamoto, I., Hayashi, K., Yamaguchi, T., and Imada, T. (2004). "Growth Rate of Aortic Diameter in Patients with Type B Aortic Dissection during the Chronic Phase." *Circulation* 110(11 SUPPL.):256–61.

Sun, Z., and Chaichana, T. (2010). "Fenestrated Stent Graft Repair of Abdominal Aortic Aneurysm: Hemodynamic Analysis of the Effect of Fenestrated Stents on the Renal Arteries." *Korean Journal of Radiology* 11(1):95–106.

Šutalo, I. D., Lawrence-Brown, M .M. D., Ahmed, S., Liffman, K., and Semmens, J. B. (2008). "Modeling of Antegrade and Retrograde Flow into a Branch Artery of the Aorta: Implications for Endovascular Stent-Grafting and Extra-Anatomical Visceral Bypass." *Journal of Endovascular Therapy* 15(3):300–309.

Svensson, L. G., Kouchoukos, N. T., Miller, D.C., Bavaria, J. E., Coselli, J. S., Curi, M. A., Eggebrecht, H., Elefteriades, J. A., Erbel, R., Gleason, T. G., Lytle, B. W., Mitchell, R. S., Nienaber, C. A., Roselli, E.

E., Safi, H. J., Shemin, R. J., Sicard, G. A., Sundt, T. M., Szeto, W. Y., and Wheatley, G. H. (2008). "Expert Consensus Document on the Treatment of Descending Thoracic Aortic Disease Using Endovascular Stent-Grafts." *Annals of Thoracic Surgery* 85(1 SUPPL.).

Sweet, M. P., Starnes, B. W., and Tatum, B. (2015). "Endovascular Treatment of Thoracoabdominal Aortic Aneurysm Using Physician-Modified Endografts Presented at the Plenary Session of the Twenty-Ninth Annual Meeting of the Western Vascular Society, Coronado, Calif, September 20-23, 2014." *Journal of Vascular Surgery* 62(5):1160–67.

Tadros, T. M., Klein, M. D., and Shapira, O. Z. (2009). "Ascending Aortic Dilatation Associated with Bicuspid Aortic Valve. Pathophysiology, Molecular Biology, and Clinical Implications." *Circulation* 119(6):880–90.

Tan, F. P. P., Borghi, A., Mohiaddin, R. H., Wood, N. B., Thom, S., and Xu, X. Y. (2009). "Analysis of Flow Patterns in a Patient-Specific Thoracic Aortic Aneurysm Model." *Computers and Structures* 87(11–12):680–90.

Tan, F. P. P., Soloperto, G., Bashford, S., Wood, N. B., Thom, S., Hughes, A., and Xu, X. Y. (2008). "Analysis of Flow Disturbance in a Stenosed Carotid Artery Bifurcation Using Two-Equation Transitional and Turbulence Models." *Journal of Biomechanical Engineering* 130(6):1–12.

Tan, F. P. P., Torii, R., Borghi, A., Mohiaddin, R. H., Wood, N. B., and Xu, X. Y. (2009). "Fluid-Structure Interaction Analysis of Wall Stress and Flow Patterns in a Thoracic Aortic Aneurysm." *International Journal of Applied Mechanics* 1(1):179–99.

Tan, M. E. S. H., Morshuis, W. J., Dossche, K. M. E., Kelder, J. C., Waanders, F. G. J., and Schepens, M. A. A. M. (2005). "Long-Term Results after 27 Years of Surgical Treatment of Acute Type A Aortic Dissection." *Annals of Thoracic Surgery* 80(2):523–29.

Tang, A. Y. S., Fan, Y., Cheng, S. W. K., and Chow, K. W. (2012). "Biomechanical Factors Influencing Type b Thoracic Aortic Dissection: Computational Fluid Dynamics Study." *Engineering Applications of Computational Fluid Mechanics* 6(4):622–32.

Tang, B. T., Cheng, C. P., Draney, M. T., Wilson, N. M., Tsao, P. S., Herfkens, R. J., and Taylor, C. A., (2006). "Abdominal Aortic Hemodynamics in Young Healthy Adults at Rest and during Lower Limb Exercise: Quantification Using Image-Based Computer Modeling." *American Journal of Physiology - Heart and Circulatory Physiology* 291(2):668–76.

Taylor, C. A., and Figueroa, C. A. (2009). "Patient-Specific Modeling of Cardiovascular Mechanics." *Annual Review of Biomedical Engineering* 11(1):109–34.

Taylor, C. A., Cheng, C. P., Espinosa, L. A., Tang, B. T., Parker, D., and Herfkens, R. J. (2002). "In Vivo Quantification of Blood Flow and Wall Shear Stress in the Human Abdominal Aorta during Lower Limb Exercise." *Annals of Biomedical Engineering* 30(3):402–8.

Thrumurthy, S. G., Karthikesalingam, A., Patterson, B. O., Holt, P. J. E., and Thompson, M. M. (2012). “The Diagnosis and Management of Aortic Dissection.” *BMJ (Online)* 344(7839):2537–41.

Thubrikar, M. J., Agali, P., and Robicsek, F. (1999). “Wall Stress as a Possible Mechanism for the Development of Transverse Intimal Tears in Aortic Dissections.” *Journal of Medical Engineering and Technology* 23(4):127–34.

Thurnher, S. A., and Grabenwöger, M. (2002). “Endovascular Treatment of Thoracic Aortic Aneurysms: A Review.” *European Radiology* 12(6):1370–87.

Tokuda, Y., Oshima, H., Narita, Y., Abe, T., Araki, Y., Mutsuga, M., Fujimoto, K., Terazawa, S., Yagami, K., Ito, H., Yamamoto, K., Komori, K., and Usui, A. (2016). “Hybrid versus Open Repair of Aortic Arch Aneurysms: Comparison of Postoperative and Mid-Term Outcomes with a Propensity Score-Matching Analysis.” *European Journal of Cardio-Thoracic Surgery* 49(1):149–56.

Tokuda, Y., Song, M. H., Ueda, Y., Usui, A., Akita, T., Yoneyama, S., and Maruyama, S. (2008). “Three-Dimensional Numerical Simulation of Blood Flow in the Aortic Arch during Cardiopulmonary Bypass.” *European Journal of Cardio-Thoracic Surgery* 33(2):164–67.

Torii, R., Kalantzi, M., Theodoropoulos, S., Sarathchandra, P., Xu, X. Y., and Yacoub, M. H. (2013). “Predicting Impending Rupture of the Ascending Aorta with Bicuspid Aortic Valve: Spatiotemporal Flow and Wall Shear Stress.” *JACC: Cardiovascular Imaging* 6(9):1017–19.

Trimarchi, S., Eagle, K. A., Nienaber, C. A., Rampoldi, V., Jonker, F. H. W., Vincentiis, C. D., Frigiola, A., Menicanti, L., Tsai, T., Froehlich, J., Evangelista, A., Montgomery, D., Bossone, E., Cooper, J. V., Li, J., Deeb, M. G., Meinhardt, G., Sundt, T. M., and Isselbacher, E. M. (2010). “Role of Age in Acute Type A Aortic Dissection Outcome: Report from the International Registry of Acute Aortic Dissection (IRAD).” *Journal of Thoracic and Cardiovascular Surgery* 140(4):784–89.

Tsai, T. T., Evangelista, A., Nienaber, C. A., Myrmel, T., Meinhardt, G., Cooper, J. V., Smith, D. E., Suzuki, T., Fattori, R., Llovet, A., and Froehlich, J. (2007). “Partial Thrombosis of the False Lumen in Patients with Acute Type B Aortic Dissection.” *New England Journal of Medicine* 357(4):349–59.

Tsai, T. T., Schlicht, M. S., Khanafer, K., Bull, J. L., Valassis, D. T., Williams, D. M., Berguer, R., and Eagle, K. A. (2008). “Tear Size and Location Impacts False Lumen Pressure in an Ex Vivo Model of Chronic Type B Aortic Dissection.” *Journal of Vascular Surgery* 47(4):844–51.

Tse, K. M., Chang, R., Lee, H. P., Lim, S. P., Venkatesh, S. K., and Ho, P. (2013). “A Computational Fluid Dynamics Study on Geometrical Influence of the Aorta on Haemodynamics.” *European Journal of Cardio-Thoracic Surgery* 43(4):829–38.

Tse, K. M., Chiu, P., Lee, H. P., and Ho, P. (2011). “Investigation of Hemodynamics in the Development of Dissecting Aneurysm within Patient-Specific Dissecting Aneurismal Aortas Using Computational Fluid Dynamics (CFD) Simulations.” *Journal of Biomechanics* 44(5):827–36.

Ueda, T., Fleischmann, D., Dake, M. D., Rubin, G. D., and Sze, D. Y. (2010). "Incomplete Endograft Apposition to the Aortic Arch: Bird-Beak Configuration Increases Risk of Endoleak Formation after Thoracic Endovascular Aortic Repair." *Radiology* 255(2):645–52.

van Bakel, T. M., Arthurs, C. J., Van Herwaarden, J. A., Moll, F. L., Eagle, K. A., Patel, H. J., Trimarchi, S., and Figueroa, C, A. (2018). "A Computational Analysis of Different Endograft Designs for Zone 0 Aortic Arch Repair." *European Journal of Cardio-Thoracic Surgery* 54(2):389–96.

van Bakel, T. M., de Beaufort, H. W., Trimarchi, S., Marrocco-Trischitta, M. M., Bismuth, J., Moll, F. L., Patel, H. J., and van Herwaarden, J. A. (2018). "Status of Branched Endovascular Aortic Arch Repair." *Annals of Cardiothoracic Surgery* 7(3):409–16.

van Bogerijen, G. H., Auricchio, F., Conti, M., Lefieux, A., Reali, A., Veneziani, A., Tolenaar, J. L., Moll, F. L., Rampoldi, V., and Trimarchi, S. (2014). "Aortic Hemodynamics after Thoracic Endovascular Aortic Repair, with Particular Attention to the Bird-Beak Configuration." *Journal of Endovascular Therapy* 21(6):791–802.

van Puyvelde, J., Verbeken, E., Verbrugghe, P., Herijgers, P., and Meuris, B. (2016). "Aortic Wall Thickness in Patients with Ascending Aortic Aneurysm versus Acute Aortic Dissection." *European Journal of Cardio-Thoracic Surgery* 49(3):756–62.

Verma, S., and Siu, S. C., (2014). "Aortic Dilatation in Patients with Bicuspid Aortic Valve." *New England Journal of Medicine* 370(20):1920–29.

Versteeg, H. K., and Malalasekera, W. (2007). *An Introduction to Computational Fluid Dynamics: The Finite Volume Method*. Pearson education.

Vignon-Clementel, I. E., Figueroa, C. A., Jansen, K. E., and Taylor, C. A. (2006). "Outflow Boundary Conditions for Three-Dimensional Finite Element Modeling of Blood Flow and Pressure in Arteries." *Computer Methods in Applied Mechanics and Engineering* 195(29–32):3776–96.

Vorp, D. A., and Geest, J. P. V. (2005). "Biomechanical Determinants of Abdominal Aortic Aneurysm Rupture." *Arteriosclerosis, Thrombosis, and Vascular Biology* 25(8):1558–66.

Wan Ab Naim, W. N., Ganesan, P. B., Sun, Z., Osman, K., and Lim, E. (2014). "The Impact of the Number of Tears in Patient-Specific Stanford Type b Aortic Dissecting Aneurysm: CFD Simulation." *Journal of Mechanics in Medicine and Biology* 14(2):1450017.

Waterford, S. D., Chou, D., Bombien, R., Uzun, I., Shah, A., and Khoynezhad, A. (2016). "Left Subclavian Arterial Coverage and Stroke during Thoracic Aortic Endografting: A Systematic Review." *Annals of Thoracic Surgery* 101(1):381–89.

Wei, L., Leo, H. L., Chen, Q., and Li, Z. (2019). "Structural and Hemodynamic Analyses of Different Stent Structures in Curved and Stenotic Coronary Artery." *Frontiers in Bioengineering and Biotechnology* 7(December):1–13.

Weltert, L., De Paulis, R., Scaffa, R., Maselli, D., Bellisario, A., and D'Alessandro, S. (2009). "Re-Creation of a Sinuslike Graft Expansion in Bentall Procedure Reduces Stress at the Coronary Button Anastomoses: A Finite Element Study." *Journal of Thoracic and Cardiovascular Surgery* 137(5):1082–87.

Wen, J., Zheng, T., Jiang, W., Deng, X., and Fan, Y. (2011). "A Comparative Study of Helical-Type and Traditional-Type Artery Bypass Grafts: Numerical Simulation." *ASAIO Journal* 57(5):399–406.

Wenstrup, R. J., Meyer, R. A., Lyle, J. S., Hoechstetter, L., Rose, P. S., Levy, H. P., and Francomano, C. A. (2002). "Prevalence of Aortic Root Dilation in the Ehlers-Danlos Syndrome." *Genetics in Medicine* 4(3):112–17.

Westaby, S., Saito, S., and Katsumata, T. (2002). "Acute Type A Dissection: Conservative Methods Provide Consistently Low Mortality." *The Annals of Thoracic Surgery* 73(3):707–13.

Westerhof, N., Lankhaar, J. W., and Westerhof, B. E. (2009). "The Arterial Windkessel." *Medical and Biological Engineering and Computing* 47(2):131–41.

White, G. H., Yu, W., and May, J. (1996). "To the Editors: 'Endoleak'—A Proposed New Terminology to Describe Incomplete Aneurysm Exclusion by an Endoluminal Graft." *Journal of Endovascular Therapy* 3(1):124–25.

Wilcox, D. C. (1998). *Turbulence Modeling for CFD, Volume 2*. La Canada, CA: DCW industries.

Williams, L. R., and Leggett, R. W. (1989). "Reference Values for Resting Blood Flow to Organs of Man." *Clinical Physics and Physiological Measurement* 10(3):187–217.

Womersley, J. R. (1955). "Method for the Calculation of Velocity, Rate of Flow and Viscous Drag in Arteries When the Pressure Gradient Is Known." *The Journal of Physiology* 127(3):553–63.

Wood, N. B. (1999). "Aspects of Fluid Dynamics Applied to the Larger Arteries." *Journal of Theoretical Biology* 199(2):137–61.

Xiao, N., Alastruey, J., and Figueroa, C. A. (2014). "A Systematic Comparison between 1-D and 3-D Hemodynamics in Compliant Arterial Models." *International Journal for Numerical Methods in Biomedical Engineering* 30(2):204–31.

Xu, H., Li, Z., Dong, H., Zhang, Y., Wei, J., Watton, P. N., Guo, W., Chen, D., and Xiong, J. (2017). "Hemodynamic Parameters That May Predict False-Lumen Growth in Type-B Aortic Dissection after Endovascular Repair: A Preliminary Study on Long-Term Multiple Follow-Ups." *Medical Engineering and Physics* 50:12–21.

Yao, J. S. T., and Eskandari, M. K. (2012). "Transfemoral Intraluminal Graft Implantation for Abdominal Aortic Aneurysms: Two Decades Later." *Annals of Vascular Surgery* 26(7):895–905.

Yin, H., and Pickering, J. G. (2016). "Cellular Senescence and Vascular Disease: Novel Routes to Better Understanding and Therapy." *Canadian Journal of Cardiology* 32(5):612–23.

Yu, H. Y., Chen, Y. S., Huang, S. C., Wang, S. S., and Lin, F. Y. (2004). "Late Outcome of Patients with Aortic Dissection: Study of a National Database." *European Journal of Cardio-Thoracic Surgery* 25(5):683–90.

Yunoki, J., Kuratani, T., Shirakawa, Y., Torikai, K., Shimamura, K., Kin, K., and Sawa, Y. (2014). "Clinical Experience with the RELAY NBS PLUS Stent–Graft for Aortic Arch Pathology." *Surgery Today* 44(12):2263–68.

Zamir, M., Sinclair, P., and Wonnacott, T. H. (1992). "Relation between Diameter and Flow in Major Branches of the Arch of the Aorta." *Journal of Biomechanics* 25(11):1303–10.

Zamor, K. C., Eskandari, M. K., Rodriguez, H. E., Ho, K. J., Morasch, M. D., and Hoel, A. W. (2015). "Outcomes of Thoracic Endovascular Aortic Repair and Subclavian Revascularization Techniques." *Journal of the American College of Surgeons* 221(1):93–100.

Zhang, P., Liu, X., Sun, A., Fan, Y., and Deng, X. (2015). "Hemodynamic Insight into Overlapping Bare-Metal Stents Strategy in the Treatment of Aortic Aneurysm." *Journal of Biomechanics* 48(10):2041–46.

Zhang, P., Sun, A., Zhan, F., Luan, J., and Deng, X. (2014). "Hemodynamic Study of Overlapping Bare-Metal Stents Intervention to Aortic Aneurysm." *Journal of Biomechanics* 47(14):3524–30.

Zhang, Y., Lu, Q., Feng, J., Yu, P., Zhang, S., Teng, Z., Gillard, J. H., Song, R., and Jing, Z. (2014). "A Pilot Study Exploring the Mechanisms Involved in the Longitudinal Propagation of Acute Aortic Dissection through Computational Fluid Dynamic Analysis." *Cardiology (Switzerland)* 128(2):220–25.

Zhang, Y., Lu, Q., Zhao, Z., Bao, J., Feng, X., Feng, R., and Jing, Z. (2014). "Multiple Overlapping Uncovered Stents as an Alternative Flow-Diverting Strategy in the Management of Peripheral and Visceral Aneurysms." *Journal of Vascular Surgery* 60(5):1209–17.

Zierer, A., Voeller, R. K., Hill, K. E., Kouchoukos, N. T., Damiano, R. J., and Moon, M. R. (2007). "Aortic Enlargement and Late Reoperation After Repair of Acute Type A Aortic Dissection." *Annals of Thoracic Surgery* 84(2):479–87.

Appendix A: Presentations and Publications

A.1 Presentations

- **Zhu, Y.,** Xu, X.Y., Asimakopoulos, G., Gambaro, A., Ulrich, R., Pepper, J., Mirsadraee, S. “Use of computational fluid dynamics in predicting progressive aortic dilatation following type A aortic dissection surgical repair.” Abstract accepted for SCTS (Society for Cardiothoracic Surgery) Annual Meeting (SCTS 2020), ICC Wales, UK, 22nd – 24th March 2020 (Oral Presentation).

- **Zhu, Y.,** Xu, X.Y., Asimakopoulos, G., Gambaro, A., Ulrich, R., Pepper, J., Mirsadraee, S. “Use of computational fluid dynamics in predicting progressive aortic dilatation following type A aortic dissection surgical repair.” SCTS National Cardiothoracic Meeting, Leicester, UK, 2nd November 2019 (*Oral Presentation*). **Winner of the Mixed Oral Session.**

- **Zhu, Y.,** Zhan, W.B., Hamady, M., Xu, X.Y. “A pilot study on aortic flow before and after endovascular repair with a novel branched stent-graft for the thoracic aortic aneurysm.” Advanced Techniques and Therapies in Cardiovascular Care (ATTICC 2018), Venice, Italy, 11st-12nd September 2018 *(Oral Presentation)*.

- **Zhu, Y.,** Zhan, W.B., Hamady, M., Xu, X.Y. “A Case Analysis of Aortic Flow before and after Endovascular Repair with Branched Stent Graft for Thoracic Aortic Aneurysm.” Young Researches’ Conference in UCL, London, UK, 19th – 20th July 2018 (*Oral Presentation*).

- **Zhu, Y.,** Zhan, W.B., Hamady, M., Xu, X.Y. “A Pilot Study on Aortic Flow before and after Endovascular Repair with a Novel Branched Stent Graft for Thoracic Aortic Aneurysm.” 8th World Congress of Biomechanics (WCB 2018), Dublin, Ireland, 8th – 12nd July 2018 (*Poster Presentation*).

- **Zhu, Y.,** Hamady, M., Xu, X.Y. “Effect of geometric variations on the performance of a novel endovascular device- Thoracoabdominal Branch Endoprosthesis.” 23rd Chinese Life Science Society-UK (CLSS-UK 2017), London, UK, 24th – 25th August 2017 (*Poster Presentation*).

A.2 Journal Publications

- **Zhu, Y.,** Zhan, W.B., Hamady, M., Xu, X.Y. (2020) A pilot study of aortic hemodynamics before and after thoracic endovascular repair with a double-branched endograft. *Medicine in Novel Technology and Devices*, 100027. https://doi.org/10.1016/j.medntd.2020.100027

- **Zhu, Y.,** Xu, X.Y., Asimakopoulos, G., Gambaro, A., Ulrich, R., Pepper, J., Mirsadraee, S. (2020) Use of computational fluid dynamics in predicting progressive aortic dilatation following type A aortic dissection surgical repair. (Submitted to *JACC: Cardiovascular Interventions)*

Appendix B: Copyright Permissions

Permission has been requested to reproduce figures protected by copyright. License numbers are presented in Table C.1. For Open Access journals and figures published elsewhere under a Creative Common License, license numbers have been listed as \Not Available" (N/A).

Table B. 1. *Figure Copyright permissions.*

Figure No.	Source	Copyright Holder	Licence No.
1.1	Blum et al. (1997)	Massachusetts Medical Society	N/A
1.2a	https://thoracickey.com/10-systemic-vascular-disease/	Thoracic Key	N/A
1.2b	Kuratani (2014)	AME Publishing Company	1018760
2.1a	https://my.clevelandclinic.org/health/treatments/17527-thoracic-aortic-aneurysm-surgery	Cleveland Clinic	N/A
2.1b	Peate and Nair (2016)	Wiley Books	4771991248013
2.2	https://weillcornell.org/aortic-aneurysm-and-dissection-repair	Weill Cornell Medicine	N/A
2.4	David et al. (2015)	Elsevier	4772000874647
2.5 (a)-(c)	Lemaire et al. (2011)	Elsevier	501549440
2.5 (d)-(e)	Kourliouros et al. (2011)	Elsevier	N/A
2.6	van Bakel et al. (2018)	AME Publishing Company	1018755
2.7	Patel et al. (2013)	Springer Nature	4772020581269
2.8	Mendes et al. (2016)	Elsevier	4772040041521
2.9	Nienaber et al. (2016)	Springer Nature	4772020768756
2.10	Nienaber and Eagle (2003)	Wolters Kluwer Health	501547834
3.1	Versteeg and Malalasekera (2007)	Pearson	N/A
3.3	Roy et al. (2012)	(Roy et al. 2012)	N/A
3.4	Rachid (2017)	Rachid (2017)	N/A
8.1	Pirola et al. (2019)	IEEE	N/A